COMPREHENSIVE SIMULATION AND EXPERIMENTAL CHARACTERIZATION OF VARIOUS CONFIGURATIONS OF A GROUND-LEVEL INTEGRATED DIVERSE ENERGY STORAGE (GLIDES) SYSTEM

A Dissertation
Presented to
The Academic Faculty

by

Adewale O. Odukomaiya

In Partial Fulfillment
of the Requirements for the Degree
Doctor of Philosophy in the
George W. Woodruff School of Mechanical Engineering

Georgia Institute of Technology
May 2018

COMPREHENSIVE SIMULATION AND EXPERIMENTAL CHARACTERIZATION OF VARIOUS CONFIGURATIONS OF A GROUND-LEVEL INTEGRATED DIVERSE ENERGY STORAGE (GLIDES) SYSTEM

Approved by:

Dr. Samuel Graham, Advisor
School of Mechanical Engineering
Georgia Institute of Technology

Dr. Sheldon Jeter
School of Mechanical Engineering
Georgia Institute of Technology

Dr. Ayyoub M. Momen
Energy & Transportation Science Division
Oak Ridge National Laboratory

Dr. Thomas F. Fuller
School of Chemical and Biomolecular Engineering
Georgia Institute of Technology

Dr. Shannon Yee
School of Mechanical Engineering
Georgia Institute of Technology

Date Approved: December 7th, 2017

ACKNOWLEDGEMENTS

I would first like to acknowledge the various sources of funding support that helped fund my work. I am grateful to the NSF IGERT fellowship program, the ORNL GO! program, the ORNL LDRD program, the GEM fellowship program, the Alfred P. Sloan Foundation fellowship program and the DOE EERE Building Technologies and Water Power Technologies programs. The list of people that had a positive influence and played a role in my academic achievements to date is far too long to thank everyone by name. As they say, it truly takes a village, and I am grateful to all these people. I would like to start off by thanking the members of my research groups, both at Oak Ridge National Laboratory and Georgia Tech. At ORNL, I am grateful to Ahmad Abu-Heiba, Alla Akinina, Kyle Gluesenkamp, Omar Abdelaziz, and Roderick Jackson for numerous things including the many brainstorming sessions, serving as co-authors and reviewers on paper manuscripts, and funding support. At Georgia Tech, I am grateful to my colleagues Georges Pavlidis, Anne Mallow, Luke Yates, Kenechi Agbim, Kyungjin Kim, and Nick Hines for many helpful conversations and general moral support. Next, I would like to thank my PhD reading committee, Dr. Shannon Yee, Dr. Sheldon Jeter, Dr. Thomas Fuller. Special thanks to my two research advisors, Dr. Sam Graham at Georgia Tech, for his mentorship and flexibility in allowing me to collaborate with ORNL on a PhD topic that is of interest to me and very dear to my heart, and Dr. Ayyoub Momen at ORNL, for his constant enthusiasm, never ending stream of ideas, and the deliberate effort he made to expose me to all aspects of research, good and bad, from grant writing and budget management, to having a seat at the table with high-level collaborators and visitors, to mentoring undergraduate students, to dealing with frustrating vendors and craft-hands. I am eternally grateful to my family, my three older siblings for paving the way before me, and

specifically my parents Anthony and Nike for emphasizing the importance of education and providing their unending love, emotional support, financial support, etc. Last but certainly not least, I must always thank God for placing the dreams in my heart and providing the means to chase after them.

TABLE OF CONTENTS

LIST OF TABLES

LIST OF FIGURES

NOMENCLATURE

ABBREVIATIONS

AA-CAES	Advanced-Adiabatic Compressed Air Energy Storage
CAES	Compressed Air Energy Storage
ED	Energy Density
GLIDES	Ground-Level Integrated Diverse Energy Storage
HVAC	Heating Ventilation and Air Conditioning
LAES	Liquid Air Energy Storage
LTA-CAES	Low Temperature Adiabatic Compressed Air Energy Storage
ORNL	Oak Ridge National Laboratory
PD	Positive Displacement
PHES	Pumped Heat Electricity Storage
PSH	Pumped Storage Hydroelectricity
RTE	Round Trip Efficiency
RK	Redlich-Kwong

T-CAES	Trigenerative Compressed Air Energy Storage

SYMBOLS

ED	Energy density [kWh/m^3]
m	Mass [kg]
c	Specific heat capacity [J/kg-K]
T	Temperature [K]
h	Heat transfer coefficient [W/m^2-K]
A	Heat transfer area [m^2]
UA	Overall heat transfer coefficient [W/K]
p	Pressure [bar]
V	Volume [m^3]
$\dot{m}$	Mass flow rate [kg/s]
t_T	Wall thickness [m]
k	Thermal conductivity [W/m-K]
v	Velocity [m/s]
D	Diameter [m]

g	acceleration due to gravity [m/s^2]
C_D	Drag coefficient
t	time [s]
L	Length [m]
N	number or speed (RPM)
$\dot{N}$	Number of droplets per unit time [s^{-1}]
$\dot{V}$	Volumetric flow rate [m^3/s]
Nu	Nusselt number
Re	Reynolds number
Pr	Prandtl number
$\dot{Q}$	Heat transfer rate [W]
W	Work [J]
Q	Heat [J]
num	Number of
jet	Pelton turbine jets
$pause$	Idle period

$\dot{W}$	power [W]
R	air specific gas constant [J/kg]
i	specific enthalpy [J/kg-K]
SE	specific energy [kWh/kg]
E	energy [J]
p*	dimensionless pressure
V*	dimensionless volume
t*	dimensionless time
x	quality
P	power [kW]
PV	present value [$]
C	annual savings [$]
i	interest rate
N	desired payback period [years]
n	polytropic exponent
w	work per unit volume

INDICES

v	at constant volume
G	of gas (Ch. 2, 3, 4) or grid (Ch. 7)
L	of liquid (Ch. 2, 3, 4) or load (Ch. 7)
amb	of ambient air
T	of tank walls, or of turbine
i	inner
o	outer
ave	average
min	minimum
dr	of the drop(s)
ini	initial
spr	of the spray
in	inlet or input
term	terminal (velocity)
trav	travel (residence)

S	surface or storage (Ch. 7)
out	outlet or output
max	maximum
mixed	mixture of bulk and spray liquid
WH	waste heat
ind	indicated (i.e. hydraulic or thermodynamic)
elec	electrical (after all component losses)
Carnot	Carnot (efficiency)
c	charging or compression
pump	of pump
gen	generator
dc	discharge
shaft	of shaft
air	air
0	at time zero
f	liquid (fluid) or final

sat	saturated
e	expansion
fg	of vaporization
∞	ambient temperature
cond	condensation/condensed
liq	of the liquid
vap	of the vapor
CO_2	of carbon dioxide (liquid and vapor)
h	hydraulic
s	shaft
atm	atmospheric
uu	unused
u	useful
st	storage

GREEK LETTERS

ΔT	temperature difference

η_{elec} electric roundtrip efficiency

η_{ind} indicated efficiency

η_{Ex} exergetic efficiency

ρ density [kg/m^3]

τ thermal time constant [s]

ε heat exchanger effectiveness

η_{shaft} shaft-to-electrical efficiency (or shaft-to-shaft)

τ_{shaft} shaft torque [Nm]

ω_{shaft} shaft speed [rev/s]

η efficiency

π dimensionless compression figure of merit

SUMMARY

Increasing the penetration of renewable electricity while ensuring grid stability requires low-cost, high roundtrip efficiency energy storage solutions. GLIDES (Ground-Level Integrated Diverse Energy Storage) is a novel mechanical energy storage concept developed at Oak Ridge National Laboratory that hybridizes the existing compressed-air (CAES) and pumped-storage (PSH) approaches to energy storage. Energy is stored by pumping a liquid into high pressure vessels which are pre-pressurized with a gas, until the gas pressure reaches the maximum system operating pressure. Energy is then extracted by allowing the high-pressure gas to expand, pushing the high-head water through a hydraulic turbine coupled to an electrical generator dispatching electricity. In addition to electrical energy input via the hydraulic pump, the system can also be hybridized to receive heat as an input. Low/medium temperature heat can be utilized to further boost the gas pressure, increasing roundtrip efficiency (RTE) and energy density (ED). GLIDES is scaleable, relatively low cost and de-couples the energy capacity from the power capacity, a challenge faced with existing storage solutions. Analyses predict that GLIDES could achieve roundtrip efficiencies in the 65-85% range. Analytical, transient, physics-based system models of various configurations of GLIDES have been developed and theoretical performance analyses completed. A first generation 1.5 kWh prototype has been designed and built, and experimental characterizations and model calibration/validation completed. A second generation, 1 kWh prototype which is mobile/portable and integrates spray cooling/warming to manage the heat of compression and cold of expansion as well as waste-heat has also been designed, built, and characterized. In addition to the above, the use of condensable gases as an alternative working fluid to air is explored as a means of improving system efficiency and energy density. Some consideration is given to the choice and design of the energy recovery hydraulic machine. The

first-generation GLIDES prototype utilizes a Pelton turbine; a few aspects related to the design of such machines are explored. The second-generation prototype utilizes a hydraulic axial-piston type motor, thus a qualitative discussion of the pros and cons of utilizing an impulse Pelton turbine versus a hydraulic motor as the energy recovery turbomachine is given. Finally, cost-analysis of the scale-up prospects of GLIDES is conducted via backward and forward analyses.

CHAPTER 1. INTRODUCTION

1.1 Background & Motivation

In recent years, energy storage has emerged as a growing area of research and technology development for several reasons. In the late 1980's and 1990's, energy storage as a technology was driven by the demands in the areas of mobile devices and personal electronics [1]. In more recent years, a critical need to ensure continued stability of aging electrical grids, and facilitate the integration of intermittent renewable energies to the grid at large scales has emerged for energy storage technologies at much greater power and energy capacities, but lower cost [2]. Historically, the power grid has been governed by the constraint that power generation and consumption must be matched both temporally, and in capacity; efficient, affordable energy storage comes with the potential to relax this constraint [1]. As economies continue to evolve and become more energy intensive, and humans continue to find new ways to consume energy, fluctuations in energy demand throughout the day will become more drastic and less predictable, and power quality will suffer if energy supply cannot be adjusted accordingly [3].

In addition to the important implications that energy storage has for the power grid and energy supply/demand management, energy storage will also play a key role in increasing the integration of renewable energy technologies with the current grid infrastructure which poses a challenge due to their inherent intermittency [4]. Wind and solar energy for example are intermittent in supply, but typically available in excess when available. This presents a large challenge in trying to match energy generation with demand when such renewable sources are used. There exists an opportunity to store excess renewable energy while available and to be dispatched during intermittency, bridging the temporal gap between generation and energy

demands. Considering all the above, there is a great need for high-efficiency, highly scalable, cost-effective storage systems that are environmentally benign, flexible, easily dispatched, and easily integrated with renewable sources. To this end, a Ground-Level Integrated Diverse Energy Storage (GLIDES) system was recently invented and is under development at Oak Ridge National Laboratory [5], which is a hybrid compressed air-hydro energy storage concept. The GLIDES technology targets energy storage applications for power capacities under 10 MW, storage times of a few minutes to a few (4-6) hours, and response times on the order of seconds.

GLIDES stores energy by compressing a gas in high-pressure tanks but uses a high efficiency hydraulic pump with minimal frictional losses instead of the usual lower efficiency gas compressor used in most gas compression schemes. The system is charged by pumping water into the tanks, squeezing the gas above from an initial pressure until the pressure reaches the maximum design pressure. When electricity is required, the now high pressure gas pushes liquid out of the tanks through a hydraulic turbine which is coupled to a high efficiency electrical generator, efficiently dispatching electricity. As an option, the system can be hybridized by leveraging any available waste heat to heat the gas during discharge, fight the cold of expansion, maintain pressure, and boost extractable energy. Even low/medium temperature (40-90 °C) waste heat available from solar thermal receivers, turbine or CHP exhaust, geothermal sites, etc., could be leveraged. Because the system is charged by pumping water using a high efficiency positive displacement pump (typically η>90%) [6] and energy is extracted using a high efficiency hydraulic turbomachine (also η>90%) [7], the gas experiences minimal temperature swings (compared with conventional gas compression/expansion schemes) which significantly reduces the thermodynamic losses due to expansion/compression. Other system losses are due to ancillary components (motor and generator). GLIDES is predicted to achieve electric roundtrip efficiency

in the 0.60-0.82 range; this coupled with the fact that energy inputs can come in the form of electricity or low/medium grade heat, makes it a first-in-kind, unique, high potential energy storage solution. Comprehensive, physics-based analytical modeling/simulation of the base (prototype) configuration and modified configurations has been completed [8, 9], two working prototypes have been developed and demonstrated, experimental characterization has been performed, and thermo-economic analysis of system scale-up performed.

1.2 Review of Bulk Energy Storage Technologies & Research

1.2.1 Existing Bulk Energy Storage Technologies

To increase the penetration of renewable energy technologies, low-cost, high roundtrip efficiency (RTE) energy storage solutions are necessary to avoid grid instability resulting from the intermittent nature of renewable sources [4, 10]. About 99% of currently installed electrical energy storage capacity worldwide consists of pumped-storage hydroelectricity (PSH) [11, 12], which is a large-scale/capacity (MW-GW), high RTE (65–87%), technologically mature solution [12, 13], costing up to $100/kWh [12-14]. PSH operates via a simple principle: during charging, water is pumped from a lower reservoir to an upper reservoir and during discharging, or energy extraction, the water flows from the upper reservoir down to the lower reservoir, through a turbine which dispatches electricity via an electrical generator. Site selection for PSH has been difficult because it is geographically limited to sites where a large head of water can be developed by large differences in height (>500 m ideally) [15]. Additionally, market conditions for large-scale storage systems vary and are unfavorable in some countries, which hinders the development of new projects.

Compressed air energy storage (CAES) is another large-scale/capacity storage technology that has been considered where PSH is not feasible. With CAES, off-peak electricity is used to compress atmospheric air into underground hard-rock or salt caverns using reversible motors/generators turning a chain of gas compressors. An above-ground system of vessels or pipes can also be used instead of underground caverns, for smaller scale CAES systems [13, 16]. For electricity extraction, the compressed air is released and mixed with natural gas as it expands and is burned through a gas turbine. Similarly to PSH, large-scale CAES is limited to suitable geographical locations, in this case, locations where the topography allows for naturally occurring underground caverns [17]. So far, there are only two commercial CAES plants in operation; they are located in Huntorf, Germany, and MacIntosh, Alabama [18]. Conventional CAES suffers from low roundtrip efficiency (~40–50%) because of the significant energy losses in gas compressors and turbines [13, 19]. These CAES systems are reported to cost up to $120/kWh [13]. CAES as a technology is undergoing rapid improvement. It is attracting much research interest [14], and a number of more advanced CAES concepts are currently at the research and development stage.

More recently, advanced adiabatic CAES (AA-CAES) systems have been proposed, and the development is ongoing [20, 21]. This advanced CAES concept produces higher efficiencies than conventional CAES configurations by storing the heat of compression for use during discharging. Efficiencies around 70% have been reported for AA-CAES [13, 19, 20]. Furthermore, technical comparisons among various adiabatic CAES plant configurations have been reported [22]. Plans for the world's first demonstration of an AA-CAES plant were underway in Germany [23]; however, development was stopped because of poor economic feasibility.

A variation of AA-CAES that results in trigeneration (T-CAES) (combined energy storage, heating, and cooling) for microscale CAES systems has been proposed [24-26]. Similar to AA-

CAES, the heat of compression is removed and stored; however, instead of being dispatched during expansion at the turbine inlets, it is used to fulfill a heating need. This causes the discharge phase air inlet temperature to be low, and cooling energy is obtained at the end of the expansion stage which can then be used to fulfill a cooling demand. With such a configuration, a T-CAES plant would need to be co-located with the energy, heating, and cooling demands because of the technological challenges associated with transferring thermal energy over large distances [25]. Hybridization for trigeneration has a moderate effect on cycle efficiency, as peak efficiencies in the 30–60% range (depending on ambient conditions, component efficiencies, and other configuration specifications) are reported [25, 26].

The low-temperature adiabatic CAES (LTA-CAES) is another proposed variant to AA-CAES [27]. This concept aims to avoid the technical challenges of dealing with the high thermal energy storage temperatures and high pressures with AA-CAES [27]. In Ref. [27], it is shown analytically that reducing the maximum process temperature does not incur roundtrip efficiency penalties, and a plant design which reduces TES operating temperature to a 90–200°C range from the typical 600°C value is presented. Roundtrip efficiencies in the range of 52–60% are reported, which is lower than AA-CAES; however, advantages over AA-CAES are reported which include fast start-up and superior part-load performance [27]. These advantages are reported to compensate for lower cycle efficiency with regard to plant profitability [27].

A hybrid energy storage concept that is comprised of an aboveground CAES system supplemented with a liquid air energy storage (LAES) system [28] has been proposed [29]. This concept attempts to take advantage of the relatively higher roundtrip efficiency of CAES and lower cost and high energy density of LAES. The LAES hybridization serves primarily as a capacity extension mechanism. If electricity prices are low, or if energy is available from renewable sources

while the CAES component of the system is already fully charged, electricity input can still be accepted by liquefying some of the compressed air to liquid air. Conversely, when electricity dispatch is needed but compressed air reserves are low or exhausted, electricity can still be dispatched by converting some liquid air back to compressed air [29]. The key component of this concept is a liquefaction subplant, which would have varying efficiency depending on scale. A roundtrip efficiency of 53% is reported in Kantharaj *et. al.* [30]; however, the capacity extension achieved through the LAES hybridization offers the possibility for larger-scale aboveground CAES, which was previously only possible at smaller scales.

The pumped heat electricity storage (PHES) concept was recently introduced. This system stores energy by pairing a heat pump with a heat engine using thermal storage as the cold and hot reservoirs [31]. PHES systems store electrical energy via a heat pump, which pumps thermal energy from the cold storage reservoir to the hot storage reservoir. To discharge, or recover the stored energy, the heat pump operation is reversed, turning it into a heat engine cycle which spins an electrical generator for electricity dispatch. PHES is reported to be cost effective with the potential to reach high roundtrip efficiency in the range of 75–80% [32]; however, achieving this is dependent on achieving extremely low thermodynamic losses in the compressor and expander machines [33]. Such high turbomachine efficiencies for the reciprocating devices presented for use have yet to be proven [33]. Due to the thermally activated nature of this technology, it is conceivable that heat might potentially be provided directly as an energy input; however, this has not been proposed in the literature. A pilot demonstration PHES facility was under development as recently as January 2015 [33]; the project was suspended in January 2016 [34].

Effective management of heat remains one of the primary challenges associated with compression-based energy storage schemes [29]. To this end, a number of concepts have been

proposed to address the heat management challenge [35-41]. These concepts include utilizing advanced heat transfer via sprayed liquid droplets to achieve isothermal or near-isothermal compression [35-37], utilizing dense foams for the same purpose [40], designing under water systems [39], and utilizing liquid-piston compression and expansion among other strategies [35, 41]. As is described in subsequent sections, the GLIDES concept presented here also makes use of sprayed liquid droplets to achieve near-isothermal compression and expansion. However, this approach is taken one step further in the concept and also provides a medium for waste heat integration/storage.

Currently, batteries are the most widely used energy storage technology in building applications [17]. Batteries rely on storing energy in the form of electrochemical energy. In batteries, several electrochemical cells are connected in series or parallel to produce electricity at a desired voltage. In general, each battery cell contains an anode (negative lead), a cathode (positive lead), and an electrolyte, which can be in solid or liquid form. When connected to an electrical circuit, chemical reactions in the battery cause electrons to build up at the anode, and charge flows through the circuit. The electrolyte serves as a source of ions. During discharging, the reverse reaction occurs. Lead-acid batteries are the oldest, most developed, and most widely used battery chemistry [13, 15]. They have been implemented in several applications, including wind energy, solar energy, and automotive use [13]. Challenges/drawbacks with lead-acid batteries include toxicity/environmental hazards [15], challenging scale-up prospects due to limited lifespan and higher cost [15], as well as poor deep discharge capabilities, relatively low cycling times, energy density, and challenging thermal management [13, 14]. Lithium-ion (Li-ion) technology is a newer battery chemistry which has been the focus of significant research and development efforts in recent years. Li-ion batteries have been proposed and have emerged in building applications,

especially as part of integrated building energy management solutions, including smart grid initiatives [17]. More recently, Tesla has announced a 3.3 kW, 6.4 kWh, residential-scale Li-ion battery solution with reported roundtrip efficiency of 92.5%, and cost below $500/kWh [42]. Li-ion technology offers a number of advantages over lead-acid, including, high cycle lifetime, high peak power capability, lower environmental impact, higher energy density, and higher cycle efficiency [13, 15, 17]. Batteries in general have higher energy capital costs than the previously discussed storage technologies, with Li-ion being even more expensive than lead-acid; this can be seen in Table 1.1. Furthermore, Li-ion battery chemistries have been associated with a higher risk of fire/explosion incidents [43]. With the exception of CAES, other storage solutions are unable to exploit the opportunity to use waste heat as an input in addition to electricity. Table 1.1 provides a summary of the technical characteristics of the energy storage technologies discussed. There remains a need for high-efficiency, cost-effective storage systems that are environmentally friendly, flexible, easily dispatched, easily integrated with renewable sources, and scalable across various applications from individual buildings (kW) to plant-scale (MW-GW).

Table 1.1: Technical characteristics of several energy storage technologies

Technology	Scale[12, 13, 17]	RTE [%]	ED [kWh/m^3]	Capital Cost* [$/kWh]	Cycle Life [cycles]	Lifetime [years]	Maturity	Advantages	Disadvantages
PSH	GW	70-87[13] 70-80[12] 65-80[14] 75-80[44]	0.5-2[13] 0.2-0.6[12]	5-100[12, 13] 10-80[14]	10,000-30,000[13] 15,000+[12] 20,000-50,000[14]	30+[13] 50+[12] 30-50[14]	Mature	High capacity, low cost	Geographically limited, poor expansion prospects
CAES (conventional)	MW-GW	42,54[13] 42[19]	3-6[13] 2-6[12]	2-120[13] 2-50[12] 3-80[14]	8,000-12,000[13] 10,000+[12] 10,000-30,000[14]	20+[13] 25+[12] 30,40[14]	Commercialized	High capacity, heat input	Geographically limited, lower efficiency
CAES (other)	kW-MW	a)60-70[45] b)69,[20] 70[13, 19] c)30-60[25, 26] d)52-60[27] e)53[30]	a)Higher than conventional CAES[13]	a)200-250[13] b)30-40% higher than conventional CAES[19]	a)30,000[13]	a)23+[13]	a,b)R&D, Demonstration c,d,e)Concept	a,e)Geographic flexibility, b)higher RTE	c)Geographically limited, a,c,d,e)lower RTE
Lead-Acid	kW-MW	63-90[13] 75-90[12] 70-80[14]	50-90[13] 50-80[12]	200-400[12] 350-3800[45]	500-1,000[13] 250-1,500[12] 200-1,800[14]	5-15[13, 14] 3-15[12]	Mature	High energy density	High cost, challenging scale-up
Lithium-Ion	kW-MW	75-97[13] 65-75[12] 78,88[14]	150-500[13] 200-400[12]	600-3800[13] 600-2,500[12] 900-1,300[14]	1,000-20,000[13] 600-1,200[12] 1,500-3,500[14]	5-16[13] 14-16[14]	R&D, Demonstration	High energy density, high efficiency	High cost, chemical recycling, challenging scale-up

*Capital cost is defined as costs associated with the capital or investment expenditures per unit of energy storage capacity
a) Aboveground CAES
b) AA-CAES (advanced-adiabatic)
c) T-CAES
d) LTA-CAES (low temperature adiabatic)
e) LA-CAES (liquid-air)

1.2.2 Similar Hydro-Pneumatic Energy Storage (HyPES) Concepts

The push to achieve isothermal or near-isothermal compression and expansion has resulted in the emergence of a sub-category of I-CAES known as hydro-pneumatic energy storage (HyPES). In this category of storage devices, a liquid is utilized to compress the gas. The liquid (water or hydraulic oil) is pumped into the storage vessel, serving as a liquid-piston, squeezing the gas above, reducing its volume and increasing pressure. To recover the stored energy, the liquid is allowed to flow in the reverse direction through a hydraulic turbine which drives an electrical generator. The HyPES concept is the general premise of the GLIDES technology presented here. A number of these concepts have been presented in the literature [41, 46-50]. These concepts have notable similarities and differences to the GLIDES concept. Wang *et al.* [46] proposed a concept

which also utilizes high efficiency hydraulic pump and turbine, and pressure vessels as the storage medium. However, a number of differences were found between their analysis and the present one. Constant pump and turbine efficiencies were assumed in the analysis, and variation in the performance of these components with varying operating conditions was not considered. In addition, the physical model presented assumes the pressure vessels are adiabatic, and expansion and compression isothermally, thus not accounting for expansion/compression losses due to non-isothermal operation which would likely be the case in reality. This study does discuss the potential to use liquid spraying during charging and discharging, similarly to GLIDES, however, no system roundtrip efficiency is reported. Furthermore, this work is purely theoretical, and no mention of a prototype or experimental investigation was made.

Yao *et al.* [47] proposed a novel constant-pressure pumped hydro combined with compressed air energy storage system which has the advantage of operating at constant pressure which allows for operation at the design condition. However, the model presented in this work also assumes adiabatic high pressure vessels and constant pump and turbine efficiencies. While there is an efficiency advantage due to constant pressure operation, a gas compressor is still required and flow controllers are utilized to maintain pressure, causing a hit on efficiency. System efficiency between 50-72% and energy density between 0.42-1.06 kWh/m^3 were reported. Similarly to Wang *et al.* this study is also purely theoretical. Kim *et al.* [48] reported on the operating characteristics of a constant-pressure compressed air energy storage system combined with pumped hydro storage. This concept is a true CAES-PSH hybrid, as it includes the full working principles of both technologies, but a column of water is utilized to maintain gas pressure on the CAES side, instead of the usual throttling of the gas compressor upstream air to keep the inlet pressure constant. This provides a boost in system efficiency and the water column is also

passed through a water turbine as it displaces the gas in the CAES side, dispatching additional electricity. Unlike the previous two, this study does account for heat transfer between the various mediums in the model, but also assumes constant water pump and water turbine efficiencies. Similarly to conventional CAES, this concept relies on underground salt formations/caverns for use as the storage medium. Lemofouet-Gatsi's work is the single work found in the literature which studied the concept theoretically as well as experimentally at very small scale (15 Wh_e max) [50].

Table 1.2 summarizes the main characteristics of the concepts presented in the aforementioned works. All the studies presented above utilize a simple state-by-state thermodynamic approach to system modelling, and not a transient model which enables capturing real, time-dependent effects such as heat transfer. Furthermore, with the exception of Lemofouet-Gatsi's work, no operational prototype or experimental demonstration of these systems has been reported, and none have demonstrated the HyPES system with waste-heat integration. To our knowledge, GLIDES is largest-scale, end-to-end (electrical-to-electrical) demonstration of a fully operational HyPES prototype system.

Table 1.2: Summary of comparison of similar HyPES storage concepts found in the literature

	System Efficiency [%]	**Energy Density [MJ/m^3]**	**Constant Pressure**	**Heat Input**	**Prototype**
Wang *et al.*	not reported	0.42-3.33	no	no	no
Yao *et al.*	50-72	0.42-1.05	yes	no	no
Kim *et al.*	43-76.5	0.14-5.56	yes	no*	no
Lemofouet	19-59	0.23-0.5	no	no	yes
GLIDES$^+$	66-82	0.68-1.00	no	yes	yes

*no heat input but heat of compression is recovered and used during expansion

1.3 Research Contributions

While the overall research effort discussed herein is aimed at the modelling, design, demonstration and optimization of the novel GLIDES system, the fundamental research questions being asked are:

1. Can isothermal or near-isothermal compression and expansion be achieved via the use of a liquid-piston?
2. Is liquid-piston based hydro-pneumatic compressed gas energy storage viable? If so, can it achieve comparable or better efficiency and energy density to conventional CAES?
3. What are the major loss mechanisms in the complete end-to-end energy storage system?
4. What are the maximum theoretical efficiency/energy density and what innovations can be made to meet or approach these?
5. Going beyond the scientific and engineering questions, can a liquid-piston based hydro-pneumatic compressed gas storage system be cost-competitive with, or cheaper than existing solutions?

Pursuant to these, four specific research contributions are made. First, the development of an analytical, transient, physics-based model of multiple configurations of the GLIDES gas cycle and complete energy system going beyond ideal state-by-state point analyses and capturing all loss mechanisms is presented. Development of this type of detailed modelling framework is important in order to guide system design, provide a test-bed to conduct more nuanced system performance analyses that would be difficult to carry-out experimentally, and determine major loss mechanisms. Furthermore, the addition of the transient terms to the governing equations provide the opportunity to investigate in detail the heat-transfer phenomena at play during gas expansion

and compression, and investigate the feasibility/effectiveness of carrying out heat transfer enhancement strategies such as spray cooling/warming in order to achieve isothermal or near-isothermal compression/expansion. Such analysis is difficult to carry-out using the conventional state-by-state point modelling techniques used in thermodynamic system evaluations. Second, experimental demonstration of the HyPES-based GLIDES concept in multiple configurations is demonstrated. This is the largest end-to-end demonstration of the application of liquid-piston gas expansion/compression to a compressed-air energy storage device and provides a benchmark for its performance and further development. To our knowledge, this is also the first experimental demonstration of the HyPES concept integrating waste-heat to improve system performance. Additionally, the use of condensable gases as an alternative working fluid to air for the GLIDES system to improve performance is explored. Thirdly, the research on Pelton turbines is extended to the ultra-high head, ultra-low flow rate application regime, where existing rules-of-thumb for key design parameters such as bucket geometry, jet diameter, and jet alignment cannot necessarily be applied. Given the high-head, low-flow rate nature of the GLIDES turbine application regime, and considering existing knowledge about application regimes of impulse turbomachines, a Pelton turbine is one obvious choice of machine. However, this application pushes the envelope of pressure head and flow rate regime of Pelton turbine use that have been documented, and so some effort to characterize performance of various design aspects in this regime and test the validity of existing Pelton turbine design rules and rules-of-thumb in this application regime is necessary. In addition, the second-generation GLIDES prototype utilizes an axial-piston type hydraulic motor as the energy recovery turbomachine, instead of the Pelton turbine used in the first generation prototype, thus, a qualitative discussion on the pros and cons of each of these two types of energy

recovery machines for use in HyPES concepts is given. Via these research contributions, the fundamental questions asked in the beginning of this section are answered.

1.4 Dissertation Outline

The subsequent chapters in this dissertation are organized as follows: Chapter 2 provides an overview of the comprehensive physics-based system simulations of various configurations of the GLDIES system conducted in support of the prototype design. Chapter 3 presents the design and experimental evaluation of the first-generation GLIDES system. The experimental results from the first-generation system are also used to calibrate the system model; these results are also presented in Chapter 3. In Chapter 4 the research conducted on utilizing condensable gases as an alternative working fluid to air in the GLIDES system is presented. First, an initial investigation at low pressure is conducted with refrigerant R134a. The success with R134a led to a second effort with CO_2, which would be the choice condensable gas for a scaled-up system, owing to its high saturation pressure. Next, Chapter 5 presents the design and characterization of the second-generation prototype which features several performance enhancement measures compared with the first-gen prototype. In Chapter 6, considerations on the energy recovery (discharge) turbomachine is given. Aspects related to the design of the Pelton turbine for this application are discussed, and the use of a hydraulic motor instead of a Pelton turbine is also discussed. In Chapter 7, methods and results of cost-scaling and market value analysis for the prospects of a commercial-scale GLIDES are given. Finally, a summary of the dissertation is provided in conclusion, and remaining “white-spaces” needing to be addressed with future research efforts are revealed.

CHAPTER 2. COMPREHENSIVE SYSTEM SIMULATIONS

Content in this chapter (figures and text) adapted from:

1. Odukomaiya, A., *et al.*, Thermal analysis of near-isothermal compressed gas energy storage system. Applied Energy, 2016. 179: p. 948-960. [51]

This chapter introduces multiple configurations of the GLIDES concept and explores the feasibility of a strategy to integrate waste heat utilization with direct contact heat exchange via spray cooling and warming. GLIDES is predicted to achieve electric roundtrip efficiency (η_{elec}) in the 70–82% range (after accounting for non-isothermal compression/expansion and conversion losses in pump/motor and turbine/generator) and energy input can come in the form of electricity or low- or medium-grade heat. This chapter focuses on the analytical comparison of the performance of different GLIDES design configurations for a system with the same size and maximum pressure rating as the first-generation proof-of-concept prototype and presents the results of energy analyses used to assess and quantify the feasibility of performance enhancement strategies.

2.1 Description of the System Components & Configurations

As seen in Figure 2.1, the GLIDES system consists of an atmospheric pressure water storage reservoir, a pump, a pressure tank containing a gas (i.e., air, nitrogen, CO_2), and a turbine and generator used to generate electricity. Positive displacement (PD) pumps are chosen to pressurize the tank and are designed for low-flow, high-head applications (e.g., 200–300 bar or about 2–3 km water head) in which their mechanical efficiencies do not substantially change over a wide pressure head or flow rate range. The mechanical efficiency of PD liquid pumps can be

over 90% [6]. High-efficiency PD pumps are commercially available in a wide size range (1–500 kW). A Pelton turbine was chosen because it is a low-cost hydraulic impulse turbomachine suitable for low-flow, high-head applications (greater than 80 m water head). Pelton turbines are quite scalable and are available in a range from a few kilowatts to 300 MW. A beneficial feature of Pelton turbines is that their peak efficiency is fairly insensitive to flow rate [52]. A typical Pelton turbine can have one to five impinging jets; the flow rate and the output power can be adjusted by turning each impinging jet on or off without significantly affecting the turbine efficiency. The mechanical efficiency of Pelton turbines can exceed 93% [7]. High-pressure gas tanks, chosen as the storage reservoir (10–1000 liters), are commercially available for pressures higher than 300 bar (3 km of water head).

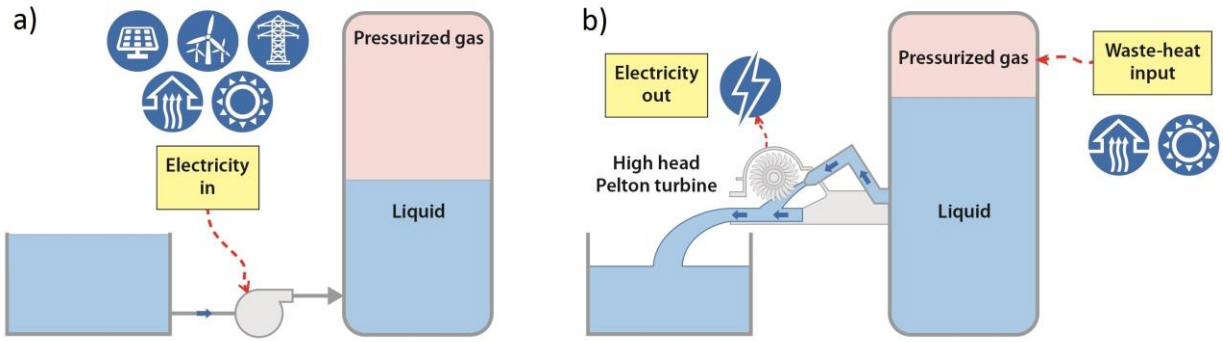

Figure 2.1: GLIDES layout during charging (a) and discharging (b)

2.2 Thermodynamic Flexibility

The liquid in the GLIDES system is analogous to a gigantic, slow but no-leak piston inside a large cylinder (liquid-piston). Due to the large length scale (large-scale system) and long time

scale (slow charging/discharging) seen in operation of the GLIDES system, it is possible to closely control the gas cycle and the associated heat transfer. As a result, the gas cycle can be controlled to mimic almost any major thermodynamic cycle found in the literature and also introduce opportunities for introducing even more complex thermodynamic cycles by controlling the heat transfer rate. Individual processes can be controlled to be near isothermal, and heat addition/removal can be isobaric or isochoric. Figure 2.2 below shows *p*-*v* diagrams for a subset of ideal thermodynamic cycles that can be approached with the GLIDES cycle. In the cycle shown in Figure 2.2 a), charging occurs isothermally from state 1 to state 2, after which discharging also occurs isothermally back to state 1. In the cycle shown in Figure 2.2 b), charging is achieved via isothermal compression as the cycle proceeds from state 1 to state 2, then isochoric heat input occurs to state 3, after which the gas expands isentropically back to state 1. In Figure 2.2 c), process 1-2 is isothermal compression, followed by isobaric heat input to state 3, then isothermal expansion to state 4, and, finally, the system returns to state 1 as isochoric heat removal occurs. The cycle shown in Figure 2.2 d) is similar to Figure 2.2 c), except process 2-3 is an isochoric heat addition. Note that Figure 2.2 d) is known as a Stirling cycle.

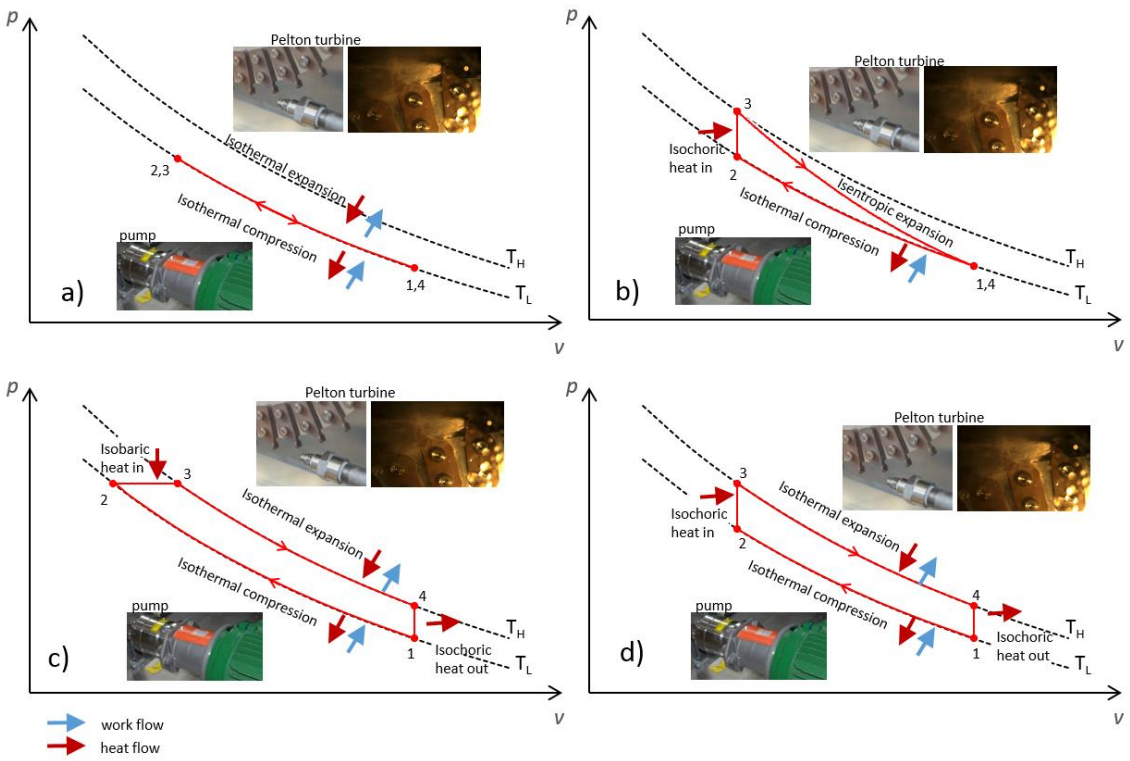

Figure 2.2: Thermodynamic flexibility of the GLIDES concept

Departure from the ideal cycles shown in Figure 2.2 occurs due to real effects such as the shell heat losses during standby between charging/discharging, limited heat transfer during charging/discharging, and heat transfer enhancement strategies such as spray cooling/heating. These will be discussed in further detail in subsequent sections. Particularly, the deviation from the ideal cycle seen in Figure 2.2 a) and d) due to real effects will be examined as a starting point for operation of the GLIDES system.

2.3 Studied Configurations

Figure 2.3 depicts the three different GLIDES configurations investigated in this study. The image at the left shows the base GLIDES configuration described earlier; specifications and performance for this configuration are also reported in Odukomaiya et al. [8].

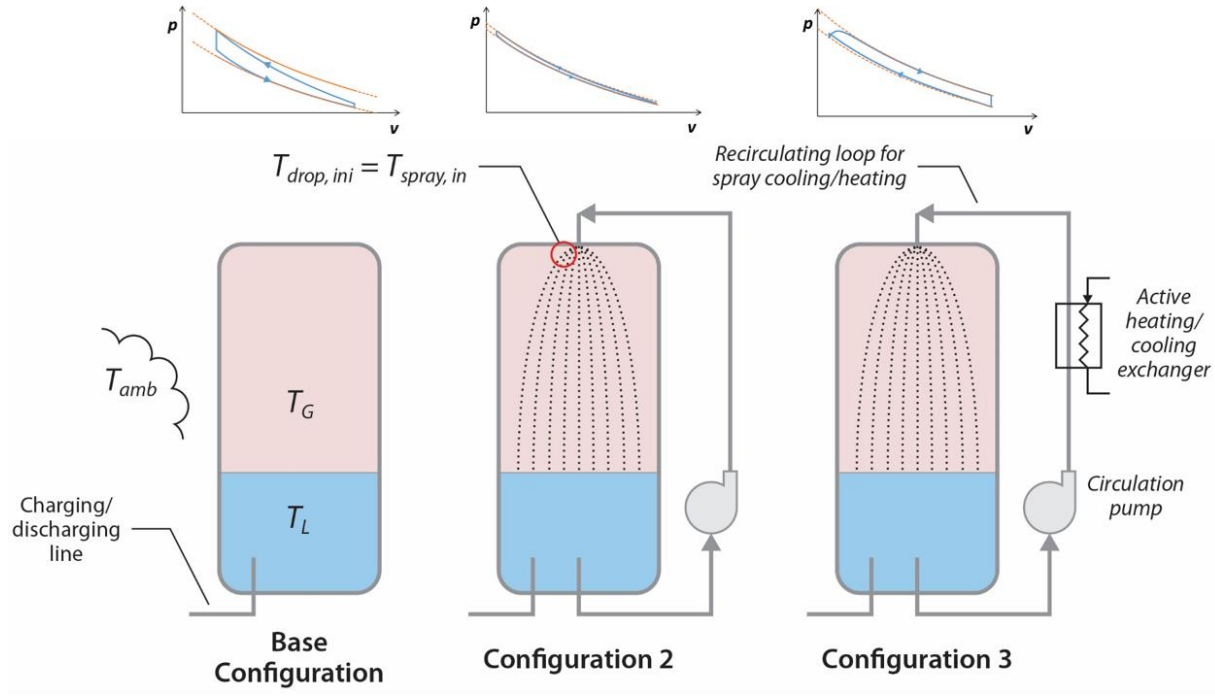

Figure 2.3: Investigated alternative configurations of GLIDES system

Configuration 2 aims to leverage the orders-of-magnitude difference in thermal capacitance between the gas and the liquid in GLIDES by recirculating the GLIDES liquid in a secondary loop and spraying it over the gas during charging and discharging. The previous study [8] shows that because of the large thermal capacity of the liquid, its temperature experiences a very narrow temperature swing during the entire cycle. Therefore, the liquid is cooler than the gas during compression and warmer than the gas during expansion. Spraying the liquid into the gas

provides a favorable cooling effect during charging and warming effect in discharging. Spraying the liquid into the gas can be accomplished by pumping water from the bottom of the vessels into the top through a spray nozzle and a low-head pump. This imposes high pressure on the suction port of the pump. Pumps that can endure such high suction pressure are commercially available at high cost. This is mainly because their applications are limited and their production volume is low. In Configuration 3 a heat exchanger is added downstream of the recirculation pump to take advantage of any available waste heat to further boost the expansion temperature of the gas.

2.4 Energy & Heat Transfer Modeling Formulations

2.4.1 Base Configuration Formulation

In this section, a detailed overview of the model is presented. A set of coupled differential equations representing the three major thermal masses (gas, liquid, tank walls) is developed to model the transient thermodynamic response of the GLIDES system. All the equations herein presented were implemented in a script written using the MATLAB programming environment. The script implementation of the model can be found in Appendix A. Figure 2.4 presents each of the control volumes being considered. The tank walls are modeled as two separate control volumes. The first is the top portion of the tank walls in contact with the gas (T_G). The second is the bottom portion of the tank in contact with the liquid (T_L). Both control volumes have a dynamic mass that changes as the liquid level changes. Several assumptions are used in the development of this transient model: no spatial temperature gradients within each medium (lumped capacitance), an ambient temperature constant in time, constant thermophysical properties for the tank wall material, modeling of the gas inside the tanks as a Redlich-Kwong (RK) fluid using the RK equation of state (for better prediction than an ideal gas at high pressures) [53], negligible heat

transfer between the tank upper (T_G) and tank lower (T_L) masses, and all processes occurring at quasi-steady state.

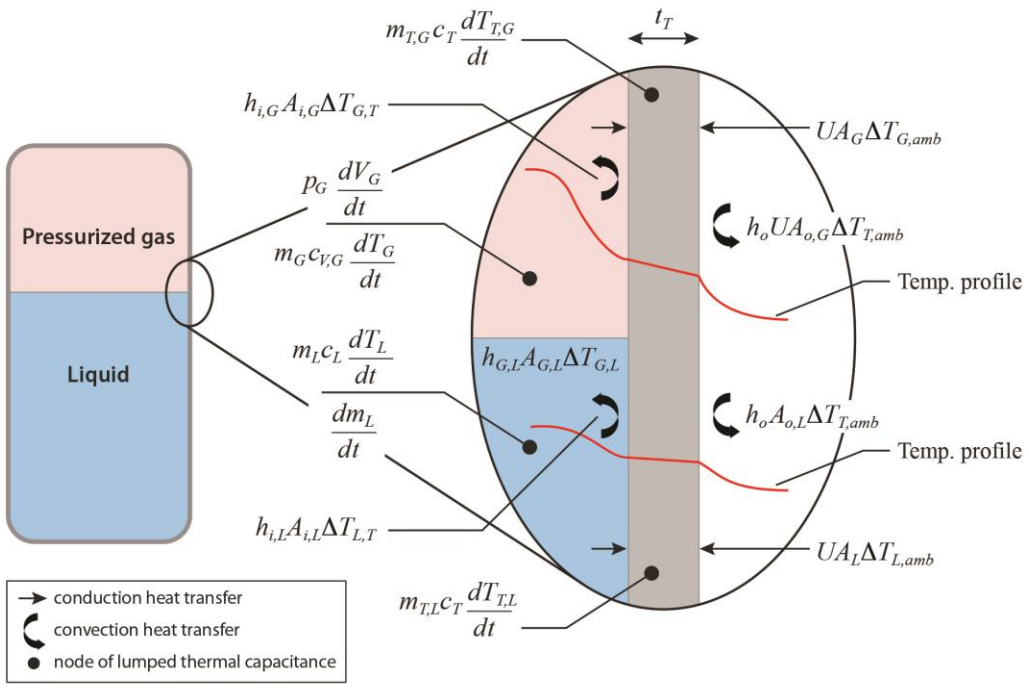

Figure 2.4: GLIDES base configuration energy formulation

The energy equation for the gas is Eq. (2.1). The term on the left is the time rate of change of the energy contained within the gas at time *t*; the first term on the right is the net rate at which energy is transferred in by heat transfer with the liquid; the second term on the right is the net rate at which energy is transferred in by heat transfer through the tank walls from the ambient; and the last term on the right is the net rate at which energy is transferred out by boundary work.

$$m_G c_{v,G}\frac{dT_G}{dt} = -h_{G,L}A_{G,L}(T_G - T_L) - UA_G(T_G - T_{amb}) - p_G\frac{dV_G}{dt} \tag{2.1}$$

The energy equation for the liquid is Eq. (2.2). The term on the left is the time rate of change of the energy contained within the liquid at time *t*; the first term on the right is the net rate at which energy is transferred in by heat transfer with the gas; the second term on the right is the net rate at which energy is transferred in by heat transfer through the tank walls from the ambient; and the last term on the right is the net rate of energy transfer into the control volume accompanying mass flow.

$$m_L c_L \frac{dT_L}{dt} = h_{G,L} A_{G,L} (T_G - T_L) - U A_L (T_L - T_{amb}) + \dot{m}_L c_L (T_{amb} - T_L) \tag{2.2}$$

The energy equation for the tank walls in contact with the gas is Eq. (2.3). The term on the left is the time rate of change of the energy contained within the corresponding mass at time *t*; the first term on the right is the net rate at which energy is transferred in by heat transfer with the gas on the inside; and the second term on the right is the net rate at which energy is transferred in by heat transfer with the ambient air on the outside.

$$m_{T,G} c_T \frac{dT_{T,G}}{dt} = h_{i,G} A_{i,G} \left(T_G - T_{T,G}\right) - h_o A_{o,G} \left(T_{T,G} - T_{amb}\right) \tag{2.3}$$

The energy equation for the tank walls in contact with liquid is Eq. (2.4). The term on the left is the time rate of change of the energy contained within the corresponding mass at time *t*; the first term on the right is the net rate at which energy is transferred in by heat transfer with the liquid on the inside; and the second term on the right is the net rate at which energy is transferred in by heat transfer with the ambient air on the outside.

$$m_{T,L} c_T \frac{dT_{T,L}}{dt} = h_{i,L} A_{i,L} \left(T_L - T_{T,L}\right) - h_o A_{o,L} \left(T_{T,L} - T_{amb}\right) \tag{2.4}$$

The continuity equation for the gas is Eq. (2.5). The term on the left is the time rate of change of the volume of the gas at time *t*, and the term on the right is the volumetric flow rate of liquid displacing the gas.

$$\frac{dV_G}{dt} = -\frac{\dot{m}_L}{\rho_L} \tag{2.5}$$

The continuity equation for the liquid is Eq. (2.6). The term on the left is the time rate of change of the mass of liquid contained within the tanks at time *t*, and the term on the right is the mass flow rate of liquid into the tanks.

$$\frac{dm_L}{dt} = \dot{m}_L \tag{2.6}$$

Equations (2.1) through (2.6) are discretized using a finite-difference method and used to solve the transient temperature response of the gas and liquid in 1 second time steps. The overall heat transfer coefficients UA_G and UA_L are calculated using an effective thermal resistance network with convection on the inner surface, conduction through the tank wall, and convection on the outer surface. The resulting expressions are seen in Eqs. (2.7) and (2.8).

$$UA_G = \frac{1}{\left(\frac{1}{h_{i,G} A_{i,G}}\right) + \left(\frac{t_T}{k_T A_{ave,G}}\right) + \left(\frac{1}{h_o A_{o,G}}\right)} \tag{2.7}$$

$$UA_L = \frac{1}{\left(\frac{1}{h_{i,L}A_{i,L}}\right) + \left(\frac{t_T}{k_T A_{ave,L}}\right) + \left(\frac{1}{h_o A_{o,L}}\right)} \tag{2.8}$$

The gas-to-liquid heat transfer coefficient $h_{G,L}$ is calculated using correlations by Lloyd and Moran (1974) [54] for natural convection over a flat plate. The inner heat transfer coefficients $h_{i,G}$ and $h_{i,L}$ are calculated using LeFevre's [55] correlation by approximating the inside surface of a tank as a vertical wall. Finally, the outer heat transfer coefficient h_o is modeled assuming forced convection over a vertical cylinder with a representative outdoor wind velocity of ~3 m/s using a Churchill and Bernstein [56] correlation.

The charging process via the PD pump occurs at an approximately constant flow rate of liquid and is modeled as such. The discharge liquid flow rate—which is not constant and decreases as the gas pressure inside the tanks decreases—is calculated using a flow model that provides the instantaneous flow rate given the instantaneous gas pressure in the tanks over a given time step. It accounts for frictional piping losses from the tank discharge to the Pelton turbine nozzle discharge. The GLIDES model also captures the time-varying heat transfer areas, mass of liquid, mass of the two tank control volumes, the temperature- and pressure-dependent thermophysical properties of the gas, and the temperature-dependent thermophysical properties of the liquid. The PD pump and electric generator efficiency profiles have been incorporated into the model. An 11 kW, 35 L/min motor/pump assembly and 6 kW electrical generator are used for simulation. The respective efficiency curves can be seen in Figure 2.5 and Figure 2.6. A conventional small-scale Pelton turbine efficiency profile is also incorporated [8, 52]. The following sections describe the additions to the baseline model [8] that enable the active heating and cooling modeling capabilities required for alternative system configurations 2 and 3 shown in Figure 2.3.

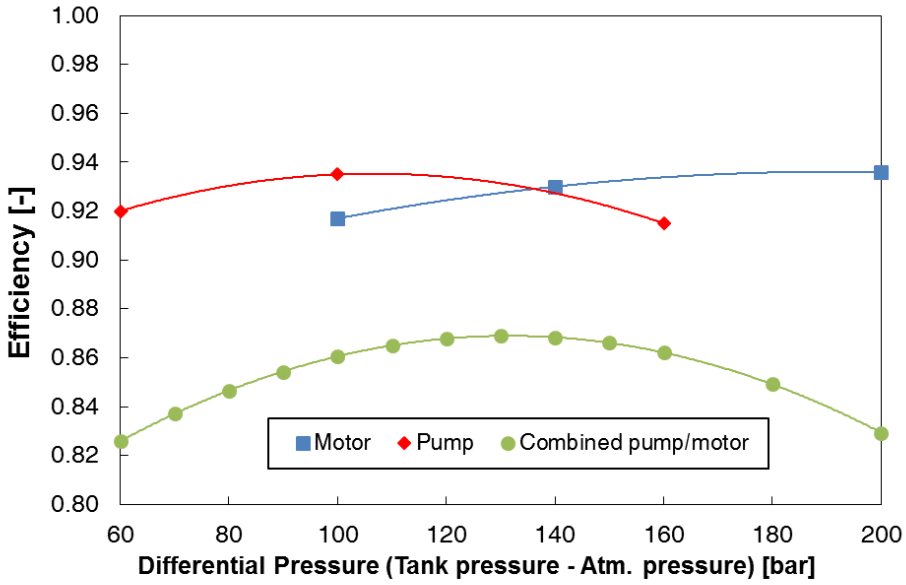

Figure 2.5: Pump/Motor efficiencies

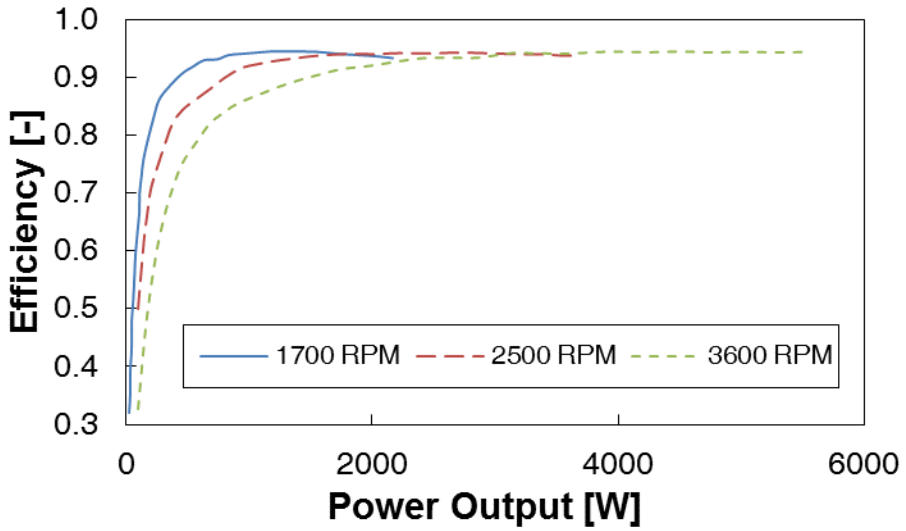

Figure 2.6: Electrical generator efficiency

2.4.2 Direct Contact Heat-Exchange Via Sprayed Droplets

In this section, the formulation used to model the effect of the direct-contact heat exchange between the gas and the liquid obtained via spraying is described. Note that at such elevated pressures, the evaporation of the liquid is very small; hence, in this study, the liquid-gas mass diffusion has been neglected. First, it is assumed that a single droplet falls at constant terminal velocity; therefore, the drag and the gravity forces on each droplet are balanced, and the terminal velocity can be calculated with Eq. (2.9):

$$v_{term} = \sqrt{\frac{4D_{dr}\rho_{dr}g}{3\rho_G C_D}} \tag{2.9}$$

Because the droplets do not reach terminal velocity instantaneously, using the terminal velocity is a conservative estimate for droplet speed as it relates to heat transfer. In addition, the droplets could be falling faster as a result of coagulation of droplets sprayed from the nozzle. Obtaining the terminal velocity allows for the calculation of the droplet travel time or residence time in the gas using Eq. (2.10) since the distance from the top of the GLIDES tank to the liquid level below, *L(t)*, is known. Thus, the droplet travel time can be defined as

$$t_{trav} = \frac{L(t)}{v_{term}} \tag{2.10}$$

The flow rate of the liquid being sprayed is a fixed parameter; therefore, since this value is known, the number of droplets being generated per unit time can be calculated with Eq. (2.11):

$$\dot{N}_{dr} = \frac{6\dot{V}_{spr}}{\pi D_{dr}^3} \tag{2.11}$$

Using the value obtained from Eq. (2.11) and the residence times of droplets, the total number of droplets of liquid traveling through the gas at any given instance in time is computed using Eq. (2.12).

$$N_{dr} = \dot{N}_{dr} \cdot t_{trav} \tag{2.12}$$

Next, using an expression for the transient temperature profile for a falling droplet [Eq. (2.13)][57], the temperature change for a droplet as it travels from the top of the gas to the bottom can be calculated. This expression assumes lumped capacitance (Bi<1), which is verified by calculation. The temperature of the droplets right before they hit the bulk liquid at the bottom of the tank is calculated (T_{dr}), given the gas temperature and the initial temperature of the drop at the outlet of the spray nozzle. Equations (2.11), (2.12), (2.13) were adapted from Ref. [57], which outlines a procedure for modeling direct-contact heat exchange between a gas and liquid.

$$\frac{T_{dr,out} - T_G}{T_{dr,in} - T_G} = e^{-\frac{t_{trav}}{\tau_{dr}}} \tag{2.13}$$

Tau (τ_{dr}) is interpreted as the thermal time constant of the liquid droplet and can be expressed with Eq. (2.14):

$$\tau_{dr} = \frac{\rho_{dr} V_{dr} c_{dr}}{h_{dr} A_{s,dr}} \tag{2.14}$$

Next, the Nusselt number for the drops is calculated using the Ranz and Marshall correlation [Eq. (2.15)] for a falling drop. Development of this Nusselt number correlation is outlined in Ref. [58].

$$Nu_{dr} = 2 + 0.6Re^{1/2}Pr^{1/3} \tag{2.15}$$

The resulting heat transfer coefficient is calculated in Eq. (2.16):

$$h_{dr} = \frac{Nu \cdot k_{dr}}{D_{dr}} \tag{2.16}$$

Given the results of these calculations, the heat loss (or gain) from the drops can be calculated using Eq. (2.17), given the temperatures of the drops as they enter and leave the gas. Note again that the outlet temperature is taken as the temperature of the drop right before it hits the bulk liquid at the bottom of the tank, and the inlet temperature is taken as the temperature of the drop upon exiting the spray nozzle.

$$Q_{dr} = \rho_{dr} V_{dr} c_{dr} (T_{dr,out} - T_{dr,in}) \tag{2.17}$$

The rate of heat loss from the entire spray is then calculated as follows in Eq. (2.18):

$$\dot{Q}_{spr} = \dot{N}_{dr} . Q_{dr} \tag{2.18}$$

A mixing equation [Eq. (2.19)] is then applied to calculate the effect of the droplets on the temperature of the bulk liquid at the bottom of the tank. At each time step, the enthalpy of the drops plus the enthalpy of the bulk liquid (pre-mixing) must equal the enthalpy of the combined liquid mixture (droplets plus bulk liquid):

$$T_{L,mixed} = \frac{\dot{m}_{spr}\,\Delta t\,c_{dr}T_{dr} + m_L c_L T_L}{(\dot{m}_{spr}\,\Delta t + m_L)c_L} \tag{2.19}$$

This new mixed liquid temperature is then taken as the new bulk liquid temperature for the beginning of the next time step (T_L=$T_{L,mixed}$), and Eq. (2.2) is solved with this new value. The effect of this heat transfer is included in the energy balance for the gas as follows. The rate of heat loss from the spray is added to the right-hand side of Eq. (2.1) to account for heat loss or gain due to spray cooling or warming, resulting in Eq. (2.20).

$$m_G c_{v,G}\frac{dT_G}{dt} = -h_{G,L}A_{G,L}(T_G - T_L) - UA_G(T_G - T_{amb}) - \dot{Q}_{spr} - p_G\frac{dV_G}{dt} \tag{2.20}$$

2.4.3 Waste-Heat Integration

To integrate the waste-heat exchanger, the heat exchanger effectiveness method is used assuming a 90% efficient heat exchanger (ε = 0.9) [59]. Liquid water is modeled as the heat transfer fluid on the waste-heat side, and it is analyzed for various waste-heat source temperatures. Figure 2.7 and Eqs. (2.21) and (2.22) show the waste-heat exchanger model.

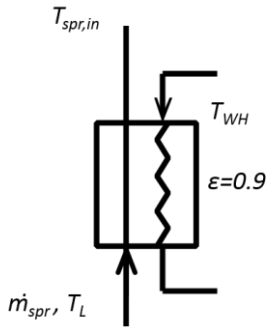

Figure 2.7: GLIDES waste-heat exchanger

$$\varepsilon = \frac{\dot{m}_{spr}(T_{spr,in} - T_L)}{\dot{m}_{min}(T_{WH} - T_L)} \tag{2.21}$$

$$T_{spr,in} = T_L + \varepsilon \frac{\dot{m}_{min}}{\dot{m}_{spr}} (T_{WH} - T_L) \tag{2.22}$$

2.4.4 Performance Indicators

The performance of the GLIDES system is evaluated using four key indicators. The indicated efficiency (η_{ind}), which includes only thermodynamic losses from expansion and compression; the electric roundtrip efficiency (η_{elec}), which includes all losses; and the electrical energy density (ED) are calculated for all three GLIDES configurations. For configuration 3, since a combination of work and heat is fed into the system, the exergetic efficiency (η_{Ex}) is used in addition to the other three indicators. The performance indicators are defined as follows in Eqs. (2.23)–(2.26):

$$\eta_{ind} = \frac{W_{ind,out}}{W_{ind,in}} \tag{2.23}$$

$$\eta_{elec} = \frac{W_{elec,out}}{W_{elec,in}} \tag{2.24}$$

$$ED = \frac{W_{elec,out}}{V_T} \tag{2.25}$$

$$\eta_{Ex} = \frac{W_{elec,out}}{W_{elec,in} + \eta_{Carnot} Q_{WH}} \tag{2.26}$$

2.5 Results

2.5.1 Simulation Parameters

Table 2.1 summarizes the system parameters used in simulating the scenarios presented in this section. Optimization of key system design parameters, such as maximum operating pressure, is not addressed here. This work focuses on a model of the cycle, using system design parameters that were selected for a proof-of-concept base configuration prototype assembled at ORNL. In this study, liquid water is taken as the liquid, and air is taken as the gas.

Table 2.1: GLIDES system simulation parameters

Parameter	Description	Value
$V_{gas,ini}$	Gas initial volume	1.98 m^3
num_{jets}	Number of Pelton turbine jets	1
T_{amb}	Ambient temperature	25°C
p_{min}	Minimum (initial) gas pressure	77 bar
p_{max}	Maximum (after charging) gas pressure	132 bar
$\dot{V}_L$	Liquid charging flow rate	35 L/minute
t_{pause}	Pause time between charge/discharge	43,200 s (12 hours)
$T_{G,ini}$	Initial gas (air) temperature	25°C
$T_{L,ini}$	Initial liquid (water) temperature	25°C
$\dot{V}_{spr}$	Spraying flow rate*	12 L/minute
t_T	Pressure vessel wall thickness	0.02 m

*Spraying flow rate used only for configurations 2 and 3

2.5.2 Base Cycle (Configuration 1)

Figure 2.8 through Figure 2.10 show the temperature profiles, a p-V diagram, and an energy breakdown of the GLIDES base configuration (configuration at left in Figure 3). These assume a usage profile of charging followed by a 12-hour pause, then discharging. In Figure 2.8, charging occurs during the first hour. The gas temperature increases as the gas is compressed, and some heat is lost via heat transfer to the cooler water and the ambient. The charging process is followed by a 12-hour pause period, during which the system temperature is allowed to return to equilibrium with the ambient. The pause period is accompanied by a slight reduction in pressure due to heat loss to ambient. Note that this pause period is not an operational requirement but was added in simulation for performance evaluation purposes as worst-case scenario due to heat loss during the pause. Actual operation is flexible. Charging can be followed by pause of any length, or no pause at all, and the system can switch from charging to discharging and vice-versa in a timescale on the order of seconds. During discharging (hour 12–13), initially the temperature

decreases rapidly as the gas expands and cools. However, cooling due to expansion and warming due to heat transfer to the gas (from the now warmer ambient) oppose each other. As the gas volume increases, and the water level in the tanks goes down, the corresponding heat transfer surface area increases, and the heat transfer from the now warmer ambient to the gas begins to overcome and reverse the cooling due to expansion. The maximum and minimum gas temperatures are 62 and 13°C, respectively, and are marked by the isotherms in the p-V diagram (Figure 2.9). The work input needed for compression (the area under the curve from state 1 to state 2 in Figure 2.9) minus the work output during expansion (the area under the curve from state 2 to state 3) represents the lost work due to non-isothermal compression and expansion; this is the area enclosed by the four state points. In Figure 2.10, the breakdown of the efficiency and the system losses for the base configuration (configuration 1) are given; the largest contribution to losses is from non-isothermal expansion and compression. The pump/motor and turbine/generator losses are calculated using the respective characteristic efficiency curves for those components [8]; they are 6 and 7%, respectively, for the pump/motor and 6 and 5%, respectively, for the turbine/generator. An indicated efficiency of $\eta_{ind} = 0.90$ is achieved, corresponding to an electrical (120 V, 60 Hz) RTE of $\eta_{elec} = 0.66$ and an ED = 0.69 kWh/m^3. Note that this energy density corresponds to operation with maximum operating pressure around 130 bar, which was selected based on the maximum operating pressure of the pressure vessels used in the proof-of-concept prototype. Energy density increases as the maximum operating pressure of the pressure vessels increases [8]. When operated with a single Pelton turbine jet, this configuration produces a maximum power output of 2.4 kW at the beginning of discharging, and a minimum of 1.2 kW at the end of discharging. Note that the system is not constrained to the operation described here. If the charging process does not occur continuously (such as might be the case if it were tied to

intermittent renewable sources), the temperature gain during charge would be decreased, and the subsequent pressure/temperature loss immediately following the charging process would also be lessened. This would result in lower expansion/compression losses and higher RTE. Furthermore, if the discharging process is initiated immediately following the charge (i.e., no pause time), the pressure/temperature losses due to standby would be eliminated, also resulting in higher RTE. If instead this base configuration is run with no pause time, as opposed to 12 hours of pause time, the RTE improves from η_{elec} = 0.66 to η_{elec} = 0.69.

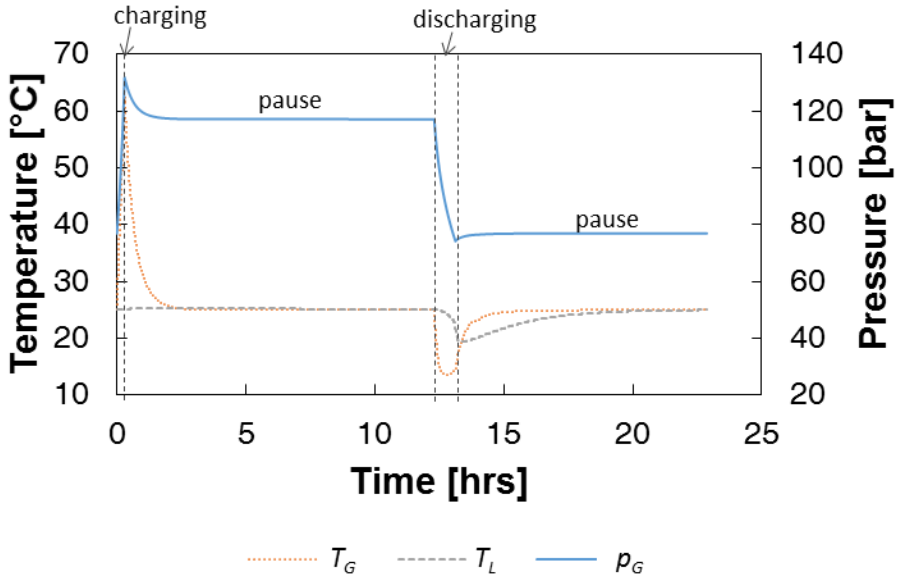

Figure 2.8: GLIDES base configuration cycle transient temperature and pressure profiles

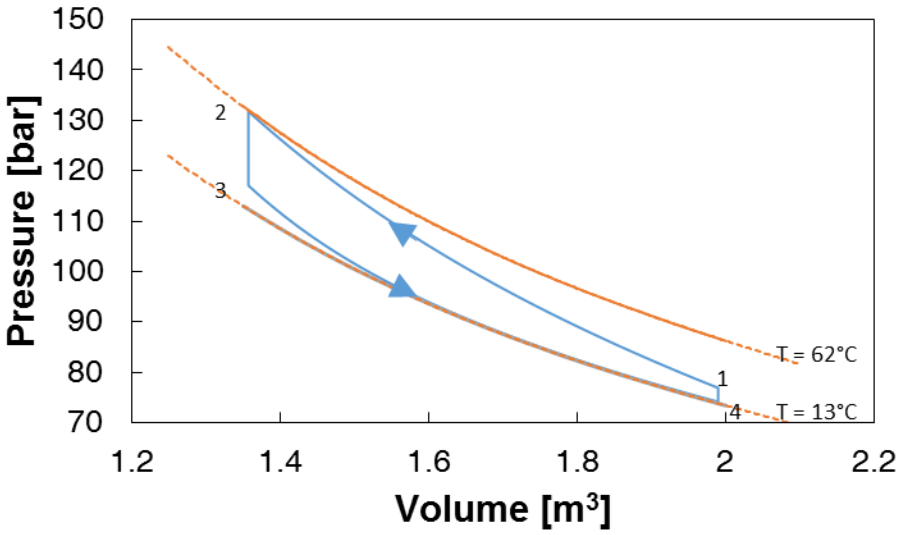

Figure 2.9: GLIDES base configuration cycle pressure-volume diagram

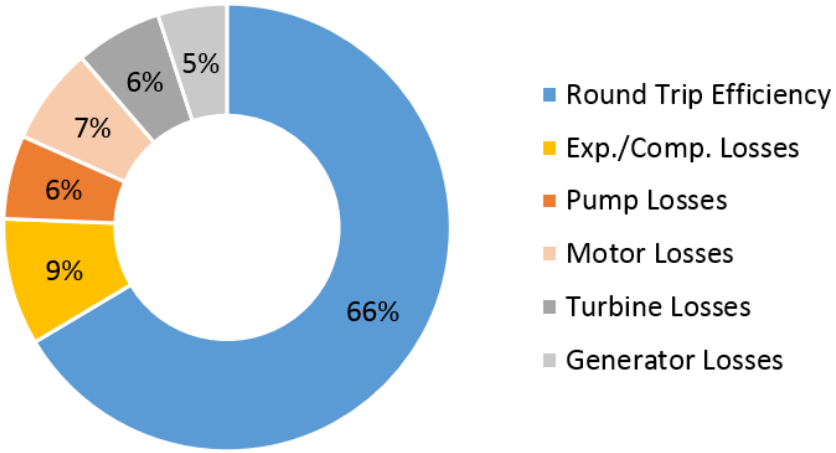

Figure 2.10: GLIDES base configuration efficiency and losses summary

2.5.3 Near-Isothermal Expansion/Compression (Configuration 2)

Figure 2.11 shows the transient temperature and pressure profiles for the gas and the temperature profile for the liquid for operation of configuration 2 (the middle image in Figure 2.3). It can be seen that compared with the base configuration, spraying improves efficiency by reducing the maximum gas temperature (from 62 to 32°C) and increasing the minimum gas temperature (from 13 to 22°C).

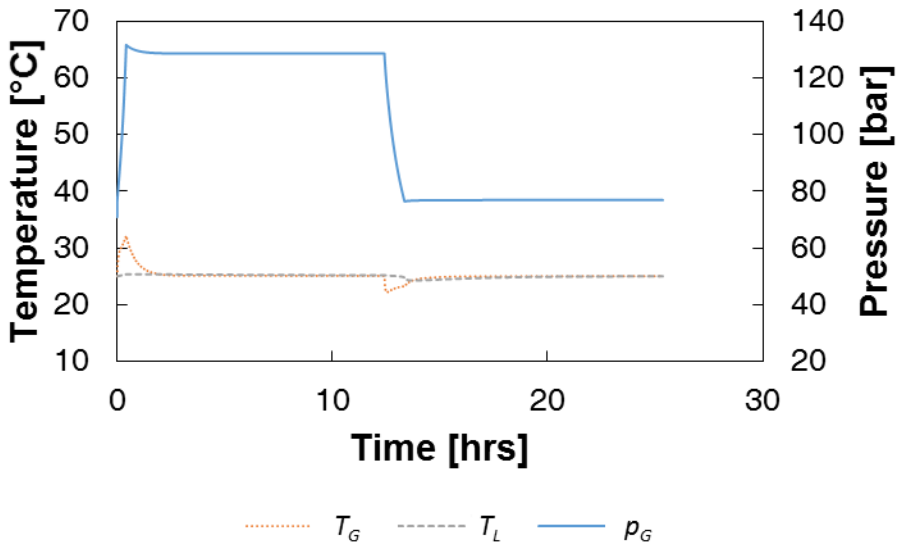

Figure 2.11: GLIDES configuration 2 cycle transient temperature and pressure profiles

A p-V representation of the configuration 2 gas cycle can be seen in Figure 2.12. Spraying at 12 liters per minute with a nozzle producing an average drop diameter of D_{dr} = 50 μm results in a 6 percentage point boost in η_{ind}, from 0.90 to 0.96, corresponding to an ED = 0.86 kWh/m^3 and η_{elec} = 0.70. There is a noticeable decrease in lost work due to expansion and compression,

represented in the thinner p-V curve, as the isotherms are brought closer together. When taken individually, the compression and expansion p-V curves (state 1 to 2 and state 3 to 4) are very nearly isothermal. This is depicted by the small deviation from the 22°C and 32°C isotherms which are shown with orange dashed lines. When operated with a single Pelton turbine jet, this configuration produces a maximum power output of 2.76 kW at the beginning of discharging, and the minimum is 1.25 kW at the end of discharging, a slight improvement over the base configuration.

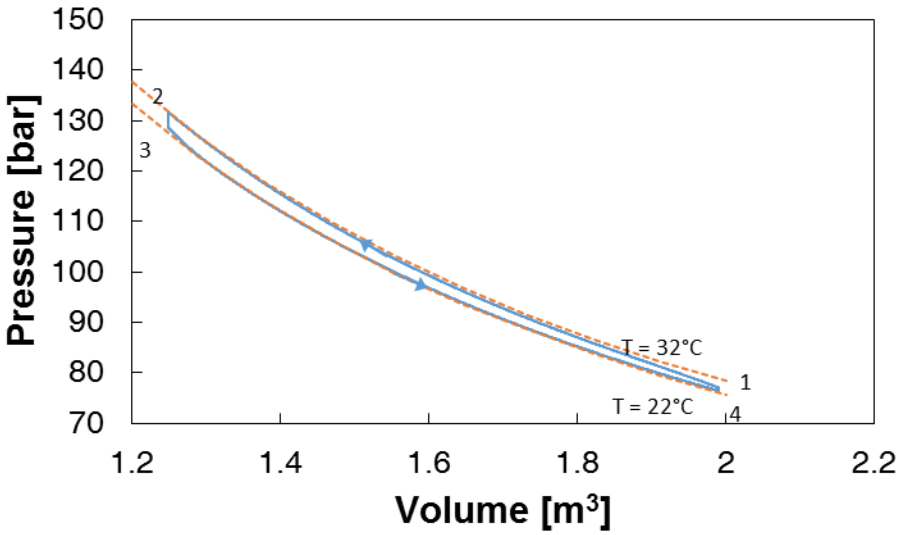

Figure 2.12: GLIDES configuration 2 cycle pressure-volume diagram

Accounting for the pumping power required to overcome the spray nozzle pressure drop introduces a new category of loss, as seen in Figure 2.13; but it accounts for only a 1% efficiency loss.

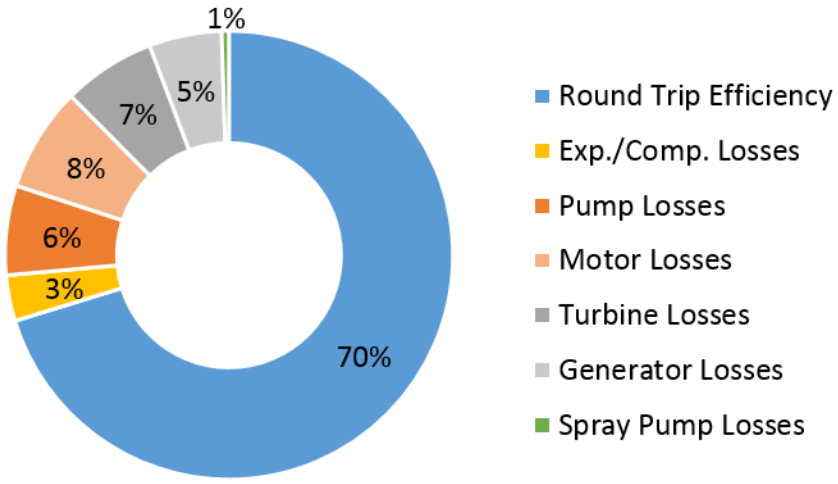

Figure 2.13: GLIDES configuration 2 efficiency and losses summary

The electrical RTE η_{elec} was studied for various spray flow rates and droplet diameters ranging between 50 and 5000 μm. A smaller average droplet diameter results in improved RTE due to an increase in the heat transfer surface area between the bulk gas and the sprayed liquid droplets. However, the increase in pump energy that would be required to produce smaller droplet sizes is not accounted for. The spray flow rate was optimized near 12 liters per minute, as seen in Figure 2.14; at a higher flow rate, the benefits of increased RTE are outweighed by the increased additional spray nozzle pressure drop and pumping power required.

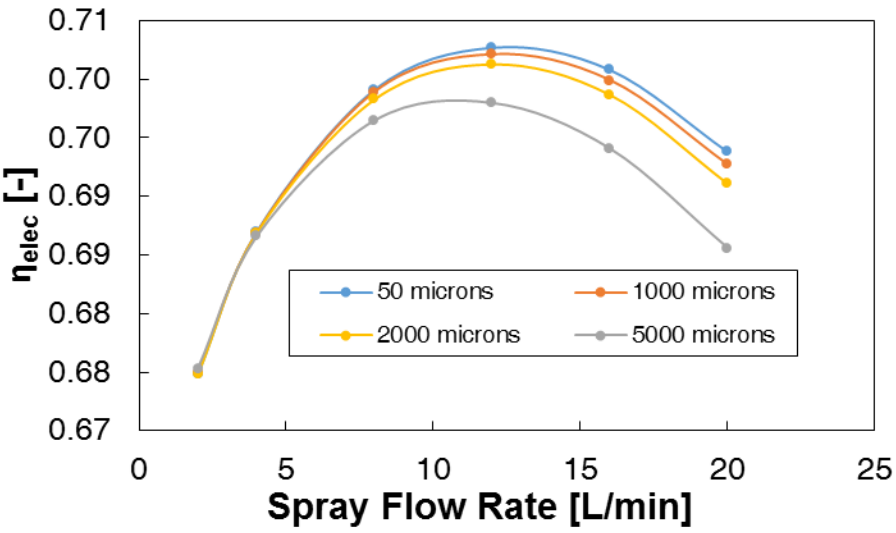

Figure 2.14: RTE vs. spray flow rate for various average droplet diameters

2.5.4 Waste-Heat Integrated (Configuration 3)

In configuration 3 (the image at the right in Figure 2.3), a heat exchanger is added downstream of the spray pump to preheat the spray liquid, using any available waste heat to further enhance the effect of spray warming during gas expansion. In this case, waste heat is simulated as a stream of water with a source temperature of 70°C. With a 90% efficient waste-heat exchanger, the spray stream is introduced into the gas at 65°C. After the sprayed droplets exchange heat with the gas, the gas is warmed to a maximum of 59°C, resulting in the temperature and pressure profiles seen in Figure 2.15. Immediately after the discharging process begins, a boost in pressure occurs as heat is added to the gas. The cooling during expansion (which occurred in configuration 2) is reversed to a net warming to 59°C. The thermodynamic cycle becomes very similar to a high efficiency Stirling cycle, as seen in Figure 2.16.

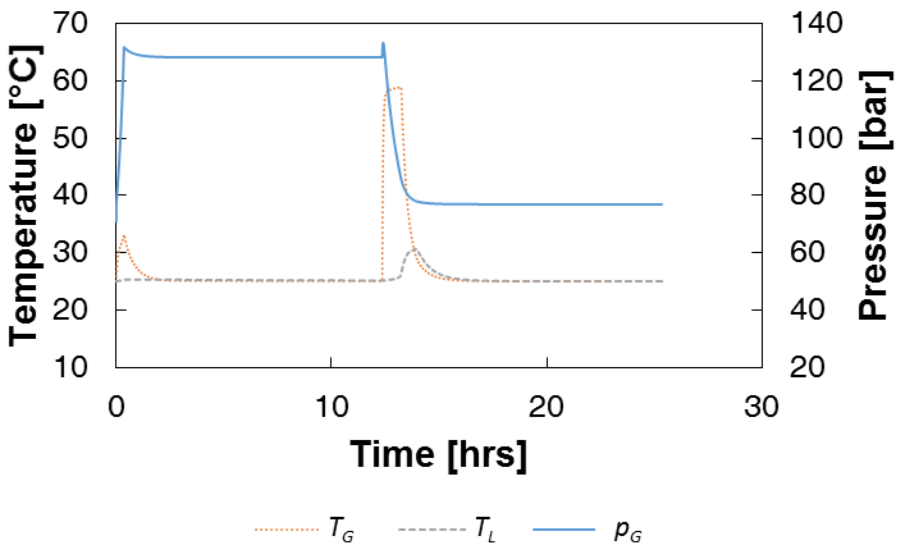

Figure 2.15: GLIDES configuration 3 cycle transient temperature and pressure profiles (waste-heat source at 70 °C)

The effect of using the waste-heat exchanger on the GLIDES gas cycle and on the shape of the p-V curve can be seen in Figure 2.16. During compression, spray recirculation is used, leveraging the orders-of-magnitude difference in thermal capacitance between the gas and the liquid to keep the compression near-isothermal. During expansion, the waste-heat exchanger is used in addition to spray-recirculation to precondition the spray stream, effectively storing heat. Because of the large boost in expansion temperature, the area under the expansion curve (state 3 to 4) is now larger than the area under the compression curve (state 1 to 2), meaning that more hydraulic work is extracted from the system than was stored via the pump; essentially, $\eta_{ind} = 1.07$. The cycle begins at state 1 with compression to state 2 via the pump while using the spray stream to keep the process near-isothermal. During the pause after compression, some heat is lost through the tank walls to the cooler ambient (state 2 to 3). As expansion begins, the waste-heat exchanger

comes into use, adding heat and boosting the pressure above state 2, providing an increase in the electricity extracted. Some of the ancillary losses due to the pump/motor and turbine/generator are recovered, resulting in η_{elec} = 0.78 and ED = 0.95 kWh/m^3. Note that this is for a waste-heat input temperature of 70°C, and the performance further increases for higher waste-heat temperatures, as seen in Table 2.2 and Figure 2.18. If waste-heat input were to begin at state point 2, instead of at state point 3, the p-V diagram would approach a high–efficiency Stirling cycle. For reference, an ideal Stirling cycle operating between two thermal energy reservoirs at 25°C (ambient temperature) and 70°C (waste-heat source temperature) is shown in Figure 2.16 with a green dotted line. With the addition of waste-heat input, and operation with a single Pelton turbine jet, maximum power output is 2.9 kW, and minimum is 1.5 kW; an increase in power output is achieved due to the pressure boost provided by addition of waste heat.

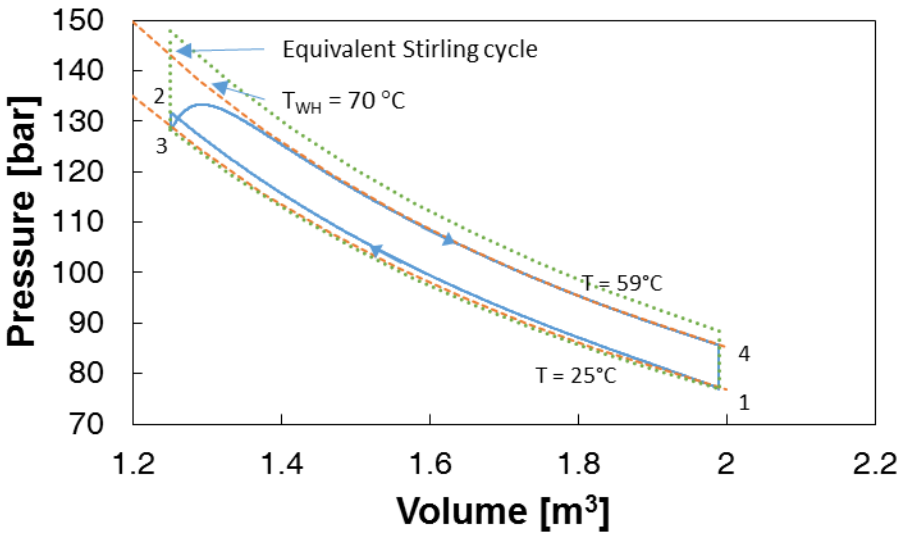

Figure 2.16: GLIDES configuration 3 cycle pressure-volume diagram (waste-heat source at 70 °C)

For configuration 3, the sum of the RTE and itemized losses is greater than 100%. In other words, some of the losses are recovered by the addition of waste heat. Figure 2.17 shows the fraction of exergy inputs (a), as well as the roundtrip efficiency and system losses (b). This configuration of the GLIDES system represents a combined energy storage and heat engine cycle, with low- or medium-grade heat used to boost electricity production.

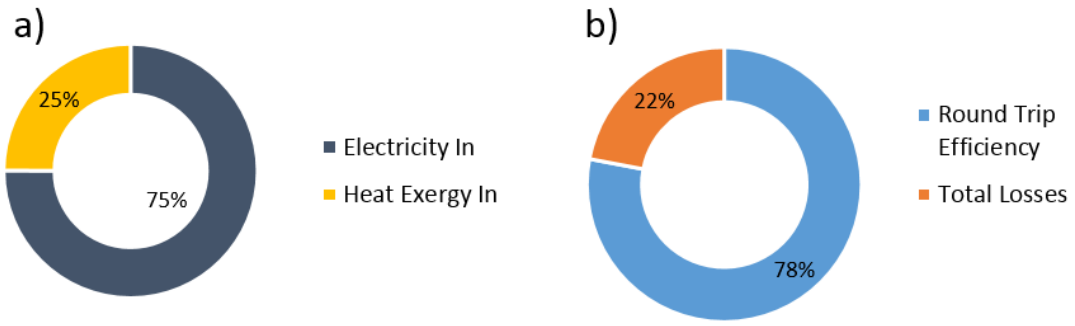

Figure 2.17: GLIDES configuration 3 performance summary (waste-heat source at 70 °C)

2.6 Summary of Simulation Effort

Table 2.2 and Figure 2.18 summarize the performance of the three GLIDES configurations and of configuration 3 with various waste-heat source temperatures.

Table 2.2: Summary of simulated performance of GLIDES configurations

	Base configuration (configuration 1)	**Configuration 2***	**Configuration 3***		
			T_{WH} = 50 °C	**T_{WH} = 70 °C**	**T_{WH} = 90 °C**
η_{elec} [–]	0.66	0.70	0.75	0.78	0.82
η_{ind} [–]	0.90	0.96	1.03	1.07	1.12
η_{Ex}	0.66	0.70	0.66	0.59	0.52
ED [kWh/m^3]	0.68	0.86	0.91	0.95	1.00

*with $\dot{V}_{spr}$ = 12 liters per minute

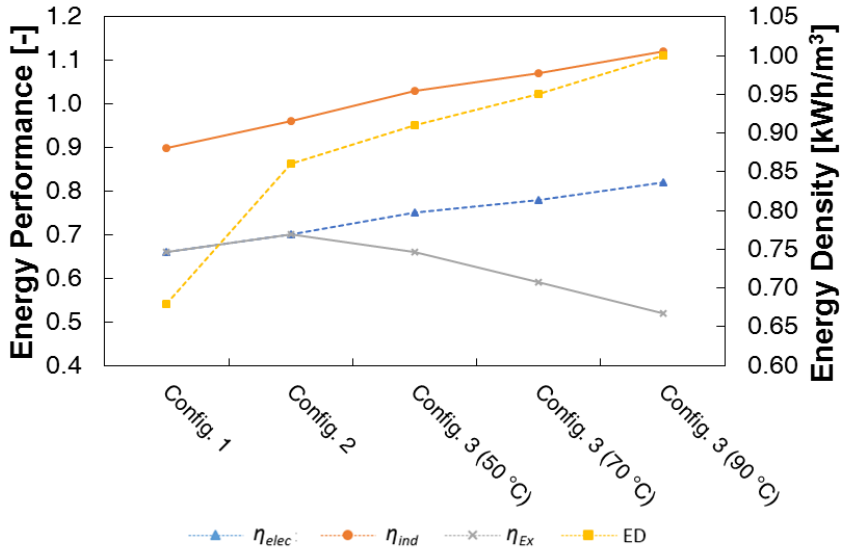

Figure 2.18: Summary of performance of GLIDES configurations

The simulation and analysis presented in this chapter show that GLIDES has great potential as an energy storage technology. The maximum operating pressure simulated in this study was limited to not exceed 140 bar due to laboratory pressure system design protocols. A system designed for higher allowable operating pressure would achieve higher energy density. This study demonstrates that additional efficiency gains can be realized by using heat transfer enhancement strategies, such as liquid spraying, to achieve direct-contact heat exchange between gas and liquid

and leveraging any available waste heat to counter the expansion cooling and provide a thermal boost. Waste heat could be harnessed, for example, from the condensers of air-conditioning systems, solar-thermal hot water receivers, combined heat and power systems, geothermal wells, or waste heat exhaust from turbines or stacks. Due to promising simulation results and predicted performance on par and even surpassing existing energy storage technologies, research efforts proceeded with the development of a first-generation proof-of-concept prototype. These efforts are discussed in the following chapters.

CHAPTER 3. EXPERIMENTS & MODEL CALIBRATION

Content in this chapter adapted from:

1. Odukomaiya, A., et al. Preliminary Performance Evaluation of a Ground-Level Integrated Diverse Energy Storage (GLIDES) Prototype System. in TechConnect World Innovation Conference & Expo. 2017. Washington D.C., United States. [60]
2. Odukomaiya, A., Experimental and Analytical Evaluation of a Hydro-Pneumatic Compressed-Air Ground-Level Integrated Diverse Energy Storage (GLIDES) System. 2017: Applied Energy (submitted). Manuscript APEN-S-17-12334. [61]

In the previous chapter, the GLIDES concept was introduced and studied analytically. This chapter reports on the experimental performance of the first GLIDES proof-of-concept prototype at several operating conditions. Additionally, based on the experimental results, slight modifications are made to the simulation model presented in Chapter 2 to better capture the actual system performance, resulting in a calibrated/validated model. This model is then used to conduct a parametric sweep, capturing the performance of the system across a wide range of operating conditions, resulting in the empirical development of a set of simple algebraic equations which can be used to predict the performance of such systems as a function of the overall system parameters.

3.1 First Generation Proof-of-Concept Prototype

3.1.1 System Description

A first lab-scale proof-of-concept GLIDES prototype has been built at Oak Ridge National Laboratory (ORNL). The system is sized at a nominal 3 kWh; energy is recovered using a Pelton

turbine which can operate with two jets, delivering a peak 5.5 kW hydraulic power per jet. Figure 3.1 shows a schematic of the GLIDES prototype system; it is comprised of a 500-gallon water storage tank, four 500-liter carbon steel pressure vessels with maximum allowable working pressure of 160 bar, an 11 kW, 42 liter/min positive displacement pump/motor assembly, a custom-made, 2-jet Pelton turbine, and a 5 kW single phase 120 VAC 60 Hz electrical generator. A custom-made Pelton turbine was specially designed for GLIDES due to the higher than typical operating pressures. The main difference relative to conventional Pelton turbines is that the very high-head allows for much lower flow rates, which requires much smaller jet diameter and much smaller Pelton buckets.

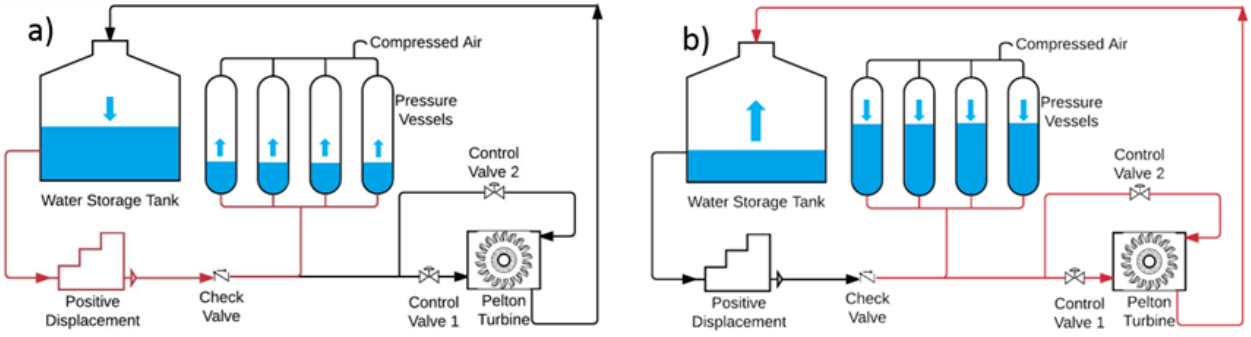

Figure 3.1: GLIDES gen. 1 prototype schematic during a) charging and b) discharging

The system was designed to operate with air as the gas and water as the liquid at pressures from minimum of 70 bar to maximum of 130 bar. Maximum pressure is limited to 130 bar in compliance with laboratory safety protocol. Figure 3.1 shows the prototype and water flow path during charging (left) and discharging (right). Figure 3.2 shows images of the prototype and components installed at ORNL.

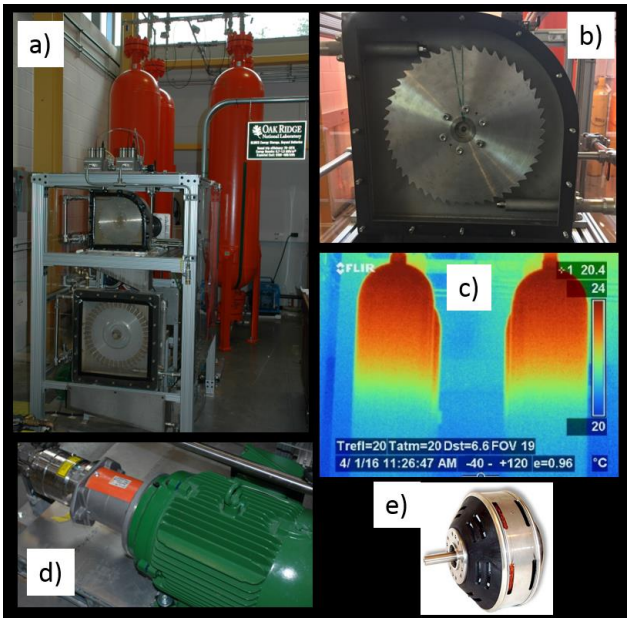

Figure 3.2: GLIDES porotype a) overall system and pressure vessels, b) Pelton turbine, c) IR image of pressure vessels during charging, d) charging pump/motor, e) electric generator

3.1.2 Instrumentation, Controls, & Data Acquisition

Several instruments were installed to capture the performance of the prototype. Eight thermocouples and four pressure transducers were installed on the pressure vessels to measure air/water temperature and pressure. For each pressure vessel, one thermocouple was installed at the top to measure air temperature, and another at the bottom to measure water temperature. A pressure transducer was installed at the top of each vessel to measure pressure. A water level (pressure-head) transducer was used at the bottom of the water storage reservoir to measure water level; this measurement was used to calculate charging/discharging flowrates and pressure vessel air volume. Watt transducers were installed on the pump motor and electrical generator to measure system electrical power input and output. A torque meter was installed between the turbine and

generator shafts to measure torque and shaft speed. Thermocouples were also added to measure the ambient air temperature and water temperature inside the water storage reservoir. Table 3.1 presents a summary of the various instruments used to capture system performance as well as their rated instrument uncertainties.

Table 3.1: GLIDES Gen. 1 prototype instrumentation summary

Measurement	**Instrument**	**Measuring Range**	**Instrument Accuracy**
Air Pressure	Omega PXM459 Pressure Transducer	0-350 bar	1%
Air Temperature	Omega Type T Thermocouple	0-350 °C	0.5 °C or 0.4%
Water Temperature	Omega Type T Thermocouple	0-350 °C	0.5 °C or 0.4%
Turbine/Generator Shaft Torque	Magtrol TM207HS TorqueMaster	0-10 Nm	0.1%
Turbine/Generator Shaft Speed	Magtrol TM207HS TorqueMaster	20-50,000 RPM	10 RPM
Storage Water Tank Level	Omega PX709 Submergible Pressure Transducer	250-3500 mmH2O	1%
Storage Water Tank Temperature	Omega Type T Thermocouple	0-350 °C	0.5 °C or 0.4%
Ambient Air Temperature	Omega Type T Thermocouple	0-350 °C	0.5 °C or 0.4%
Power Input (pump)	Ohio Semitronics Compound Transducer	0-40,000 watts	1.5%
Power Output (generator)	Ohio Semitronics Compound Transducer	0-10,000 watts	0.5%

All instrumentation was calibrated across the full expected ranges of measurement per NIST traceable calibration procedures. A controls and data acquisition system utilizing National Instruments LabVIEW software and hardware was used to control the system and log measurements. A screenshot of the LabView user interface can be seen in Figure 3.3.

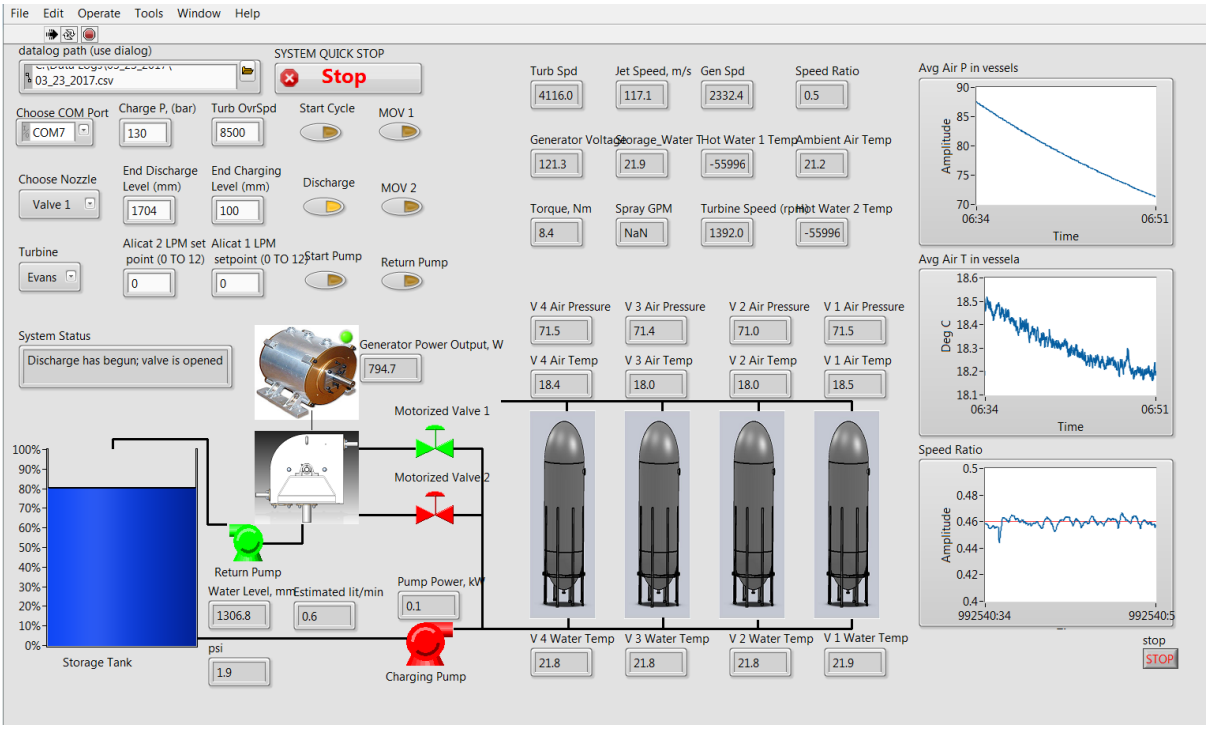

Figure 3.3: National Instruments LabVIEW Control and Data Acquisition System Interface

3.1.3 Data Reduction

The performance of each GLIDES cycle (charge/discharge) is evaluated using several variations of two key indicators, cycle efficiency and energy density. Three efficiency metrics are used, η_{elec}, η_{shaft}, and η_{ind}. The roundtrip electrical-to-electrical efficiency (η_{elec}) is defined as the ratio of electrical work output to input. The shaft efficiency (η_{shaft}) is the ratio of output shaft mechanical work to input electrical work. The indicated (or thermodynamic) efficiency is defined as the ratio of indicated work output to indicated work input. Equations (3.1) through (3.5) are used to calculate the respective work inputs and outputs, and Equations (3.6) through (3.8) to calculate the electrical, shaft, and indicated efficiencies.

$$W_{in,elec} = \int_{t_{c,i}}^{t_{c,f}} \dot{W}_{pump,elec} dt \tag{3.1}$$

$$W_{out,elec} = \int_{t_{dc,i}}^{t_{dc,f}} \dot{W}_{gen,elec} dt \tag{3.2}$$

$$W_{out,shaft} = \int_{t_{dc,i}}^{t_{dc,f}} \dot{W}_{shaft} dt = \int_{t_{dc,i}}^{t_{dc,f}} \tau_{shaft} \omega_{shaft} dt \tag{3.3}$$

$$W_{in,ind} = \int_{t_{c,i}}^{t_{dc,f}} \dot{W}_{in,ind} dt = \int_{t_{c,i}}^{t_{c,f}} p_{air} \dot{V}_c dt = \int_{V_{c,i}}^{V_{c,f}} p_{air} dV \tag{3.4}$$

$$W_{out,ind} = \int_{t_{dc,i}}^{t_{c,f}} \dot{W}_{out,ind} dt = \int_{t_{dc,i}}^{t_{c,f}} p_{air} \dot{V}_{dc} dt = \int_{V_{dc,i}}^{V_{dc,f}} p_{air} dV \tag{3.5}$$

$$\eta_{elec} = \frac{W_{out,elec}}{W_{in,elec}} \tag{3.6}$$

$$\eta_{shaft} = \frac{W_{out,shaft}}{W_{in,elec}} \tag{3.7}$$

$$\eta_{ind} = \frac{W_{out,ind}}{W_{in,ind}} \tag{3.8}$$

In addition to the efficiencies, the electrical, shaft, and indicated energy densities are also reported. These energy densities are defined using Equations (3.9) through (3.11). The electric and indicated specific energy is defined by Equations (3.12) and (3.13) respectively.

$$ED_{elec} = \frac{W_{out,elec}}{V_0} \tag{3.9}$$

$$ED_{shaft} = \frac{W_{out,shaft}}{V_0} \tag{3.10}$$

$$ED_{ind} = \frac{W_{out,ind}}{V_0} \tag{3.11}$$

$$SE_{elec} = \frac{ED_{elec}}{\rho_i} \tag{3.12}$$

$$SE_{ind} = \frac{ED_{ind}}{\rho_i} \tag{3.13}$$

Full cycle (charge and discharge) tests were conducted to evaluate the performance of the GLIDES prototype. A full cycle begins with the pressure vessels containing just air at the initial pressure, the system is then charged by pumping water into the vessels until the maximum desired pressure is reached. The system is then allowed to standby and equilibrate during a pause period lasting about 5 hours. Finally, the discharge cycle begins and continues until the vessels are emptied of water. In these tests the energy is recovered using only one of the two Pelton turbine jets, to not exceed the torque sensor's maximum allowable torque. Three tests were run in this manner: the first, across the whole range of working pressures (70 bar to 130 bar), the second, in the lower end of the range (70 bar to 100 bar), and the third, in the upper end of the range (100 bar to 130 bar). A final fourth test similar to the third test but with no standby pause period between charging and discharging was also run. The following charts are results from the first test. All tests showed similar qualitative trends. The results of all four tests are later summarized in Table 3.2.

3.1.4 Thermodynamic Performance

Figure 3.4 shows the transient air and water temperatures and air pressure through the duration of the experiment. Both air and water are initially at 21 °C. As charging begins and water is pumped into the pressure vessels, the temperature of the air begins to increase as it is compressed by the rising liquid piston. It increases to a maximum of 35 °C when charging is completed, then decreases during the pause period as heat is lost to ambient through the vessel walls and to the water below. The pressure behaves similarly, increasing from 70 bar to 130 bar, after which some pressure is lost during the pause period due to the drop in temperature resulting from heat loss.

During discharge, the temperature of the air drops as water is forced out of the pressure vessels through the Pelton turbine and the air atop the water inside the vessel expands. The rate of change (slope) of the temperature decreases with time during discharge. This can be attributed to heat transfer through the vessel walls into the air from the now warmer ambient. This heat transfer counteracts and slows the cooling due to expansion. Once the cycle is complete, the system temperatures return to equilibrium with ambient.

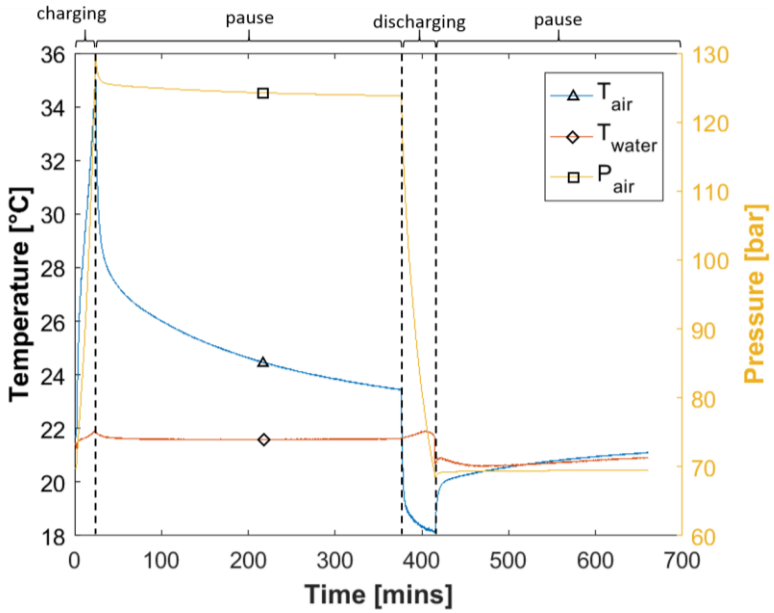

Figure 3.4: Air/water measured transient temperature and pressure profiles during GLIDES prototype operation

The pressure-volume diagram of the air during the test run can be seen in Figure 3.5. Beginning at state point 1, charging begins, pressure increases and volume decreases until charging is completed at state point 2 when 130 bar pressure is reached. Process 2 to 3 is the standby period; the volume remains constant while pressure and temperature drop. The discharge process (3 to 4) then occurs. As water is discharged from the vessels, the gas expands resulting in pressure decrease and volume increase, until state point 4 when all water is discharged. Lastly, as the air temperature returns to equilibrium with ambient, the air returns to the initial state.

The area under the pressure-volume curve from state 1 to state 2 represents the indicated work input, while the indicated work output is the area under the curve from state 3 to 4. The indicated storage efficiency is the ratio of output to input. The area enclosed by the curve is lost work due to non-isothermal expansion and compression.

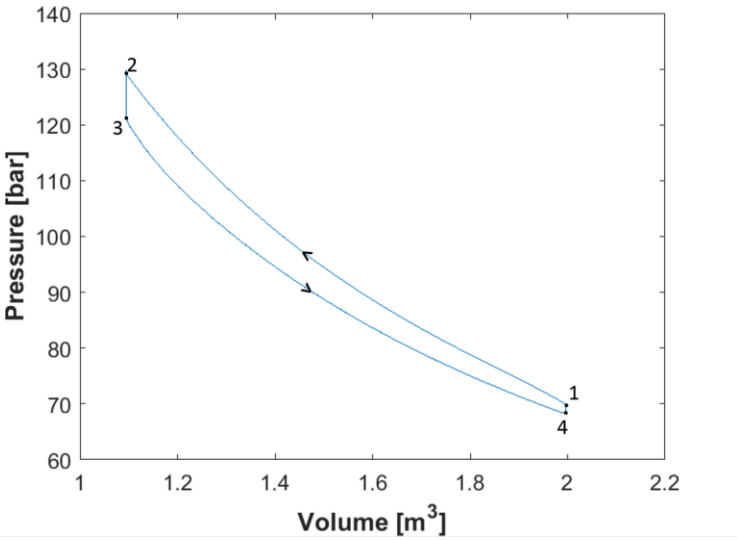

Figure 3.5: Pressure-volume diagram of GLIDES air

3.1.5 Energy Storage (Charging)

The input indicated (thermodynamic) power and electrical pump power during energy storage (charging) are shown in Figure 3.6 versus time (a) and pressure (b). The indicated power is the product of the pressure and the water flow rate, while the electric power is the electricity consumed by the pump-power as measured by the watt transducer. The difference between the curves is the power loss due to inefficiencies in the pump and motor.

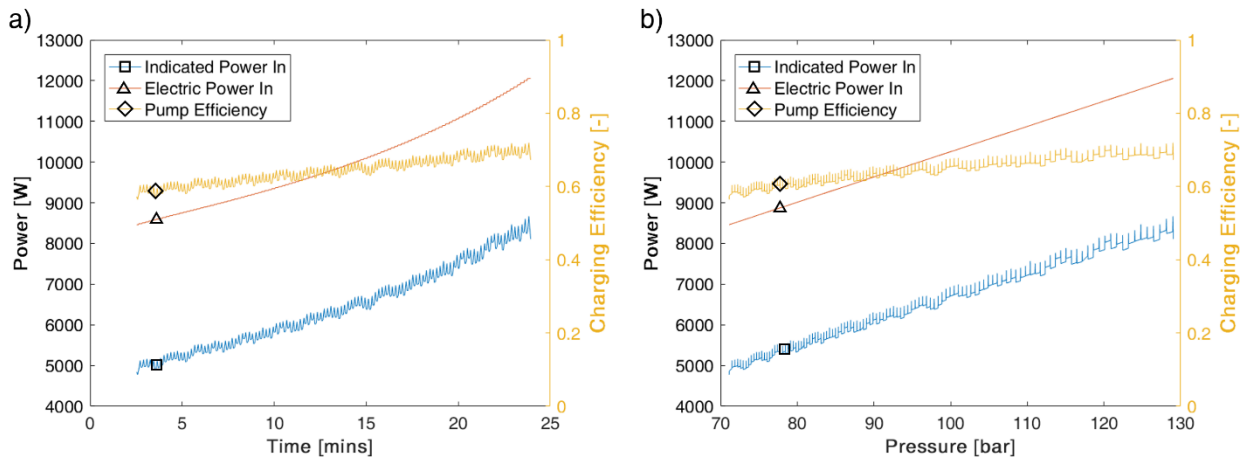

Figure 3.6: GLIDES prototype power inputs and charging efficiency versus time (a) and pressure (b)

The lost power is also shown in Figure 3.6 as the pump efficiency (ratio of indicated power to electric power). The pump efficiency ranges from a minimum of 60% to a maximum of 70%. As expected for a positive displacement pump, as the pressure increases during the charging, the pump efficiency slightly increases.

3.1.6 Energy Recovery (Discharging)

Figure 3.7 shows the indicated, shaft, and electric power outputs from the GLIDES prototype during energy recovery versus time (a) and pressure (b). The indicated power is the product of pressure and flow rate, the shaft power is the product of turbine shaft torque and speed, and the electric power is the electricity generated by the electric generator. The power output decays in time due to the decay of pressure in the vessels as the air expands. The difference between the indicated power and the shaft power is power loss in the Pelton turbine and any flow friction, which is negligible in this case, while the difference between the shaft power and the electrical power is due to the inefficiencies in the electric generator. The indicated, shaft, and electrical

energy densities are calculated to be 1.18, 0.55, and 0.39 kWh/m^3, respectively. The turbine and generator efficiencies are also shown in Figure 3.7. The turbine efficiency remains fairly constant throughout discharge at an average about 50%. This is because the electrical load on the system is controlled to maintain the ratio of Pelton turbine runner speed to water jet speed around 0.46, which is an optimal value for Pelton turbine efficiency [52]. The generator efficiency decays slightly throughout discharge from a maximum of 75% to a minimum of 68%.

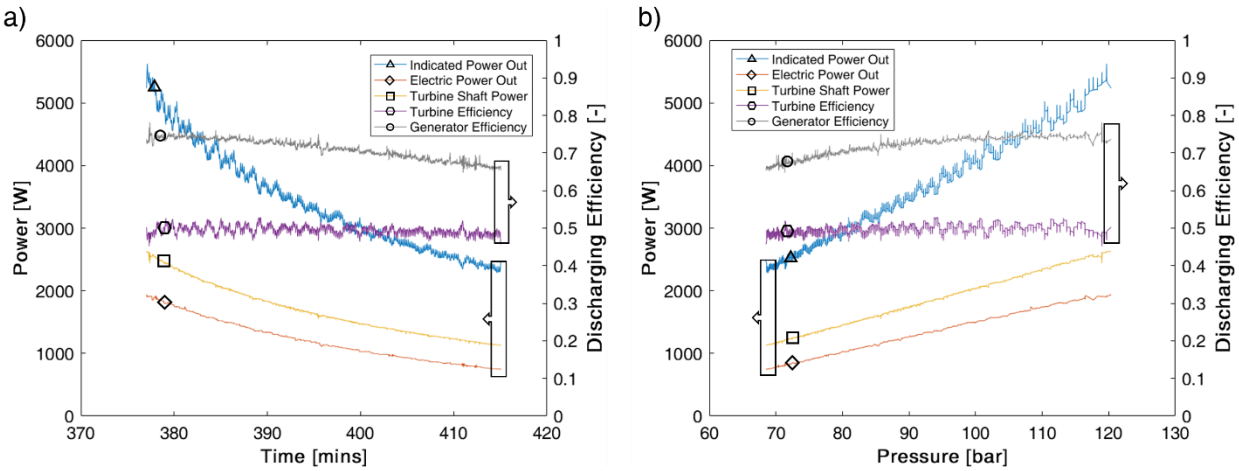

Figure 3.7: GLIDES prototype power outputs and discharging efficiencies versus time (a) and pressure (b)

By accounting for the energy inputs and outputs, the energy losses incurred throughout each energy conversion step can be characterized and itemized, as shown in the pie chart in Figure 3.8. The electrical roundtrip, shaft and indicated efficiencies are found to be 21%, 30%, and 94% respectively. A relatively small fraction (5%) of energy is lost due to non-isothermal expansion/compression as heat is transferred to and from the air. The majority of energy losses are incurred in the turbine (29%) and pump (36%). The generator is responsible for 8% of the lost

energy. This indicates that there is a significant potential to improve the efficiency of the system by optimizing, re-scoping these components, particularly at large scales, where hydraulic pumps and turbines can have efficiencies in excess of 90%.

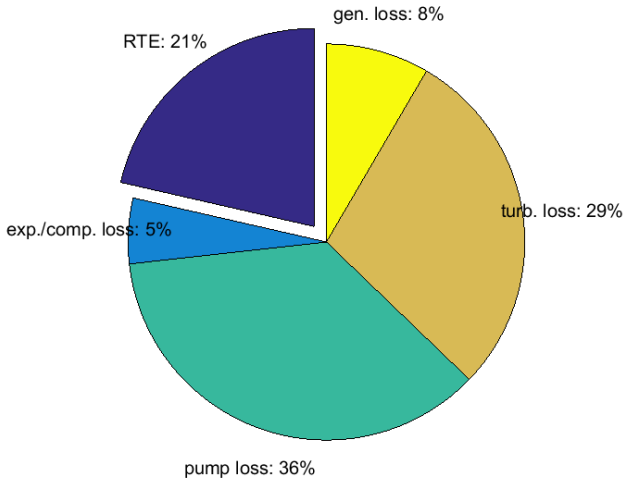

Figure 3.8: GLIDES roundtrip efficiency and losses

The results of all four GLIDES prototype test runs are summarized in Table 3.2.

Table 3.2: Summary of GLIDES Gen. 1 prototype results

Test	**p_{min} [bar]**	**p_{max} [bar]**	**Pause [mins]**	**η_{elec}**	**η_{shaft}**	**η_{ind}**	**ED_{elec} [kWh/m^3]**	**ED_{shaft} [kWh/m^3]**	**ED_{ind} [kWh/m^3]**
Test 1	70	130	352	0.21	0.3	0.94	0.39	0.55	1.11
Test 2	70	100	344	0.18	0.27	0.97	0.19	0.29	0.63
Test 3	100	130	339	0.21	0.3	0.96	0.21	0.29	0.62
Test 4	100	130	0	0.24	0.32	0.97	0.23	0.31	0.62

As expected, test 4 achieves the highest electrical and indicated efficiency. This is because there is no pause between the end of charging and discharging, so the pressure is not allowed to decay as heat is lost from the air. Discharge begins promptly at 130 bar pressure. Also as expected, test 1 achieves the highest energy densities, which can be explained by test 1 having the largest pressure range (largest difference between minimum and maximum pressure. Test 4 has higher electrical efficiency than test 2, even though the indicated efficiencies are similar. This is likely due to the electrical generator operating in a higher efficiency range due to higher pressure and as a result higher RPM.

3.2 Model Formulation, Calibration & Validation

3.2.1 Model Formulation

As a reminder, the formulation of the GLIDES physics-based model is presented again in this section. A set of coupled differential equations were developed to model the transient thermodynamic response of the three major thermal masses (gas, liquid, tank walls).

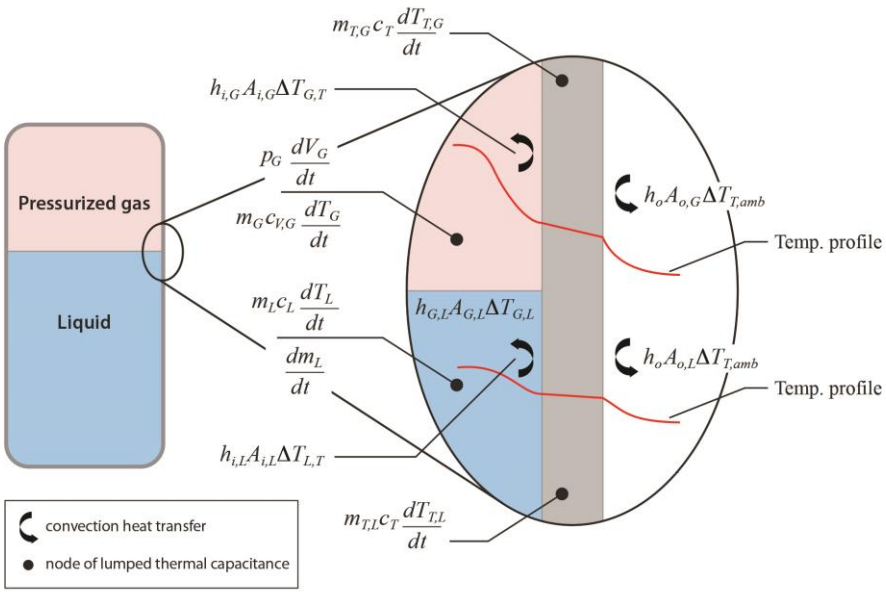

Figure 3.9: GLIDES physics-based model formulation

Figure 3.9 presents all of the control volumes in consideration. The tank wall is measured as two separate control volumes, the top portion in contact with the air, and the bottom portion in contact with the water. The mass of both control volumes is varied dynamically as the water level in the vessels changes during charging and discharging. The simulation model relies on several assumptions: spatial temperature gradients within each medium are not considered (lumped capacitance), constant thermophysical properties for the tank wall material, the compressed air is assumed to behave as an ideal gas and modeled using the ideal gas equation of state, negligible heat transfer between the tank upper and lower masses, and quasi-steady processes.

The energy equation for the gas (air) is given by Equation (3.14). The term on the left is the time rate of change of the energy contained within the gas at time *t*; the first term on the right is the net rate at which energy is transferred in by heat transfer with the liquid; the second term on

the right is the net rate at which energy is transferred in by heat transfer with the tank walls; and the last term on the right is the net rate at which energy is transferred out by boundary work due to the liquid piston acting on the gas.

$$m_G c_{v,G} \frac{dT_G}{dt} = -h_{G,L} A_{G,L} (T_G - T_L) - h_{i,G} A_{i,G} \left(T_G - T_{T,G}\right) - p_G \frac{dV_G}{dt} \tag{3.14}$$

Equation (3.15) is the energy equation for the liquid. The term on the left is the time rate of change of the energy contained within the liquid at time *t*; the first term on the right is the net rate at which energy is transferred in by heat transfer with the gas; the second term on the right is the net rate at which energy is transferred in by heat transfer with the tank walls; and the last term on the right is the net rate of energy transfer into the control volume accompanying mass flow of water. The enthalpy of the inflowing water (i_L) is given by Equation (3.14), where the first term is the saturation enthalpy of the liquid at the ambient temperature, $v_f(T_L)$ is the specific volume of the liquid at the temperature of the liquid, p_G is the pressure of the gas and $p_{L,sat}(T_{L,amb})$ is the saturation pressure of the liquid at the ambient temperature. This formulation for the liquid energy equation was modified slightly from the version presented in Equation (2.2) in Chapter 2. The term for the rate of energy transfer into the control volume accompanying mass flow of water was altered to utilize an expression for the enthalpy of the inflowing water instead of using a simple temperature difference, which likely causes excessive error.

$$m_L c_L \frac{dT_L}{dt} = h_{G,L} A_{G,L} (T_G - T_L) - h_{i,L} A_{i,L} \left(T_L - T_{T,L}\right) + \dot{m}_L i_L \tag{3.15}$$

$$i_L = i_f \left(T_{L,amb}\right) + v_f (T_L) \cdot \left(p_G - p_{L,sat}\left(T_{L,amb}\right)\right) \tag{3.16}$$

Equation (3.17) is the energy equation for the portion of the tank walls in contact with the gas. The term on the left is the time rate of change of the energy contained within the corresponding mass at time *t*; the first term on the right is the net rate at which energy is transferred in by heat transfer with the gas on the inside; and the second term on the right is the net rate at which energy is transferred in by heat transfer with the ambient air on the outside.

$$m_{T,G} c_T \frac{dT_{T,G}}{dt} = h_{i,G} A_{i,G} \left(T_G - T_{T,G}\right) - h_o A_{o,G} \left(T_{T,G} - T_{amb}\right) \tag{3.17}$$

Equation (3.18) is the energy equation for the portion of the tank walls in contact with the liquid. The term on the left is the time rate of change of the energy contained within the corresponding mass at time *t*; the first term on the right is the net rate at which energy is transferred in by heat transfer with the liquid on the inside; and the second term on the right is the net rate at which energy is transferred in by heat transfer with the ambient air on the outside.

$$m_{T,L} c_T \frac{dT_{T,L}}{dt} = h_{i,L} A_{i,L} \left(T_L - T_{T,L}\right) - h_o A_{o,L} \left(T_{T,L} - T_{amb}\right) \tag{3.18}$$

Equation (3.19) is the continuity equation for the gas. The term on the left is the time rate of change of the volume of the gas at time *t*, and the term on the right is the volumetric flow rate of liquid displacing the gas.

$$\frac{dV_G}{dt} = -\frac{\dot{m}_L}{\rho_L} \tag{3.19}$$

Equation (3.20) shows the liquid continuity equation. The term on the left is the time rate of change of the mass of liquid contained within the tanks at time *t*, and the term on the right is the mass flow rate of liquid into the tanks.

$$\frac{dm_L}{dt} = \dot{m}_L \tag{3.20}$$

The air is assumed to behave as an ideal gas obeying the ideal gas equation of state (Equation (3.21) which was used to solve for the pressure of the gas at each time step.

$$p_G = \frac{m_G R_G T_G}{V_G} \tag{3.21}$$

Equations (3.14)-(3.19) were discretized using a finite difference scheme and used to solve the temperature and pressure response of the gas in time increments of one second. The MATLAB programming environment was used to implement the model. The implementation of the model is similar to the code found in Appendix A, with the appropriate equation modifications described in the previous sections.

3.2.2 Model Calibration & Validation

The experimental data collected from Test 1 of the GLIDES prototype was utilized to calibrate the simulation model described in the previous section. A number of calibration measures were taken to improve the extent to which the model reflected experimental results. The charging and discharging flow rates through the pump and Pelton turbine measured experimentally were correlated with the system pressure and used in the simulation model. To calculate/update the air pressure, it was found that the ideal gas equation of state captured the transient system pressure

behavior more effectively than the Redlich-Kwong (RK) equation of state initially used in the simulation effort in Chapter 2. The model formulation described in the previous section requires four heat transfer coefficients, $h_{G,L}$ (gas-to-liquid), $h_{i,G}$ (gas to inner tank wall), $h_{i,L}$ (liquid to inner tank wall), and h_o (outer tank wall to ambient air). The outer heat transfer coefficient h_o is modeled assuming forced convection over a vertical cylinder with a representative outdoor wind velocity of ~3 m/s using a Churchill and Bernstein correlation [56]. The liquid to inner tank wall heat transfer coefficient $h_{i,L}$ is calculated using LeFevre's correlation [55], approximating the inner wall of the tank as a vertical wall. The remaining two heat transfer coefficients, $h_{G,L}$, and $h_{i,G}$ are assumed to be constant values and are the primary parameters used to calibrate the model to achieve reasonable agreement between the simulated and experimental results. $h_{G,L}$ is varied between 200-500 W/m^2*K, and $h_{i,G}$ is varied between 75-100 W/m^2*K.

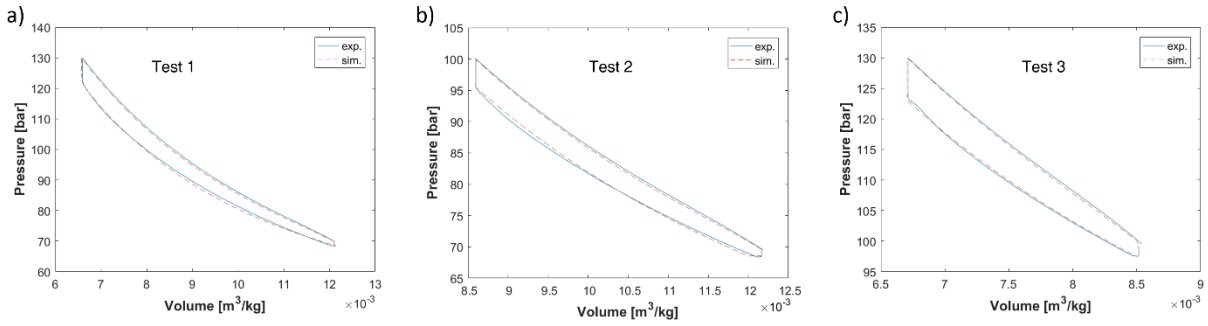

Figure 3.10: Experimental versus simulated pressure-volume diagrams for three different test conditions

The calibrated model was then run for the same conditions as Tests 1-3 described in Table 3.2. Figure 3.10 shows a comparison of the experimental versus simulated pressure-volume

diagrams for Tests 1-3. It can be seen visually and qualitatively from Figure 3.10 that there is strong agreement between the simulated and experimental test profiles. The primary purpose of the model is to predict the indicated efficiency and energy density of the system. Maximum error of 5.75% and 3.51% for the efficiency and energy density respectively were achieved. Table 3.3 below shows the error for the two parameters for all three tests.

Table 3.3: Experimental versus simulated efficiency and energy density percentage errors

Test	**η_{ind} error [%]**	**ED error [%]**
Test 1	5.75	1.28
Test 2	2.34	3.51
Test 3	0.30	0.42

3.3 Parametric Analysis

The calibrated model was then used to conduct parametric simulations of the GLIDES system. Parameters of interest include the minimum pressure, the maximum pressure, and the auxiliary component efficiencies (pump/motor and turbine/generator). In the following sections, the combined pump/motor efficiency is referred to as the charging efficiency, and the combined turbine/generator efficiency is referred to as the discharging efficiency. These efficiencies are assumed to be constant values throughout charging and or discharging.

Figure 3.11 shows the relationship between pressure ratio (p_{min}/p_{max}) and efficiency as well as energy density, for both electrical efficiency and energy density (a) and indicated efficiency and energy density (b) for several p_{max}. The minimum pressure p_{min} is varied from 40 bar to 90 bar, and the maximum pressure p_{max} is varied from 100 bar to 160 bar. The arrow head on each curve

in Figure 3.11 points in the direction of the applicable y-axis (left or right) The electrical data assumes state-of-the-art charging (pump/motor) and discharging (turbine/generator) efficiencies of 90% [6, 7, 62]. As seen in the Figure, in general, there is a tradeoff between efficiency and energy density. As the pressure ratio increases (i.e. the difference between p_{min} and p_{max}) decreases, the efficiency improves, but the energy density declines. This trend can be attributed to the fact that, as the pressure ratio approaches unity, less compression/expansion is required and the temperature swing of the air is reduced, so the expansion/compression losses are reduced, efficiency improves, but energy density suffers.

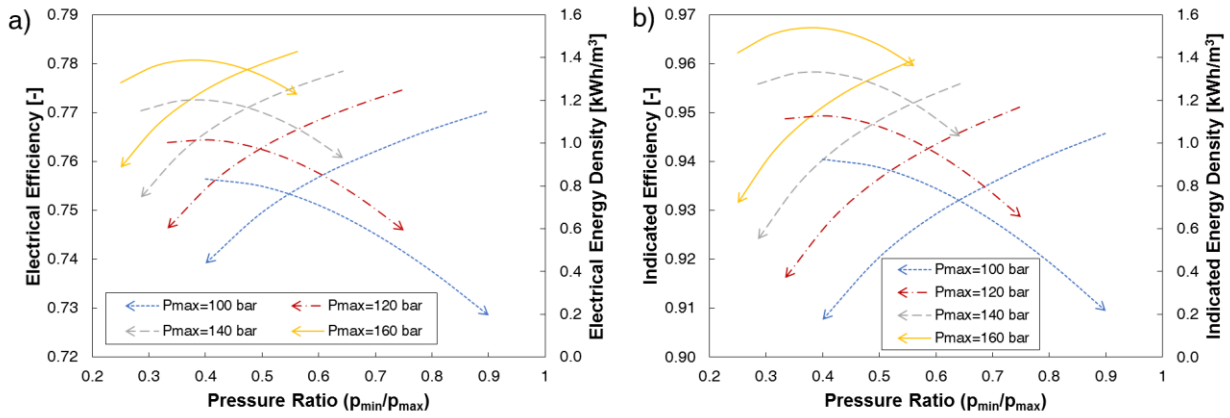

Figure 3.11: Electrical (a) and indicated (b) efficiency and energy density versus GLIDES operating pressure ratio. Note: each curve's arrowhead points in direction of applicable y-axis (left or right).

To simplify the data contained in Figure 3.11, the efficiencies and energy densities are normalized. The efficiencies are normalized by multiplying them by the pressure ratio (p_{min}/p_{max}), while the energy densities are normalized by dividing them by the initial air density (density at p_{min}), yielding the specific energy in kWh/kg of air. The result of these normalizations is shown in

Figure 3.12. The different curves for each value of p_{max} are reduced to overlapping curves. These normalizations and the data shown in Figure 3.12 are valuable because only the pressure ratio and system size (mass of air) are needed to predict the efficiency and indicated energy capacity of a given GLIDES system. To do so, the curves in Figure 3.12 can be fit to yield equations for the efficiency and specific energy. The indicated curves (Figure 3.12 b) are fit and result in Equations (3.22) and (3.23). Goodness of fit (R^2) values of 1 and 0.99 respectively are achieved for equations (3.22) and (3.23). Multipliers for the pump/motor and turbine/generator can be added to obtain the electrical efficiency and specific energy.

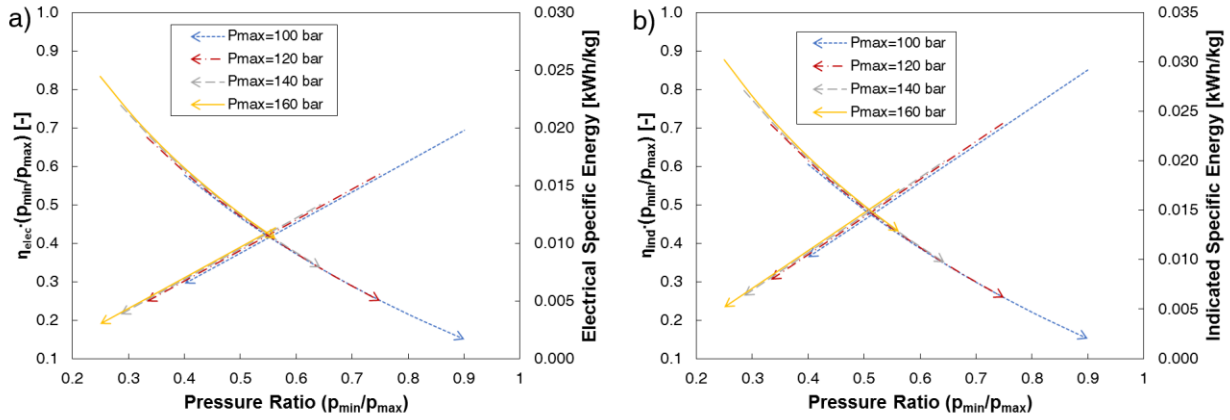

Figure 3.12: Normalized electrical (a) and indicated (b) efficiency and energy density versus GLIDES operating pressure ratio. Note: each curve's arrowhead points in direction of applicable y-axis (left or right)

$$\eta_{ind} = 0.9762 - 0.0278\left(\frac{p_{max}}{p_{min}}\right) \tag{3.22}$$

$$SE_{ind} = 0.0231\left(\frac{p_{min}}{p_{max}}\right) - 0.0651 + 0.0419\left(\frac{p_{max}}{p_{min}}\right) \tag{3.23}$$

Next, the charging (pump/motor) efficiency and discharging (turbine/generator) efficiency are varied to examine the sensitivity of the system overall electrical roundtrip efficiency (η_{elec}) and energy capacity (energy density and specific energy) to the auxiliary component efficiencies. Both the charging and discharging efficiencies are varied from 50% to 100%. For this study, a GLIDES system operating between 70 bar and 130 bar is simulated. The resulting data is shown in Figure 3.13 and Figure 3.14. Figure 3.13 shows η_{elec} for various values of charging and discharging efficiency. Achieving high system efficiency is very reliant on utilizing auxiliary components with high individual efficiencies. Individual component efficiencies above 80% are needed to achieve overall electrical roundtrip efficiency above 60%. As the charging and discharging efficiencies approach unity or 100%, the GLIDES system approaches the indicated efficiency, which can be considered as the maximum theoretical efficiency.

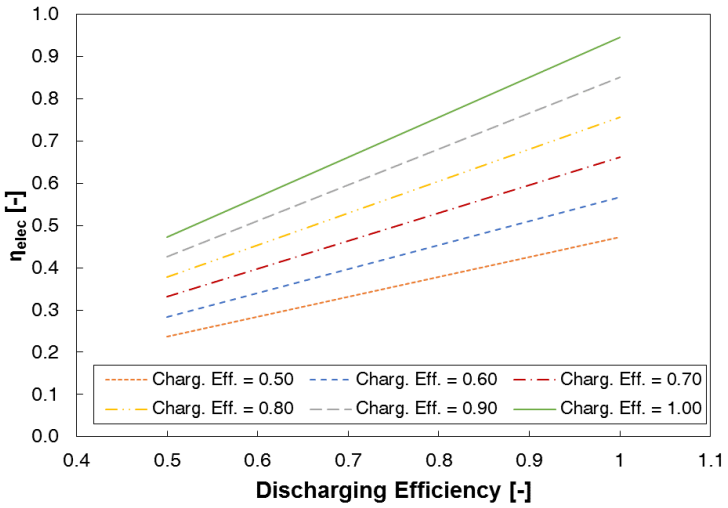

Figure 3.13: GLIDES electrical roundtrip efficiency as a function of charging and discharging component efficiencies

Similarly, to Figure 3.12 a), Figure 3.14 shows the normalized electrical roundtrip efficiency and normalized energy density (specific energy) for various values of charging (pump/motor) and discharging (turbine/generator) efficiencies, as well as the equations for the curve fits. Figure 3.14 a) is for charging/discharging efficiency of 90%, while b), c) and d) are for charging/discharging efficiencies of 80%, 70%, and 60% respectively. With the data in Figure 3.14, the roundtrip electrical efficiency and capacity for any size GLIDES system, operating with any pressure ratio, for any charging/discharging efficiency between 60% and 90% can be approximated. To do so, Equations (3.24) and (3.25) can be used along with the coefficients in Table 3.4.

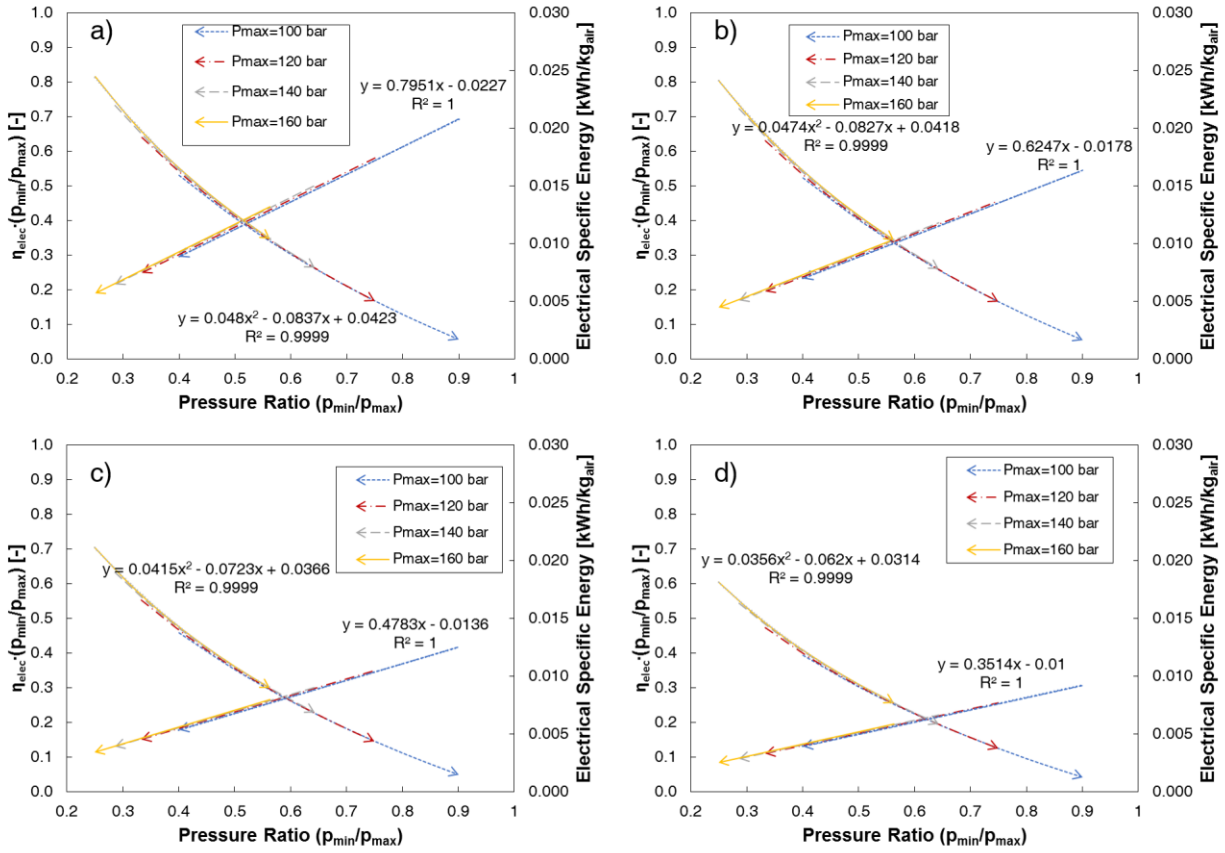

Figure 3.14: Normalized electrical efficiency and energy density versus GLIDES operating pressure ratio for various charging/discharging efficiencies. a) 90%, b) 80%, c) 70%, and d) 60%. Note: each curve's arrowhead points in direction of applicable y-axis (left or right)

$$\eta_{elec} = \mathrm{a} - \mathrm{b}\left(\frac{p_{max}}{p_{min}}\right) \tag{3.24}$$

$$SE_{elec} = \mathrm{c}\left(\frac{p_{min}}{p_{max}}\right) - \mathrm{d} + \mathrm{e}\left(\frac{p_{max}}{p_{min}}\right) \tag{3.25}$$

Table 3.4: Coefficients for use with Equations 3.24 and 3.25

$\eta_{P/T}$	*a*	*b*	*c*	*d*	*e*
0.90	0.7951	0.0227	0.0480	0.0837	0.0423
0.80	0.6247	0.0178	0.0474	0.0827	0.0418
0.70	0.4783	0.0136	0.0415	0.0723	0.0366
0.60	0.3514	0.0100	0.0358	0.0620	0.0314

In summary, experimental electrical roundtrip efficiency and indicated efficiency of 24% and 97%, and electrical and indicated energy density of 0.23 kWh/m^3 and 0.62 kWh/m^3 respectively were achieved for the system with peak pressure limited to 130 bar. Low electrical roundtrip efficiency was due to large energy losses in auxiliary components (pump/motor and turbine/generator. Auxiliary component efficiencies were relatively low and not optimized for the specific application at hand. In addition to the experimental performance results, a comprehensive, physics based model of the GLIDES system was developed and also presented. The physics based model was calibrated and validated using the experimental data, and good agreement between experimental and simulated data was achieved. The validated model was then used to conduct parametric analysis of the performance of the GLIDES system. It was found that in general, when plotted against pressure ratio, there is a trade-off between system efficiency and energy density.

However, the indicated efficiency dependence on pressure ratio is fairly weak. The results show that the cycle thermodynamic efficiency is very high and there is not much more room for improvement; thus achieving high system efficiency is very dependent on utilizing auxiliary components with high individual efficiencies, therefore, proper sizing and optimized selection of auxiliary components is critical. Only pressure ratio and system size are needed to accurately predict the efficiency and energy capacity of a given GLIDES system. One potential strategy to improve auxiliary component operating efficiency is to narrow the range of pressure variation to reduce off-design point operation. One way of pursuing this is to try to achieve isobaric (or near-isobaric) compression and expansion; this can be done by utilizing alternative working fluids to air, such as condensable gases. This strategy is investigated in the following chapter.

CHAPTER 4. CONDENSABLE GASES AS WORKNG FLUID

Some content in this chapter (figures and text) adapted from:

1. Odukomaiya, A., et al., Near-isothermal-isobaric compressed gas energy storage. Journal of Energy Storage, 2017. 12: p. 276-287. [63]

In this chapter, the effectiveness of storing energy by compressing and expanding a condensable gas is evaluated. Utilizing heat transfer techniques and replacing the non-condensable air with a condensable gas (i.e. CO2, synthetic refrigerants, hydrocarbon refrigerants, etc.) has been proposed as methods to improve energy density and roundtrip efficiency of such systems, leading to near isothermal and near isobaric charge/discharge processes. In order to investigate the effectiveness of the proposed concept, miniature lab-scale experimental setups were designed and built to investigate the compression/expansion characteristics and energy storage efficiency of a system utilizing condensable gases as the energy storage (primary) working fluid, and mineral refrigerant oil as the liquid piston (secondary) working fluid. R134a was initially studied (low pressure), followed by carbon dioxide (high pressure). Several tests were carried out to quantify energy storage efficiency and energy density. It is found that improving heat transfer rates from/into the storage fluid results in increased efficiency and energy density. A heat-transfer enhancement strategy to achieve near isothermal, isobaric expansion and compression to a greater extent is investigated experimentally on the R134a tests. Some results are generalized and presented in non-dimensional form which can be applied to describe and/or design scaled-up systems. In addition to the experimental work, a physics-based model is created and used to achieve a deeper understanding of the underlying physics of the compression and expansion behavior of condensable gases.

4.1 Why Condensable Gases?

Successful use of a condensable gas provides a number of advantages over the current system. There are several potential benefits of switching the primary working fluid to be a condensable gas. The first such benefit is the potential of operating with constant temperature/pressure during compression and expansion. This is possible due to gas/liquid (during compression) and liquid/gas (during expansion) phase change. Currently, the system utilizing air results in an unsteady power profile due to non-constant pressure expansion during discharge. Constant pressure expansion due to phase change would allow for a steady power delivery profile, for applications where variable capacity power delivery is not acceptable. These effects can be further explained by examining Figure 4.1. Figure 4.1 shows theoretical pressure-volume diagrams for an isothermal storage cycle versus an isobaric (and isothermal) storage cycle, the isothermal cycle operates between a low and high operating pressure, while the isobaric cycle operates at the high operating pressure. For the isothermal cycle, it begins at state point 1, as the liquid piston fluid is pumped into pressure vessel(s) the volume of the gas decreases as it is displaced, and the pressure increases isothermally until the high pressure is reached at state point 2. After an idle period, the pressure remains the same (no pressure is lost to the ambient as the heat of compression is lost to the ambient, as would be the case in an actual cycle utilizing air). Energy extraction then begins from state 3, as the gas expands, pressure decreases and volume increases back down to state point 4, which is also the initial state 1. Now, consider the isobaric system, beginning with the condensable gas as a saturated vapor at state point 1. Compression begins as the liquid piston fluid is pumped into the pressure vessel(s), the volume decreases as the gas is displaced by the liquid piston, however, due to vapor to liquid phase change, the pressure remains constant, until only saturated liquid remains at state point 2. After an idle period, the energy extraction process

begins from state 3; the saturated liquid expands, as it evaporates back to vapor phase, the pressure is maintained constant. The constant pressure during discharge (state 3 to 4) allows for a steady power delivery profile. Also, due to constant operation at the higher pressure, the energy density is higher; this can be seen by comparing the integral of the isobaric curve (area under the curve), to the integral of the isothermal curve. Note that this comparison is only valid for a condensable gas having saturated pressure equal or near the high pressure of the non-condensable system. Also note that a perfectly isobaric condensable gas system would also be isothermal. Furthermore, because the pressure would be constant (or varying within a narrower band) efficiency losses in auxiliary components (pump/motor and turbine/generator) due to variable (off-design point) operation can be minimized or avoided. In addition to the above, the density change associated with compression from a saturated vapor to a saturated liquid means that larger volume displacement is achievable and more secondary pumping liquid (liquid piston fluid) is introduced into the system. This means that more liquid can be passed through the hydraulic turbine during discharge, meaning that the power delivery period is longer and more energy can be extracted.

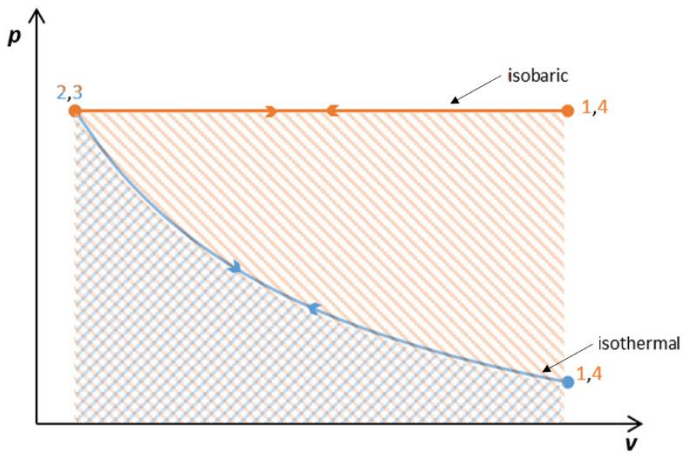

Figure 4.1: Comparison of ideal isothermal (non-condensable) and isobaric (condensable) storage pressure-volume diagrams

There have been a few attempts at achieving isobaric compressed-air/gas energy storage in the literature. A couple of concepts approach the problem by displacing the air volume during charging or discharging using a liquid to maintain constant pressure. Nielsen and Leithner [64] displace the air volume by using a brine shuttle pond at the surface which gravity feeds the storage cavern and enables near isobaric storage. Because the volume displacement is gravity fed, the reverse process cannot be completed during discharge (energy recovery), so this strategy can only be leveraged during half of the cycle. Similarly, Mazloum *et al.* [65] utilized the volume displacement technique, however, they utilize a secondary loop to pump water into the storage medium during charging. The loop also includes a Pelton turbine to recover energy from the pumped water as it is evacuated during discharge. While the system would incur additional energy use during charging due to running a high pressure hydraulic pump in addition to a compressor during charging, it is not clear how much of this additional energy is recovered via the Pelton turbine during discharge. A few concepts attempt to achieve near-isobaric operation by siting the storage medium underwater to leverage the hydrostatic pressure exerted by the surrounding water during charging and discharging [66-68], however, geographic restrictions remain an issue with these concepts, and placing systems underwater introduce a host of new logistical and engineering challenges. Lastly, Chen *et al.* [69] approached the challenge using a combination of the volume displacement approach and utilizing condensable (volatile) gases. The storage medium is split into two compartments separated by a sliding piston. One side is utilized for air storage, while the other side is charged with a condensable gas. During charging or energy storage, the condensable gas condenses, providing a sort of pressure relief or buffer against pressure increasing. During discharge or energy recovery, the opposite occurs, the condensable gas vaporizes providing a pressure boost to maintain pressure during discharge. Although a differen approach than the one

presented in this chapter, at the writing of this thesis, this last concept is the only one found in the literature which attempts to use condensable or volatile gases to achieve isobaric compression/expansion for energy storage.

4.2 R134a – Experiment Overview

To assess the feasibility of a proposed system utilizing condensable gas. An experimental system was built to investigate the energy storage potential and compression/expansion characteristics of utilizing R134a as a condensable gas (primary working fluid) and mineral refrigerant oil (secondary pumping liquid). The information gained from this research effort will provide insight into the potential of condensable gases for energy storage, and help guide the design of a scaled-up system operating at higher pressure, with appropriate selection of working fluids. The success of the R134a experiments led to the development of a similar experiment utilizing Carbon Dioxide as the condensable gas. This effort is also described in subsequent sections in this chapter.

4.2.1 Initial Configuration

The purpose of this experiment is to investigate the potential of utilizing a condensable gas as the primary working fluid in the GLIDES energy storage system, instead of the non-condensable air or nitrogen which have previously been proposed. The storage tank of the system is a clear polycarbonate tube 241 cm in length, inner diameter of 1.9 cm, outer diameter of 2.54 cm; inside this tube there is a freely traveling, leak-free rubber piston separating the primary working fluid from the fluid serving as the liquid piston (mineral oil in this case). Markings were made along the tube to measure gas volume throughout the progression of experiments. On the upper side of the piston is the chamber containing the condensable fluid, R-134a in this case. R134a is a common

refrigerant that condenses at room temperature under relatively low pressures (approximately 6 bar at 20 °C). R134a was chosen as the condensable gas for these experiments because it is readily available and its saturation pressure is low enough for clear tubing to be utilized without the need for specialized high pressure pumps or opaque vessels. On the other side of the piston is immiscible mineral oil. Mineral oil is used as the coupling fluid to act as the liquid piston. It was chosen because it is immiscible with liquid R134a. An experiment hand pump is utilized to pump the mineral oil into the storage polycarbonate tube. Located at the top of the tube is a pressure gauge, pressure transducer, and thermocouple. These measurement instruments were used along with a National Instrument data acquisition module and LabView program to collect experiment data from the system. Data was collected every one second for the duration of each experiment. Located at the bottom of the tube is the mineral oil inlet/outlet. This acts as a valve to control charging and discharging rates. A schematic of the test rig can be seen in Figure 4.2. The insert shows the rubber piston which slides freely up and down inside of the clear tube, with the R134a above, and the mineral oil below.

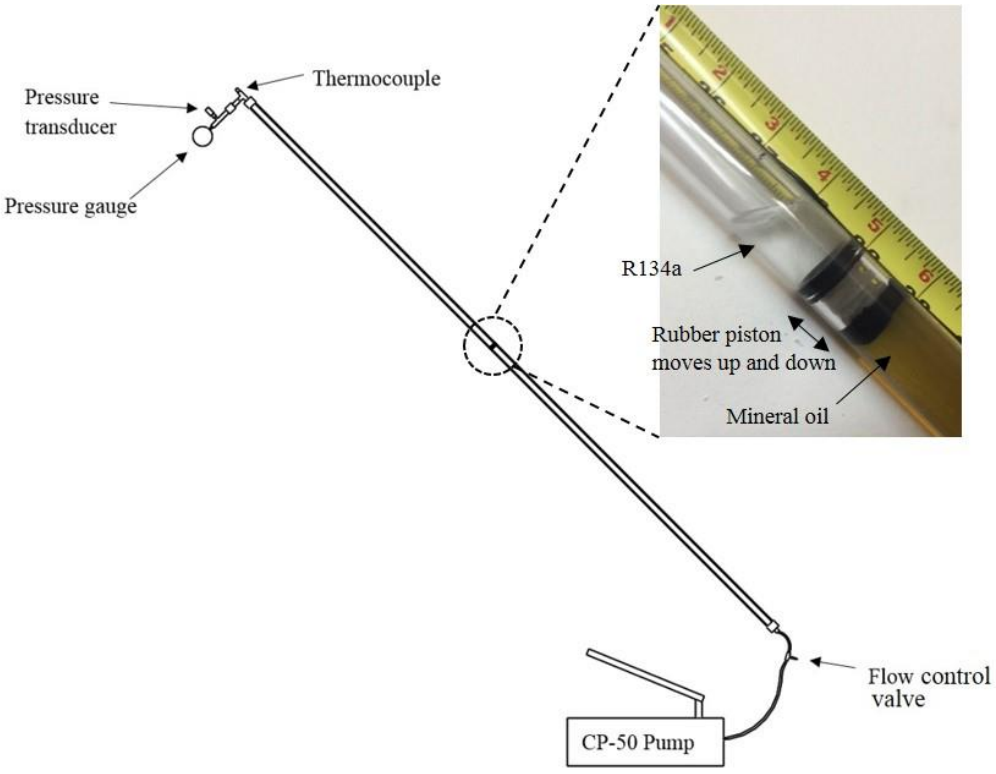

Figure 4.2: Schematic of R134a experimental setup

4.2.2 Improved Configuration

To improve heat transfer performance during experiments, a heat pipe, heat sink, and fan arrangement are added to the experimental setup as seen in Figure 4.3.

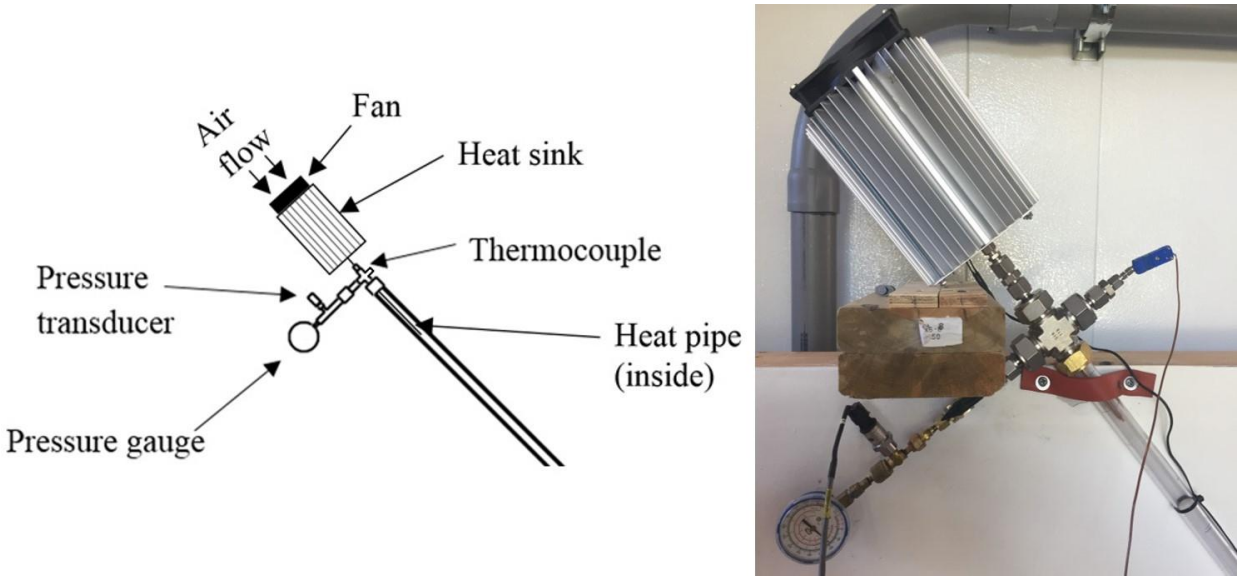

Figure 4.3: Schematic and image of modifications made to R134a experimental setup for improved heat transfer

The heat pipe used in the experiment is a 6-mm diameter, 12-inch length copper heat pipe with deionized water as the working fluid and a sintered wick. An aluminum heat sink with radial fin profile, measuring 109 mm width and height, with 1.52 mm fin thickness and 43 mm base thickness is used. A 6-inch, 50 CFM square fan is utilized for forced convection to faster dissipate the heat of compression transferred from the refrigerant via the heat pipe and heat sink. The majority of the length of the heat pipe is introduced into the vapor refrigerant from the top of the storage tube. The top of the heat pipe which is not inside the storage tube is thermally connected to a radial heat sink using thermal paste and a fan is used to achieve forced convection. This arrangement helps to increase heat transfer from the working fluid refrigerant during compression (charging). As the refrigerant is compressed and heat of compression is generated, the heat pipe, heat sink, and fan help to remove this heat from the refrigerant, reducing the resulting temperature

increase. This allows the compression process to be closer to isothermal, and consequently, closer to isobaric. In this design, most of the condensation takes place on the surface of the heat pipe.

4.2.3 Measurement, Instrumentation and Data Reduction

Three measurements were used in the experimental setup described in the previous section. These measurements were pressure, temperature, and length of the refrigerant column (used to calculate volume). Pressure measurements were collected using a Sentra 3100R230PG1G9 pressure transducer with 0-230 psig range and 0.25% of full scale accuracy. Temperature measurements were taken using an Omega T-type 12-inch probe type thermocouple with -250 – 300 °C range and maximum uncertainty of ±0.5 °C. Refrigerant column length measurements were obtained optically using a 50-ft. tape measure with smallest increments of 1/16 inch installed alongside the storage tube. Uncertainty of the length measurements is therefore taken as ±1/32 inch. This length measurement uncertainty results in uncertainty in the calculated volume of 4.5E-07 m^3.

The experiment procedure consists of two parts, first the charging process (energy storage stroke), and second the discharging process (energy recovery stroke). A test begins with the storage tube initially containing only R134a as saturated vapor. The initial state is the point at which a small amount of R134a is already liquid (to ensure saturation) and if pressurized, more R134a would condense immediately. The data collection program is then run. The oil flow valve is opened and the hand pump is operated to pressurize the system by pumping oil acting as the liquid piston into the storage tube at pre-determined rates. Pressurizing continues until the final state where the flow valve is closed. The time at which the gas volume reaches each marking on the tube is recorded. The work input is calculated by numerically integrating the charging pressure-volume

curve from the initial volume to the end of compression to determine the area underneath, as seen in Equation (4.1). After waiting for a long enough pause period to allow for condensation to go to completion, and temperature to return to equilibrium with ambient, the discharging process is ready to begin. The flow valve is opened. Once again, the volume is recorded incrementally by recording the timestamp at which each marking along the tube is reached. When the oil is fully evacuated, the flow valve is closed, marking the end of the experiment, and the data-logging program is stopped. Again the work extracted from the system is calculated via numerical integration of the discharging pressure-volume curve from the volume at the end of compression to the volume at the end of expansion, as seen in Equation (4.2).

$$W_{in} = \int_{V_0}^{V_c} p_f dV_f = \sum_{V_0}^{V_c} p_f \Delta V_f \tag{4.1}$$

$$W_{out} = \int_{V_c}^{V_e} p_f dV_f = \sum_{V_c}^{V_e} p_f \Delta V_f \tag{4.2}$$

The system indicated efficiency is then calculated by dividing the work output by the work input. The system energy density is also calculated by dividing the work output by the initial volume. These calculations are shown in Equations (4.3) and (4.4).

$$\eta = \frac{W_{out}}{W_{in}} \tag{4.3}$$

$$ED = \frac{W_{out}}{V_0} \tag{4.4}$$

4.3 R134a – Results & Analysis

4.3.1 Initial Configuration

Three tests were conducted under this configuration of the system; each having a varying charge and discharge time. The charge time was varied simply by adjusting the pumping rate of the oil. The discharge time was adjusted by adjusting the extent to which the flow valve evacuating the oil was opened. The test parameters and results are shown in Table 4.1.

Table 4.1: R134a test parameters and results

Tests	**Figure Reference**	**Charge Time (mins)**	**Discharge Time (mins)**	**Efficiency**	**Energy Density (kJ/m^3)**	**Min/Max Pressure (bar)**	**Min/Max Volume (m^3)**
Test 1	Figure 4.4	5.45	7.13	82.00%	476.39	5.02/7.03	6.33E-5/6.78E-4
Test 2	Figure 4.5	22.08	23.65	86.56%	507.00	5.35/6.90	5.97E-5/6.78E-4
Test 3	Figure 4.6	61.97	63.92	89.97%	515.36	5.53/6.66	5.97E-5/6.78E-4

The general trend of an increase in efficiency as charge and discharge time increases due to decreasing slopes of the pressure-volume curve is expected and observed. This decrease in slope equates to less pressure change for each unit change in volume. Increase in the time allowed for charging and discharging allows for improved heat transfer; heat transfer is a relatively slow process. In order to achieve truly isothermal and isobaric compression, heat transfer must be good enough to sufficiently dissipate the heat of compression generated. Otherwise, the heat remains in the system, resulting in an incremental increase in gas temperature, and subsequent increase in saturation pressure. This results in a required increase in mechanical work per unit volume required

to continue condensation. By increasing the charging time, more time is allowed for heat transfer to occur, improving performance. The opposite is true during discharge, adequate heat transfer is needed to allow heat to flow into the system, counter-acting the cooling due to expansion. When heat transfer is not adequate, gas temperature falls, resulting in associated decrease in saturation pressure, which means the amount of work per unit volume that can be extracted from the system decreases. In practical energy storage systems designed for application in solar or wind energy, the charging/discharging time is typically several hours, depending on the availability of renewable resources and/or system size. The transient pressure/temperature profiles and pressure-volume diagrams for tests 1-3 can be seen in Figure 4.4, Figure 4.5, and Figure 4.6. For both the temperature and pressure transient profiles, the beginning of the charging process (time zero) sees temperature and pressure increase until the charging process is complete; this is where the peak temperature and pressure occur. The charging process is then followed by an idle period where temperature and pressure decrease slowly. The discharge process then sees a decrease in temperature and pressure (occurs around 120-minute mark for Test 1), followed by another pause period during which the temperature and pressure increase slowly. These four distinct processes can be seen in the pressure-volume diagram in Figure 4.5 b). First, charging from state 1 to state 2, during which volume decreases and pressure increases, then a pause (idle period) during which volume remains constant but pressure decreases as heat is lost to the ambient. This is followed by discharging from state 3 to state 4, as pressure decreases and volume increases. Finally, another pause (idle) period from state 4 back to state 1, as the volume remains constant, but the pressure increases due to heat transfer to the gas inside the tube.

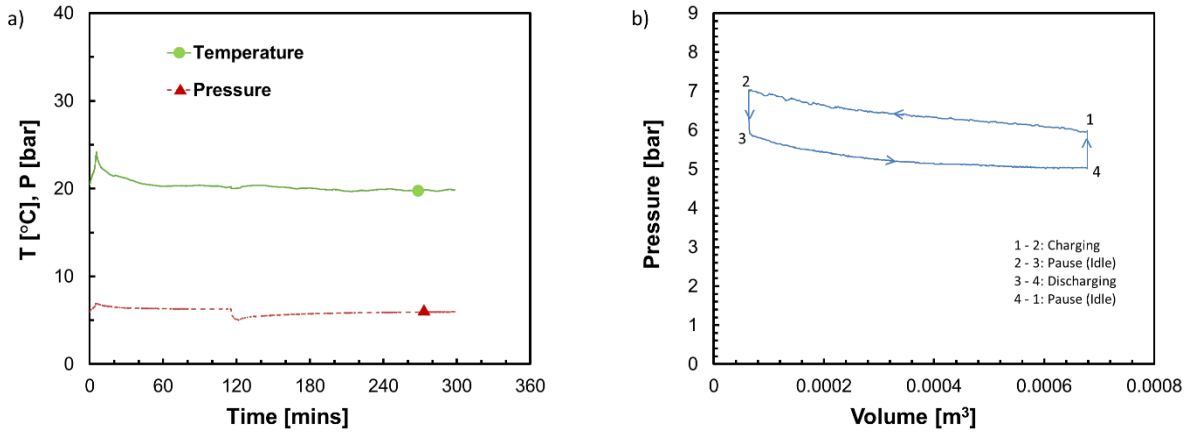

Figure 4.4: R134a Test 1 transient temperature/pressure profiles and pressure-volume diagram

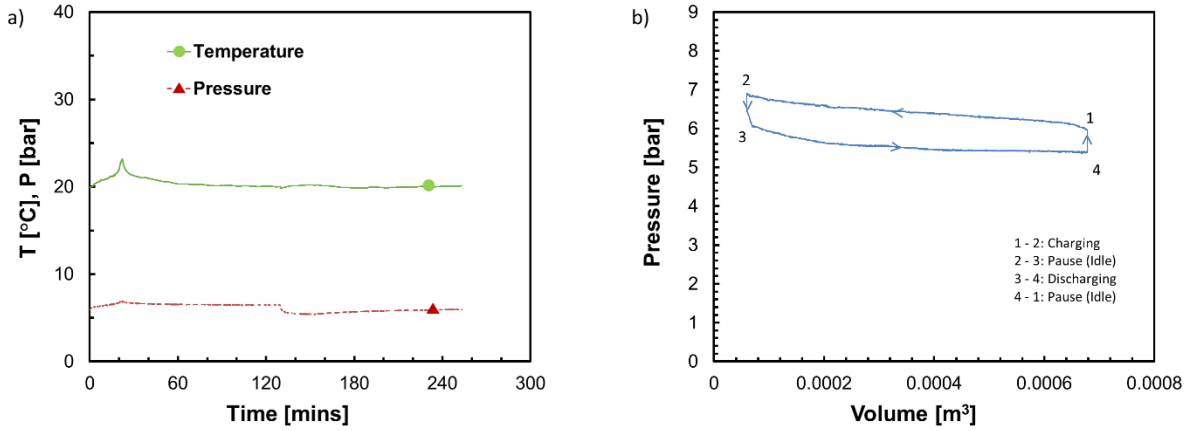

Figure 4.5: R134a Test 2 transient temperature/pressure profiles and pressure-volume diagram

Further increases in efficiency can be achieved by adding passive or active heat transfer strategies, which would reduce gas temperature changes (i.e. maintain condensation/evaporation pressure constant or near constant). This would make the charging and discharging processes to approach isothermal processes and reduce energy loss. One such method is discussed in subsequent sections.

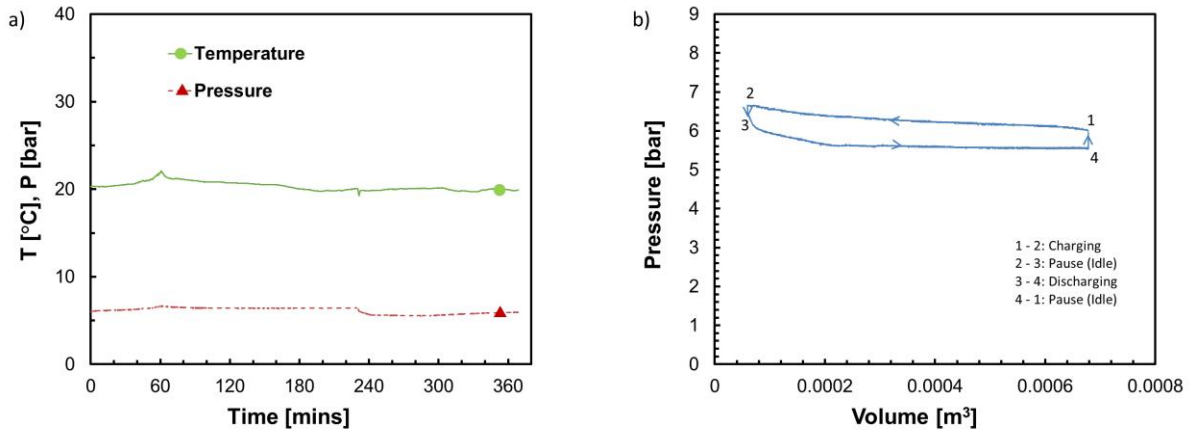

Figure 4.6: R134a Test 3 transient temperature/pressure profiles and pressure-volume diagram

4.3.2 Improved Configuration

As previously mentioned, achieving adequate heat transfer during charging and discharging is important to maximize system efficiency. Achieving adequate heat transfer rates helps to minimize temperature change, which in turn minimizes changes in saturation pressure of the working refrigerant. This effect can be further explained by examining the energy equation (first law of thermodynamics) for a control volume comprising of the vapor portion of the working fluid, as seen in the following equations.

$$\frac{dE_v}{dt} = \dot{Q} - \dot{W} + \frac{dm_{v,l}}{dt} h_{fg} \tag{4.5}$$

The terms in Equation (4.5) can be expanded as seen in Equation (4.6):

$$m_v c_v \frac{dT_v}{dt} = \dot{Q} - p_v \frac{dV_v}{dt} + \frac{dm_{v,l}}{dt} h_{fg} \tag{4.6}$$

The term on the left-hand side of the equation is the rate of change of the energy contained within the control volume, namely, product of the mass of the vapor contained in the control volume, the specific heat, and the rate of change of the temperature of the vapor. The first term on the right is the net rate at which heat enters the control volume. The second term on the right is the net rate at which work (boundary) is done by the control volume. The last term on the right is the net rate of energy transfer from the control volume due to gas/liquid phase change. To achieve zero increase in temperature (i.e. no change in saturation pressure), it is necessary that the right side of Equation (4.6) sum to zero, meaning that the rate of boundary work must equal the sum of the other two terms on the right. By assuming a sign convention of heat input and work output being positive, and examining the compression processes of tests 1-3 presented in the previous section, it can be deduced from the increasing gas temperature that the input power is larger than the sum of the other two terms on the side of the equation (in all three cases). Thus, by increasing the heat transfer to decrease the sum of the right-hand side to be closer to zero, a near isothermal or isothermal condition can be achieved. The same is true of the decreasing fluid temperature during expansion, with the signs of the terms on the right-hand side being opposite. This is the basis for the hypothesis that by introducing active or passive heat transfer enhancement strategies, energy storage efficiency can be improved, and isothermal-isobaric operation can be approached.

Three additional tests with similar charging and discharging times as test 1-3 are then conducted with the improved configuration. As described in the ‘Experiment Overview’ section of this chapter, the improved configuration features the addition of a heat pipe, heat sink, and fan,

in order to enhance heat transfer to and from the gas inside of the tube. A fourth test was also conducted to investigate the effect of significantly longer charging and discharging times, in an attempt to match the indicated efficiency of configuration 2 of the air system presented in the 'Previous Work' section of this paper. The test parameters and results can be seen in Table 4.2.

Table 4.2: R134a improved configuration (active HT using heat pipe/heat sink) test parameters and results

Tests	**Figure Reference**	**Charge Time (mins)**	**Discharge Time (mins)**	**Round Trip Efficiency**	**Energy Density (kJ/m^3)**	**Min/Max Pressure (bar)**	**Min/Max Volume (m^3)**
Test 4	Figure 4.7	4.50	9.92	86.97%	516.50	5.37/6.98	5.6E-5/6.8E-4
Test 5	Figure 4.8	18.85	21.77	86.52%	521.74	5.53/7.09	6.5E-5/6.8E-4
Test 6	Figure 4.9	54.58	79.52	94.00%	539.91	5.64/6.59	6.2E-5/6.8E-4
Test 7	Figure 4.10	178.70	187.32	95.80%	544.33	5.74/6.55	6.4E-5/6.8E-4

It can be seen from the data in Table 4.2 that heat transfer enhancement due to the addition of the heat pipe, heat sink, and fan arrangement does result in an improvement in the energy storage efficiency and energy density. This can be illustrated by comparing the efficiencies and energy densities in Table 4.2 and Table 4.1. Based on the charging and discharging times, test 1 can be compared with test 4, test 2 with test 5, and test 3 with test 6. A three-hour (180 min) test was not run in the initial configuration without the heat pipe, heat sink, and fan modification. Although the charging/discharging times are roughly the same, the efficiencies and energy densities obtained with the improved configuration are higher.

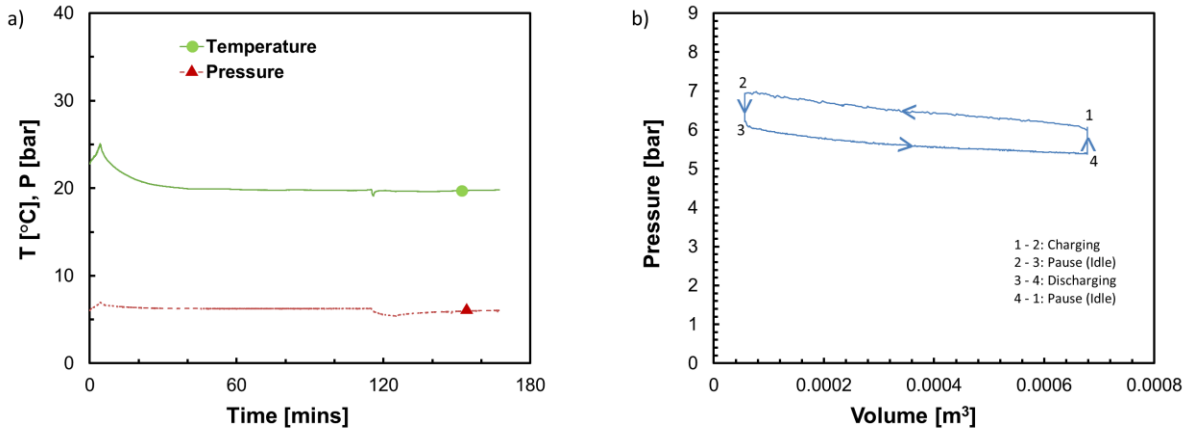

Figure 4.7:R134a Test 4 transient temperature/pressure profiles and pressure-volume diagram

The improvements resulting from the modifications can also be illustrated graphically. The transient pressure/temperature and pressure-volume diagrams for Tests 6-8 can be seen in Figure 4.7, Figure 4.8, Figure 4.9.

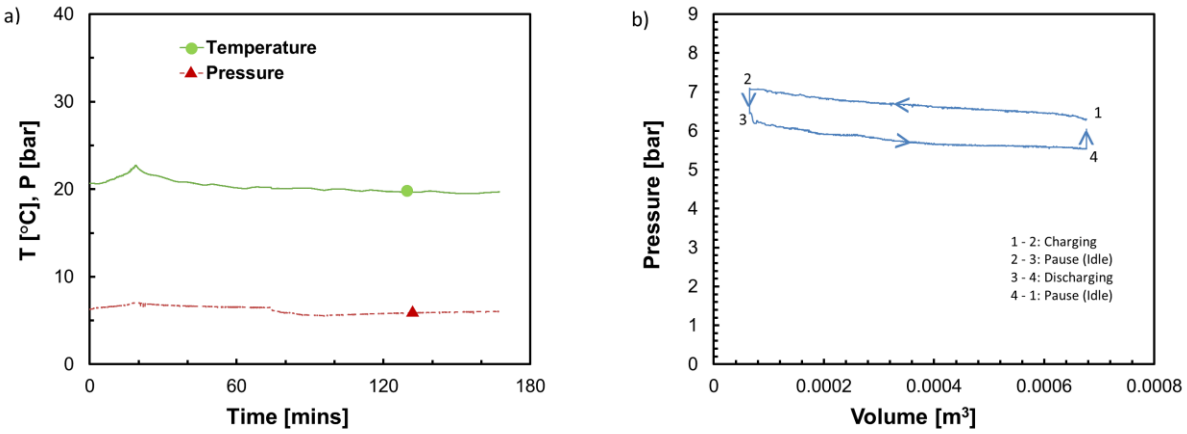

Figure 4.8: R134a Test 5 transient temperature/pressure profiles and pressure-volume diagram

The improvements due to the modifications made for tests 4-7 can be most easily described by comparing the change in pressure due to expansion and compression (ΔP_c, ΔP_e), of the short (tests 1,4), medium (tests 2,5), and long (tests 3,6) tests. In each case, the modified system results in a reduction in ΔP_c and ΔP_e.

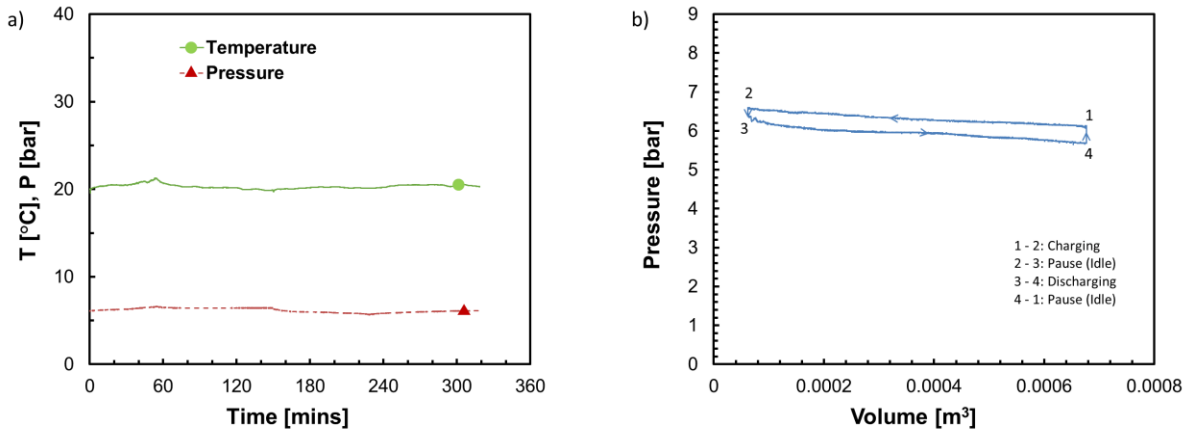

Figure 4.9: R134a Test 6 transient temperature/pressure profiles and pressure-volume diagram

The exact numbers can be seen in and expansion can be achieved.

Table 4.3 along with the percentage reductions. This shows that with adequate enhancement to achieve the necessary heat transfer rates, isobaric (and therefore isothermal) compression and expansion can be achieved.

Table 4.3: Improvements in R134a compression and expansion due to heat transfer enhancement

Test Length	**Test**	**HP/HS?**	***ΔP_c (bar)***	***ΔP_c* Percent Decrease (%)**	***ΔP_e (bar)***	***ΔP_e* Percent Decrease (%)**
Short	1	No	1.08	8.96	1.27	12.64
	4	Yes	0.98		1.11	
Medium	2	No	0.93	13.79	1.13	37.09
	5	Yes	0.81		0.71	
Long	3	No	0.66	24.39	0.89	9.07
	6	Yes	0.50		0.81	

The transient pressure/temperature and pressure-volume diagrams for test 7 which had significantly longer (180 mins) charging and discharging times are shown in Figure 4.10 a) and b). The indicated efficiency of 95.8% achieved here is as good as the highest indicated efficiencies of the air system discussed in Chapters 2 and 3. It is likely that a system utilizing a condensable gas as is described in this work, with equal indicated efficiency as an equivalent system utilizing air would achieve higher roundtrip efficiency and energy density, due to the near isobaric characteristic resulting in reduced conversion losses. Efficiency losses due to off-design operation of auxiliary machines (pump/motor, turbine/generator) would be reduced due to the narrower range of pressures seen with the near isobaric condensable gas system.

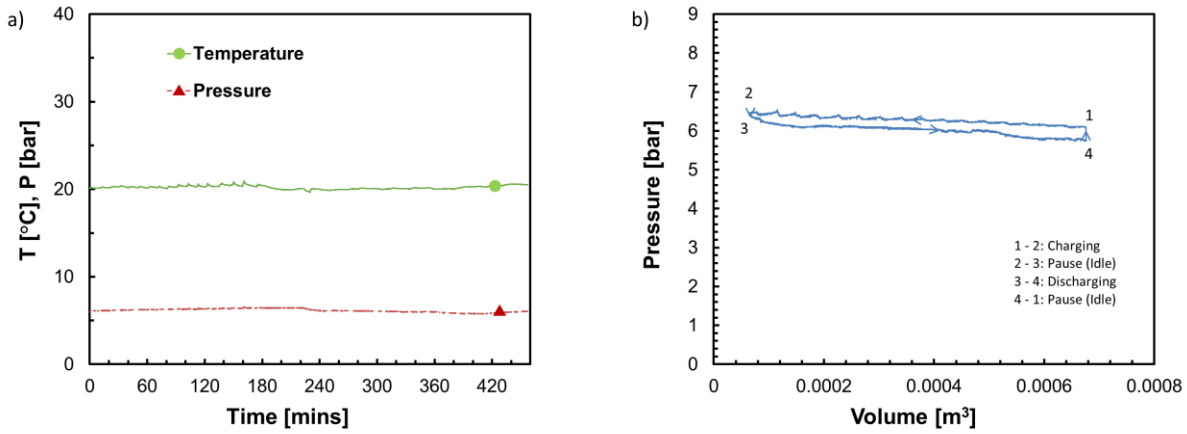

Figure 4.10: R134a Test 7 transient temperature/pressure profiles and pressure-volume diagram

4.3.3 Dimensionless analysis of storage (compression) process

In order to generalize some of the results presented above and present them in a format more readily useful for future analyses, it is possible to non-dimensionalize the compression process by which energy is stored in the working fluid. This analysis yields a new dimensionless number, hereby referred to as π, which can be used to describe the extent to which the compression of a condensable gas approaches isothermal-isobaric compression. It is particularly useful for relative comparisons of different systems. We begin by recognizing that the amount of heat removed from a condensing gas over any given period of time is proportional to the mass of vapor condensed times the enthalpy of vaporization of said vapor, this is shown in Equation (4.7), where *UA* is the overall heat transfer coefficient, T_{sat} is the saturation temperature of the working fluid at the beginning of charging (compression), T_{∞} is the ambient or surrounding temperature, m_{cond} is

the mass of working fluid condensed within the same time frame, and h_{fg} is the enthalpy of vaporization of the working fluid evaluated at the initial temperature and pressure.

$$UA(T_{sat} - T_{\infty})dt \approx m_{cond}h_{fg} \tag{4.7}$$

The mass of the condensed gas on the right-hand side can be re-written as the product of the density of the saturated vapor and change in volume as seen in Equation (4.8).

$$UA(T_{sat} - T_{\infty})dt \approx \rho_{sat,v}dVh_{fg} \tag{4.8}$$

Separating variables yields the subsequent expression in Equation (4.9):

$$\frac{dV}{dt} \approx \frac{UA(T_{sat} - T_{\infty})}{\rho_{sat,v}h_{fg}} \tag{4.9}$$

The term on the right-hand side of Equation (4.9) is the basis of the dimensionless number π. By defining dimensionless time (t*), volume (V*), and pressure (p*) as follows in Equation (4.10), where t_{charge} is the time spent to charge, V_0 is the initial volume at the beginning of charging, and p_{sat} is the saturation pressure of the working fluid, a fully dimensionless number π is obtained and the compression process for a condensable gas can be shown on a dimensionless pressure-volume diagram.

$$t^* = \frac{t}{t_{charge}} \ , \ \ V^* = \frac{V}{V_0} \ , \ \ p^* = \frac{p}{p_{sat}} \tag{4.10}$$

This results in the following dimensionless number shown in Equation (4.11), which describes the entire compression process. The dimensionless number shows the scale of the heat removal rate to the heat generation rate. Since the compression rate (t_{charge}) and the heat transfer effectiveness (UA) are the main parameters determining how close to isobaric-isothermal behavior the compression process gets, the dimensionless number presented here is a good measure of compression performance. The higher the number, the closer the compression process is to isothermal-isobaric compression.

$$\frac{dV^*}{dt^*} \approx \frac{UA(T_{sat} - T_\infty)t_{charge}}{\rho_{sat,v} h_{fg} V_0} = \pi \tag{4.11}$$

By inspecting this new dimensionless number, it can be seen that a given compression process can be improved (to approach isothermal-isobaric) by enhancing heat transfer (UA) or slowing down the compression process (i.e. increasing t_{charge}). UA is a system dependent parameter, while t_{charge} is an application dependent parameter. Both would need to be considered in system design.

The above parameterization can be applied to the compression processes of tests 1-7 above. In the initial configuration, the system UA is estimated by considering a thermal resistance network of convection inside the tube, conduction through the tube, and convection outside the tube. With condensation occurring inside the tube, it can be assumed that the inner thermal resistance is much less than the conduction and outer thermal resistances, and thus can be neglected. The conduction and exterior convection resistances can be easily estimated using the thickness and thermal conductivity of the tube, and assuming a representative value for heat transfer coefficient due to natural convection at ambient temperature. In the modified configuration, the UA is estimated by placing a thermal resistance network comprising of the thermal resistances of the heat pipe, heat

sink, and exterior forced convection due to the fan, in parallel with the previous conduction and outer thermal resistances. The result of this analysis can be seen in Figure 4.11, with the values of the dimensionless number π for each test's compression process also shown. Note that the cyclic pattern seen in the curves is due to the cyclic action of the hand test pump during charging.

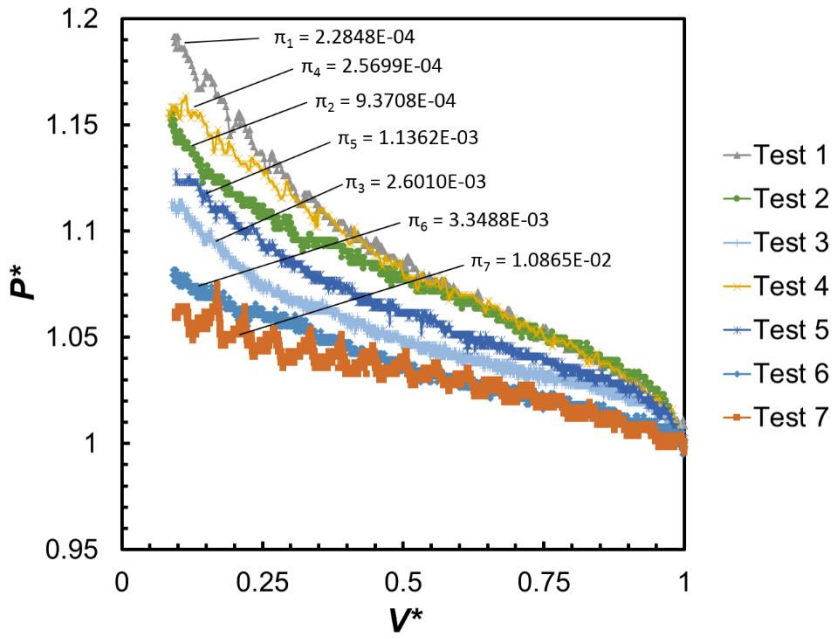

Figure 4.11: Dimensionless pressure-volume curves for R134a compression

Finally, using the above dimensionless pressure-volume compression curves, it is possible to define a compression efficiency as the ratio of the integral of the dimensionless pressure-volume compression curve (dimensionless work input), to the integral of the equivalent curve if the compression process were to be isobaric. This compression efficiency is defined in Equation (4.12).

$$\eta_{comp} = \frac{isobaric\ dimensionless\ work\ input}{actual\ dimensionless\ work\ input} = \frac{p_0^*(V_c^* - V_0^*)}{\int_0^c p^* dV^*} \tag{4.12}$$

The compression efficiency can then be plotted versus the dimensionless π number, yielding the chart in Figure 4.12. It can be seen that there is a general trend of increasing compression efficiency with increasing dimensionless π number. This is an expected result, as the closer to isothermal-isobaric the compression process, the higher the dimensionless π number. This dimensionless number is also proportional to a dimensionless energy density, for systems operating between the same initial and final pressures. The errors shown with the error bars are obtained by calculating the uncertainty propagation in the pressure and height (used for volume) measurements into the compression efficiency calculation.

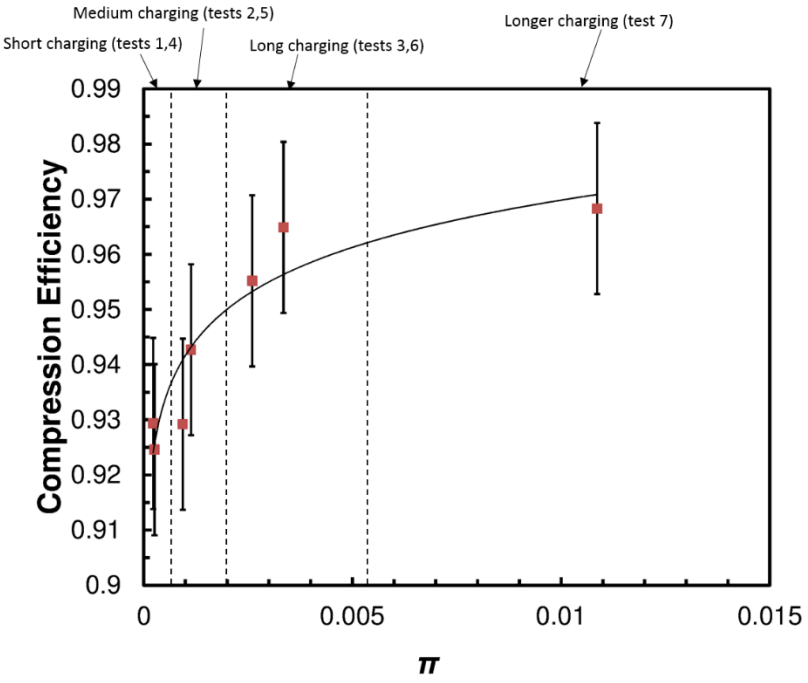

Figure 4.12: Compression efficiency versus dimensionless π number for R134a tests

4.4 Considerations on use of R134a

Due to the low saturation pressure of R134a, it would not be a suitable working fluid for use in a scaled-up, commercial system, as it such a system would suffer from exceedingly low energy density. A system utilizing a condensable gas would require a working condensable gas with much higher saturation pressure, in order to store an appreciable amount of energy. One such candidate for a working fluid is Carbon Dioxide (CO_2). CO_2 boasts a saturation pressure of 57 bar, and isobaric specific work of 21.77 kJ/kg at room temperature (20 °C), assuming compression from saturated vapor to saturated liquid. For such an ideal system operating between saturated vapor and saturated liquid at 57 bar pressure, 20 °C temperature, the energy density is estimated to be 4290 kJ/m^3 (1.19 kWh/m^3). As an example, for scale, a system sized at 50 kW, for 2 hours of storage (100 kWh) would require about 84 m^3 of storage. This could be comprised of several smaller pressure vessels (i.e. 168 × 500 liter vessels), or fewer larger vessels (i.e. 42 × 2000 liter vessels). Pressure vessels are generally commercially available for a large range of sizes (1-500,000 liters). In addition to the high saturation pressure, CO_2 is non-toxic, non-flammable, has a low global-warming potential, and is readily available. The selection of an appropriate secondary fluid (liquid piston fluid) is an important consideration for system design. Water is used as the working fluid in the air system, mineral refrigerant oil is used for the experiments using R134a. One option for a scaled-up system utilizing CO_2 is to utilize water as the secondary fluid, with a column of oil as a barrier between the CO_2 and the water. When the CO_2 is fully condensed into liquid form, water is the heaviest of the three fluids and thus would sit at the bottom of a vertical vessel/container, with the oil remaining right above it, separating it from the CO_2. The CO_2 which is the lightest of three fluids would remain at the top. This would also prevent any dissolution of CO_2 into the water. Another option would be to use an oil as the secondary fluid. This would be

advantageous in some settings, as there is wider availability of hydraulic turbomachines designed for oils, often available at lower cost than water hydraulic turbomachines.

Based on the success of the R134a experiments, a similar experiment was designed and setup, this time to evaluate Carbon Dioxide experimentally. The experimental setup is nearly identical to the setup for R134a, with the only differences being that a polycarbonate tube with smaller diameter was used to withstand the much higher saturation pressure of CO_2. This study is presented in the following sections.

4.5 Carbon Dioxide – Experiment Overview

As mentioned in the previous paragraph, an almost identical experiment as the R134a experiment was designed and setup to evaluate the compression and expansion behavior of Carbon Dioxide (CO_2) for consideration to be used as a working fluid for the GLIDES system. The differences between the two systems are precautions taken for the higher saturation pressure of CO_2. A clear polycarbonate tube is used again as the test tube, but with slightly different geometry. This tube measured 1/2-inch outer diameter with 1/8-inch wall thickness and a length of 8 feet. The smaller tube diameter was chosen to withstand the higher pressure. Similarly to the R134a setup, a T-type Omega thermocouple, pressure gauge, and pressure transducer were placed at the top of the tube. A high-pressure hand cylinder pump with built-in discharge flow control valve was used at the bottom to charge and discharge the tube of oil. A larger diameter clear polycarbonate tube was installed around the test tube as a precaution to serve as secondary containment to protect any personnel or equipment from pressure release in the event of test tube failure. Unlike the R134a tube, a rubber piston inside the tube to separate mixing of the liquid refrigerant and oil was not needed in the case of CO_2 because liquid CO_2 is much lighter than oil,

and sits atop the oil when condensed without mixing. Once again, the measurement instruments were used along with a National Instrument data acquisition module and LabView program to collect experiment data from the system. The same parameters and data reduction equations in Section 4.2.3 are used to evaluate the performance of CO_2. An image of the experiment setup can be seen in Figure 4.13.

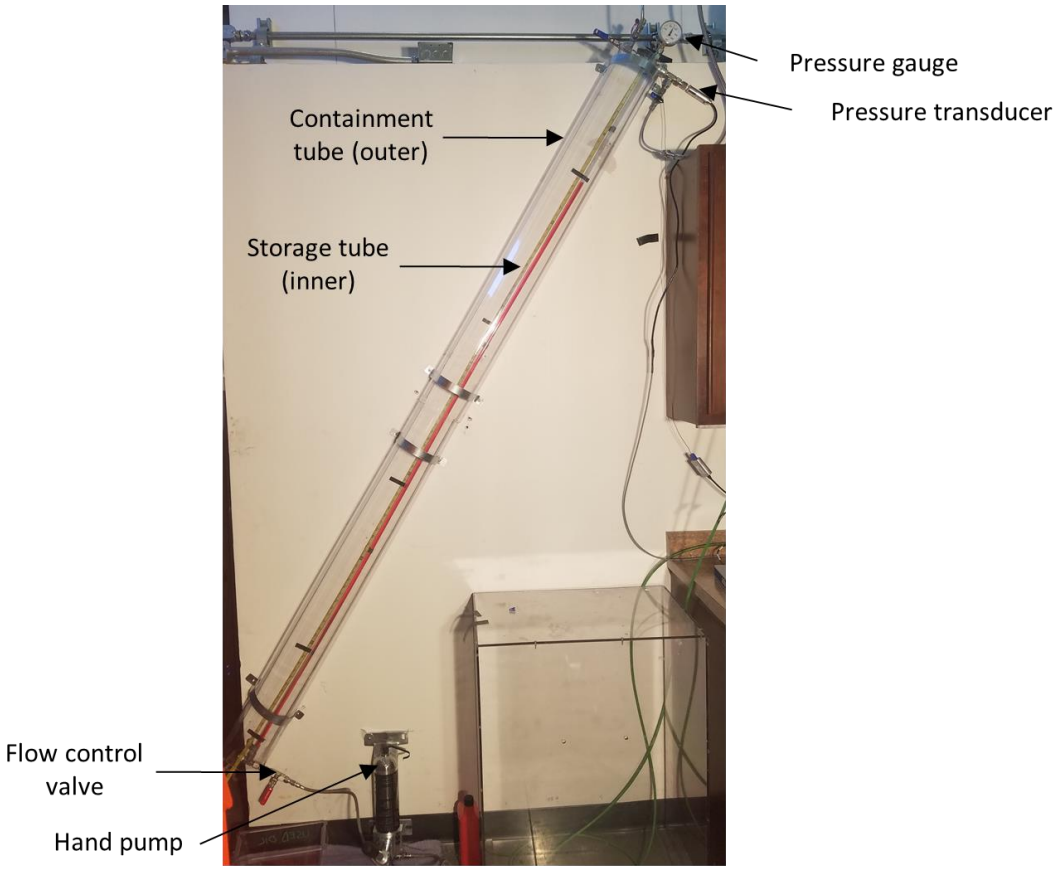

Figure 4.13: Schematic of CO_2 experimental setup (storage tube is smaller diameter inner tube with red hydraulic oil visible, larger outer diameter tube is used as secondary containment due to high pressure system)

4.6 Carbon Dioxide – Results & Analysis

Three tests were run with Carbon Dioxide as a working fluid. Similarly to the R134a experiments, tests with short, medium, and long charging/discharging times were run. Th results are summarized in Table 4.4. In general, it seems the longer the charging/discharging time, the closer to isobaric compression/expansion, and the higher the compression efficiency. Test 3 achieved slightly lower efficiency than Test 2, even though it had longer charging and discharging time. This is likely due to having much longer pause (idle) time between charging and discharging. Test 3 had 209 minutes of pause compared with 40 minutes and 129 minutes respectively for Test 1 and Test 2. Even though Test 3 has slightly lower efficiency than Test 2 due to the longer pause time, it still achieves higher energy density than Test 2; this can be attributed to the longer discharge time which enables the expansion to closer to isobaric.

Table 4.4: CO_2 test parameters and results

Tests	**Charge Time (mins)**	**Discharge Time (mins)**	**Efficiency**	**Energy Density (kJ/m^3)**	**Min/Max Pressure (bar)**	**Min/Max Volume (m^3)**
Test 1	9.42	10.93	83.98%	1.17	46.42/68.91	1.24E-5/7.64E-5
Test 2	17.90	21.28	88.91%	1.21	50.55/64.46	1.29E-5/7.64E-5
Test 3	32.73	37.32	86.52%	1.25	49.32/66.68	1.17E-5/7.64E-5

Figure 4.14 shows the pressure-volume diagrams of the full charge-pause-discharge-pause cycles for Tests 1-3. By inspection, it can be seen that each charge and discharge process is progressively closer to isobaric from Test 1 to Test 2 to Test 3.

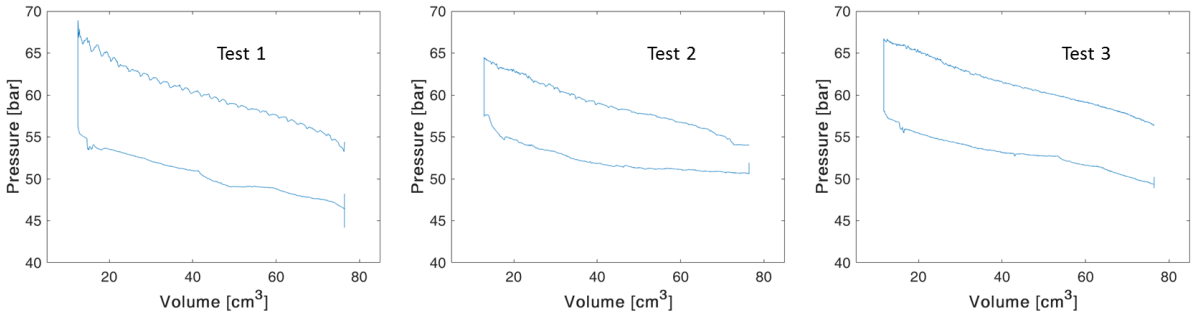

Figure 4.14: CO_2 Tests 1-3 pressure-volume diagrams

Like with the R134a experiments, it is possible to plot the compression on dimensionless pressure-volume diagram and compute π the dimensionless figure of merit which describes the extent to which the compression (energy storage) process is isobaric. As expected, Test 1, the least isobaric of the three has the lowest π number and the steepest curve dimensionless pressure-volume curve, followed by Test 2, and finally Test 3, which is the closest to isobaric and has the largest π number.

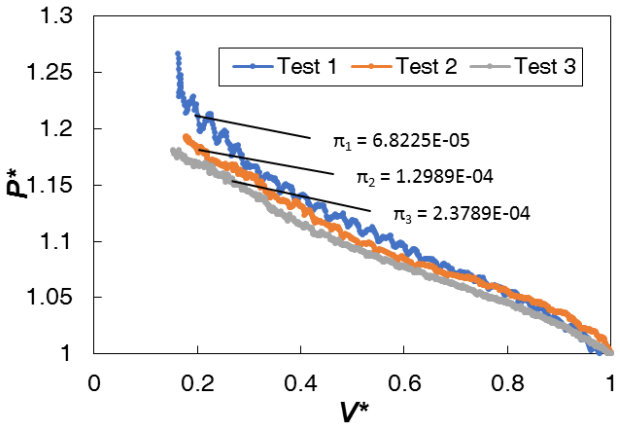

Figure 4.15: Dimensionless pressure-volume curves for CO_2 compression process

Another interesting exercise is to qualitatively and quantitatively compare Figure 4.15 for CO_2 to Figure 4.11 for R134a to see if this dimensionless π number effectively captures the compression behavior across two different working fluids. This comparison reveals that based on the π numbers, CO_2 Test 1 and Test 2 should have a dimensionless pressure volume curve which is steeper (aka less isobaric) than all the R134a curves, due to their smaller π numbers, which is indeed the case. Based on its π number, CO_2 Test 3 should fall between R134a Test 1 and Test 4, which by inspection, is also indeed the case. The dimensionless π number presented here appears to effectively capture the extent to which the compression of a condensable gas is isobaric, even across different working fluids; this is a significant result.

4.7 Carbon Dioxide – Modeling & Simulation

Owing to its relatively high saturation pressure, carbon dioxide is a good choice of condensable gas working fluid for the GLIDES system at larger scales. This circumstance begs for a deeper understanding of the physics of the compression and expansion behavior of CO_2.

Furthermore, extensive experimental investigation beyond that presented in the previous section is challenging due to the high-pressure nature of the endeavor. To further complicate matters, experiments involving condensation of CO_2 can be tricky because if the gas contains trace amounts of water vapor, the two hydrogen atoms and oxygen atom can combine with the CO_2 molecules in the condensed state to form Carbonic Acid (H_2CO_3) which can compromise the structural integrity of the high-pressure storage tube walls, causing it to not be able to withstand high pressure long enough to conduct a high number of experiments. The above reasons motivated the development of a model to investigate the compression/expansion behavior of CO_2 without the need for difficult experiments.

4.7.1 Model Formulation

To model the energy storage (compression) and energy recovery (expansion) processes using CO_2 as the working fluid, a set of transient equations were developed and an algorithm implemented in MATLAB with the CoolProp [70] opensource thermodynamic properties package and its MATLAB wrapper. The algorithm then solves the transient response (pressure, temperature, liquid/vapor volume) of the CO_2 with specified time step. The temperature is assumed to be uniform throughout the CO_2 and uniform for the liquid and vapor CO_2. A flowchart for the algorithm is shown in Figure 4.16. The script implementation of the algorithm can be found in Appendix B.

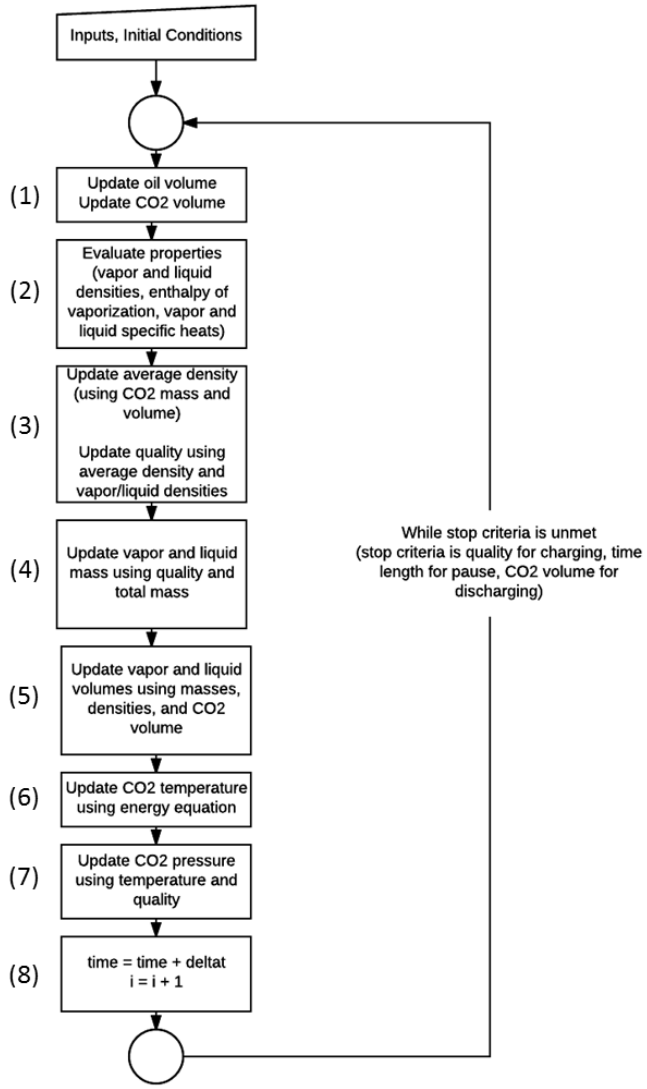

Figure 4.16: Carbon Dioxide simulation model algorithm

The algorithm begins with the inputs and initial conditions being provided by the user. The inputs include the volume of the storage medium, the flow rate of oil, the overall heat transfer coefficient (*UA*), the ambient temperature, the initial quality of the CO_2, and the pause length for the idle periods between charging and discharging and after discharging. Using the ambient temperature and/or initial quality, the initial conditions for the simulation, including pressure,

volume of CO_2 liquid, volume of CO_2 vapor, liquid/vapor densities, mass of liquid/vapor, enthalpy of vaporization, and liquid/vapor specific heats.

The algorithm consists of a series of steps which are taken in each time step to solve the response of the CO_2. In step 1, the volume of oil and volume of CO_2 in the storage tank are updated using the oil flow rate. In step 2, the vapor/liquid/bulk CO_2 properties are evaluated using the temperature in the previous timestep and quality of 0 or 1 for vapor and liquid respectively. In step 3, the average density is evaluated using the total CO_2 mass and the volume obtained in step 1; the quality is then updated using the average density and vapor/liquid densities using Equation (4.13).

$$x = \frac{v_{ave} - v_{liq}}{v_{vap} - v_{liq}} = \frac{\frac{1}{\rho_{ave}} - \frac{1}{\rho_{liq}}}{\frac{1}{\rho_{vap}} - \frac{1}{\rho_{liq}}} \tag{4.13}$$

In step 4, the mass of the vapor and liquid CO_2 are updated using the quality and the total CO_2 mass. In step 5, the vapor and liquid volumes are updated using the masses from step 4 and the densities from step 2. In step 6, the CO_2 temperature is updated using the energy equation for the CO_2, which is shown in Equation (4.14),

$$m_{CO_2}\left[x c_{vap} + (1-x) c_{liq}\right] \frac{dT_{CO_2}}{dt} = -\rho_{vap} \frac{dV_{vap}}{dt} h_{fg} - UA(T - T_\infty) - p\dot{V}_{oil} \tag{4.14}$$

where the term on the left-hand side of the equation is the time rate of change of the energy contained within the CO_2 at time *t*; the first term on the right side is the rate of energy absorption or desorption within the control mass due to vapor-liquid or liquid-vapor phase change, the second term on the right is the net rate at which energy is transferred into the CO_2 by heat transfer with

the surroundings, and the last term on the right is the net rate at which energy is transferred out by boundary work. Next, in step 7, the CO_2 pressure is updated using the temperature from step 7 and the quality from step 3. Finally, the time t is updated by adding the timestep Δt, the iteration number is also updated, and the algorithm returns to step 1 and is repeated to solve the response for the next timestep.

4.7.2 Simulation Results

A system of 1 m^3 of CO_2, initially saturated vapor (quality 1), at 25 °C is simulated, with 10 L/min oil flow rate during charging/discharging and one hour pause between charging/discharging and after discharging. Charging occurs until the CO_2 is completely saturated liquid (quality 0), and discharging occurs until the CO_2 volume is recovered (i.e. returns to original volume). To assess the ability of the model to describe the physics at play, the simulation is ran for two extreme cases: an adiabatic system (UA = 0 W/K) and isothermal/isobaric system ($UA \rightarrow \infty$, very large), and the results are inspected for qualitative correctness. A third case, with a finite value of heat transfer (UA = 200 W/K) is also simulated and inspected for qualitative reasonableness.

Figure 4.17 shows the results of the adiabatic simulation. The a), b), c), and d) frames show the transient temperature and pressure profiles, pressure-volume diagram, transient volume phase profile, and transient quality profile of the CO_2 throughout the process. During charging, the temperature increases from 25 °C to slightly above 30 °C and then remains constant through the one hour pause (no heat is lost to the cooler ambient because system is adiabatic), then decreases back down to the initial temperature of 25 °C, and again remains constant throughout the second pause period. The pressure follows the same profile, as it increases from just above 64 bar (the saturation pressure at 25 °C) to slightly above 72 bar during charging, then remains constant during

the pause, and decays back down to the initial pressure during discharging. The symmetric process is also shown on a pressure-volume diagram in frame b). Because the process is symmetric, unity efficiency is achieved, and an energy density of 1.12 kWh/m^3 of CO_2 is achieved. Frame c) shows the change in the various volumes (total CO_2 volume, liquid/vapor CO_2 volume, and oil volume). The system contains only CO_2 vapor at the beginning of charging, then as charging occurs and oil is pumped into the system, the oil volume increases, the total CO_2 volume decreases as it is compressed, the vapor CO_2 volume decreases and the liquid CO_2 volume increases as condensation occurs. By the end of charging, the vapor has completely condensed into liquid and all the CO_2 is in liquid phase. This can also be seen in frame d) which shows the vapor quality throughout the entire process.

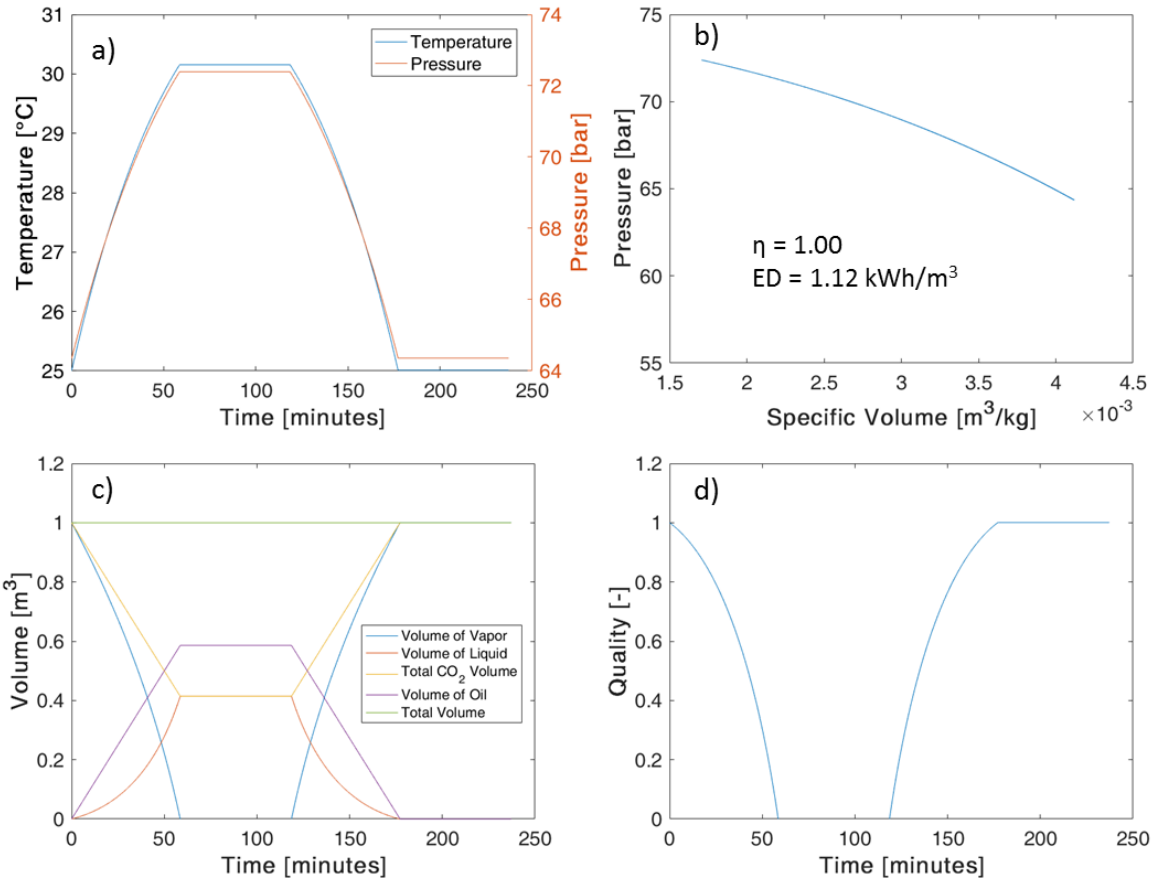

Figure 4.17: Results of CO_2 storage simulation for adiabatic case

Figure 4.18 shows the results of the isothermal/isobaric simulation. As can be seen in frame a) the process is largely isothermal/isobaric, although there is a very small temperature difference (0.07 °C) which is the temperature difference needed for the second term on the right-hand side of Equation (4.14) to kick in. This has an associated pressure difference of about 0.1 bar. This isothermal/isobaric process is also symmetric, as can be seen in the pressure-volume diagram in frame b) which shows an essentially flat pressure-volume curve, indicating isothermal/isobaric behavior. While this case also achieves efficiency of unity, the energy density is higher than the adiabatic case (1.17 kWh/m^3). The reason for this is best explained by examining frame c). As oil

is pumped into the system and charging occurs, because the temperature of the CO_2 remains the same, the vapor and liquid densities do not increase and decrease with temperature, as is the case in the adiabatic case. This means that the liquid in its condensed state takes up less space, and more oil is required to be pumped for all the CO_2 to fully condense. The minimum CO_2 volume in the isothermal case is lower than in the adiabatic case. This larger volume displacement in the isothermal case versus the adiabatic case leads to higher energy density. Note that isothermal/isobaric behavior can also be achieved by slowing down the charging/discharging flow rate (i.e. increasing charge/discharge time), as illustrated by the dimensionless figure of merit in Equation (4.11).

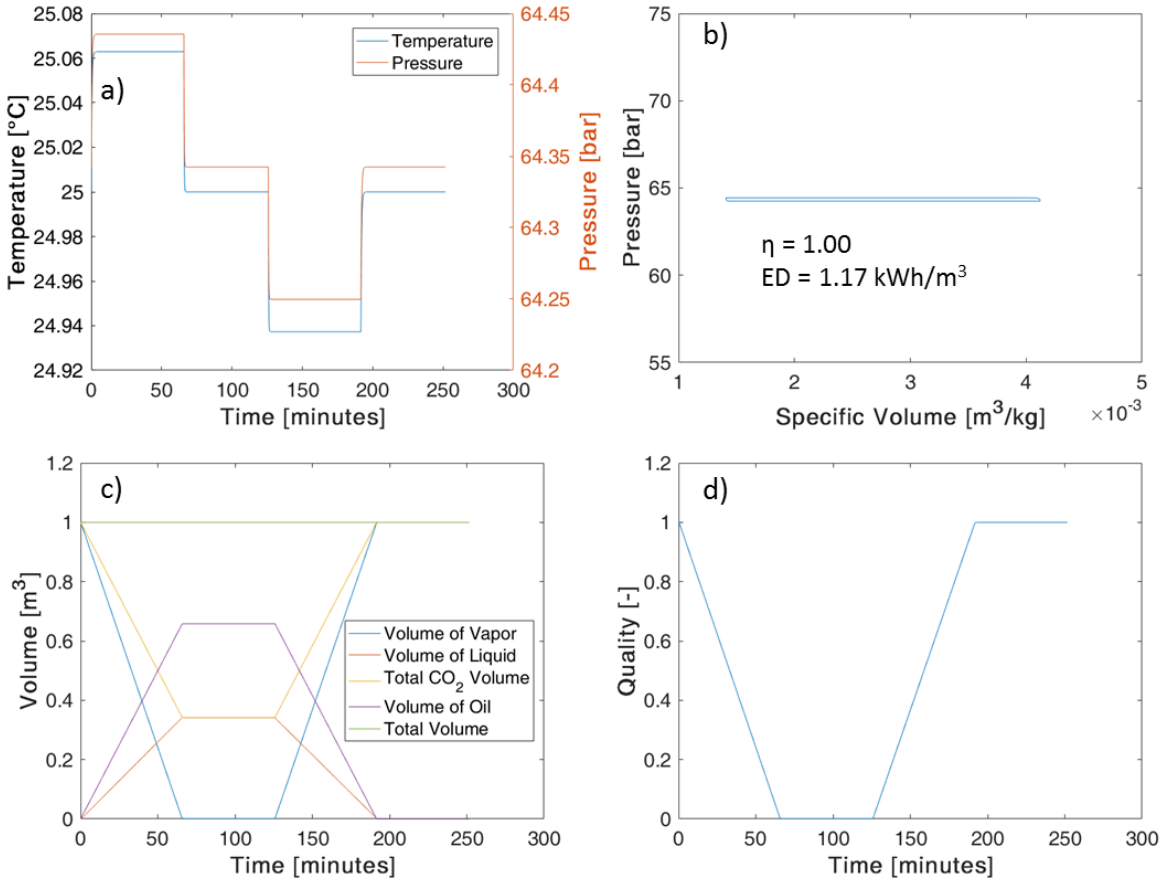

Figure 4.18: Results of CO_2 storage simulation for isothermal/isobaric case

A third case with a finite value of *UA* = 200 W/K is also simulated to present a more realistic case. These results are shown in Figure 4.19. In this case, the profiles are no longer symmetric and the efficiency drops below unity due to heat transfer losses. The efficiency is 0.93 and the energy density 1.05 kWh/m^3. During charging, heat is lost to the surrounding ambient as the CO_2 temperature increases due to compression. During discharging, heat continues to be lost to the surrounding while the CO_2 temperature is above the ambient temperature of 25 °C. Once the CO_2 temperature drops below 25 °C, the heat transfer is reversed and the CO_2 starts to gain heat from ambient. One notable difference between this case and the adiabatic and

isothermal/isobaric cases, is that the system is not static during the pause periods. Heat transfer continues throughout the pause periods which causes the CO_2 temperature and pressure to decrease during the pause after charging, and increase during the pause after discharging. This phenomenon drives phase change to continue during the pauses, even though the CO_2 is not being compressed or expanded. There is a tradeoff at play. During the pause after charging, the temperature decrease favors condensation, but the pressure decrease favors vaporization. In this case, the pressure decrease dominates and some of the liquid vaporizes. In the pause after discharging, the temperature increase favors vaporization, but the pressure increase favors condensation. In this case, the temperature increase dominates, and vaporization continues throughout the pause. These phenomena were also confirmed during the CO_2 experiments. As can be seen in frame c), at the end of discharge, there is still liquid CO_2 remaining. If another energy storage cycle begins shortly after discharge, the system is at risk of hysteresis, as there is already some liquid condensed at the beginning of the cycle. This means the amount of liquid left after discharge of the second cycle will be even greater than the first. This will lead to the efficiency and energy density being lower for the second cycle than the first. This is an important peculiarity to consider in the design of a scaled-up system utilizing CO_2.

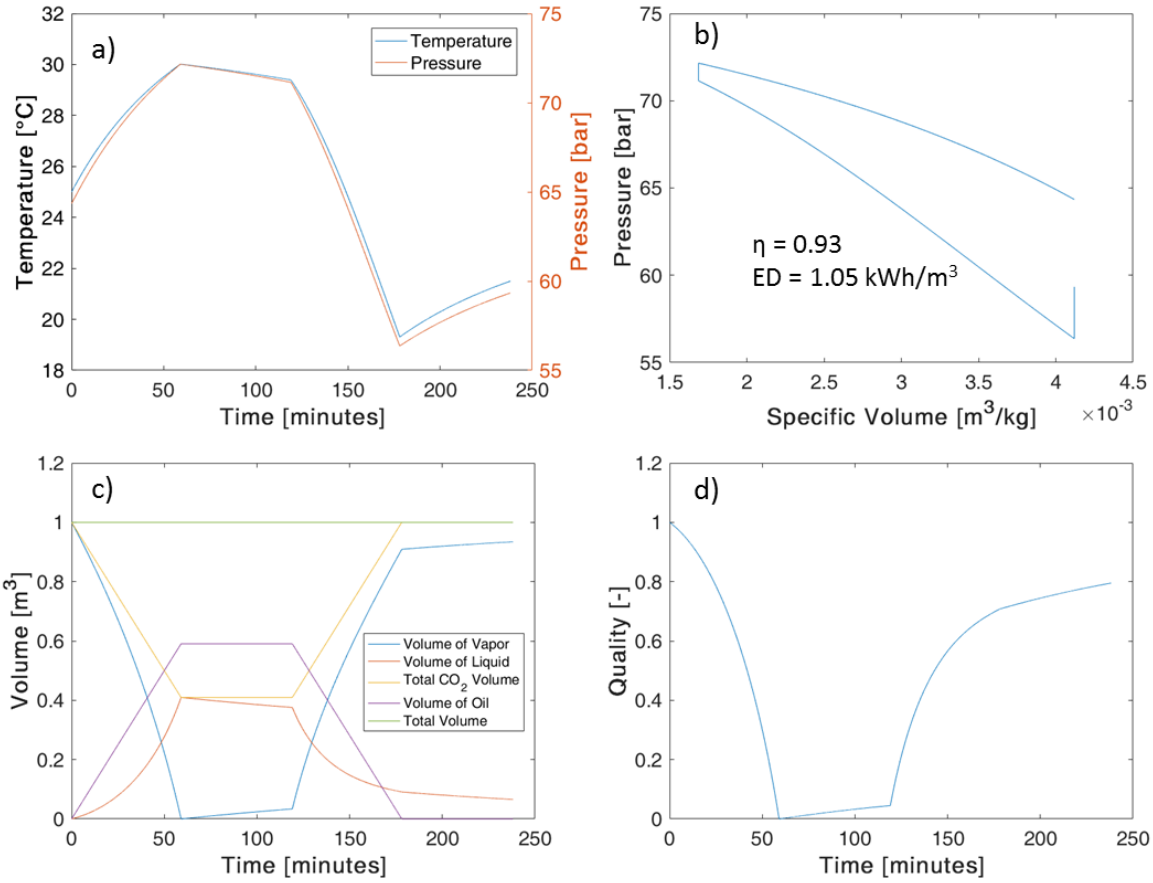

Figure 4.19: Results of CO_2 storage simulation for UA = 200 W/K case

4.8 Considerations on use of Carbon Dioxide

Due to the relatively higher saturation pressure of CO_2 compared with other pure, non-toxic, non-flammable refrigerants or working fluids, CO_2 is a promising working fluid option for use as the primary fluid in a GLIDES system. As demonstrated in the previous sections, it has several promising characteristics including that it has relatively high saturation pressures at/around room temperatures, achieves near-isothermal and near-isobaric compression and expansion, and relatively high storage efficiencies were achieved both experimentally and via physics-based simulation. While the use of CO_2 has many advantages, it also has some challenges. Some of these

challenges include the possibility of hysteresis if the pause between storage cycles is not long enough to allow complete vaporization of the liquid CO_2, the selection of compatible secondary (or liquid piston) fluid, and the need for very pure CO_2 to be used due to the risk of trace amounts of water vapor combining with the CO_2 in condensed state to form Carbonic Acid, which can be corrosive to certain pressure vessel materials or other system component materials.

On the basis of high saturation pressure alone, there are a number of working fluids and working fluid blends that fare better than CO_2, however, all of these fluids or fluid blends consist of some sort of hydrocarbon, all of which are toxic, most of which are flammable and explosive, and some of which are carcinogenic. Despite these chemical concerns, some of these working fluids or blends may still be considered for certain applications, given that the necessary precautions are put in place. Table 4.5 presents the saturation pressure for many fluid blends that may be considered for the GLIDES working fluid at 20 °C, 30 °C, and 40 °C system temperature. Some of the blends have saturation pressure above 100 bar; use of these fluids in GLIDES would improve the system energy density by several-fold. The density ratio (ratio of liquid density to vapor density) is also listed in Table 4.5. The density ratio is a secondary consideration for the choice of condensable gas because the larger the density ratio, the less likely the occurrence of any stability issues, as the liquid refrigerant will likely sink to the bottom of the pressure vessel(s) and remain below the vapor fluid, maintaining a stable liquid/vapor interface, even with any physical perturbations. Note that some of the blends shown in Table 4.5 are blends containing non-condensable gases such as nitrogen. These blends will not exhibit fully condensable behavior, and completely isobaric behavior cannot be achieved with these fluids. Rather, saturation will occur across a glide of pressures centered around the listed saturation pressure.

Table 4.5: Saturation (vapor) pressure of various working fluid blends

	Saturation Pressure, bar (Density Ratio)*		
Fluid Blend	T = 20 °C	T = 30 °C	T = 40 °C
65% Propane, 35% Nitrogen	135.0	129.1	130.8
	(18.2)	(13.1)	(9.5)
7% n-Pentane, 93% Carbon Dioxide	50.5	62.0	133.8
	(44.7)	(27.1)	(20.0)
98% Carbon Dioxide, 2% n-Heptane	55.0	68.2	82.6
	(175.0)	(94.9)	(48.5)
40% Carbon Dioxide, 60% Propane	32.5	38.9	45.8
	(18.2)	(13.1)	(9.3)
82% Carbon Dioxide, 18% IsoButane	45.4	55.5	66.2
	(17.8)	(12.2)	(7.6)
80% Carbon Dioxide, 20% IsoPentane	41.7	50.5	60.0
	(88.6)	(59.3)	(40.0)
95% Carbon Dioxide, 5% IsoPentane	52.3	87.9	94.0
	(21.0)	(12.9)	(7.0)
60% IsoButane, 40% Nitrogen	202.8	172.9	147.9
	(49.9)	(35.8)	(25.8)
21% n-Butane, 79% Carbon Dioxide	43.8	53.1	63.2
	(30.6)	(20.3)	(13.2)
74% n-Pentane, 26% Nitrogen	201.4	194.0	187.1
	(319.7)	(221.9)	(157.8)

*Density ratio = Density of liquid/Density of vapor

CHAPTER 5. DESIGN & EVALUATION OF GEN. 2 PROTOTYPE

To further advance the technology readiness level of GLIDES, a second-generation prototype system was designed and built. Three main objectives were sought after with the development of the gen. 2 prototype: reduce costs by consolidating components (using dual-use components) and using a different type of pressure vessel, improve efficiency and energy density by integrating spray cooling/heating and waste-heat, and improve overall system reliability and packaging. This Chapter provides a detailed overview of these features and the gen. 2 prototype, as well as initial performance results.

5.1 Description of Gen. 2 Prototype Design

A second-generation ~1 kWh proof-of-concept prototype was designed and fabricated. This prototype is mobile (on wheels) and measures 3’ × 4’ × 7’. A number of research objectives were sought after with the second-generation prototype, mostly centered around improving system roundtrip efficiency (RTE) and energy density (ED), and demonstrating configuration 2 and 3 of the GLIDES system presented in Figure 2.3 in Chapter 2 which aim to achieve near-isothermal compression/expansion and waste heat integration during expansion (energy recovery) respectively. A piping and instrumentation diagram of the gen. 2 GLIDES system which shows entire system and components is shown in Figure 5.1. Major system components include an atmospheric pressure storage reservoir, a reversible hydraulic pump/motor and reversible electric motor/generator (PM1), a pressure vessel serving as the air storage medium, and a secondary pump (PM2) and heater in a secondary loop for waste heat integration via sprayed droplets (configuration 3 in Figure 2.3). Other system components include a filter upstream of PM1 to filter water being charged into the pressure vessel, a pressure relief valve set to relief at 140 bar pressure, and ½”

stainless steel tubing, and a series of several valves (manual valves, solenoid valves, check valve). Solenoid valves S1-S5 are used to control the various modes of operation (i.e. charging/discharging, charging from top/bottom, charging with waste heat loop). The entire system is plumbed together using ½" high pressure stainless steel tubing. Several instruments were installed in the system to capture system performance. From left to right in Figure 5.1, a pressure transducer (PT2) was placed at the bottom of the water storage tank to measure water level inside the tank, thermocouples (TC1, TC5) were installed to measure the water storage tank temperature and ambient temperature respectively, a pressure gauge (PG), pressure transducer (PT1), and thermocouple (TC2) were installed to measure the air side pressure and temperature inside the pressure vessel, thermocouples (TC6, TC7) were installed on the outside of the pressure vessel to measure the vessel wall temperatures, a differential pressure transducer (DPT) was installed across the spray pump (PM2), and thermocouples (TC3, TC4) were installed before and after the heater which simulates waste heat integration. A torque transducer (not shown in Figure 5.1) was also installed between the reversible hydraulic pump/motor and reversible electric motor/generator to measure the speed and torque during charging and discharging to enable calculation of the shaft power. A bidirectional watt transducer was also installed to measure the electrical power input/output to/from the reversible electric motor/generator. Table 5.1 summarizes all the instrumentation used in the gen. 2 GLIDES prototype and their associated accuracies.

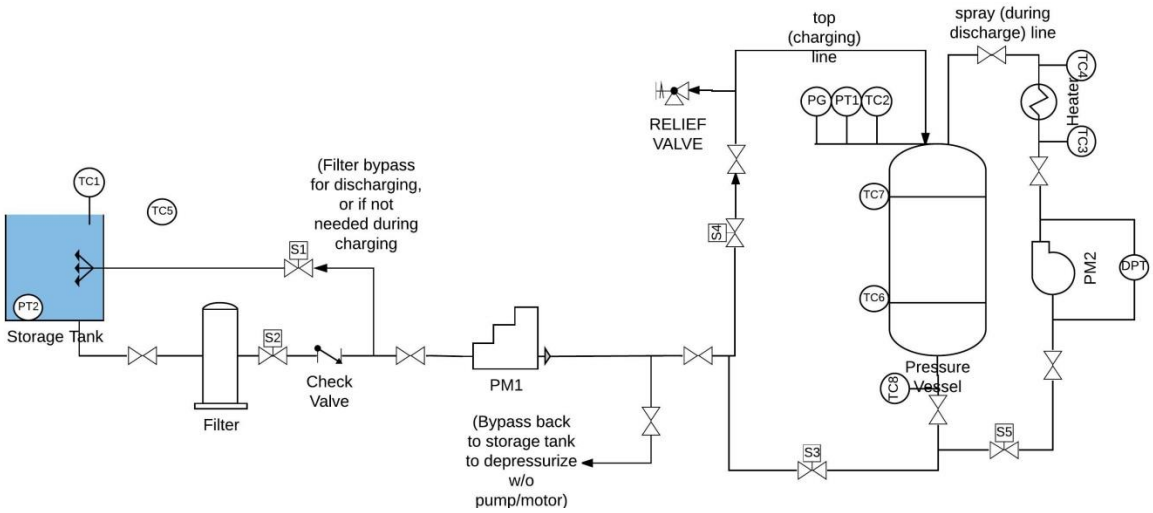

Figure 5.1: Schematic of Gen. 2 GLIDES system and components (piping and instrumentation diagram)

Table 5.1: GLIDES Gen 2. prototype instrumentation summary

Instrument	Measurement	Instrument Type	Measuring Range	Instrument Accuracy
PT1	Storage Vessel Air Pressure	Westward Pressure Transducer, 4to20mA	0-3,000 PSI	+/-0.50%
PT2	Water Tank Level	Omega PX709 Submergible Pressure Transducer	250-3500 mmH2O	1%
DPT	Spray Pump (PM2) Differential Pressure	Kobold PAD Differential Pressure Transmitter	1-100 PSIG	±0.075 %
PG	Storage Vessel Pressure Gauge	High-Accuracy Corrosion-Resistant Pressure Gauge	0-3,000 PSI	±1% of full scale
TC1	Water Tank Temperature	Omega Type T Thermocouple	0-350 °C	0.5 °C or 0.4%
TC2	Storage Vessel Air Temperature	Omega Type T Thermocouple	0-350 °C	0.5 °C or 0.4%
TC3	Heater Upstream Temperature	Omega Type T Thermocouple	0-350 °C	0.5 °C or 0.4%
TC4	Heater Downstream Temperature	Omega Type T Thermocouple	0-350 °C	0.5 °C or 0.4%
TC5	Ambient Air Temperature	Omega Type T Thermocouple	0-350 °C	0.5 °C or 0.4%
TC6	Pressure Vessel Lower Wall Temperature	Omega Type T Thermocouple	0-350 °C	0.5 °C or 0.4%
TC7	Pressure Vessel Upper Wall Temperature	Omega Type T Thermocouple	0-350 °C	0.5 °C or 0.4%
TT	Pump-Motor/Motor-Generator Shaft Speed	Magtrol TMB306 Torque Transducer	0-6,000 RPM	1 RPM
TT	Pump-Motor/Motor-Generator Shaft Torque	Magtrol TMB306 Torque Transducer	0-5 Nm	±0.1% of full scale
WT	Motor/Generator Electrical Power Input/Output	Ohio Semitronics Compound Transducer	0-10,000 W	0.5%

Figure 5.2: Gen. 2 GLIDES prototype

5.1.1 Detailed Description of Gen.2 GLIDES Components

The major gen. 2 GLIDES system components include a 55-gallon atmospheric water storage reservoir, a reversible hydraulic pump/motor which acts as both the charging pump and as a hydraulic motor during discharge for energy recovery, an associated reversible electric motor/generator, a polymer lined, carbon fiber pressure vessel, and a second pump used in a secondary spray loop which includes a heater to simulate waste heat integration. The heater used is a 1200-watt wrap-around heat cable which was wrapped around the exterior of the stainless-steel tubing.

For the reversible hydraulic pump/motor, a 1.7 kW, 4 cm^3/revolution axial piston hydraulic pump was selected which can operate in reverse as a hydraulic motor for energy recovery. For the electric motor/generator, a 2 horsepower, 115/208-230 volts, 6 amp, 60 Hz brushless permanent

magnet reversible motor/generator was selected. A 3600 PSI, 287-liter polymer-lined carbon fiber pressure vessel was utilized as the air storage medium. A secondary loop was added to the system to simulate waste-heat integration via sprayed liquid droplets as described in configuration 3 (Figure 2.3) in chapter 2. The secondary loop includes a high operating pressure (1500 PSI max), low head (125 PSI max), 1.82 mL/revolution micropump which pulls water from the bottom of the pressure vessel, after which it is heated by the wrap-around cable and then routed to the top of the pressure vessel where it is reintroduced (sprayed) into the pressure vessel during discharge.

5.1.2 Charging (Energy Storage)

The gen. 2 GLIDES prototype has the capability of charging by pumping water into the pressure vessel from the bottom (like gen. 1 prototype), or sprayed into the vessel from the top. Figure 5.3 shows the prototype schematic with the flow paths highlighted in red for charging from the bottom a), and top via sprayed droplets, b). Solenoid valves S2 and S3 are used to control whether charging occurs from the top or bottom. The top charging line includes a spray nozzle at the end which is inserted into the pressure vessel. The spray nozzle is a full cone type spray nozzle with spray angle of 80-85°, producing droplets with average diameter of 660 μm. The advantage of charging from the top via sprayed droplets is that the falling droplets have a cooling effect on the warming air, removing heat generated due to compression; this leads to a compression process which is nearer to isothermal and leads to higher roundtrip efficiency and energy density. Having the option of charging from the top or bottom allows for the quantification of the effect of the improved heat transfer achieved via spraying charge from the top, compared to charging conventionally from the bottom. In addition to the option of charging from the bottom or top, the charging pump PM1 has the capability of operating at variable speeds from a minimum of 700

RPM (2 L/min), to 1800 (6.5 L/min) RPM. This allows for the investigation of the effect of charging speed on system efficiency and energy density.

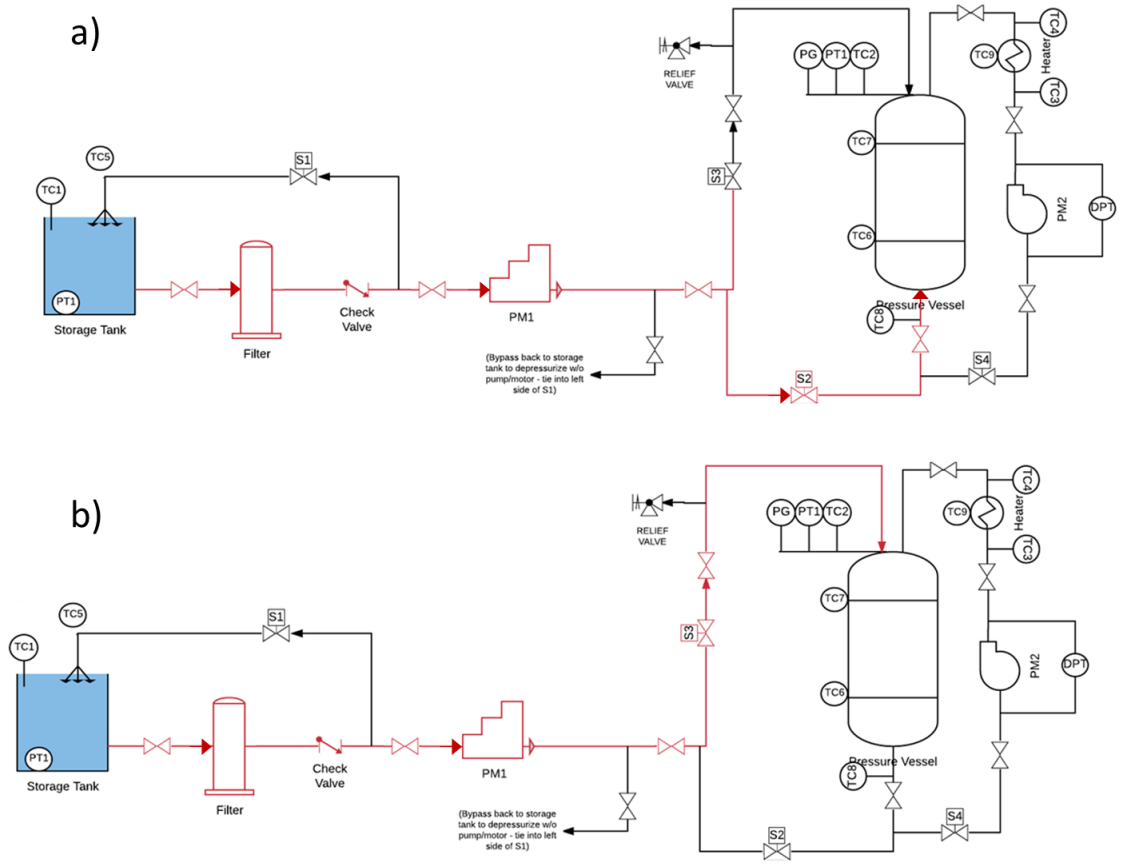

Figure 5.3: Gen. 2 GLIDES schematic during charging a) from the bottom, b) from the top

5.1.3 Discharging (Energy Recovery)

As seen in Figure 5.4, the gen. 2 GLIDES prototype has two possible discharge (energy recovery modes). In the normal discharge cycle, shown in Figure 5.4 a) with the water flow path highlighted in red, solenoid valve S2 is opened and the high-pressure water flows out of the

pressure vessel and into PM1 in reverse, spinning the machine backwards as it now acts as a hydraulic motor. In this mode, the electric machine now serves as an electric generator being driven by PM1, and dispatches electricity to a load bank consisting of a resistive heater connected to variable transformer to control the load.

Figure 5.4 b) shows the second discharge mode of the GLIDES gen. 2 prototype with the water flow path shown in red. In this mode, the secondary loop to simulate the integration of waste heat during discharge is activated by opening solenoid valve S4 and running PM2. The wrap around heater can deliver up to 1200 watts of heat to the exterior of the stainless-steel tubing which can be picked up by the water being circulated inside the tubing. The rope heater is also connected to a variable transformer which allows for the control of how much heat is delivered via the heater. The spray pump (PM2) motor is connected to a power supply with a PWM (pulse-width modulation) device which allows for the control of the motor speed, i.e. the flow rate. Between the heater control and the flow rate control, parametric experiments can be run for various waste-heat rates to determine the impact on system performance and the second law efficiency.

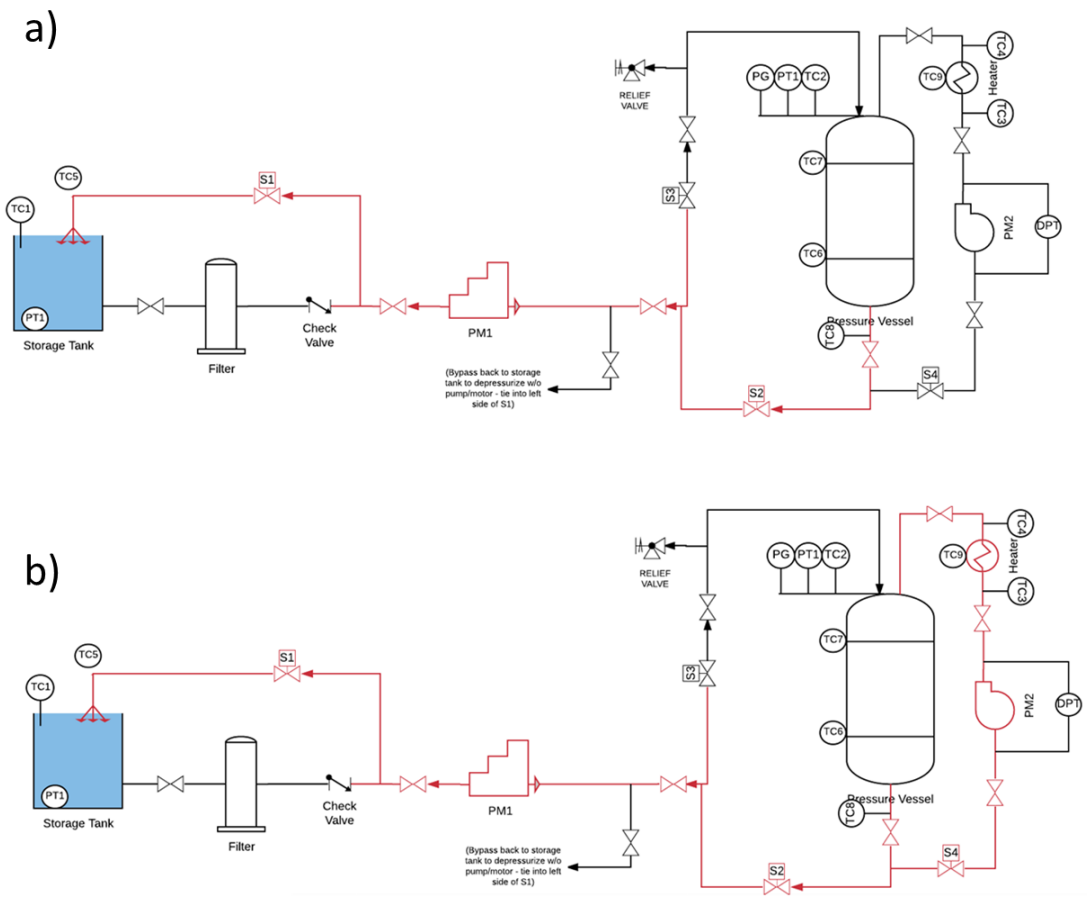

Figure 5.4: Gen. 2 GLIDES schematic during discharging a) normal discharge cycle, b) with waste heat integrated loop active

5.2 Gen. 1 to Gen. 2 Design Improvements

Several deliberate design changes were made between GLIDES gen. 1 and gen. 2 prototypes. All changes were made to either decrease system cost, or improve roundtrip efficiency and/or energy density. Unlike the gen. 1 prototype which utilized conventionally manufactured carbon steel pressure vessels, the gen. 2 prototype uses a polymer-lined carbon fiber pressure vessel which is rated for higher pressure (248 bar versus 160 bar), but cheaper (thanks to automated manufacturing). In addition to being cheaper and having a higher pressure rating than the gen. 1

carbon steel vessels, this carbon fiber vessel also resolves the issue of the inside of the steel tanks corroding due to oxidation from contact with water because the inside of the carbon fiber vessel is lined with a polymer liner which does not react when brought into contact with water. The gen. 1 prototype uses four separate energy conversion devices, a hydraulic pump/electric motor for charging, and hydraulic (Pelton) turbine/electric generator for discharging. These four devices are consolidated into two devices in the gen. 2 prototype by utilizing a reversible hydraulic turbomachine to serve as the pump/turbine, and a reversible electric machine to serve as the electric motor/generator. A positive displacement, axial-piston device is used as the charging pump. In charging mode, the low-pressure side is the inlet, and the outlet is the high-pressure side. In discharging mode, the pump is run in reverse and operates as a hydraulic motor; the high-pressure side becomes the inlet, and the low-pressure side the outlet. This consolidation of the hydraulic machines is made possible by utilizing an electric machine which is a brushless permanent magnet device which operates as an electric motor when a voltage is applied (during charging), but when spun in the reverse direction (during discharging), operates as an electric generator.

In addition to the above, the gen. 2 GLIDES prototype was designed to be able to operate in all three configurations shown in Figure 2.3, the base configuration, spraying during charging/discharging to achieve near-isothermal operation, and waste-heat integration during discharging. Furthermore, this system lends itself well to retrofitting to utilize CO_2/condensable gases as the working fluid as opposed to air.

5.3 Initial Experimental Performance

At the time of the writing of this dissertation, one full-cycle (charging, pause, discharging, pause) experiment of the gen. 2 GLIDES prototype in the standard configuration (no spray or

waste-heat integration) has been conducted. These are the results presented in this section. Many additional experiments of the gen. 2 prototype are planned and will be published in a future work. Unfortunately, at the time of the full-cycle experiment for which the results are presented here, system commissioning/troubleshooting was ongoing, and not all measurement instrumentation was fully functional. As such, the electrical power input/output data was not measured, and the electrical-to-electrical roundtrip efficiency and electrical energy density is not reported here. However, the indicated (thermodynamic) and shaft-to-shaft roundtrip efficiency and indicated and shaft energy density are reported here.

For this test, the system was charged from a minimum pressure slightly above 60 bar to a maximum pressure near 125 bar. The charging pump was run between a minimum of 985 and maximum of 990 RPM which resulted in a charging flow rate between 3.93-3.96 L/min. The pressure vessel was initially empty of any water and the entire 287 L of volume was charged with air at the minimum pressure. The charging process lasted for 38 minutes, after which a 150 minute pause was held, following by discharging which lasted for 16 minutes, until the pressure vessel was evacuated of all water that was pumped in during charging. Discharging was followed by a 48 minute pause. During discharge, the now hydraulic motor speed was kept constant at around 1800 RPM, which resulted in a flow rate of about 7 L/min. The RPM was controlled by using the variable transformer to control the load on the electrical generator, keeping the RPM constant.

Figure 5.5 presents the pressure-volume diagram of the gen. 2 GLIDES prototype base configuration cycle. As with the simulations and the gen. 1 prototype results, the process begins at state point 1 with the charging process. The carbon fiber pressure vessel is initially empty of water but charged with air at 65 bar pressure. The charging process then begins and water is pumped into the vessel via the charging pump, this causes the air pressure to increase and the volume decrease,

as the air is compressed by the rising water liquid piston below. This continues until the pressure reaches 122 bar at state point 2, after which there is a pause period (process 2-3) during which some pressure is lost as the air temperature decreases due to heat loss from the air which heated up due to compression. Discharging then begins from a starting pressure of 115 bar as the water in the vessels is evacuated through the hydraulic machine which is now rotating in reverse as a hydraulic motor. The pressure decreases and the air volume increases as it undergoes expansion until all the water is evacuated and discharge is complete at state point 4, pressure of 61 bar. This is immediately followed by another pause period (process 4-1), during which the pressure increases as the temperature increases to return to equilibrium with the ambient following the cooling due to expansion during discharge. This results in an indicated efficiency of 0.96, and associated indicated energy density of 1.21 kWh/m^3 of air.

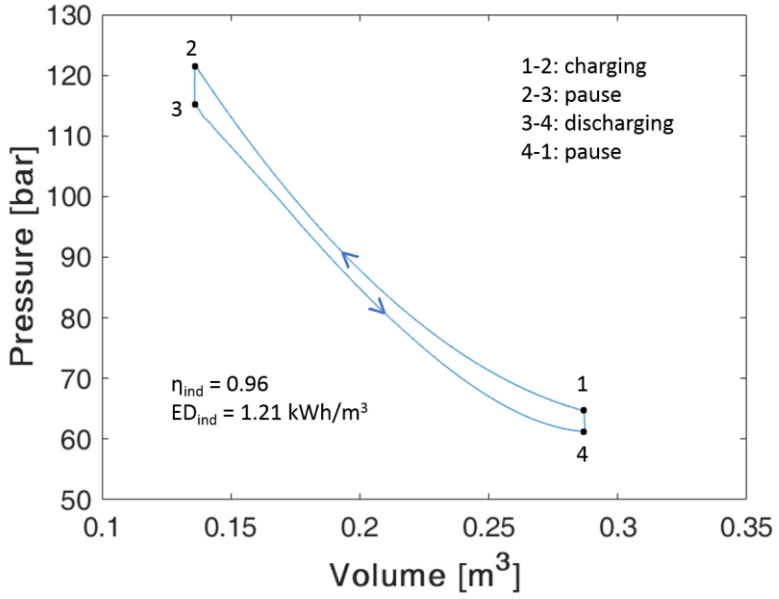

Figure 5.5: Pressure-volume diagram of gen. 2 GLIDES prototype base configuration cycle

Figure 5.6 shows the air temperature and tank wall temperatures throughout the entire duration of the cycle. The cycle begins with the air essentially at ambient temperature around 20 °C, then heats up all the way to a maximum of 46 °C at the end of charging. The temperature then begins to drop during the pause period, and reaches 26 °C when discharging begins. During discharge, the temperature drops as the air expands, and reaches a minimum of 5 °C. Note the trend of the temperature decrease during expansion. The slope of the temperature curve gradually decreases throughout the discharge. As noted in Chapter 2, this is due to conflicting effects from the air cooling due to expansion, but also receiving heat transfer from the ambient after the air temperature drops below the ambient temperature. The slope of the temperature curve during discharge begins to decrease once the heat input from the ambient starts to overcome the cooling due to expansion. This effect was also observed during operation of the gen. 1 prototype, and was also captured accurately by the simulation presented in Chapter 2 of this thesis.

It is interesting that the temperature swings seen during charging and discharging for the gen. 2 prototype are markedly larger than those seen for the gen. 1 prototype for similar pressure ratio. This is in spite of the charging flow rate being much faster for gen. 2 compared to gen.1, even when corrected for system total volume. This result can be attributed to the different heat transfer behavior of the composite carbon fiber pressure vessel compared with gen. 1's carbon steel vessel. Even though at the material level, carbon fiber has higher thermal conductivities than carbon steel, the composite overall thermal conductance of the combined carbon fiber and inner polymer liner, including contact resistances and any air gaps, is apparently lower than that of the carbon steel counterpart.

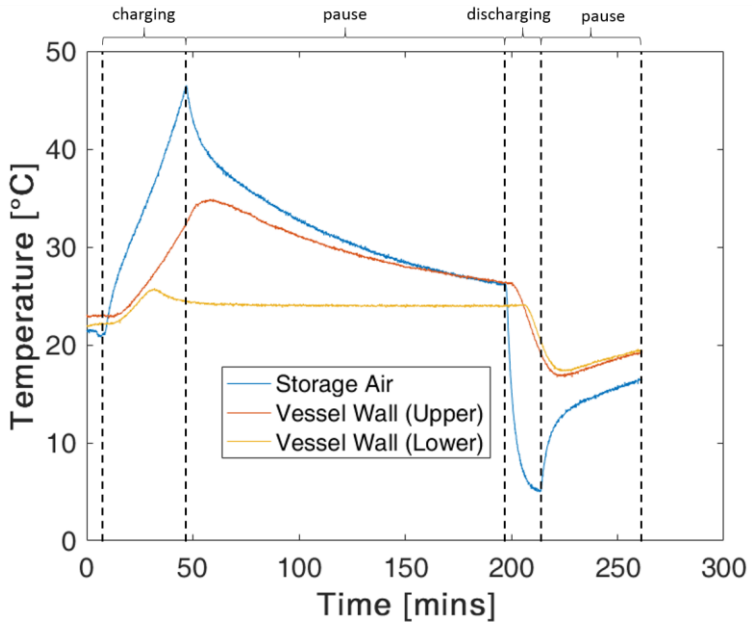

Figure 5.6: Transient temperature profile of gen. 2 GLIDES prototype base configuration cycle

In Figure 5.7, infrared thermal images of the carbon fiber pressure vessel are shown during charging and discharging. In the base configuration, a significant amount of heating and cooling are generated during charging and discharging respectively. This indicates that utilizing the spray functions (spray charging from the top during charging and spray waste-heat integration during discharging) have the potential to make significant contributions to improving the performance of the system.

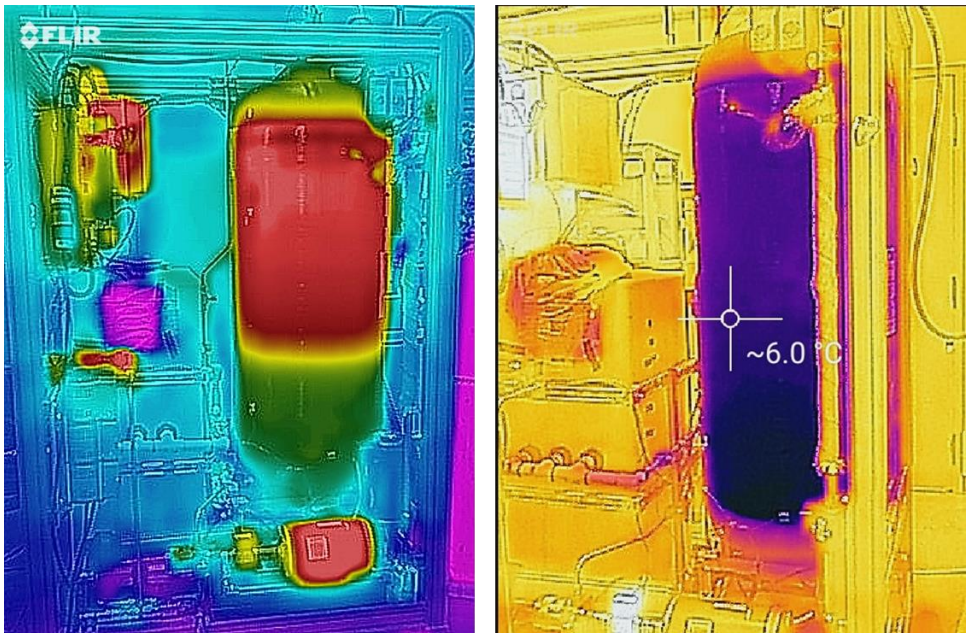

Figure 5.7: Infrared thermal images of gen. 2 GLIDES prototype storage vessel during charging (left) and discharging (right)

The power performance of the system during charging and discharging are shown in Figure 5.8 and Figure 5.9 respectively. The indicated (hydraulic) power, shaft power, and hydraulic machine efficiency (ratio of shaft power to hydraulic power) are plotted versus time and versus

pressure. As described in Chapter 3, the indicated power is the product of the pressure and flow rate, and the shaft power is the product of shaft speed and torque. During charging, the indicated power increases from a minimum of 423 watts to a maximum of 802 watts, which corresponds to shaft power increasing from a minimum of 506 watts to 939 watts. The aforementioned values are increasing in value as the system pressure increases which in turn causes the hydraulic machine to see more torque. This performance corresponds to pump efficiency around 0.85, which is essentially constant throughout charging.

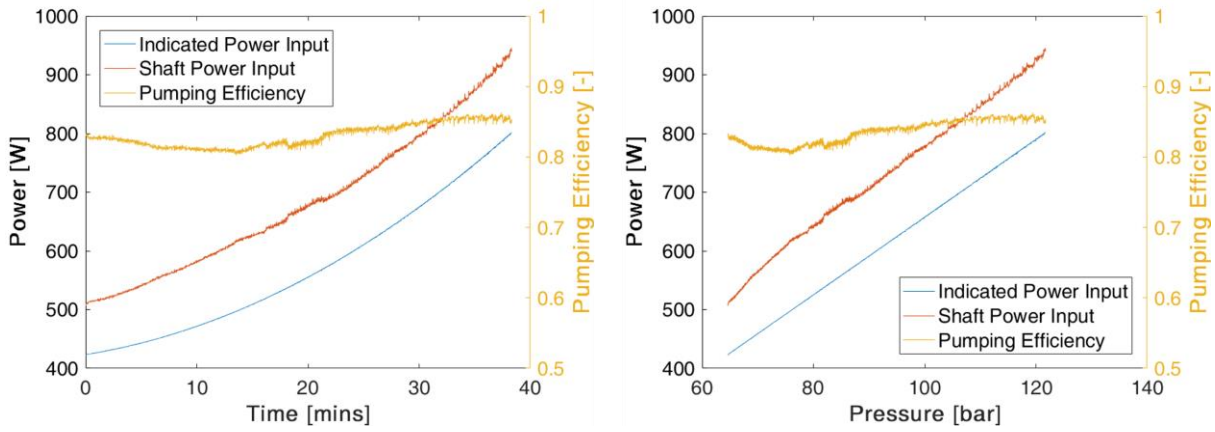

Figure 5.8: Gen. 2 GLIDES prototype power input and charging efficiency profiles versus time (left) and pressure (right)

During discharge, the indicated power output spikes momentarily to above 3000 watts at the beginning. This initial transient is due to the hydraulic motor ramping up to very high RPM/flow rate when it was initially exposed to flow from the vessel, before enough time was allowed for the electric load applied to the generator to ramp up to a high enough level to maintain the RPM at/around 1800 RPM. Following this initial transient, the power quickly drops to around

2500 watts, and then slowly ramps down to a minimum of 747 watts at the end of discharge, as the pressure falls. The shaft power output reduces from a maximum around 1100 watts, to a minimum of 650 watts at the end of discharge. The associated hydraulic motor efficiency varies between a maximum of 0.90 to a low near 0.40 at the beginning of discharge, excluding the initial transient spike at the beginning of discharge. The Figure 5.9 right-hand side plot showing the output data plotted versus pressure. The hydraulic motor efficiency is considerably higher at lower operating pressures, despite the RPM being controlled to be constant. This contrasts with the Pelton turbine used in the gen. 1 prototype, which displayed quite constant efficiency as a function of pressure, when specific speed was controlled to be constant. This yielded shaft energy density of 0.78 kWh/m^3, and shaft-to-shaft roundtrip efficiency of 0.52.

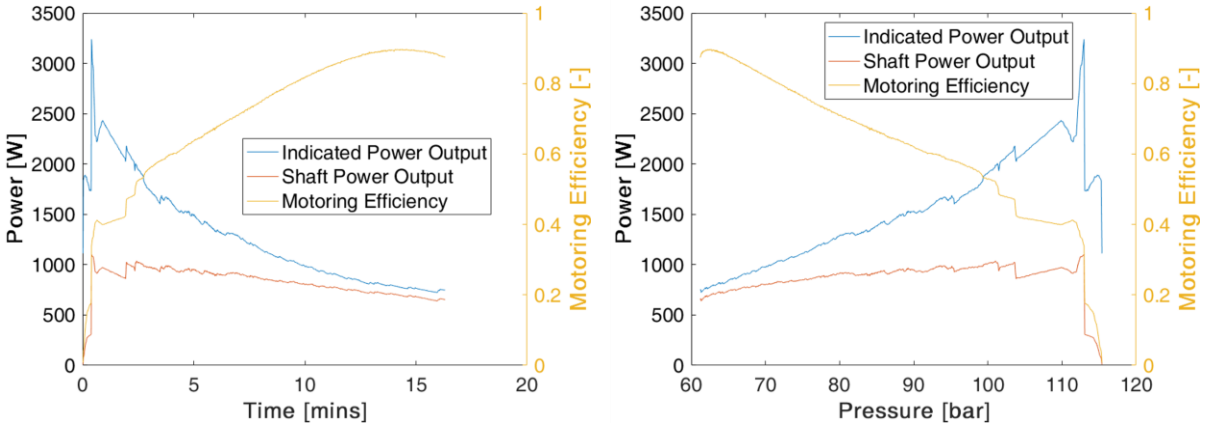

Figure 5.9: Gen. 2 GLIDES prototype power output and discharging efficiency profiles versus time (left) and pressure (right)

5.4 Summary

The GLIDES second generation prototype features several design improvements over the first-generation prototype, both in terms of system performance and prototype packaging/size, and component selection/consolidation. The GLIDES technology readiness level was clearly advanced with the development of the gen. 2 prototype. While the prototype was designed with several features and the possibility to operate in all three configurations presented in Chapter 2, at the time of this dissertation, only test data from operation in the base configuration was collected, which resulted in shaft energy density of 0.78 kWh/m^3, and shaft-to-shaft roundtrip efficiency of 52%. This represents improvements of 14% and 145% respectively from the gen. 1 prototype. Due to the large temperature swings seen in operation, there is a significant opportunity to improve system performance to approach isothermal operation, when operated with the spray cooling/heating integrated configurations. These results will be presented in a future publication. One interesting aspect of the gen. 2 prototype is the use of a reversible hydraulic pump/motor instead of separate pump and Pelton turbine utilized in the gen. 1 prototype. This allows for a quantitative and qualitative discussion of what the preferred energy recovery turbomachine for the GLIDES system would be: an impulse machine such as the Pelton turbine utilized in the gen. 1 prototype, or a reaction machine such as the hydraulic motor used in the gen. 2 prototype. The following chapter is a stab at that discussion in the context of the two GLIDES prototypes created thus far.

CHAPTER 6. OPTIONS FOR ENERGY RECOVERY MACHINE

With the majority of the GLIDES components, there is a clear technology choice for the application at hand. Pressure vessels are clearly the storage medium of choice due to the rigidity and ability to withstand high pressures. Furthermore, as experienced with the first-generation prototype, corrosion of the inside of steel tanks is an issue due to the water use. Consequently, vessels with non-metallic inner surfaces are preferred. With the charging pump, high efficiency positive displacement pumps are the technology of choice due to their ability to pump across large differential pressure, and operate at high efficiency across a wide range of pressures and RPMs. With the turbine or energy recovery turbomachine, the choice of ideal technology for the application is not as obvious. The conception of GLIDES introduces a new category of application for hydraulic turbines due the ultra-high head (>1,000 m), ultra-low flow (<50 L/min) nature of the application. One option of hydraulic turbine is Pelton turbines, which are traditionally used for high-head, low-flow applications. However, Pelton turbines are typically used in situations where the head is developed as a result of elevation difference, and the maximum pressure head seen in GLIDES is only limited by the maximum operating pressure of available pressure heads, which is orders of magnitude higher than any naturally occurring elevation difference seen in the world. There currently exists pressure vessels which can accommodate water pressure head of several thousands of meters. At such high heads and low flow-rates, Pelton turbine jet diameter is reduced to be on the order of a few millimeters, consequently, Pelton buckets must also be scaled down to overall dimensions on the order of millimeters. Because of such high head, these micro-Pelton turbines operate at much higher rotational speeds (several thousands of RPMs) than conventional Pelton turbines, and runner drag losses become significant. Due to the above-mentioned reasons,

conventional Pelton turbine designs are not necessarily well-suited to the GLIDES application. As part of the GLIDES research, a few Pelton turbine designs are evaluated, including two Pelton turbine designs which were manufactured for use with the gen. 1 GLIDES prototype. Specifically, the effect of runner design on rotational drag and the sensitivity of turbine performance to jet diameter are examined. The findings of this study will help form a starting point for the design optimization of ultra-high head, ultra-low flow Pelton turbines. Another good turbomachine option is positive displacement machines, specifically of the axial-piston hydraulic motor type, due to their ability to extract work from high pressure hydraulic streams with efficiency fairly insensitive to RPM and pressure. Utilizing an axial-piston type machine in GLIDES comes with the added advantage of the possibility of using the same machine in reverse as the pump and turbine, consolidating components, as was done with the gen. 2 GLIDES prototype. The gen. 2 prototype offers a look at how such a machine performs as the turbine in a GLIDES system. Lastly, a high-level qualitative discussion of the advantages and disadvantages of using a Pelton turbine versus a hydraulic motor in a GLIDES system is given.

6.1 Pelton Turbine

6.1.1 Pelton turbine design configurations studied via CFD

Several Pelton turbine configurations were studied via a combination of computational fluid dynamics and experiments on the physical machines. CFD simulations on three Pelton turbine configurations were conducted by the SimCenter at the University of Tennessee at Chattanooga and two of the Pelton turbine configurations were installed on the GLIDES gen. 1 prototype. These studies looked at two main Pelton turbine design parameters, the design of the runner and associated effect on drag and turbine efficiency, and the effect of the water jet diameter

(jet diameter to bucket diameter ratio) on the turbine efficiency. The goal of the CFD study was to examine the effect of the runner design on the rotational drag, and try to optimize the design features to reduce said drag. The goal of the experimental study was to see if varying the jet diameter influenced turbine efficiency, and if so, determine what the optimal jet diameter to bucket diameter ratio is.

The geometry of the baseline (v1) configuration is shown in Figure 6.1. Figure 6.1 middle shows the overall geometry including the water nozzles and the casing within which the turbine is housed. The buckets are shown in green, while the central axis assembly is shown in red. The wheel to which the buckets are bolted on to is shown in blue. The sliding interface which separates the rotating and non-rotating parts of the mesh is shown in semi-transparent yellow. Figure 6.1 right shows a zoomed in view of the buckets. Due to their small size and complex geometric features, the Pelton turbine buckets shown in Figure 6.1 were additively manufactured out of a stainless-steel bronze matrix. Figure 6.2 shows an image of the Pelton turbine bucket, as well as the overall dimensions of the bucket.

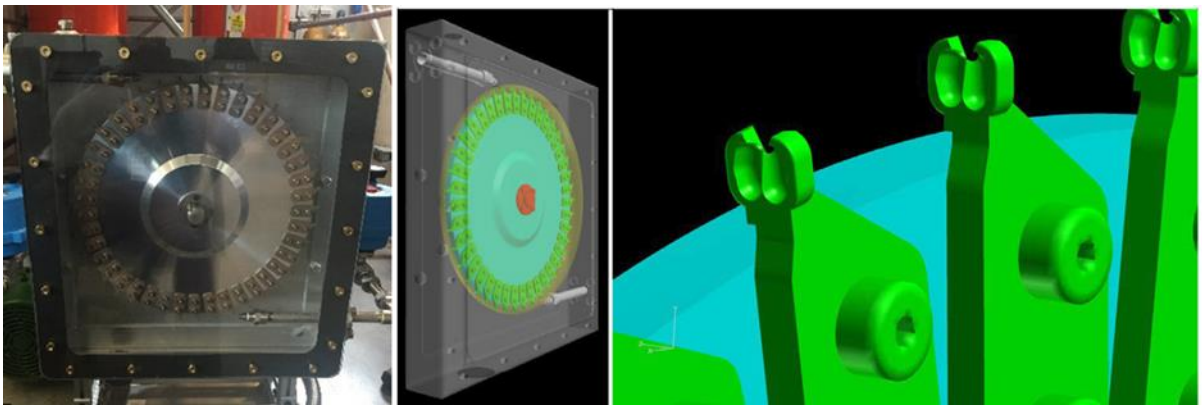

Figure 6.1: GLIDES v1 Pelton turbine configuration, left: physical turbine, middle: overall geometry, right: zoomed in view showing bucket geometry

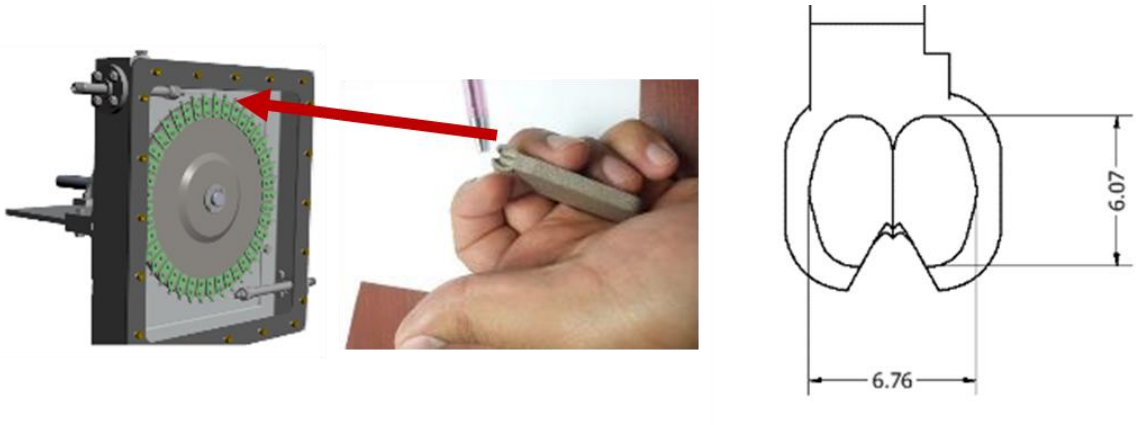

Figure 6.2: left: 3D printed Pelton turbine bucket, right: bucket dimensions in millimeters

The mesh for this configuration contained approximately 7.43 million nodes, 11.75 million tets, and 9.41 million prisms. Even though the water nozzles were present in the mesh generated for this geometry, the simulations did not include water jets. A zoomed in view of a bucket with the associated surface mesh is shown in Figure 6.3. As can be seen from the figure, a significant number of points were placed on the bucket in order to ensure that the impact of the rotation on surface forces could be captured accurately. The simulations were carried out by spinning the Pelton wheel at a constant RPM of 2,500. A time step corresponding to 360 steps per revolution (1 degree angular rotation per time step) was used.

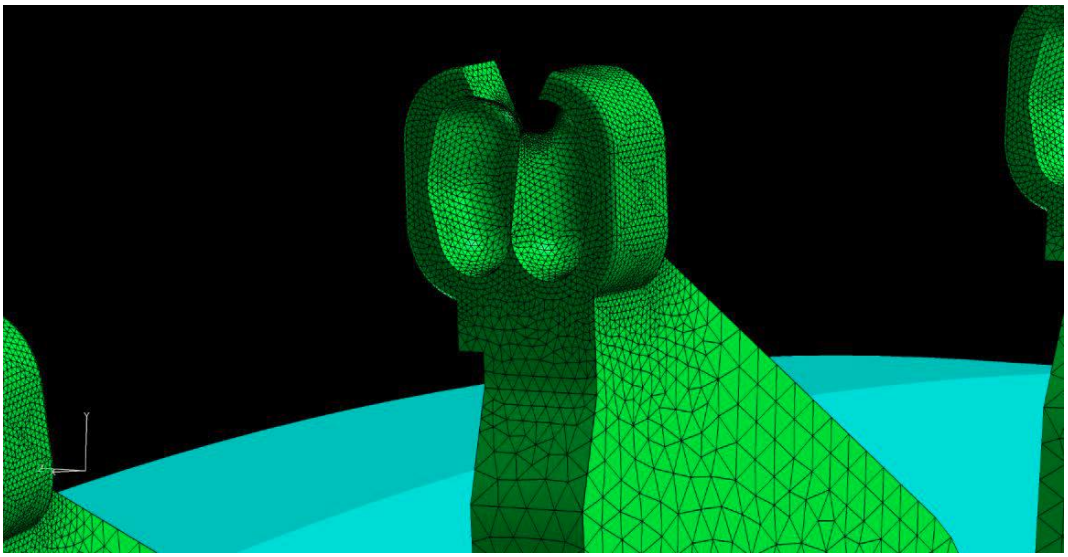

Figure 6.3: Zoomed in view showing surface mesh on buckets (baseline configuration)

A detailed view of the buckets and the hardware that affixes it to the wheel is shown in Figure 6.1 right. From this figure, it is quite clear that the bolt heads protrude a significant height above the surface of the wheel. Likewise, the material that is holding up the bucket has a significant height above the wheel. It was hypothesized that these two protrusions could result in a significant increase in the drag forces, which consequently results in a significant increase in the torque required to turn the wheel.

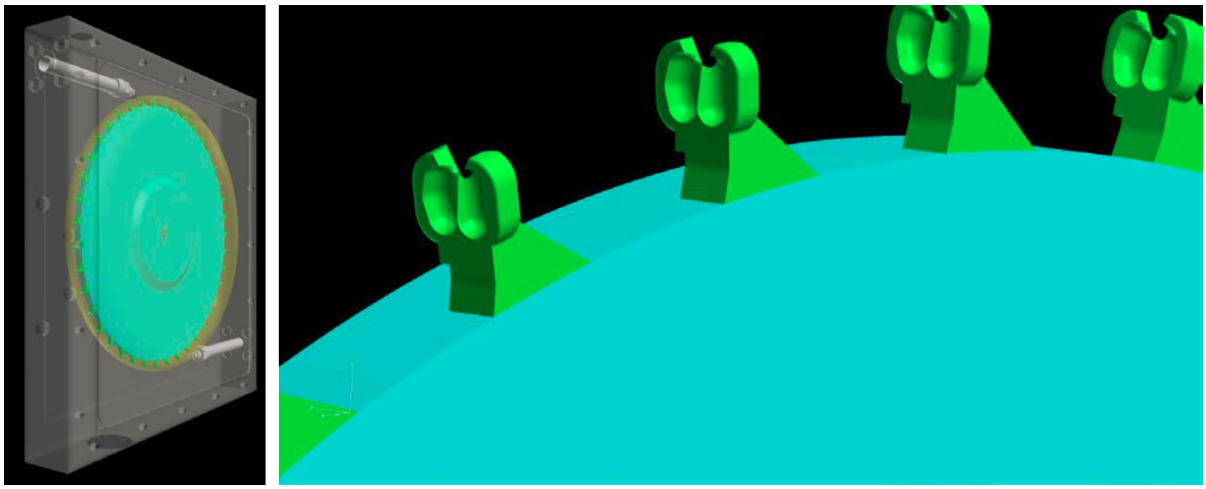

Figure 6.4: GLIDES v2 Pelton turbine configuration (aerodynamic modification), left: overall geometry, right: zoomed in view showing bucket geometry

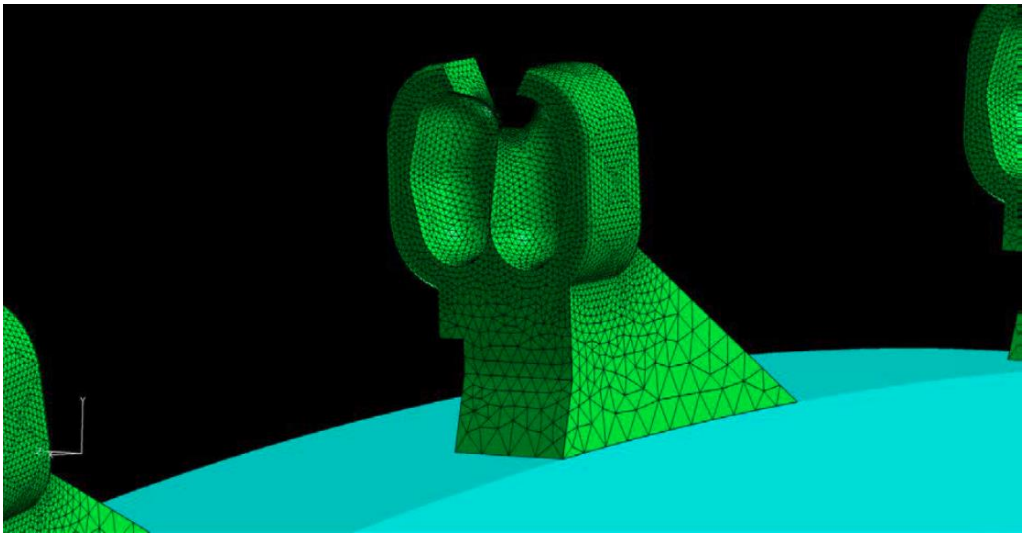

Figure 6.5: Zoomed in view showing surface mesh on buckets (aerodynamic modification configuration)

This hypothesis was put to the test by modifying the geometry as shown in Figure 6.5 and carrying out simulations using the same parameters as the simulation for the baseline configuration. The mesh for the v2 configuration contained approximately 5.73 million nodes, 10 million tets and 7

million prisms. A detailed view of the surface mesh on the modified buckets is shown in Figure 6.5.

The third configuration analysed, the GLIDES v3 Pelton turbine, is similar to the v2 configuration, except for the fact that the diameter of the Pelton wheel is significantly smaller for the v3 runner. Consequently, this configuration spins at a much higher speed of 4,500 RPM compared to the Baseline v1 and aerodynamic modification v2 configurations. Note that that the v1 and v3 configurations are the two configurations for which the physical Pelton turbines are available and installed on the gen. 1 GLIDES prototype. A view of the v3 runner geometry and a close up of the bucket geometry is shown in the right frame of Figure 6.6. The casing is shown in grey, while the sliding interface is shown in yellow. The nozzles were not included in this simulation.

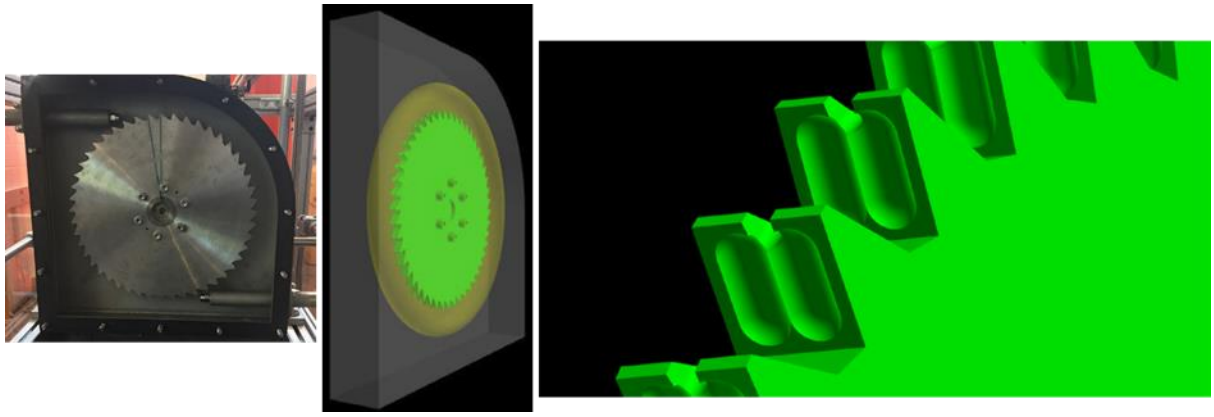

Figure 6.6: GLIDES v3 Pelton turbine configuration, left: physical turbine, middle: overall geometry, right: zoomed in view showing bucket geometry

The mesh for this configuration contained approximately 4.4 million nodes, 5.4 million tetrahedra, and 5.58 million prisms. Additionally, it contained about 320,000 prisms and 430,000 hexadedra. A detailed view of the mesh around the buckets is shown in Figure 6.7.

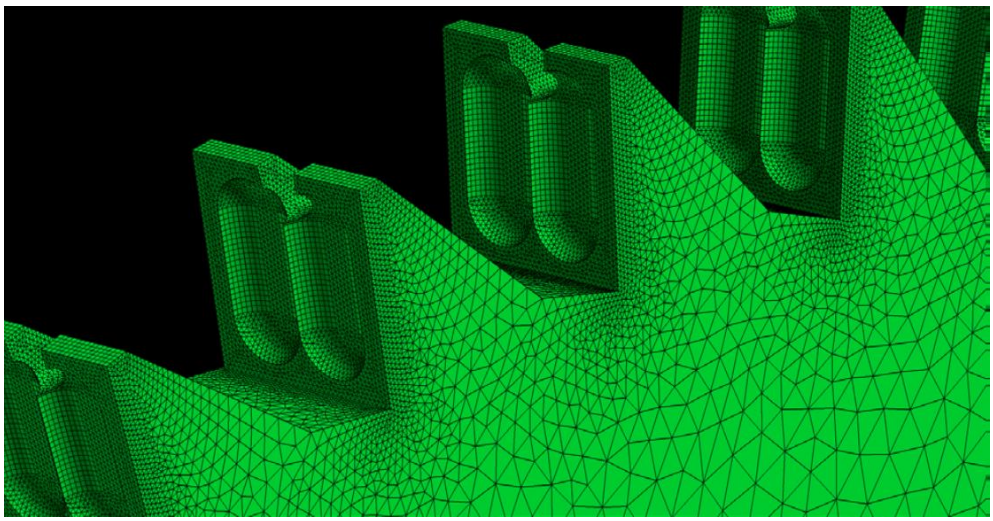

Figure 6.7: Mesh around the GLIDES v3 Pelton turbine runner

6.1.2 CFD simulation results

A comparison of the overall torque for the three configurations is shown in Figure 6.8. As can be seen from this figure, it takes the torque for the baseline configuration a lot longer to settle down to something resembling a periodic state while the v2 configuration appears to reach this state a lot faster. Similarly, the v3 runner configuration settled down a lot faster compared to the baseline. Furthermore, the torque for the v2 configuration is almost 40% lower than that of the baseline configuration. Likewise, the torque of the v3 runner configuration is a further 60% lower than the v2 case. A significant part of this reduction can be attributed to the fact that the diameter

of the Pelton wheel for the v3 runner is almost half that of the v2 and baseline cases. Furthermore, the number of buckets in the v3 configuration is 48, while the number is 42 for the baseline and v2 configurations. The significant difference in diameters between the configurations results in a very “dense” configuration for the v3 runner compared to the other two configurations. This has an impact on the size of the recirculation zones that form around the buckets (Figure 6.9), which could in turn impact the overall torque. This is similar to a situation where race cars are drafting behind each other, wherein the cars that are in the wake experience less drag.

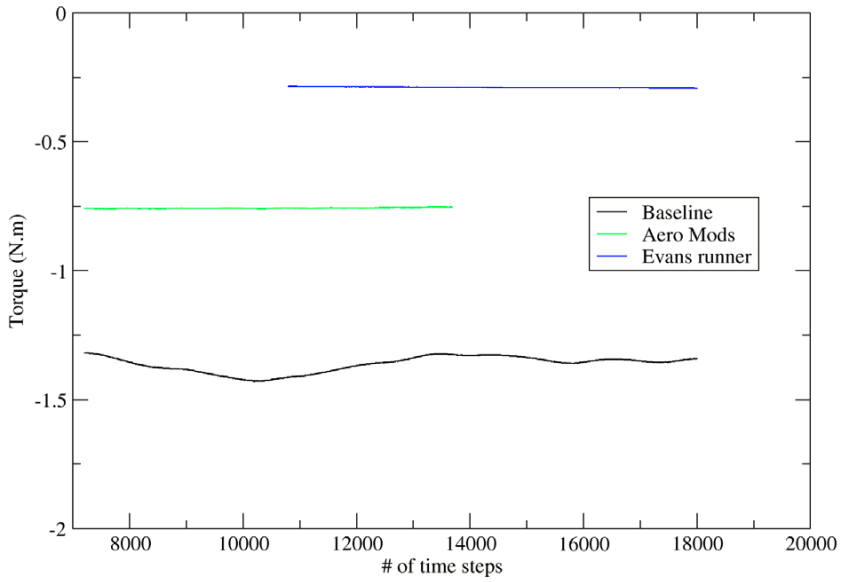

Figure 6.8: Comparison of overall torque for the baseline (v1), v2, and v3 Pelton turbine configurations

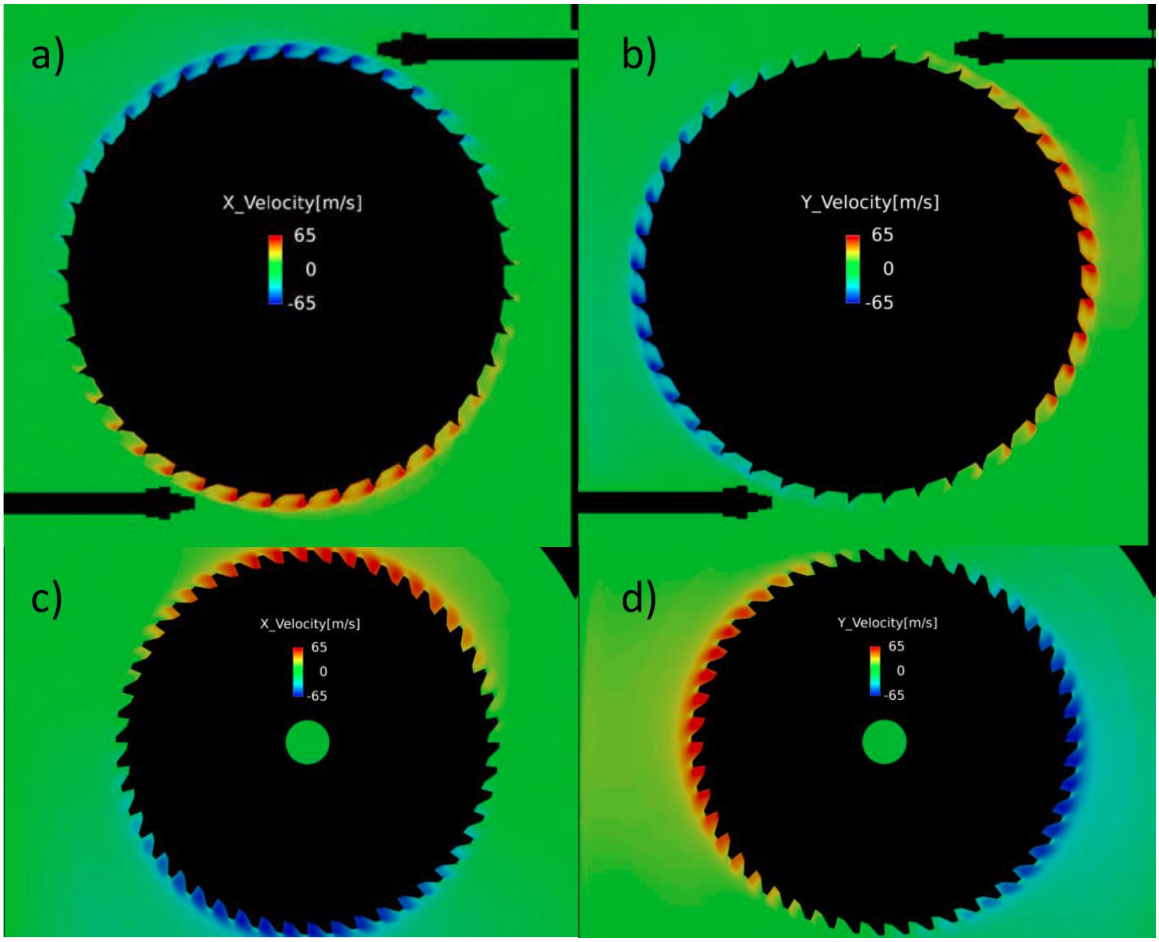

Figure 6.9: Velocity distributions showing the recirculation zones behind the buckets on a plane passing through the center of the buckets a) v2 turbine x-velocity, b) v2 turbine y-velocity, c) v3 turbine x-velocity, d) v3 turbine y-velocity

A breakdown of the torque for the buckets only is shown in Figure 6.10. For the baseline configuration, the buckets only breakdown did not include the bolts that attached the buckets to the wheel, while the section shown in green in Figure 6.5 is included in the buckets only breakdown for the v2 configuration. The overall trends of the time it takes for the torque of the baseline configuration to settle down compared to the v2 configuration persists in this comparison also. It can be seen from Figure 6.10 that the bolts have a significant contribution to the overall torque as the improvement of the v2 configuration is now down to around 17%. Note that the v3 runner

simulations were not run with the buckets “tagged” separately, therefore, a breakdown of the torque acting on just the buckets is not included in this figure.

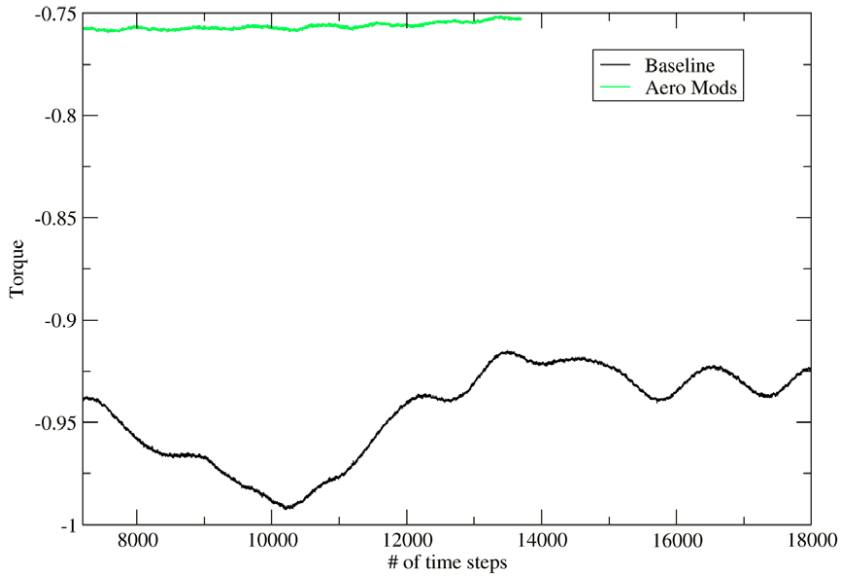

Figure 6.10: Comparison of torque (buckets only) for the Baseline and v2 configurations

Based on the results of the CFD simulations, the v2 configuration results in a significant reduction in the torque it requires when rotated at 2,500 RPM, compared to the v1 configuration. This means that all else equal, under the impulse provided by the water jets, the v2 configuration requires a significantly smaller head in order to produce power compared to the Baseline configuration. This also means that a GLIDES system utilizing the v2 Pelton turbine configuration would achieve higher system roundtrip efficiency. Similarly, the v3 runner configuration requires a smaller head to operate, therefore, has higher efficiency and would result in higher roundtrip efficiency when used in a GLIDES system compared to the v2 and v1 configurations.

6.1.3 Experimental study

For this very-high head, very-low flow application regime of Pelton turbines, it is not clear what the optimal jet diameter to bucket diameter ratio is. Pursuant to this the v3 Pelton turbine on the gen. 1 GLIDES prototype was used to study the performance of various jet diameters. This turbine has interchangeable nozzles. The nozzles were interchanged to achieve various jet diameters. With each different nozzle, performance was tested by discharging GLIDES system from 110 bar to 100 bar. As with the gen. 1 GLIDES prototype tests, during the tests, loads were controlled to maintain the bucket speed to jet speed ratio near 0.46 by utilizing resistive heaters with a variable transformer to adjust the loads. The gen. 1 prototype was used to conduct this testing, details about the setup and measurement instruments used can be found in Chapter 3. Details about the parametric testing conducted and the various nozzles utilized are shown in Table 6.1. According to conventional Pelton turbine design rules, jet diameter to bucket diameter ratio plays a role in turbine efficiency and can be optimized, with the optimal range being a jet diameter between 0.3-0.33 of the bucket diameter or width [71]. Presumably, the turbine efficiency drops off rapidly outside of this range.

Table 6.1: Parametric turbine jet diameter tests conducted

Test	**Orifice Diameter (in)**	**Orifice Diameter (mm)**	**Nozzle GPM (@1,000 PSI)**	**Nozzle Diameter to Jet Diameter Ratio**
1	0.05	1.27	2.5	0.21
2	0.06	1.52	3.5	0.25
3	0.07	1.78	5	0.29
4	0.08	2.03	6	0.33
5	0.09	2.29	7.5	0.38

For the five tests, four transient parameters were calculated and plotted versus time, the hydraulic power, the shaft power, the turbine specific speed, and the turbine efficiency which is the ratio of the turbine shaft power to the hydraulic power. The efficiency can be thought of as how efficiently the turbine is converting the hydraulic power to shaft power. The equations for the four performance parameters respectively can be seen in Equations (6.1)-(6.4) below.

$$\dot{W}_h = p \cdot \dot{V} \tag{6.1}$$

$$\dot{W}_s = 0.105 \cdot \frac{1}{3} \cdot N \cdot \tau \tag{6.2}$$

$$N_s = \frac{N \cdot \dot{W}_h^{\frac{1}{2}}}{\rho^{\frac{1}{2}} \cdot \left(\frac{p}{\rho}\right)^{\frac{5}{4}}} \tag{6.3}$$

$$\eta_T = \frac{\dot{W}_s}{\dot{W}_h} \tag{6.4}$$

where p is the measured pressure, $\dot{V}$ is the water flow rate (calculated from measured data), N is the measured shaft rotational speed, τ is the measured torque, and ρ is the water density.

Figure 6.11 presents the results of the tests, all four performance parameters described in the previous paragraph. For both the indicated power and the shaft power, as expected, in moving from the smallest nozzle (2.5 GPM nozzle) to the largest nozzle (7.5 GPM) the magnitude of the power increases, and the slope of the curve increases, as the rate of change of the pressure as it decreases from 110 bar to 100 bar is greater. While increasing the jet diameter (at given pressure) results in greater power output due to larger flow rate, Figure 6.11 d) suggests that the turbine efficiency is essentially insensitive to the jet diameter, since there are no real differences between

the various turbine efficiencies with the different jet diameters. This is contrary to conventional Pelton turbine design knowledge. This result suggests that in this ultra-high head, ultra-low flow Pelton turbine application regime, jet diameter to bucket diameter ratio is seemingly not an important design parameter when it comes to efficiency. This is a significant result because power output can then be maximized by increasing jet diameter, without adversely affecting turbine efficiency and consequently system roundtrip efficiency.

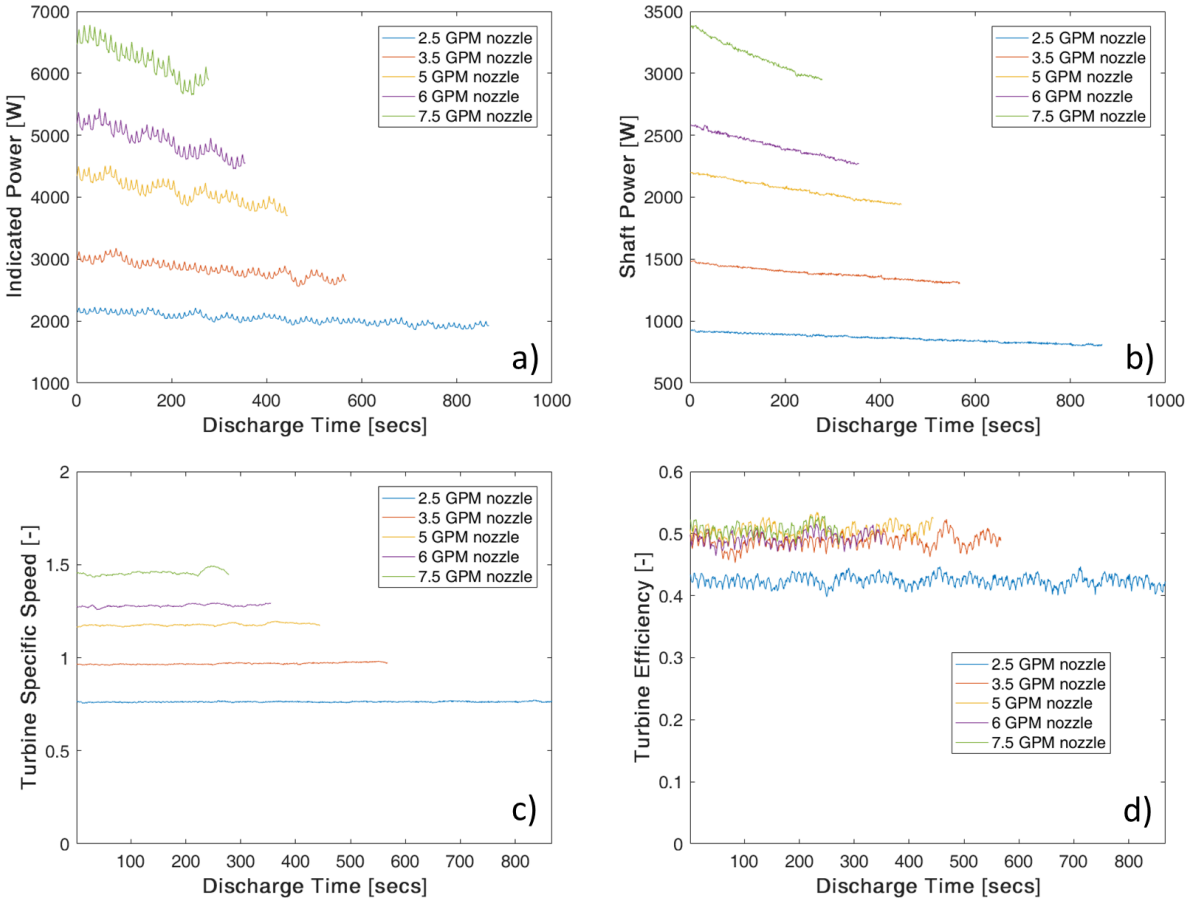

Figure 6.11: Parametric Pelton turbine jet diameter test results, a) indicated power, b) shaft power, c) turbine specific speed, d) turbine efficiency

6.2 Discussion of Pelton turbine vs. hydraulic motor

A hydraulic motor differs from a Pelton turbine in that it is a reaction machine as opposed to an impulse machine. Impulse turbines change the direction of flow of a high velocity fluid, and thus are driven primarily by fluid velocity, whereas, reaction turbines develop torque by reacting to the fluids pressure, so are primarily driven by inlet to outlet pressure difference. In impulse turbines, as soon as the water jet exits the inlet nozzle, it is at atmospheric pressure and remains so as it enters (strikes) and exits the turbine blades. In contrast, with reaction machines, the fluid enters the machine at high pressure, enters the blades or pistons still at high pressure, and then exit at lower pressure. It requires a fixed volume of water to achieve a complete revolution in an axial-piston type reaction machine, whereas this is not the case with impulse machines. This means that in an axial-piston machine, the flow rate is fully coupled to the RPM, meaning that the RPM sets the flow rate. This is in contrast with an impulse machine, where the flow rate is dependent on the system pressure and nozzle design, so the RPM and flow rate are somewhat decoupled. Practically, this means that in a GLIDES system discharging using a Pelton turbine, if you continue to load the system, the turbine speed will gradually slow down until it stalls and eventually stops, but the flow rate would not decrease proportionally. Flow would continue for as long as there is positive pressure in the pressure vessel(s). Essentially, we would be discharging the system, but not extracting any useful work out of it. In a GLIDES system discharging through a hydraulic motor, this would not happen. If you continued to load the system, the turbine speed will gradually slow, begin to stall, and come to a stop, but as it slowed down, the flow would decrease proportionally until the turbine completely stops spinning and the flow rate goes to zero.

Figure 6.12 presents a comparison between the operating characteristics of a hydraulic motor versus a Pelton turbine. The data shown was collected from the GLIDES gen. 2 and gen. 1

prototypes respectively. The top row shows the data for the hydraulic motor, and the bottom row shows the data for the Pelton turbine. The first two plots compared on the left show the torque, the shaft power, and the operating efficiency for the hydraulic motor versus the Pelton turbine respectively. As expected, the measured shaft torque increases for both machines as the pressure increases. The same for the shaft power. However, with the efficiency, the efficiency of the hydraulic motor decays with increasing pressure, while that of the Pelton turbine remains flat. The middle plot show the efficiency plotted versus the torque for both machines. Once again, the Pelton turbine curve is flat, while the hydraulic motor sees a decaying efficiency with increasing torque. The last two figures on the right show the efficiency plotted versus the RPM. For the hydraulic motor, the loads were controlled to keep the RPM at or around 1800 RPM, yet the efficiency varies between 0.5 and 0.9. But with the Pelton turbine, once again the efficiency is flat with respect to speed. The hydraulic motor on average has higher efficiency, but it is variable, while the Pelton turbine efficiency is lower, but very flat.

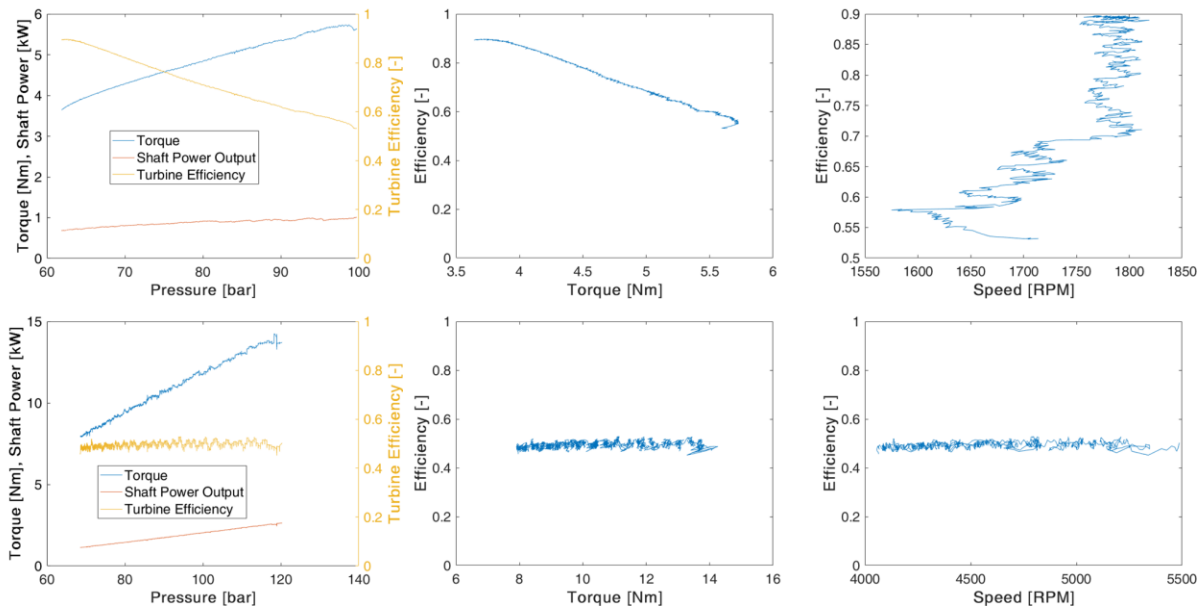

Figure 6.12: Comparison of several operating characteristics for a hydraulic motor (top row) versus a Pelton turbine (bottom row)

In terms of selecting an energy recovery machine of choice for use in s GLIDES system, there is no clear choice, and there are advantages and disadvantages of each. Decision should be made on a case-by-case basis, and the individual system design characteristics and energy storage application at hand should be considered. In the case of the GLIDES gen. 1 and gen. 2 prototypes, it was easier to control the Pelton turbine to achieve constant efficiency, however the average efficiency was on the lower side. With the hydraulic motor, the average efficiency was higher, but saw more variability. In general, with a Pelton turbine, the flow rate is not coupled to the turbine RPM, so if the turbine stalls, the system continues to discharge and waste stored energy. However, with a hydraulic motor, flow rate and rotation are fully coupled, so if the machine stalls, stored energy is not wasted. A Pelton turbine can have 1-7 jets which can be used to modulate power capacity of the same machine. Various nozzle sizes can also be used on jets, so between the number

of jets and jet nozzle diameter, the system power capacity can be tuned finely. This functionality would require multiple hydraulic motors to achieve the same level of flexibility. One big advantage of using a hydraulic motor, however, is that it can be used as the charging pump as well, consolidating components, and saving cost and space, as was done with the GLIDES gen. 2 prototype. Because Pelton turbines are typically not used for such high-heads and required redesign for use in GLIDES, it is likely that with additional research, efficiencies can be improved to reach that of conventional Pelton turbines, this would add another advantage for selection of Pelton turbine.

CHAPTER 7. COST & MARKET VALUE ANALYSIS

Peak demand reduction and shifting consumption to daily periods where electricity price is lower are two effective ways to reduce the cost of electricity of large consumers. Energy storage technologies enable buildings operators to do so. GLIDES is a promising energy storage technology that can provide that benefit to buildings. In this chapter, the result of backward analysis to determine economical first costs of storage deployment as behind-the-meter resource for large commercial buildings is presented. The result of forward analysis to estimate the actual material cost of deploying a GLIDES system at various capacities and storage times is also presented. In the first section, the economic benefit of GLIDES to a large commercial building in Los Angeles, Southern Nevada, Hawaii and Alaska is quantified. The maximum viable initial cost target of GLIDES for each location through a payback analysis is also calculated. In the second section, crude models for the cost-estimation of a GLIDES system at various system capacities and storage times are used to provide cost-scaling curves. The cost of the high-pressure storage medium is by far the largest cost component, comprising well over 50% of the total equipment costs. Special attention is given to the storage medium. Three storage mediums are investigated: conventional carbon-steel pressure vessels, carbon-fiber composite pressure vessels, and high-pressure pipe segments.

7.1 Backward Analysis – Value of Storage in Buildings

7.1.1 Introduction

One major potential application of large-scale energy storage is behind-the meter as a resource for peak demand reduction and time-of-use shifting. Most utility companies charge

buildings with high power draws a monthly demand charge. This charge is based on the highest draw sustained for a certain length of time, usually 15 minutes. Furthermore, in most jurisdictions, the demand charge and energy charge vary throughout the day. They are the highest during peak demand periods. Peak demand reduction and shifting consumption to daily periods when the price of electricity is lower are two effective ways to reduce the cost of electricity to large consumers and to lower their primary energy consumption and carbon footprint. Energy storage technologies enable building operators to leverage these strategies.

In this study, the economic benefit of large-scale energy storage to large commercial buildings in Los Angeles, Southern Nevada, Hawaii, and Alaska is quantified. A payback analysis is then conducted to calculate the maximum viable initial cost target of GLIDES or any generic energy storage solution for each location. An energy storage system deployed as a behind-the-meter resource for a building can help lower overall energy utility bills by reducing the peak draw and shifting the time of electricity draws from the grid. For an acceptable return on investment, the savings enabled by the storage system needs to be enough to recover its costs within an acceptable payback period. This chapter presents the results of a study to determine a target GLIDES system cost based on electric utility bill savings resulting from peak reduction and shifting. The Department of Energy (DOE) Large Office reference building was used as a case study [72].

7.1.2 Methodology

A model was developed to determine when to charge and discharge GLIDES to maximize the reduction of the cost of electricity. GLIDES was modeled as a load, additional to the load of the

building, with a power draw that is positive when charging and negative when discharging. Figure 7.1 illustrates this model.

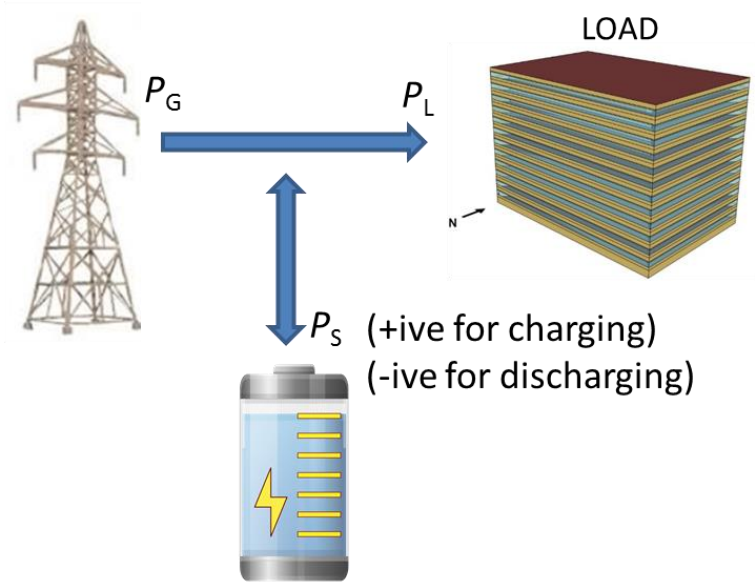

Figure 7.1: Power flows of the building and the energy storage system

The total draw from the electric grid at any time is then the sum of the energy consumption of GLIDES and the energy consumption of the building. This is repeated for each day in the year. The cost of electricity is given by Equation (7.1).

$$Cost = energy\ charge \times total\ kWh + demand\ charge \times \max power\ draw \quad (7.1)$$

Each day is divided into 96 time segments, with each being 15 minutes long. The average power draw in each period is the sum of the power draw of the building and the power draw of GLIDES energy storage. This is given by Equation (7.2) where η is the storage roundtrip efficiency which is taken as 1 when the storage system is charging and assumed to be 0.70 during discharging. A

constant value of 0.75 is taken for simplicity and is a representative value of roundtrip efficiency for the GLIDES system, from the simulation results in Chapter 2.

$$Total\ power\ draw\ = GLIDES\ power\ draw\ \times \eta + building\ power\ draw \qquad (7.2)$$

The cost function is then fed into an optimization algorithm that decides the operation mode of GLIDES at each time step (charge, discharge, or idle) to minimize the cost subject to the following three constraints:

- The total accumulated energy stored in GLIDES at any time cannot exceed its capacity.
- The total accumulated energy stored in GLIDES at any time is greater than zero.
- The power discharged from GLIDES at any time cannot exceed the power demand of the building.

The power demand of the Large Office DOE reference building was obtained by simulating the energy performance of the building in EnergyPlus [73]. Since the amount of energy that can be stored in GLIDES depended on it's the system size (kW) and storage time (hours), the optimization was run parametrically for several sizes and storage times. The optimization is then repeated for several locations across the United States.

7.1.3 Results

Simulations were run for Los Angeles, Southern Nevada, Alaska, and Hawaii. Table 7.1 through Table 7.4 present the electricity rate schedule of each location.

Table 7.1: Los Angeles, CA electricity rate structure [74]

Monthly charge, $	246.33	Tax	8%
	Time of use	**$/kWh**	**$/kW**
from 1/1 to 5/31 and from 10/1 to 12/31	from 0:00 to 8:00	0.01676	7.58
	from 8:01 to 21:00	0.01676	7.58
	from 21:01 to 24:00	0.01676	7.58
from 6/1 to 9/30	from 0:00 to 8:00	0.01676	7.58
	from 8:01 to 12:00	0.01676	8.34
	from 12:01 to 18:00	0.01676	16.42
	from 18:01 to 23:00	0.01676	8.34
	from 23:01 to 24:00	0.01676	7.58
All Weekends	from 0:00 to 24:00	0.01676	7.58

Table 7.2: Southern Nevada electricity rate structure [75]

Monthly charge, $	202.5	Tax	4%
	Time of use	**$/kWh**	**$/kW**
from 6/1 to 9/30	From 13:01 to 19:00	0.07575	16.3
	From 19:01 to 22:00	0.05675	2.59
	From 22:01 to 10:00	0.03843	0
	From 10:01 to 13:01	0.05675	2.59
All other months	From 0:00 to 24:00	0.04461	0.55

Table 7.3: Hawaii electricity rate structure [76]

Monthly charge, $	410	Tax	4%
	Time of use	**$/kWh**	**$/kW**
Mon – Fri	From 17:01 to 21:00	0.288184	24.5
Mon – Fri	From 7:01 to 17:00	0.268184	19.5
Sat – Sun	From 7:01 to 21:00	0.268184	19.5
Everyday	From 0:01 to 7:00	0.168184	0
Everyday	From 21:01 to 24:00	0.168184	0

Table 7.4: Alaska electricity rate structure [77]

Monthly charge, $	103.07	Tax	8%
	Time of use	**$/kWh**	**$/kW**
Nov thru May	From 0:00 to 24:00	0.0635	14.85
Jun thru Oct	From 0:00 to 24:00	0.0595	9.46

The extent to which stand-alone, behind-the-meter energy storage provides value is dependent on both the utility rate structure as well as the load profile (peak and diurnal variation) of the building in question. The storage provides value by reducing the power draw during periods when the rate structure is financially unfavorable, and shifting this use to other periods of the day when the rate structure is favorable. This is best illustrated by examining Figure 7.2, which presents a sample daily load profile for a building in Los Angeles with and without storage. Note that this profile is not the financially optimal size of storage for this building. A much larger than optimal size is shown in exaggeration for effect.

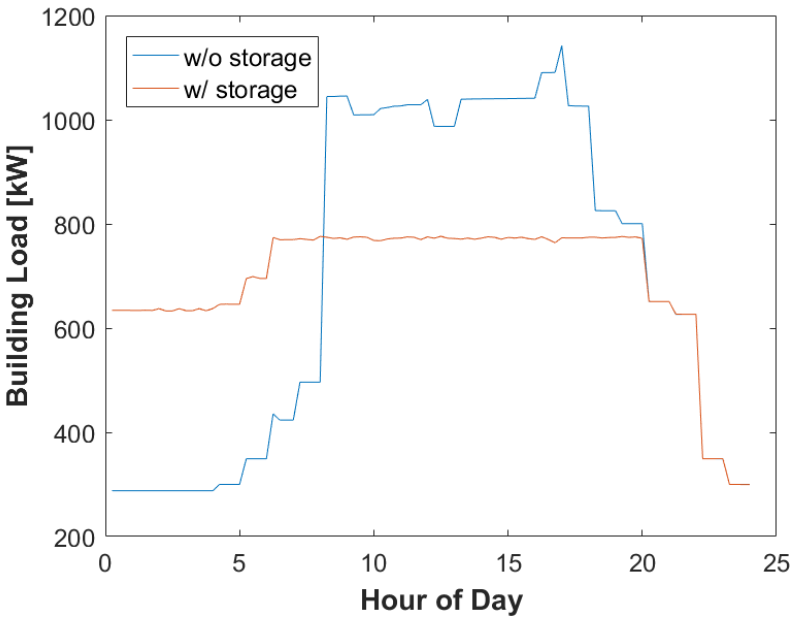

Figure 7.2: Sample building daily load profile with and without storage

During the time of day when rates are higher (approximately 7 am -9 pm), the peak draw from the grid is reduced from about 1150 kW down to under 800 kW, with the balance being met by the storage. To compensate, the draw from the grid is increased during other periods of the day when the rate structure is more favorable.

By running the optimization model parametrically for different storage capacities and times, it is possible to identify the financially optimal size (capacity and storage time) for the building in question. This was done for all four locations; the results can be seen in Figure 7.3.

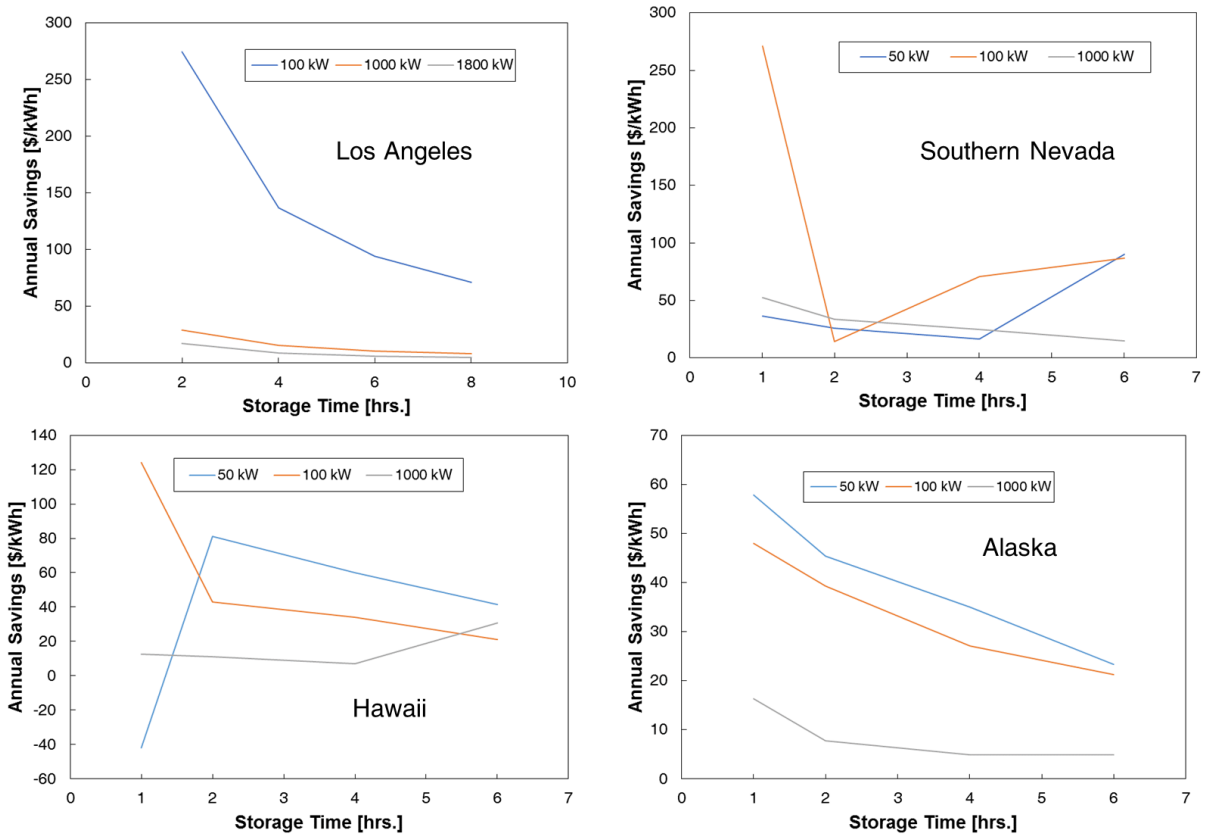

Figure 7.3: Annual savings divided by kWh of savings for different system sizes and capacities in four locations

In general, the value of storage diminishes as the storage size increases. There are some exceptions in Hawaii and Southern Nevada due to the intricacies in those particular rate structures. The most valuable storage (providing the most savings per kWh of deployed storage) is small capacity, small storage time. The optimal capacity and storage time for the four different locations and the associated annual savings is shown in Table 7.5.

Table 7.5: Optimal building energy storage size and annual savings for four different locations

Location	Capacity [kW]	Capacity Factor [kW/kW]	Storage Time [hrs]	Annual Savings [$/kWh]
Los Angeles	100	0.057	2	274.10
Southern Nevada	100	0.051	1	270.90
Hawaii	100	0.052	1	123.90
Alaska	50	0.033	1	57.80

In addition to the optimal storage size and annual savings, Table 7.5 also shows the capacity factor. The capacity factor is optimal storage capacity divided by the peak building power draw; this result shows that energy storage sized at capacity of 3-5% of peak building power draw provides the most value per kWh of deployed energy storage.

An important parameter that a building owner/operator would likely consider in deciding whether to invest in deploying energy storage is the payback period. Using the annual savings determined above, the target cost (present value) for an energy storage system based on the desired payback period can be determined by discounting the annual savings by the desired payback period in years, using Equation (7.3) and a representative discount rate or interest rate, where *PV* is the present value (i.e. target cost), *C* is the annual savings, *N* is the desired payback period, and *i* is the discount or interest rate.

$$PV = C\left[\frac{1-(1+i)^{-N}}{i}\right] \tag{7.3}$$

Carrying out this calculation for all four locations, with desired payback periods of 5 years and 10 years, yields the target costs in Figure 7.4. Building owners/operators can, in some cases, afford to spend generous amounts on deploying energy storage.

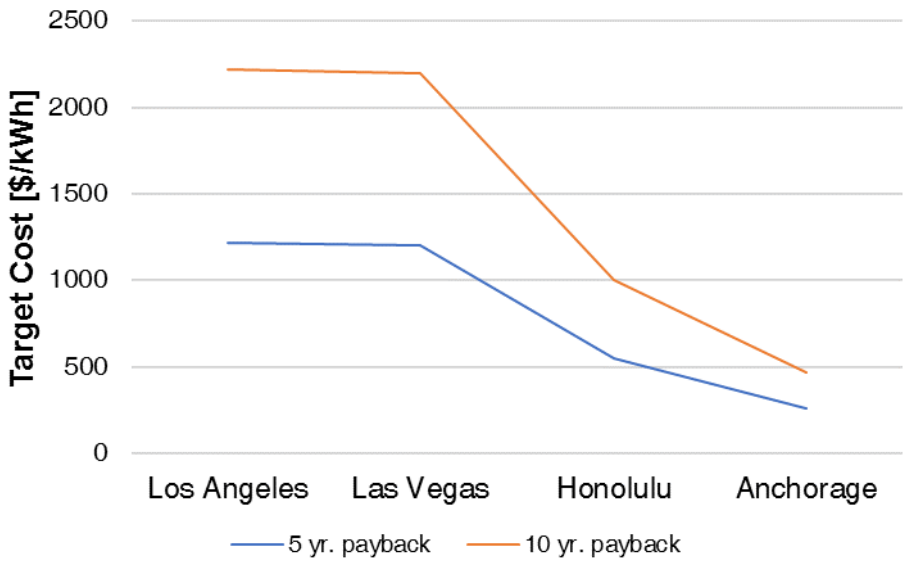

Figure 7.4: Target energy storage cost for 5 and 10-year payback periods

7.1.4 Summary

Stand-alone, behind-the-meter energy storage can provide significant value in certain markets engaging in demand charges and time-of-use utility rate structures. The size of the value opportunity is dependent on how favorable the utility rate structure is to time-of-use shifting, as well as the individual building's load profile. Buildings with large variations between peak and average power demand are particularly positioned to extract value from energy storage systems. In some cases, a building owner/operator can afford to spend generous amounts on energy storage systems, while achieving reasonable payback periods and sustained annual savings. For example, in Los Angeles or locations with similar electricity rate structures and building load profiles, storage, with a 10-year payback period, can be economically viable at an initial cost of $2,000+/kWh. The analysis and results presented here indicate that systems with small storage capacity (relative to peak building load) and storage times provide the most value.

7.2 Forward Analysis – Cost Analysis of GLIDES Scale-Up Prospects

7.2.1 Introduction

In addition to the backward cost analysis to identify cost targets providing favorable payback in selected markets, simple cost estimation has also been conducted to determine the cost of GLIDES at several scales and for different storage times. These cost estimates are based on the cost of the major components comprising a GLIDES system (storage medium, pump, turbine, and associated piping and materials). The cost of the high-pressure storage medium is by far the largest cost component, comprising well over 50% of the total equipment costs. Special attention is given to the storage medium. Due to the large degree of location dependence, labor and installation costs are not considered here.

7.2.2 Methodology

The cost estimation procedure is centered around the cost of the high-pressure storage medium. For this study, three options are considered as the storage medium for GLIDES: conventional steel pressure vessels, carbon fiber based pressure cylinders, and high-pressure pipe segments. High pressure pipe can be used as the storage medium by manifolding several long pipe segments on the ends to provide the necessary storage volume. The cost-estimation procedure for GLIDES system utilizing each of the three types of storage medium is generally the same, with a few distinct differences. The approach for all three types of storage is outlined in the following sections.

The first step in the cost-estimation process is determining the volume of storage necessary for a given system capacity (kW), and storage time (hours). First, a roundtrip efficiency (RTE),

maximum operating pressure (p_{max}), and minimum operating pressure (p_{min}) are selected for the system. The maximum operating pressure is typically dictated by the maximum allowable pressure of the specific storage medium in use. The minimum pressure is the lowest pressure at which power can reasonably be extracted from the turbine or hydraulic motor. In this study, the RTE is taken as 75%, and the minimum pressure is taken as p_{min} = 70 bar. The energy stored in the compressed air is a function of the thermodynamic variables, pressure, volume, temperature, and the polytropic exponent (n). In this application, n can range from a minimum of 1 (isothermal compression – best case scenario) to 1.4 (adiabatic compression – worst case scenario). Here, n is taken as 1.2. The energy contained in the compressed air per unit volume is given by Equation (7.4).

$$w_{max} = \frac{n}{n-1} p_{max} \left[1 - \left(\frac{p_{atm}}{p_{max}} \right)^{\frac{n-1}{n}} \right] \tag{7.4}$$

where p_{atm} is the atmospheric pressure on the exterior of the storage medium. As mentioned above, no useful work can be efficiently extracted below p_{min}, so we must subtract this unused work from w above. The unused work per unit volume is given by Equation (7.5).

$$w_{uu} = \frac{n}{n-1} p_{min} \left[1 - \left(\frac{p_{atm}}{p_{min}} \right)^{\frac{n-1}{n}} \right] \tag{7.5}$$

Considering Equations (7.4) and (7.5), the actual usable energy per unit volume is given by Equation (7.6).

$$w_u = w_{max} - w_{uu} \tag{7.6}$$

Finally, the required storage medium volume can be calculated using Equation (7.7).

$$V_{st} = \frac{E_{st}}{w_u \cdot RTE} \tag{7.7}$$

where E_{st} is the product of the system capacity and storage time.

Conventional Steel Pressure Vessels

The first type of storage medium considered is conventional steel pressure vessels, much like those used in the GLIDES proof-of-concept prototype at ORNL, as seen in Figure 7.5.

Figure 7.5: Conventional steel pressure vessels

These types of pressure vessels are typically custom manufactured and require a lot of manual labor for welding and forming, consequently, this is the most expensive of the three types of storage mediums considered. Once the required storage volume is calculated as described in the

previous section, a cost model for the cost and sizing of steel pressure vessels described in Proczka *et al.* [16] is used to optimally size the pressure vessel (including p_{max}, vessel radius and height-to-diameter ratio) to minimize total cost of pressure vessels needed to meet the required storage volume. The balance of the remaining equipment needed for a working GLIDES system is then added, using the assumptions described in Appendix C.

Carbon Fiber Based Pressure Cylinders

A promising alternative to the costly steel pressure vessels is carbon fiber based pressure cylinders. These cylinders typically consist of aluminum or high-density polymer liners fully overwrapped with carbon fiber. The manufacturing of the cylinder liners as well as the carbon fiber overwrapping process are fully automated, and so cost savings can be achieved over steel vessels. Given the nature of GLIDES requiring the storage vessels to store air as well as water, the polymer lined carbon fiber cylinders are an appealing option. Two versions of these carbon fiber cylinders can be seen in Figure 7.6.

Figure 7.6: Carbon fiber based pressure cylinders (source: Luxfer Cylinders http://www.luxfercylinders.com)

For the purposes of cost-estimation, quotes for several of these cylinders of different storage volumes were obtained from the manufacturer and can be seen in Table 7.6. The cost model then sizes and costs a given GLIDES system using each available carbon fiber cylinder, and the cylinder resulting in the lowest total cylinder cost is selected. The balance of the remaining equipment needed for a working GLIDES system is then added, using the assumptions described in the Appendix C.

Table 7.6: Carbon fiber pressure cylinder cost data

Diameter	**Length**	**Water volume**	**Cylinder cost**
[mm]	**[mm]**	**[liters]**	**[$]**
564	1524	287	3013.5
564	2184	410	4305
564	3556	727	7633.5
673	1524	376	3948
673	2032	550	5775
673	2286	638	6699
673	3048	900	9450
685	2057	579	6079.5
673	2743	795	8347.5
data from Luxfer Cylinders			

High Pressure Pipe Segments

The third option considered for use as the high-pressure storage medium is high pressure (schedule 80) carbon steel pipe segments. Pipe segments measuring anywhere from 5 feet and above can be manifolded together on the ends, providing the high-pressure storage medium required for a functioning GLIDES system. These types of high pressure pipe segments are typically used to serve as the mid-section for high-pressure steel cylinders such as the ones shown in Figure 7.5, but do not require the additional material and labor associated with manufacturing

and welding the end caps on, which is where a significant portion of the cost lies. An example of high-pressure carbon steel pipe segments can be seen in Figure 7.7.

Figure 7.7: Carbon steel pipe segments

To estimate the cost of GLIDES utilizing high-pressure pipe as storage medium, a cost estimation procedure for carbon steel piping described by McCoy & Rubin [78] was used. Their method is part of an overall cost-model developed for the cost-estimation of pipeline infrastructure projects for CO_2 capture/storage. This method assumes 30-inch diameter pipe with 153 bar maximum operating pressure. The balance of the remaining equipment needed for a working GLIDES system is then added, using the assumptions described in Appendix C.

7.2.3 Results

Conventional Steel Pressure Vessels

As expected, systems utilizing steel pressure vessels are found to be the most expensive option. The $/kWh cost of said systems is shown in Figure 7.8 for various system sizes and storage times. The costs range from a maximum near $13,000/kWh for a 1 kW, 1 hour system (very small) to a minimum approximately $1,500/kWh for a 100 MW, 6 hours system (very large).

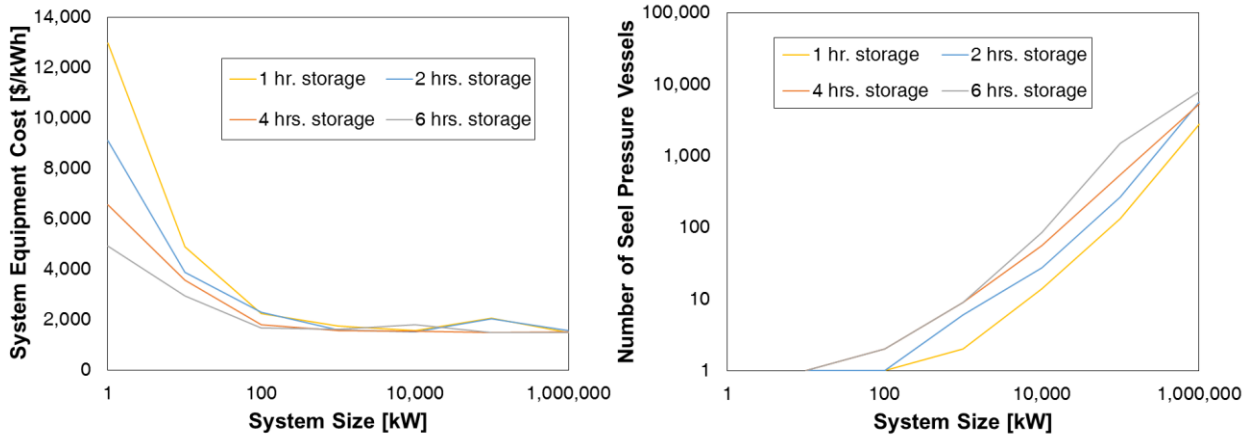

Figure 7.8: Costs of GLIDES system utilizing steel pressure vessels

The number of pressure vessels required for the corresponding system sizes are also shown in Figure 7.8. Based on the number of pressure vessels required, it is conceivable to design very large (>10,000 kW) GLIDES systems.

Carbon Fiber Based Pressure Cylinders

Carbon fiber cylinders are shown to be more cost-effective then their steel-counterparts, as shown in Figure 7.9. The cost for the very small system is reduced to about $8,800/kWh, and the cost for the very large system is reduced to $860/kWh.

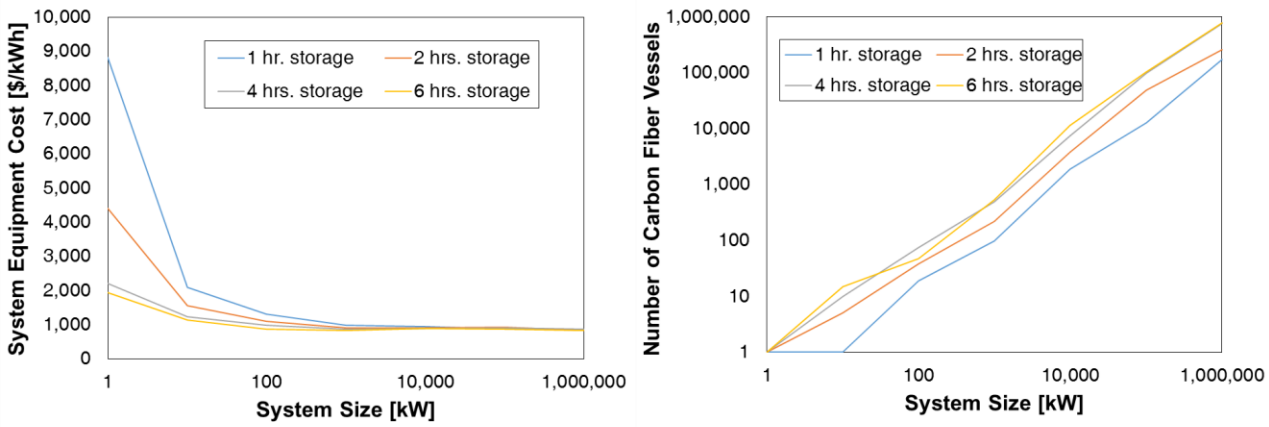

Figure 7.9: Costs of GLIDES system utilizing carbon fiber pressure vessels

The number of pressure vessels required for the corresponding system sizes are also shown in Figure 7.9. Though the carbon fiber vessels are cheaper than steel, they do require a larger number of pressure vessels, consequently, very large system sizes (i.e. >10,000 kW) might not be conceivable.

High Pressure Pipe Segments

In terms of material costs, the high-pressure pipe segments are found to be the most cost-effective storage medium option for GLIDES of the three options studied. The costs are shown in Figure 7.10. The cost for the very small system are further reduced to $5,800/kWh, and the costs for the very large system fall to $380/kWh.

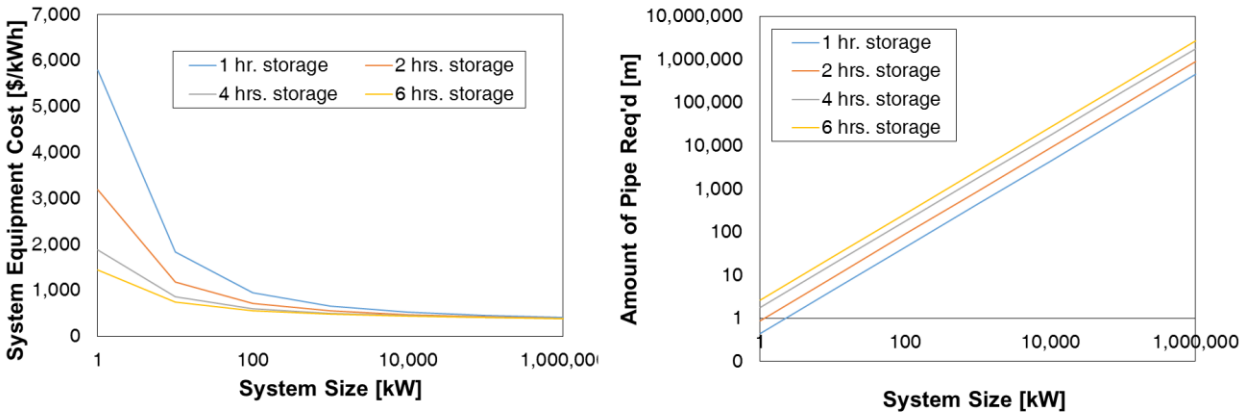

Figure 7.10: Costs of GLIDES system utilizing pipe segments

The amount of pipe required in meters is also shown in Figure 7.10 alongside the cost. This gives an indication of the footprint required for a given system size. It is important to note that though the pipe segment equipment costs are significantly reduced compared to the pressure vessel options, they would likely require more labor for installation, and thus this may erode or eliminate the cost savings over the other storage mediums.

7.2.4 Summary

The equipment capital costs for GLIDES energy storage system is studied at various system sizes and storage times, for three different high-pressure storage medium options. It is found that utilizing steel pressure vessels as storage medium is the most expensive option of the three studied, followed by carbon fiber cylinders, and then high-pressure steel pipe segments. While the steel pipe segments are found to be the most cost-effective option of the three in terms of material costs, such systems are likely to have a higher labor/installation cost, due to the additional labor required

to install/erect pipe segments and manifold them together. These costs are not studied here due to the large degree of site dependence of this cost category.

CHAPTER 8. SUMMARY & CONCLUSIONS

The ability to store a large amount of energy efficiently, flexibly, cheaply and on demand remains a strong technology need to ensure successful integration of intermittent renewable energy resources and facilitate a modern, transactive grid that is able to effectively manage energy demand/supply.

In the past, the power grid has operated in a fashion where generation and use must be matched temporally and in capacity. Affordable bulk energy storage offers the possibility of relaxing this constraint, which comes with numerous advantages including creating a more modern transactive grid, deferring or completely eliminating new major infrastructure investments, and allowing buildings to effectively transact with the grid to drastically improve overall demand/supply balancing and management when deployed as a behind-the-meter resource. As economies continue to evolve, technologies continue to advance, and humans continue to find new ways to consume energy, energy demand profiles will become more and more unpredictable and fluctuate more, which will cause power quality to suffer. This is another area where bulk energy storage can play a major role.

Beyond the transactive power grid and energy demand/supply management implication of energy storage, successfully integrating renewable sources which are typically intermittent, but available in access when on, will not be possible without being paired with cheap, efficient energy storage. Energy storage presents an opportunity to store excess renewable energy while available, to be dispatched during intermittency. Pursuant to all the above, a Ground-Level Integrated Diverse Energy Storage (GLIDES) technology was invented and continues to be developed at Oak Ridge National Laboratory. GLIDES is the topic of this thesis, which has given an in depth

description of the technology and development activities to date. In common with compressed air energy storage, the GLIDES technology is based on air compression/expansion. However, several novel features lead to near-isothermal processes, higher efficiency, greater system scalability, and the ability to site a system anywhere. The enabling features are utilization of hydraulic machines for expansion/compression, above-ground pressure vessels as the storage medium, spray cooling/heating, and waste-heat utilization. To date, comprehensive, physics-based analytical modeling/simulation of the base (prototype) configuration and modified configurations has been completed, two working prototypes have been developed and demonstrated, experimental characterization has been performed, alternative working fluids to improve system performance have been investigate, and thermo-economic analysis of system scale-up performed.

8.1 Summary of contributions

In pursuit of the answers to the fundamental research questions posed in section 1.3, several scientific and engineering accomplishments were achieved which have advanced the body of research on compressed-air energy storage, and more specifically, hydro-pneumatic energy storage. To our knowledge, the prototypes created as part of this work are the first end-to-end (electrical-to-electrical, comprising all energy conversion steps) and largest experimental/prototype demonstrations of the liquid-piston driven, hydro-pneumatic, compressed-gas energy storage concept. Furthermore, a clear path to achieving near-isothermal compression/expansion and successfully integrating the use of waste-heat during expansion to boost efficiency and energy density was demonstrated. A clear path to achieving isobaric compression/expansion to improve efficiency and energy density via the use of condensable volatile working fluids was also demonstrated. A robust, physics-based, transient modelling/simulation framework was built to simulate all the GLIDES configurations described.

The research supporting the above activities was centered around four main contributions which are listed below:

1. The development of an analytical, transient, physics-based model of multiple configurations of the GLIDES cycle and complete energy system.
2. The experimental demonstration of hydraulically-assisted liquid piston gas compression/expansion applied to an energy storage device in multiple configurations.
3. The treatment of the energy recovery turbomachine to recover work from very high-head, very low-flow hydraulic stream (Pelton turbine, axial piston hydraulic motor).
4. The cost/market value analysis for potential us of GLIDES technology deployed as a behind-the-meter resource in buildings.

A roadmap of the research contributions made is shown in Figure 8.1. The effort began with the comprehensive physics-based simulation (Chapter 2), which fed/supported the development of the first-generation prototype and associated experiments (Chapter 3). Under the first prototype development effort, the prospects of alternative working fluids (condensable gases, R134a, CO_2) was explored via a combination of experimentation and physics-based simulation (Chapter 4) and two options for the energy recovery turbomachine were studied (Chapter 6). Using the first-generation prototype results, the model developed and presented in Chapter 2 was calibrated and validated, this work is also presented in Chapter 3. In Chapter 5, the design of the second-generation proof-of-concept prototype, which featured several design improvements from the first-generation, was presented in depth, and initial experimental results presented. Finally, cost/market value analysis for one use case (buildings, behind-the-meter) was conducted, and this work presented in Chapter 7.

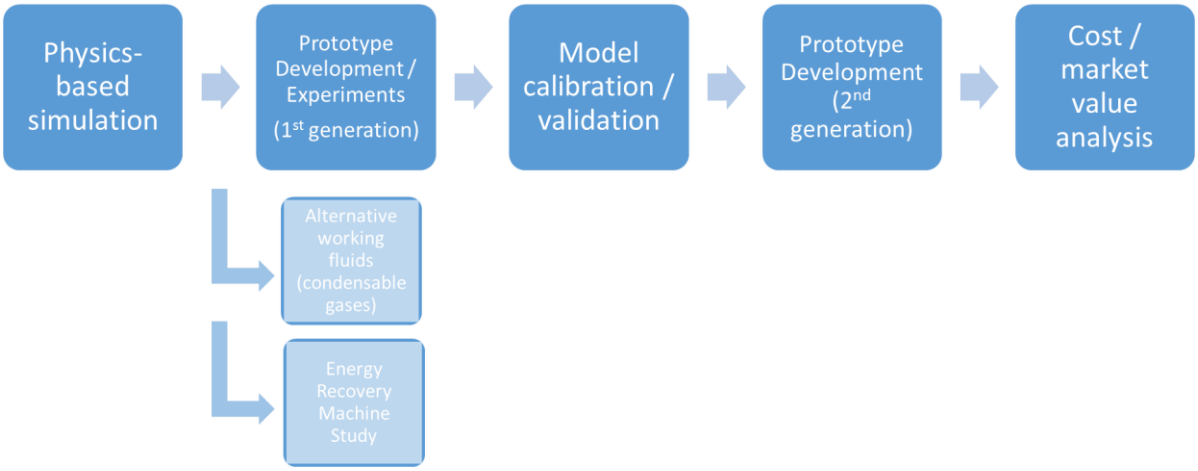

Figure 8.1: Roadmap of research contributions

8.2 Future work

The most immediate research need following the work already completed and presented in this thesis, is the complete parametric characterization of the second-generation proof-of-concept prototype, including complete characterization of the use of spray for cooling/heating to achieve isothermal or near-isothermal compression and expansion and waste-heat integration. Under the base configuration, these experiments will allow for the determination of the effect of charging speed (flow rate), and charging from the bottom versus spray charging from the top on system performance (efficiency and energy density). Furthermore, under the second and third configurations, spraying atomized water droplets into the storage vessels comes at additional cost due to added pressure drop from the spray nozzles and the use of an additional high operating pressure, low head spray pump during discharge. These experiments will allow for the characterization of this tradeoff to determine under which operating conditions (pressure ratio,

spray flow rate, heat rate, waste-heat input temperature, etc.) the improvement to efficiency and/or energy density outweighs the added incurred energy cost.

Beyond the above, there are many research activities which could be undertaken to further push the technology readiness level of GLIDES. The following are just a few of the more pressing research needs that come to mind. In order to achieve a significant, step-sized reduction in system costs, the cost of the pressure vessels used in GLIDES systems needs to be reduced dramatically. Currently, in conventional carbon steel pressure vessels, the majority of the cost comes from the labor, as these vessels are largely custom manufactured in very labor intensive, heat intensive processes. Automation provides one opportunity to reduce these costs, while finding a way to eliminate the need for heat treatment is another. More advanced carbon-fiber composite pressure vessels offer a cheaper alternative. While the material costs are higher, the labor costs are reduced by the help of manufacturing automation. By unleashing the potential of advanced manufacturing techniques such as additive manufacturing, and tapping into advanced materials such as new metal alloys and composites, the cost of manufacturing high pressure vessels can be reduced. One roadmap may be to leverage additive manufacturing to integrate complex vessel structures which can reduce the necessary wall thicknesses but still achieve high pressure ratings, and automate manufacturing.

Other relevant research areas which would advance technology development includes optimization of the working fluid including simulation and experimentation of higher pressure fluids and fluid blends, hydraulic turbomachinery design, and pursuing advanced cycle variations including combined cooling/heating and electricity generation/storage. System integration activities such as virtual integration of a GLIDES system to simulate response in a real-world grid-

connected environment would also be valuable. The transient nature of the technology poses some integration challenges that this type of simulation would help navigate.

APPENDIX A: GLIDES SYSTEM SIMULATION CODES

Main script

written in: MATLAB R2016b

This script calculates the complete, end-to-end transient response (pressure, temperature, volume) of the GLIDES system (water, air, tank walls). It also includes two sub-functions. The first is a flow model which calculates the discharge flow rate from the pressure vessel(s), the second is a sub-function which includes the characteristic curves of the auxiliary components (pump/motor, turbine/generator) and calculates roundtrip efficiency, energy density, itemized losses and transient electrical power and current during discharge. Both supporting functions need to be placed in the same folder as this script in order to run successfully. The inputs are the system parameters (number of vessels, number of Pelton turbine jets, and initial conditions).

```
clear
clc


%known constants/parameters:
%number of tanks
num_tanks=4;
%number of pelton turbine jets
num_jets=1;
%atmospheric pressure in pascals
P_atm=101325;
P_conv=100000;
%ambient temp in kelvin
T_amb_C=25;
T_amb=T_amb_C+273.15;
%130 bar max pressure converted to pascals
P_max_bar=130;
P_max=P_max_bar*P_conv;
%70 bar initial pressure converted to pascals
P_min_bar=70;
P_min=P_min_bar*P_conv;
%air gas constant in J/kg*K
```

```
R_air=286.987;
%universal gas contant
R_bar=8314;
%air molar mass
M_air=28.97;
%mass of tanks in kg
m_tank=num_tanks*1720;
%specific heat of tank material in J/kg*K
c_tank=470;
%initial mass of water
m_w_ini=0.01;
V_w_ini=m_w_ini/1000;
%initial volume of air in tanks in m^3
V_air_ini=num_tanks*0.5-V_w_ini;
%mass of air using IF equation of state
m_air=(P_min*V_air_ini)/(R_air*T_amb);
%gravitational constant in m/s^2
g=9.8;
%thermal conductivity of tank material in W/m*K
%k_tank=15.1;
k_tank=52;
%tank inner diameter in m
D_i=0.57;
%tank outer diameter in m
D_o=0.61;
%exterior air velocity in m/s
vel_air=3;
%height of tanks in m
L=2.5;
%air to water heat transfer area
A_aw=num_tanks*pi*D_i^2/4;
%total interior heat transfer area
A_i_tot=num_tanks*V_air_ini/D_o+(pi/4)*D_o^2;
%total exterior heat transfer area
A_o_tot=num_tanks*V_air_ini/D_i+(pi/4)*D_i^2;
%tank wall thickness
th=(D_o-D_i)/2;

%constants for variation of cp of air w/ temperature
alpha=3.653;
beta_cv=-1.337*10^-3;
gamma=3.294*10^-6;
delta=-1.913*10^-9;
epsilon=0.2763*10^-12;

%Redlich-Kwong equation of state constants for air
a=15.989;
b=0.02541;

%turbomachine parameters
%pump flow rate
pump_flow=35;
V_dot_pump=pump_flow/60*10^-3;
%static pump efficiency (not used)
```

```
%eta_pump=0.87;
%static turbine efficiency
%eta_turb=0.85;

%simulation length in seconds
max_time=100*60*60;
pausetime=12*60*60;

%initialize vectors
time_vec=zeros(max_time,1);
V_air=zeros(max_time,1);
v_bar_air=zeros(max_time,1);
T_air=zeros(max_time,1);
P_air=zeros(max_time,1);
m_w=zeros(max_time,1);
T_w=zeros(max_time,1);
T_tank1=zeros(max_time,1);
T_tank2=zeros(max_time,1);
m_dot_w_vec=zeros(max_time,1);
cv_air_vec=zeros(max_time,1);
cp_air_vec=zeros(max_time,1);
k_air=zeros(max_time,1);
mu_air=zeros(max_time,1);
rho_air=zeros(max_time,1);
nu_air=zeros(max_time,1);
alpha_air=zeros(max_time,1);
Pr_air=zeros(max_time,1);
mu_air_o=zeros(max_time,1);
rho_air_o=zeros(max_time,1);
nu_air_o=zeros(max_time,1);
k_air_o=zeros(max_time,1);
cp_air_o=zeros(max_time,1);
cv_air_o=zeros(max_time,1);
alpha_air_o=zeros(max_time,1);
Pr_air_o=zeros(max_time,1);
Re_air_o=zeros(max_time,1);
rho_w=zeros(max_time,1);
c_w=zeros(max_time,1);
mu_w=zeros(max_time,1);
k_w=zeros(max_time,1);
Pr_w=zeros(max_time,1);
nu_w=zeros(max_time,1);
alpha_w=zeros(max_time,1);
L_char_1=zeros(max_time,1);
L_char_2=zeros(max_time,1);
m_dot_p=zeros(max_time,1);
V_dot_w_exp=zeros(max_time,1);
T_f_aw=zeros(max_time,1);
T_f_1=zeros(max_time,1);
T_f_2=zeros(max_time,1);
T_f_o=zeros(max_time,1);
beta_aw=zeros(max_time,1);
beta_1=zeros(max_time,1);
beta_2=zeros(max_time,1);
```

```
Ra_aw=zeros(max_time,1);
Ra_1=zeros(max_time,1);
Ra_2=zeros(max_time,1);
Gr_1=zeros(max_time,1);
Gr_2=zeros(max_time,1);
g_1=zeros(max_time,1);
g_2=zeros(max_time,1);
Nu_aw=zeros(max_time,1);
Nu_1=zeros(max_time,1);
Nu_2=zeros(max_time,1);
Nu_o=zeros(max_time,1);
h_aw=zeros(max_time,1);
h_i_1=zeros(max_time,1);
h_i_2=zeros(max_time,1);
h_o=zeros(max_time,1);
UA_1=zeros(max_time,1);
UA_2=zeros(max_time,1);
A_i_1=zeros(max_time,1);
A_i_2=zeros(max_time,1);
A_o_1=zeros(max_time,1);
A_o_2=zeros(max_time,1);
A_ave_1=zeros(max_time,1);
A_ave_2=zeros(max_time,1);
R_mt_1=zeros(max_time,1);
R_mt_2=zeros(max_time,1);
m_tank1=zeros(max_time,1);
m_tank2=zeros(max_time,1);
V_dot_exp_LM=zeros(max_time,1);
ploss=zeros(max_time,1);
loss_check=zeros(max_time,1);
v_term=zeros(max_time,1);
drop_travel=zeros(max_time,1);
travel_time=zeros(max_time,1);
rho_drop=zeros(max_time,1);
N_droplets=zeros(max_time,1);
Re_droplet=zeros(max_time,1);
Pr_drop=zeros(max_time,1);
mu_drop=zeros(max_time,1);
nu_drop=zeros(max_time,1);
k_drop=zeros(max_time,1);
c_drop=zeros(max_time,1);
alpha_drop=zeros(max_time,1);
Nu_droplet=zeros(max_time,1);
h_droplet=zeros(max_time,1);
%v_term2=zeros(max_time,1);
%travel_time2=zeros(max_time,1);
%N_droplets2=zeros(max_time,1);
%Re_droplet2=zeros(max_time,1);
%Nu_droplet2=zeros(max_time,1);
%h_droplet2=zeros(max_time,1);

m_drops=zeros(max_time,1);
m_dot_spray_vec=zeros(max_time,1);
T_drop_SR_in=zeros(max_time,1);
```

```
T_air_SR=zeros(max_time,1);
T_drop_SR_out=zeros(max_time,1);
tau=zeros(max_time,1);
q_drop=zeros(max_time,1);
T_w_new=zeros(max_time,1);
q_dot_drop=zeros(max_time,1);
T_WH_out=zeros(max_time,1);


%initial values of above vectors
time_vec(1)=0;
V_air(1)=V_air_ini;
v_bar_air(1)=(V_air(1)/m_air)*M_air;
T_air(1)=T_amb;
P_air(1)=P_min;
m_w(1)=m_w_ini;
T_w(1)=T_amb;
T_tank1(1)=T_amb;
T_tank2(1)=T_amb;
T_f_aw(1)=(T_w(1)+T_air(1))/2;
T_f_1(1)=(T_air(1)+T_tank1(1))/2;
T_f_2(1)=(T_w(1)+T_tank2(1))/2;
T_f_o(1)=(T_tank1(1)+T_tank2(1)+T_amb)/3;
cv_air_vec(1)=R_air*((alpha+beta_cv*T_air(1)+gamma*T_air(1)^2+delta*T_air(1)^3+epsilon*T_air(1)^4
)-1);
cp_air_vec(1)=cv_air_vec(1)+R_air;
k_air(1)=0.009748221+5.27354*10^-10*P_air(1)+5.5243*10^-5*T_f_1(1);
mu_air(1)=6.93093*10^-6+2.35465*10^-13*P_air(1)+3.85177*10^-8*T_f_1(1);
rho_air(1)=(V_air(1)/m_air)^-1;
nu_air(1)=mu_air(1)/rho_air(1);
alpha_air(1)=k_air(1)/(rho_air(1)*cp_air_vec(1));
Pr_air(1)=nu_air(1)/alpha_air(1);
mu_air_o(1)=6.93093*10^-6+2.35465*10^-13*P_atm+3.85177*10^-8*T_f_o(1);
rho_air_o(1)=P_atm/(R_air*T_f_o(1));
nu_air_o(1)=mu_air_o(1)/rho_air_o(1);
k_air_o(1)=0.009748221+5.27354*10^-10*P_atm+5.5243*10^-5*T_f_o(1);
cv_air_o(1)=R_air*((alpha+beta_cv*T_f_o(1)+gamma*T_f_o(1)^2+delta*T_f_o(1)^3+epsilon*T_f_o(1)^4)-
1);
cp_air_o(1)=cv_air_o(1)+R_air;
alpha_air_o(1)=k_air_o(1)/(rho_air_o(1)*cp_air_o(1));
Pr_air_o(1)=nu_air_o(1)/alpha_air_o(1);
rho_w(1)=-3.9837E-03*T_w(1)^2+2.1274E+00*T_w(1)+7.1666E+02;
c_w(1)=-3.0788E-04*T_w(1)^3+3.0602E-01*T_w(1)^2-1.0086E+02*T_w(1)+1.5207E+04;
mu_w(1)=-3.7024E-09*T_w(1)^3+3.7182E-06*T_w(1)^2-1.2513E-03*T_w(1)+1.4156E-01;
k_w(1)=-7.0674E-06*T_w(1)^2+5.6853E-03*T_w(1)-4.5602E-01;
nu_w(1)=mu_w(1)/rho_w(1);
alpha_w(1)=k_w(1)/(rho_w(1)*c_w(1));
Pr_w(1)=nu_w(1)/alpha_w(1);
m_dot_p(1)=rho_w(1)*V_dot_pump;
m_dot_w_vec(1)=m_dot_p(1);
[V_dot_w_exp(1),V_dot_exp_LM(1),ploss(1),loss_check(1)]=glides_flow(P_air(1),num_jets,num_tanks,n
u_w(1),rho_w(1));
L_char_1(1)=L;
L_char_2(1)=0.0001;
```

```
beta_aw(1)=1/T_f_aw(1);
beta_1(1)=1/T_f_1(1);
beta_2(1)=1/T_f_2(1);
Ra_aw(1)=(g*beta_aw(1)*(T_w(1)-T_air(1))*D_i^3)/(nu_air(1)*alpha_air(1));
Ra_1(1)=(g*beta_1(1)*(T_tank1(1)-T_air(1))*L_char_1(1)^3)/(nu_air(1)*alpha_air(1));
Ra_2(1)=(g*beta_2(1)*(T_tank2(1)-T_w(1))*L_char_2(1)^3)/(nu_w(1)*alpha_w(1));
Gr_1(1)=Ra_1(1)/(nu_air(1)/alpha_air(1));
Gr_2(1)=Ra_2(1)/Pr_w(1);
Re_air_o(1)=(rho_air_o(1)*vel_air*D_o)/mu_air_o(1);
%if statement to determine if water is hotter than air or vice-versa and
%apply appropriate correlation
if T_w(1)>T_air(1)
    %Nu_aw(1)=0.54*Ra_aw(1)^(1/4);           %equation 9.30 in Incropera & DeWitt
    Nu_aw(1)=0.15*Ra_aw(1)^(1/3);
elseif T_w(1)<T_air(1)
    Nu_aw(1)=0.52*Ra_aw(1)^(1/5);           %equation 9.32 in Incropera & DeWitt
else
    Nu_aw(1)=(0.54*Ra_aw(1)^(1/4)+0.52*Ra_aw(1)^(1/5))/2;
end
g_1(1)=(0.75*(nu_air(1)/alpha_air(1))^(1/2))/(0.609+1.221*(nu_air(1)/alpha_air(1))^(1/2)+1.238*(n
u_air(1)/alpha_air(1)))^(1/4);  %eqn 9.20 I&D
g_2(1)=(0.75*(Pr_w(1))^(1/2))/(0.609+1.221*(Pr_w(1))^(1/2)+1.238*(Pr_w(1)))^(1/4);  %eqn 9.20 I&D
Nu_1(1)=(4/3)*(Gr_1(1)/4)^(1/4)*g_1(1);         %eqn 9.21 I&D
Nu_2(1)=(4/3)*(Gr_2(1)/4)^(1/4)*g_2(1);         %eqn 9.21 I&D
%Nu_1(1)=(0.825+(0.387*Ra_1(1)^(1/6))/((1+(0.492/Pr_air(1))^(9/16))^(8/27)))^2; %equation 9.27
from Incropera & DeWitt
%Nu_2(1)=(0.825+(0.387*Ra_2(1)^(1/6))/((1+(0.492/Pr_w(1))^(9/16))^(8/27)))^2;
%Nu_1(1)=0.68+(0.67*Ra_1(1)^(1/4))/((1+(0.492/Pr_air(1))^(9/16))^(4/9));
%Nu_2(1)=0.68+(0.67*Ra_2(1)^(1/6))/((1+(0.492/Pr_w(1))^(9/16))^(4/9));
Nu_o(1)=0.3+(0.62*Re_air_o(1)^(1/2)*Pr_air_o(1)^(1/3))/(1+(0.4/Pr_air_o(1))^(2/3))^(1/4)*(1+(Re_a
ir_o(1)/282000)^(5/8))^(4/5); %eqn 7.54 from I&D
h_aw(1)=(Nu_aw(1)*k_air(1))/D_i;                    %W/m^2*K
h_i_1(1)=(Nu_1(1)*k_air(1))/L_char_1(1);                %W/m^2*K
h_i_2(1)=(Nu_2(1)*k_w(1))/L_char_2(1);                %W/m^2*K
h_o(1)=(Nu_o(1)*k_air_o(1))/D_o;                    %W/m^2*K
A_i_1(1)=4*V_air(1)/D_o+(pi/4)*D_o^2;       %m^2, inner heat transfer surface area b/w tank air
and tank
A_i_2(1)=0.00000001;        %m^2, inner heat transfer surface area b/w water and tank
A_o_1(1)=4*V_air(1)/D_i+(pi/4)*D_i^2;           %m^2, outer heat transfer surface area b/w tank
air and tank
A_o_2(1)=0.000001;           %m^2, outer heat transfer surface area b/w water and tank
A_ave_1(1)=(A_i_1(1)+A_o_1(1))/2;    %m^2, average of air-tank surface areas for conduction
resistance
A_ave_2(1)=(A_i_2(1)+A_o_2(1))/2;    %m^2, average of water-tank surface areas for conduction
resistance
UA_1(1)=1/((1/(h_i_1(1)*A_i_1(1)))+(th/(k_tank*A_ave_1(1)))+(1/(h_o(1)*A_o_1(1)))); %W/K, tank
air to ambient air UA
UA_2(1)=1/((1/(h_i_2(1)*A_i_2(1)))+(th/(k_tank*A_ave_2(1)))+(1/(h_o(1)*A_o_2(1)))); %W/K, tank
water to ambient air UA
R_mt_1(1)=A_i_1(1)/A_i_tot;
R_mt_2(1)=A_i_2(1)/A_i_tot;
m_tank1(1)=R_mt_1(1)*m_tank;
m_tank2(1)=R_mt_2(1)*m_tank;
%T_WH_out(1)=
```

```
%sprayed mist parameters
V_dot_spray_lpm=12;
V_dot_spray=V_dot_spray_lpm/60*10^-3; %L/min to m^3/s
%V_dot_spray=50/1000;
m_dot_spray=V_dot_spray*rho_w(1);
m_dot_spray_vec(1)=m_dot_spray;
D_droplet=50*10^-6;
V_drop=pi*D_droplet^3/6;
C_D=0.8;
N_dot=(6*V_dot_spray)/(pi*D_droplet^3);
A_droplet=pi*D_droplet^2;
rho_drop(1)=-3.9837E-03*T_w(1)^2+2.1274E+00*T_w(1)+7.1666E+02;
v_term(1)=sqrt((4*D_droplet*rho_w(1)*g)/(3*rho_air(1)*C_D));
drop_travel(1)=L_char_1(1);
travel_time(1)=drop_travel(1)/v_term(1);
N_droplets(1)=N_dot*travel_time(1);
m_drops(1)=N_droplets(1)*(pi*D_droplet^3/6)*rho_w(1);
Re_droplet(1)=(rho_air(1)*v_term(1)*D_droplet)/mu_air(1);
Pr_drop(1)=Pr_w(1);
mu_drop(1)=mu_w(1);
nu_drop(1)=nu_w(1);
k_drop(1)=k_w(1);
c_drop(1)=c_w(1);
alpha_drop(1)=alpha_w(1);
Nu_droplet(1)=2+0.6*Re_droplet(1)^(1/2)*Pr_drop(1)^(1/3);
h_droplet(1)=(Nu_droplet(1)*k_drop(1))/D_droplet;

T_drop_SR_in(1)=T_w(1);
T_air_SR(1)=T_air(1);
%T_drop_SR_out(1)=T_drop_SR_in(1)-
((h_droplet(1)*A_droplet*N_droplets(1))/(m_dot_spray*c_w(1)))*(T_drop_SR_in(1)-T_air_SR(1));
%T_drop_SR_out(1)=T_drop_SR_in(1)-
((h_droplet(1)*A_droplet*N_droplets(1)*60)/(m_drops(1)*c_w(1)))*(T_drop_SR_in(1)-T_air_SR(1));
tau(1)=(rho_w(1)*V_drop*c_w(1))/(h_droplet(1)*A_droplet);
T_drop_SR_out(1)=T_air_SR(1)+(T_drop_SR_in(1)-T_air_SR(1))*exp(-travel_time(1)/tau(1));
q_drop(1)=m_dot_spray_vec(1)*cv_air_vec(1)*(T_drop_SR_out(1)-T_drop_SR_in(1));
q_dot_drop(1)=N_dot*q_drop(1);
T_w_new(1)=T_w(1);

%timestep length & initialization of counter
deltat=1;                  %seconds, timestep
time=0;                  %seconds, time progression
i=2;

%minimum amount of water to leave in tank
min_water=10;               %kg

%tuning coefficients
coeff=-1;
HTE=1;
%AC=0.000001;
AC=1;
```

```
cont=1;
num_cycles=1;
maxcont=num_cycles*4;
beginstoretime=1;
storetime=99999999;
end_exp_time=999999999999;

%pulsed charging
pulsed_charging=0;
T_pulse_max=10;
T_pulse_min=2;
redflag=0;

%sprayed mist
spray_switch=0;
spray_switch2=spray_switch;

%recirculating pump power
 eta_recirc=0.75;
% if V_dot_spray<=17/60*10^-3
%     W_dot_recirc=(3.255012E+13*V_dot_spray^3+1.603239E+09*V_dot_spray^2-
2.307698E+05*V_dot_spray+9.805349E+00)/eta_recirc;
% elseif V_dot_spray>17/60*10^-3
%     W_dot_recirc=(1.049100E+12*V_dot_spray^3+2.342596E+07*V_dot_spray^2-
1.954453E+04*V_dot_spray+4.798752E+00)/eta_recirc;
% elseif spray_switch==0 && spray_switch2==0
%     W_dot_recirc=0;
% end
%W_dot_recirc=0;

%large nozzle
if spray_switch==1 && spray_switch2==1
    W_dot_recirc=(1.049100E+12*V_dot_spray^3+2.342596E+07*V_dot_spray^2-
1.954453E+04*V_dot_spray+4.798752E+00)/eta_recirc;
    %W_dot_recirc=(1.483852E+11*V_dot_spray^3-
1.799807E+08*V_dot_spray^2+1.544611E+05*V_dot_spray+1.932680E+02)/eta_recirc;
else
    W_dot_recirc=0;
end

%waste heat utilization
WH_exp_switch=0;
V_dot_WH_lpm=15;
m_dot_WH=V_dot_WH_lpm*rho_w(1)/60*10^-3; %flow rate of waste heat water in L/min convert to kg/s
m_dot_min=min(m_dot_spray,m_dot_WH);
T_WH_in_C=70;
T_WH_in=273.15+T_WH_in_C;
eta_HX=0.9;

%sprayed mist parameters - discharging
% N_dot2=(6*V_dot_spray_DC)/(pi*D_droplet^3);
% v_term2(1)=sqrt((4*D_droplet*rho_w(1)*g)/(3*rho_air(1)*C_D));
% travel_time2(1)=drop_travel(1)/v_term2(1);
% N_droplets2(1)=N_dot2*travel_time2(1);
```

```
% Re_droplet2(1)=(rho_w(1)*v_term(1)*D_droplet)/mu_w(1);
% Pr_droplet2=Pr_w(1);
% Nu_droplet2(1)=2+0.6*Re_droplet2(1)^(1/2)*Pr_droplet2^(1/3);
% h_droplet2(1)=(Nu_droplet2(1)*k_w(1))/D_droplet;

mode='charge';

%while (time<max_time-1)
while cont<=maxcont

    m_dot_p(i)=rho_w(i-1)*V_dot_pump;

    %call subroutine to calculate water discharge flowrate
    [V_dot_w_exp(i),V_dot_exp_LM(i),ploss(i),loss_check(i)]=glides_flow(real(P_air(i-
1)),num_jets,num_tanks,real(nu_w(i-1)),real(rho_w(i-1)));

    %if statement to check if we should be using sprayed mist during
    %charging
    if (spray_switch==1) && (mod(cont,4)==1)
        spray_coeff=1;
        m_dot_spray_vec(i)=m_dot_spray;
    elseif (spray_switch2==1) && (mod(cont,4)==3)
        spray_coeff=1;
        m_dot_spray_vec(i)=m_dot_spray;
    else
        spray_coeff=0;
        m_dot_spray_vec(i)=0;
    end

    %if statement to check if we should be using sprayed mist during
    %discharging
%     if (spray_switch2==1) && ((mod(cont,2)==1) && (mod(cont,4)==3))
%         spray_coeff2=1;
%     else
%         spray_coeff2=0;
%     end

    %if statement to set water mass flow rate to positive, negative, or
    %zero based on value of cont
    if (mod(cont,2)==1) && (mod(cont,4)==1)
        m_dot_w=m_dot_p(i);
        if pulsed_charging==1
            if (T_air(i-1)-T_amb>=T_pulse_max)
                m_dot_w=0;
                redflag = 1;
            end
            if (redflag==1) & (T_air(i-1)-T_amb>=T_pulse_min)
                m_dot_w=0;
            else
                redflag=0;
            end
        end
    elseif (mod(cont,2)==0)
        m_dot_w=0;
```

```
    elseif (mod(cont,2)==1) && (mod(cont,4)==3)
        %m_dot_w=-m_dot_p(i);
        m_dot_w=-V_dot_w_exp(i)*rho_w(i-1);
    end

    %governing physical equations
    m_dot_w_vec(i)=m_dot_w;
    time_vec(i)=time_vec(i-1)+deltat;
    V_air(i)=V_air(i-1)+coeff*(m_dot_w_vec(i)/rho_w(i-1))*deltat;
    T_air(i)=T_air(i-1)+(deltat/(m_air*cv_air_vec(i-1)))*(AC*-h_aw(i-1)*A_aw*(T_air(i-1)-T_w(i-
1))-HTE*AC*UA_1(i-1)*(T_air(i-1)-T_amb)-spray_coeff*q_dot_drop(i-1)-P_air(i-1)*((V_air(i)-
V_air(i-1))/deltat));
    %adiabatic air
    %T_air(i)=T_air(i-1)+(deltat/(m_air*cv_air_vec(i-1)))*(-P_air(i-1)*((V_air(i)-V_air(i-
1))/deltat));
    P_air(i)=(m_air*R_air*T_air(i))/V_air(i);
    %v_bar_air(i)=(V_air(i)/m_air)*M_air;
    %P_air(i)=(R_bar*T_air(i))/(v_bar_air(i)-
b)+(a/(v_bar_air(i)*(v_bar_air(i)+b)*T_air(i)^(1/2)));
    m_w(i)=m_w(i-1)+coeff*-1*m_dot_w_vec(i)*deltat;
    if m_dot_w>0
        T_w(i)=T_w(i-1)+(deltat/(m_w(i)*c_w(i-1)))*(AC*h_aw(i-1)*A_aw*(T_air(i-1)-T_w(i-1))-
AC*UA_2(i-1)*(T_w(i-1)-T_amb)+m_dot_w_vec(i)*c_w(i-1)*(T_w(i-1)-T_amb));
    elseif m_dot_w<0
        T_w(i)=T_w(i-1)+(deltat/(m_w(i)*c_w(i-1)))*(AC*h_aw(i-1)*A_aw*(T_air(i-1)-T_w(i-1))-
AC*UA_2(i-1)*(T_w(i-1)-T_amb));%+m_dot_w_vec(i)*c_w(i-1)*(T_w(i-1)-T_amb));
    else
        T_w(i)=T_w(i-1)+(deltat/(m_w(i)*c_w(i-1)))*(AC*h_aw(i-1)*A_aw*(T_air(i-1)-T_w(i-1))-
AC*UA_2(i-1)*(T_w(i-1)-T_amb));
    end
    T_tank1(i)=T_tank1(i-1)+(deltat/(m_tank1(i-1)*c_tank))*(HTE*AC*h_i_1(i-1)*A_i_1(i-
1)*(T_air(i-1)-T_tank1(i-1))-AC*h_o(i-1)*A_o_1(i-1)*(T_tank1(i-1)-T_amb));
    T_tank2(i)=T_tank2(i-1)+(deltat/(m_tank2(i-1)*c_tank))*(AC*h_i_2(i-1)*A_i_2(i-1)*(T_w(i-1)-
T_tank2(i-1))-AC*h_o(i-1)*A_o_2(i-1)*(T_tank2(i-1)-T_amb));

    %update HT areas
    A_i_1(i)=4*V_air(i)/D_o+(pi/4)*D_o^2;        %m^2, inner heat transfer surface area b/w tank
air and tank
    A_i_2(i)=A_i_tot-A_i_1(i);        %m^2, inner heat transfer surface area b/w water and tank
    A_o_1(i)=4*V_air(i)/D_i+(pi/4)*D_i^2;           %m^2, outer heat transfer surface area b/w
tank air and tank
    A_o_2(i)=A_o_tot-A_o_1(i);           %m^2, outer heat transfer surface area b/w water and
tank
    A_ave_1(i)=(A_i_1(i)+A_o_1(i))/2;    %m^2, average of air-tank surface areas for conduction
resistance
    A_ave_2(i)=(A_i_2(i)+A_o_2(i))/2;    %m^2, average of water-tank surface areas for conduction
resistance

    T_f_aw(i)=(T_w(i)+T_air(i))/2;
    T_f_1(i)=(T_air(i)+T_tank1(i))/2;
    T_f_2(i)=(T_w(i)+T_tank2(i))/2;
    T_f_o(i)=(T_tank1(i)+T_tank2(i)+T_amb)/3;

cv_air_vec(i)=R_air*((alpha+beta_cv*T_air(i)+gamma*T_air(i)^2+delta*T_air(i)^3+epsilon*T_air(i)^4
```

```
)-1);

    cp_air_vec(i)=cv_air_vec(i)+R_air;
    k_air(i)=0.009748221+5.27354*10^-10*P_air(i)+5.5243*10^-5*T_f_1(i);
    %k_air(i) = CoolProp.PropsSI('L','P',P_air(i),'T',T_air(i),'Air');
    mu_air(i)=6.93093*10^-6+2.35465*10^-13*P_air(i)+3.85177*10^-8*T_f_1(i);
    rho_air(i)=(V_air(i)/m_air)^-1;
    nu_air(i)=mu_air(i)/rho_air(i);
    alpha_air(i)=k_air(i)/(rho_air(i)*cp_air_vec(i));
    Pr_air(i)=nu_air(i)/alpha_air(i);

    mu_air_o(i)=6.93093*10^-6+2.35465*10^-13*P_atm+3.85177*10^-8*T_f_o(i);
    rho_air_o(i)=P_atm/(R_air*T_f_o(i));               %using IG law
    nu_air_o(i)=mu_air_o(i)/rho_air_o(i);
    k_air_o(i)=0.009748221+5.27354*10^-10*P_atm+5.5243*10^-5*T_f_o(i);

cv_air_o(i)=R_air*((alpha+beta_cv*T_f_o(i)+gamma*T_f_o(i)^2+delta*T_f_o(i)^3+epsilon*T_f_o(i)^4)-
1);
    cp_air_o(i)=cv_air_o(i)+R_air;
    alpha_air_o(i)=k_air_o(i)/(rho_air_o(i)*cp_air_o(i));
    Pr_air_o(i)=nu_air_o(i)/alpha_air_o(i);

    rho_w(i)=-3.9837E-03*T_w(i)^2+2.1274E+00*T_w(i)+7.1666E+02;
    c_w(i)=-3.0788E-04*T_w(i)^3+3.0602E-01*T_w(i)^2-1.0086E+02*T_w(i)+1.5207E+04;
    mu_w(i)=-3.7024E-09*T_w(i)^3+3.7182E-06*T_w(i)^2-1.2513E-03*T_w(i)+1.4156E-01;
    k_w(i)=-7.0674E-06*T_w(i)^2+5.6853E-03*T_w(i)-4.5602E-01;
    nu_w(i)=mu_w(i)/rho_w(i);
    alpha_w(i)=k_w(i)/(rho_w(i)*c_w(i));
    Pr_w(i)=nu_w(i)/alpha_w(i);

    L_char_1(i)=R_mt_1(i-1)*L;
    L_char_2(i)=R_mt_2(i-1)*L;
    beta_aw(i)=1/T_f_aw(i);
    beta_1(i)=1/T_f_1(i);
    beta_2(i)=1/T_f_2(i);
    Ra_aw(i)=(g*beta_aw(i)*(T_w(i)-T_air(i))*D_i^3)/(nu_air(i)*alpha_air(i));
    Ra_1(i)=(g*beta_1(i)*(T_tank1(i)-T_air(i))*L_char_1(i)^3)/(nu_air(i)*alpha_air(i));
    Ra_2(i)=(g*beta_2(i)*(T_tank2(i)-T_w(i))*L_char_2(i)^3)/(nu_w(i)*alpha_w(i));
    Gr_1(i)=Ra_1(i)/(nu_air(i)/alpha_air(i));
    Gr_2(i)=Ra_2(i)/Pr_w(i);
    Re_air_o(i)=(rho_air_o(i)*vel_air*D_o)/mu_air_o(i);

    %if statement to determine if air is hotter than air or vice-versa and
    %apply appropriate correlation
    if T_w(i)>T_air(i)
        %Nu_aw(i)=0.54*Ra_aw(i)^(1/4);           %equation 9.30 in Incropera & DeWitt
        Nu_aw(i)=0.15*Ra_aw(i)^(1/3);
    elseif T_w(i)<T_air(i)
        Nu_aw(i)=0.52*Ra_aw(i)^(1/5);           %equation 9.32 in Incropera & DeWitt
    else
        Nu_aw(i)=(0.54*Ra_aw(i)^(1/4)+0.52*Ra_aw(i)^(1/5))/2;
    end
%     if T_w(i)>T_air(i)
%         Nu_aw(i)=0.54*Ra_aw(i)^(1/4);           %equation 9.30 in Incropera & DeWitt
```

```
%     elseif T_w(i)<T_air(i)
%         Nu_aw(i)=0.54*Ra_aw(i)^(1/4);           %equation 9.32 in Incropera & DeWitt
%     else
%         Nu_aw(i)=0.54*Ra_aw(i)^(1/4);
%     end

g_1(i)=(0.75*(nu_air(i)/alpha_air(i))^(1/2))/(0.609+1.221*(nu_air(i)/alpha_air(i))^(1/2)+1.238*(n
u_air(i)/alpha_air(i)))^(1/4);   %eqn 9.20 I&D
    g_2(i)=(0.75*(Pr_w(i))^(1/2))/(0.609+1.221*(Pr_w(i))^(1/2)+1.238*(Pr_w(i)))^(1/4);       %eqn
9.20 I&D
    Nu_1(i)=(4/3)*(Gr_1(i)/4)^(1/4)*g_1(i);             %eqn 9.21 I&D
    Nu_2(i)=(4/3)*(Gr_2(i)/4)^(1/4)*g_2(i);             %eqn 9.21 I&D
    %Nu_1(i)=(0.825+(0.387*Ra_1(i)^(1/4))/((1+(0.492/Pr_air(i))^(9/16))^(8/27)))^2; %equation
9.27 from Incropera & DeWitt
    %Nu_2(i)=(0.825+(0.387*Ra_2(i)^(1/4))/((1+(0.492/Pr_w(i))^(9/16))^(8/27)))^2;
    %Nu_1(i)=0.68+(0.67*Ra_1(i)^(1/4))/((1+(0.492/Pr_air(i))^(9/16))^(4/9));
    %Nu_2(i)=0.68+(0.67*Ra_2(i)^(1/6))/((1+(0.492/Pr_w(i))^(9/16))^(4/9));

Nu_o(i)=0.3+(0.62*Re_air_o(i)^(1/2)*Pr_air_o(i)^(1/3))/(1+(0.4/Pr_air_o(i))^(2/3))^(1/4)*(1+(Re_a
ir_o(i)/282000)^(5/8))^(4/5);
    h_aw(i)=(Nu_aw(i)*k_air(i))/D_i;                    %W/m^2*K
    h_i_1(i)=(Nu_1(i)*k_air(i))/L_char_1(i);                %W/m^2*K
    h_i_2(i)=(Nu_2(i)*k_w(i))/L_char_2(i);                %W/m^2*K
    h_o(i)=(Nu_o(i)*k_air_o(i))/D_o;                    %W/m^2*K
    UA_1(i)=1/((1/(h_i_1(i)*A_i_1(i-1)))+(th/(k_tank*A_ave_1(i-1)))+(1/(h_o(i)*A_o_1(i-1))));
%W/K, tank air to ambient air UA
    UA_2(i)=1/((1/(h_i_2(i)*A_i_2(i-1)))+(th/(k_tank*A_ave_2(i-1)))+(1/(h_o(i)*A_o_2(i-1))));
%W/K, tank water to ambient air UA

    R_mt_1(i)=A_i_1(i)/A_i_tot;
    R_mt_2(i)=A_i_2(i)/A_i_tot;

    m_tank1(i)=R_mt_1(i)*m_tank;
    m_tank2(i)=R_mt_2(i)*m_tank;

    %sprayed mist calculations - charging
    v_term(i)=sqrt((4*D_droplet*rho_w(i)*g)/(3*rho_air(i)*C_D));
    drop_travel(i)=L_char_1(i);
    travel_time(i)=L_char_1(i)/v_term(i);
    N_droplets(i)=N_dot*travel_time(i);
    Re_droplet(i)=(rho_air(i)*v_term(i)*D_droplet)/mu_air(i);
    rho_drop(i)=-3.9837E-03*((T_drop_SR_in(i-1)+T_drop_SR_out(i-
1))/2)^2+2.1274E+00*((T_drop_SR_in(i-1)+T_drop_SR_out(i-1))/2)+7.1666E+02;
    mu_drop(i)=-3.7024E-09*((T_drop_SR_in(i-1)+T_drop_SR_out(i-1))/2)^3+3.7182E-
06*((T_drop_SR_in(i-1)+T_drop_SR_out(i-1))/2)^2-1.2513E-03*((T_drop_SR_in(i-1)+T_drop_SR_out(i-
1))/2)+1.4156E-01;
    nu_drop(i)=mu_drop(i)/rho_drop(i);
    k_drop(i)=-7.0674E-06*((T_drop_SR_in(i-1)+T_drop_SR_out(i-1))/2)^2+5.6853E-
03*((T_drop_SR_in(i-1)+T_drop_SR_out(i-1))/2)-4.5602E-01;
    c_drop(i)=-3.0788E-04*((T_drop_SR_in(i-1)+T_drop_SR_out(i-1))/2)^3+3.0602E-
01*((T_drop_SR_in(i-1)+T_drop_SR_out(i-1))/2)^2-1.0086E+02*((T_drop_SR_in(i-1)+T_drop_SR_out(i-
1))/2)+1.5207E+04;
    alpha_drop(i)=k_drop(i)/(rho_drop(i)*c_drop(i));
    Pr_drop(i)=nu_drop(i)/alpha_drop(i);
```

```
    Nu_droplet(i)=2+0.6*Re_droplet(i)^(1/2)*Pr_drop(i)^(1/3);
    h_droplet(i)=(Nu_droplet(i)*k_drop(i))/D_droplet;

    %sprayed mist calculations - discharging
%     v_term2(i)=sqrt((4*D_droplet*rho_w(1)*g)/(3*rho_air(i)*C_D));
%     travel_time2(i)=drop_travel(i)/v_term2(i);
%     N_droplets2(i)=N_dot2*travel_time2(i);
%     Re_droplet2(i)=(rho_w(1)*v_term(i)*D_droplet)/mu_w(1);
%     Nu_droplet2(i)=2+0.6*Re_droplet2(i)^(1/2)*Pr_droplet2^(1/3);
%     h_droplet2(i)=(Nu_droplet2(i)*k_w(1))/D_droplet;

    %subroutine to calculate spray inlet/outlet temp and air temp change
    %these are guesses

    %subroutine to implement waste heat utilization during expansion
    if (WH_exp_switch==1) && (mod(cont,4)==3)
        %j=1;
        T_drop_SR_in(i)=T_w(i)+eta_HX*(m_dot_min/m_dot_spray)*(T_WH_in-T_w(i));
        T_WH_out(i)=T_WH_in-eta_HX*(m_dot_min/m_dot_WH)*(T_WH_in-T_w(i));
        %j=j+1;
    else
        %j=1;
        T_drop_SR_in(i)=T_w(i);
        T_WH_out(i)=T_WH_in;
        %j=j+1;
    end

    %T_air_SR(i-1)=T_air(i);
    if spray_coeff==1
        %T_air_SR(i)=T_air_SR(i-
1)+((h_droplet(i)*A_droplet*N_droplets(i)*deltat)/(m_air*cv_air_vec(i)))*(T_drop_SR_in(i)-
T_air_SR(i-1));
        %T_drop_SR_out(i)=T_drop_SR_in(i)-
((h_droplet(i)*A_droplet*N_droplets(i))/(m_dot_spray_vec(i)*c_w(i)))*(T_drop_SR_in(i)-T_air_SR(i-
1));
        tau(i)=(rho_w(i)*V_drop*c_w(i))/(h_droplet(i)*A_droplet);
        T_drop_SR_out(i)=T_air(i)+(T_drop_SR_in(i)-T_air(i))*exp(-travel_time(i)/tau(i));
        %q_drop(i)=m_dot_spray_vec(i)*c_w(i)*(T_drop_SR_out(i)-T_drop_SR_in(i));
        q_drop(i)=V_drop*rho_drop(i)*c_drop(i)*(T_drop_SR_out(i)-T_drop_SR_in(i));
        %q_dot_drop(i)=N_dot*q_drop(i);
        q_dot_drop(i)=(N_droplets(i)/travel_time(i))*q_drop(i);
        %q_dot_drop(i)=(N_droplets(i)/deltat)*q_drop(i);
        T_air_SR(i)=T_air_SR(i-1)-(q_drop(i)*deltat)/(m_air*cv_air_vec(i));
    else
        tau(i)=(rho_w(i)*V_drop*c_w(i))/(h_droplet(i)*A_droplet);
        T_drop_SR_out(i)=T_drop_SR_in(i);
        T_air_SR(i)=T_air_SR(i-1);
        %q_drop(i)=m_dot_spray_vec(i)*c_w(i)*(T_drop_SR_out(i)-T_drop_SR_in(i));
        q_drop(i)=V_drop*rho_drop(i)*c_drop(i)*(T_drop_SR_out(i)-T_drop_SR_in(i));
        %q_dot_drop(i)=N_dot*q_drop(i);
        q_dot_drop(i)=(N_droplets(i)/travel_time(i))*q_drop(i);
        %q_dot_drop(i)=(N_droplets(i)/deltat)*q_drop(i);
    end
```

```
    %calculate new water temperature after mixing

%T_w_new(i)=(m_w(i)*T_w(i)+m_dot_spray_vec(i)*deltat*T_drop_SR_out(i))/(m_w(i)+m_dot_spray_vec(i)
*deltat);

T_w_new(i)=(m_w(i)*c_w(i)*T_w(i)+m_dot_spray_vec(i)*tau(i)*c_drop(i)*T_drop_SR_out(i))/((m_w(i)+m
_dot_spray_vec(i)*tau(i))*c_w(i));

%T_w_new(i)=(m_w(i)*T_w(i)+m_dot_spray_vec(i)*deltat*T_drop_SR_out(i))/(m_w(i)+m_dot_spray_vec(i)
*travel_time(i));
    T_w(i)=T_w_new(i);

    %series of if statement to determine what current process is and update
    %cont in order to set correct water mass flow rate, also stores time at
    %which process changes occur
    if (P_air(i)>P_max) && (mod(cont,4)==1) && (P_air(i)>P_air(i-1)) && (V_air(i)<V_air(i-1))
%checks to see if in compression mode & pressure has reached max
        cont=cont+1;
        storetime=time;
        mode='pause';
    end

    if (time>storetime+pausetime) && (mod(cont,2)==0) %&& (P_air(i)<=P_air(i-1))    %checks to
see if paused & pause period has expired
       cont=cont+1;
       begin_exp_time=time;
       storetime_2=storetime;
       storetime=99999999999;
       mode='discharge';
    end

    if (m_w(i)<min_water) && (mod(cont,4)==3) && (P_air(i)<P_air(i-1)) && (V_air(i)>V_air(i-1))
%checks to see if in expansion mode & water almost out
        cont=cont+1;
        end_exp_time=time;
        end_exp_time_2=end_exp_time;
        mode='pause';
    end


    if (time>end_exp_time+pausetime) && (mod(cont,2)==0) %&& (P_air(i)>P_air(i-1))
%check to see if paused & pause period has expired
        cont=cont+1;
        end_exp_pause=time;
        if maxcont-cont>0
            beginstoretime=end_exp_pause;
        end
        end_exp_time=99999999;
    end

    %update time and i counter
    i=i+1;
    time=time+deltat;
end
```

```
Q_w_1=-h_aw.*A_aw.*(T_air-T_w);
Q_amb_1=-UA_1.*(T_air-T_amb);
Q_air_net=Q_w_1+Q_amb_1;

spec_vol=V_air/m_air;

%calculate droplet Biot number
Bi=(h_droplet.*(D_droplet./6))./k_drop;

%calculate heat input during expansion
heat_period=begin_exp_time+3:end_exp_time_2;
heat_time=1:length(heat_period);
heat_input_rate=m_dot_WH.*c_w(1).*(T_WH_in-T_WH_out(heat_period));
heat_input=real(trapz(heat_period,heat_input_rate));
heat_input_kJ=heat_input/1000;

heat_input_rate2=m_dot_min.*c_w(1).*(T_w(heat_period)-T_drop_SR_in(heat_period));
heat_input_2=real(-trapz(heat_time,heat_input_rate2));
heat_input_2_kJ=heat_input_2/1000;

heat_input_3=real(-trapz(heat_time,q_dot_drop(heat_period)));
heat_input_3_kJ=heat_input_3/1000;

%calculate spray heat transfer coefficients
UA_spray=(h_droplet.*N_droplets.*A_droplet)/1000;

%truncate all vectors
pr=1:i-1;
A_ave_1=A_ave_1(pr);
A_ave_2=A_ave_2(pr);
A_i_1=A_i_1(pr);
A_i_2=A_i_2(pr);
A_o_1=A_o_1(pr);
A_o_2=A_o_2(pr);
alpha_air=alpha_air(pr);
alpha_air_o=alpha_air_o(pr);
alpha_w=alpha_w(pr);
beta_1=beta_1(pr);
beta_2=beta_2(pr);
beta_aw=beta_aw(pr);
c_w=c_w(pr);
cp_air_o=cp_air_o(pr);
cp_air_vec=cp_air_vec(pr);
cv_air_o=cv_air_o(pr);
cv_air_vec=cv_air_vec(pr);
drop_travel=drop_travel(pr);
g_1=g_1(pr);
g_2=g_2(pr);
Gr_1=Gr_1(pr);
Gr_2=Gr_2(pr);
h_aw=h_aw(pr);
h_droplet=h_droplet(pr);
%h_droplet2=h_droplet2(pr);
```

```
h_i_1=h_i_1(pr);
h_i_2=h_i_2(pr);
h_o=h_o(pr);
k_air=k_air(pr);
k_air_o=k_air_o(pr);
k_w=k_w(pr);
L_char_1=L_char_1(pr);
L_char_2=L_char_2(pr);
loss_check=loss_check(pr);
m_dot_p=m_dot_p(pr);
m_dot_w_vec=m_dot_w_vec(pr);
m_tank1=m_tank1(pr);
m_tank2=m_tank2(pr);
m_w=m_w(pr);
mu_air=mu_air(pr);
mu_air_o=mu_air_o(pr);
mu_w=mu_w(pr);
N_droplets=N_droplets(pr);
%N_droplets2=N_droplets2(pr);
Nu_1=Nu_1(pr);
Nu_2=Nu_2(pr);
nu_air=nu_air(pr);
nu_air_o=nu_air_o(pr);
Nu_aw=Nu_aw(pr);
Nu_droplet=Nu_droplet(pr);
%Nu_droplet2=Nu_droplet2(pr);
Nu_o=Nu_o(pr);
nu_w=nu_w(pr);
P_air=P_air(pr);
ploss=ploss(pr);
Pr_air=Pr_air(pr);
Pr_air_o=Pr_air_o(pr);
Pr_drop=Pr_drop(pr);
Pr_w=Pr_w(pr);
Q_air_net=Q_air_net(pr);
Q_amb_1=Q_amb_1(pr);
Q_w_1=Q_w_1(pr);
R_mt_1=R_mt_1(pr);
R_mt_2=R_mt_2(pr);
Ra_1=Ra_1(pr);
Ra_2=Ra_2(pr);
Ra_aw=Ra_aw(pr);
Re_air_o=Re_air_o(pr);
Re_droplet=Re_droplet(pr);
%Re_droplet2=Re_droplet2(pr);
rho_air=rho_air(pr);
rho_air_o=rho_air_o(pr);
rho_w=rho_w(pr);
spec_vol=spec_vol(pr);
T_air=T_air(pr);
T_f_1=T_f_1(pr);
T_f_2=T_f_2(pr);
T_f_aw=T_f_aw(pr);
T_f_o=T_f_o(pr);
```

```
T_tank1=T_tank1(pr);
T_tank2=T_tank2(pr);
T_w=T_w(pr);
time_vec=time_vec(pr);
travel_time=travel_time(pr);
%travel_time2=travel_time2(pr);
UA_1=UA_1(pr);
UA_2=UA_2(pr);
V_air=V_air(pr);
v_bar_air=v_bar_air(pr);
V_dot_exp_LM=V_dot_exp_LM(pr);
V_dot_w_exp=V_dot_w_exp(pr);
v_term=v_term(pr);
%v_term2=v_term2(pr);
m_dot_spray_vec=m_dot_spray_vec(pr);
T_air_SR=T_air_SR(pr);
T_drop_SR_in=T_drop_SR_in(pr);
T_drop_SR_out=T_drop_SR_out(pr);
rho_drop=rho_drop(pr);
Pr_drop=Pr_drop(pr);
mu_drop=mu_drop(pr);
nu_drop=nu_drop(pr);
k_drop=k_drop(pr);
c_drop=c_drop(pr);
alpha_drop=alpha_drop(pr);
q_drop=q_drop(pr);
T_w_new=T_w_new(pr);
tau=tau(pr);
Bi=Bi(pr);
q_dot_drop=q_dot_drop(pr);
T_WH_out=T_WH_out(pr);


if cont >= 4
    charge_time=(storetime_2-beginstoretime)/60;
    power_time=(end_exp_time_2-begin_exp_time)/60;
end

%get rid of imaginary parts of results
P_air=real(P_air);
T_air=real(T_air);
T_w=real(T_w);
T_tank1=real(T_tank1);
T_tank2=real(T_tank2);
V_air=real(V_air);
m_w=real(m_w);
m_dot_w_vec=real(m_dot_w_vec);
Q_w_1=real(Q_w_1);
Q_amb_1=real(Q_amb_1);
Q_air_net=real(Q_air_net);

% disp(RTE_ind)
% disp(RTE_act)
% disp(SE_ind)
```

```
% disp(SE_act)

%series of plots
if deltat==1
    pr2=pr(beginstoretime:end);
else
    pr2=pr(1:end);
end
subplot(2,2,1)
plot(time_vec(pr2),P_air(pr2))
title('P_a')
xlabel('time [s]')
ylabel('Pressure [Pa]')

%time_vec(1:length(time_vec(beginstoretime:end)))

subplot(2,2,2)
plot(time_vec(pr2),T_air(pr2)-273.15,time_vec(pr2),T_w(pr2)-273.15,time_vec(pr2),T_tank1(pr2)-
273.15,time_vec(pr2),T_tank2(pr2)-273.15)
title('Temperatures')
legend('T_a','T_w','T_t_1','T_t_2')
xlabel('Time [s]')
ylabel('Temperature [K]')

subplot(2,2,3)
plot(time_vec(pr2),V_air(pr2))
title('Air Volume')
xlabel('Time [s]')
ylabel('Volume [m^3]')

subplot(2,2,4)
plot(time_vec(pr2),m_w(pr2))
title('Mass of Water')
xlabel('Time [s]')
ylabel('Mass [kg]')
figure
%
% plot(time_vec,m_dot_w_vec)
% title('Mass Flow Rate of Water')
% xlabel('Time [s]')
% ylabel('Mass Flow Rate [kg/s]')
% figure
%
plot(V_air(pr2),P_air(pr2))
title('p-V Diagram')
xlabel('Volume [m^3]')
ylabel('Pressure [Pa]')
%figure

% subplot(3,1,1)
% plot(time_vec(pr2),Q_amb_1(pr2))
% title('Air to ambient heat transfer rate')
% xlabel('time [s]')
% ylabel('Heat Rate [W]')
```

```
%
% subplot(3,1,2)
% plot(time_vec(pr2),Q_w_1(pr2))
% title('Air to water heat transfer rate')
% xlabel('time [s]')
% ylabel('Heat Rate [W]')
%
% subplot(3,1,3)
% plot(time_vec(pr2),Q_air_net(pr2))
% title('Air net heat transfer rate')
% xlabel('time [s]')
% ylabel('Heat Rate [W]')

%calculate efficiencies and specific energies (make sure max time & pause time are set to only
get through one full cycle)
%N=5130;
eta_carnot=1-(T_amb/T_WH_in);
if cont >= 4
    if WH_exp_switch==0
        heat_in=heat_input_kJ;
    else
        heat_in=heat_input_3_kJ;
    end

[RTE_act,RTE_ind,RTE_ex_ind,RTE_ex_elec,SE_act,SE_ind,power,I,exp_comp_loss,pump_losses,motor_los
ses,turb_losses,gen_losses,N_turb,W_ind_in,W_ind_out,W_act_in,W_act_in2,W_act_out,W_act_out2,W_re
circ_total,Q_ex_in]=RTEcalc6(P_air,ploss,V_air,V_dot_w_exp,rho_w,time_vec,beginstoretime,storetim
e_2,begin_exp_time,end_exp_time_2,m_air,W_dot_recirc,heat_in,eta_carnot);
    sum_check=exp_comp_loss+pump_losses+motor_losses+turb_losses+gen_losses+RTE_act;

    %calculate number for config 3 pie chart
%     total_in=-W_act_in2+W_recirc_total+Q_ex_in;
%     heat_in_slice=Q_ex_in/total_in;
%     elec_in_slice=(-W_act_in2+W_recirc_total)/total_in;
%     pump_loss_slice=abs((W_act_in-W_ind_in))/total_in;
%     recirc_pump_loss_slice=W_recirc_total/total_in;
%     motor_loss_slice=abs((W_act_in2-W_act_in))/total_in;
%
in_check=heat_in_slice+elec_in_slice+pump_loss_slice+recirc_pump_loss_slice+motor_loss_slice;
%
%     total_out=W_ind_out;
%     elec_out_slice=W_act_out2/total_in;
%     turbine_loss_slice=(W_ind_out-W_act_out)/total_in;
%     generator_loss_slice=(W_act_out-W_act_out2)/total_in;
%     out_check=elec_out_slice+turbine_loss_slice+generator_loss_slice;

    total_in=-W_act_in2+Q_ex_in;
    inner_pie=Q_ex_in+(-W_act_in2);
    elec_in_slice=-W_act_in2/total_in;
    heat_in_slice=Q_ex_in/total_in;

    PL=abs((W_act_in-W_ind_in));
    ML=abs((W_act_in2-W_act_in));
    TL=W_ind_out-W_act_out;
```

```
    GL=W_act_out-W_act_out2;
    outer_pie=PL+ML+TL+GL+W_act_out2+W_recirc_total;
    PL_slice=PL/outer_pie;
    ML_slice=ML/outer_pie;
    TL_slice=TL/outer_pie;
    GL_slice=GL/outer_pie;
    recirc_pie=W_recirc_total/outer_pie;
    elec_out_slice=W_act_out2/outer_pie;

    %calculate electric fraction of input energy
    elec_frac=-W_act_in2/heat_input_3;

    %calculate efficiencies
    eta_electric=RTE_act;
    eta_ind=RTE_ind;

    circ_pump_loss=1-sum_check;
    if exp_comp_loss>=0 %&& circ_pump_loss>0.005
        figure
        if sum_check<1

RTEdata=[RTE_act,exp_comp_loss,pump_losses,motor_losses,turb_losses,gen_losses,circ_pump_loss];
            explode=[1,0,0,0,0,0,0];
            RTElabels={'RTE: ';'exp/comp losses: ';'pump losses: ';'motor losses: ';'turb losses:
';'gen losses: ';'recirc pump losses: '};
        elseif sum_check>=1
            RTEdata=[RTE_act,exp_comp_loss,pump_losses,motor_losses,turb_losses,gen_losses];
            explode=[1,0,0,0,0,0];
            RTElabels={'RTE: ';'exp/comp losses: ';'pump losses: ';'motor losses: ';'turb losses:
';'gen losses: '};
        end
        pie=pie(RTEdata,explode);
        pieText = findobj(pie,'Type','text'); % text object handles
        percentValues = get(pieText,'String'); % percent values
        combinedstrings = strcat(RTElabels,percentValues); % strings and percent values
        set(pieText(1),'String',combinedstrings(1))
        set(pieText(2),'String',combinedstrings(2))
        set(pieText(3),'String',combinedstrings(3))
        set(pieText(4),'String',combinedstrings(4))
        set(pieText(5),'String',combinedstrings(5))
        set(pieText(6),'String',combinedstrings(6))
        if sum_check<1
            set(pieText(7),'String',combinedstrings(7))
        end
    end
end

% figure
%
% %plot dT_air/dt
% dT_air=diff(T_air);
% dt=diff(time_vec);
% dT_airdt=dT_air./dt;
% dT_airdt=[0;dT_airdt];
```

```
% plot(time_vec,dT_airdt)

% subplot(2,1,1)
% plot(time_vec,UA_1)
% title('Air Heat Transfer Coefficient')
% xlabel('time [s]')
% ylabel('HTC [W/K]')

% subplot(2,1,2)
% plot(time_vec,UA_2)
% title('Water Heat Transfer Coefficient')
% xlabel('time [s]')
% ylabel('HTC [W/K]')
% figure

% subplot(2,2,1)
% plot(time_vec,A_i_1)
% title('Air Inner Heat Transfer Area')
% xlabel('time [s]')
% ylabel('Area [m^2]')
%
% subplot(2,2,2)
% plot(time_vec,A_o_1)
% title('Air Outer Heat Transfer Area')
% xlabel('time [s]')
% ylabel('Area [m^2]')
%
% subplot(2,2,3)
% plot(time_vec,A_i_2)
% title('Water Inner Heat Transfer Area')
% xlabel('time [s]')
% ylabel('Area [m^2]')
%
% subplot(2,2,4)
% plot(time_vec,A_o_2)
% title('Water Outer Heat Transfer Area')
% xlabel('time [s]')
% ylabel('Area [m^2]')


%figure

% % subplot(2,1,1)
% % plot(time_vec,cv_air*ones(max_time,1),time_vec,cv_air_vec)
% % title('Evaluation of constant cv assumption')
% % xlabel('Time [s]')
% % ylabel('c_v [J/kg*K]')
% % legend('const c_v','c_v function of T_a')
% % %
% % subplot(2,1,2)
% % plot(time_vec,T_air,time_vec,T_air_const_cv)
% % title('Effect of constant cv assumption on Air Temp')
% % xlabel('Time [s]')
```

```
% % ylabel('T_air [K]')
% % legend('const c_v','c_v function of T_air')
```

Published with MATLAB® R2016b

Supporting Function 1

This function incorporates the characteristic curves and equations of the auxiliary components (pump/motor, turbine/generator) in order to calculate the roundtrip electrical efficiency and energy density and itemized losses. Inputs from the main script are the air pressure, volume, flow rate. Outputs are the electrical, indicated, and exergetic roundtrip efficiency and energy density, as well as the power and current profiles, and itemized system losses.

```
function
[RTE_act,RTE_ind,RTE_ex_ind,RTE_ex_elec,SE_act,SE_ind,power,I,exp_comp_loss,pump_losses,motor_los
ses,turb_losses,gen_losses,N_turb,W_ind_in,W_ind_out,W_act_in,W_act_in2,W_act_out,W_act_out2,W_re
circ_total,Q_ex_in]=RTEcalc6(P_air,P_loss,V_air,V_dot_exp_w,rho_w,time_vec,beginstoretime,storeti
me,begin_exp_time,end_exp_time,m_air,W_dot_recirc,heat_input_2_kJ,eta_carnot)

BST=time_vec==beginstoretime;
ST=time_vec==storetime;
charge_process=find(time_vec==beginstoretime):find(time_vec==storetime);
discharge_process=find(time_vec==begin_exp_time):find(time_vec==end_exp_time);

%pump
eta_pump_vec=(-
0.00071.*(P_air(charge_process)./10.^5).^2+0.15083.*(P_air(charge_process)./10.^5)+85.5)./100;
eta_motor_vec=(-
0.00023.*(P_air(charge_process)./10.^5).^2+0.08650.*(P_air(charge_process)./10.^5)+85.3)./100;

%turbine
%x=0.46;
D_nozzle=0.00143;
cv_nozzle=0.98;
PCD=0.4572;
%PCD=0.3;
%vel_jet2=V_dot_exp_w(begin_exp_time:end_exp_time)./(pi/4*D_nozzle^2);
%N=6250;
%N=4000;
vel_jet=cv_nozzle*sqrt(2*9.8.*(P_air(discharge_process)-
P_loss(discharge_process).*10^5)./(rho_w(discharge_process).*9.8));
%vel_bucket=65;
vel_bucket=0.46*vel_jet;
x=vel_bucket./vel_jet;
N_turb=(vel_jet.*60.*x)./(pi.*PCD);
pulley_ratio=1;
N=pulley_ratio*N_turb;
zeta=0.88;
gamma=15*pi/180;
%eta_turb=-(4*(x-0.5)^2-0.9);
eta_turb=2.*x.*(1-x).*(1+zeta*cos(gamma));
%eta_turb=eta_turb(begin_exp_time:end_exp_time);

% %generator
% eta_gen=0.9*ones(max_time,1);
% eta_gen=eta_gen(begin_exp_time:end_exp_time);

%compression/expansion losses
R_air=286.987;
T_amb=298.15;
%W_in_iso=-
m_air*P_air(beginstoretime)*spec_vol(beginstoretime)*log(P_air(storetime)/P_air(beginstoretime));
```

```
%W_out_iso=-
P_air(begin_exp_time)*V_air(begin_exp_time)*log(P_air(end_exp_time)/P_air(begin_exp_time));
%W_out_iso=-
m_air*P_air(storetime)*spec_vol(storetime)*log(P_air(beginstoretime)/P_air(storetime));
W_in_iso=-m_air*R_air*T_amb*log(P_air(ST)/P_air(BST));
W_out_iso=-m_air*R_air*T_amb*log(P_air(BST)/P_air(ST));

%indicated work/efficiency
dV_dt=diff(V_air)./diff(time_vec);
dV_dt=[dV_dt(1); dV_dt];
dV_dt_comp=dV_dt(charge_process);
dV_dt_comp(1:3)=dV_dt_comp(4);
dV_dt_exp=dV_dt(discharge_process);
dV_dt_exp(3)=dV_dt_exp(4)+3E-8;
dV_dt_exp(2)=dV_dt_exp(3)+3E-8;
dV_dt_exp(1)=dV_dt_exp(2)+3E-8;
W_dot_ind_in=P_air(charge_process).*dV_dt_comp;
W_dot_ind_out=P_air(discharge_process).*dV_dt_exp;
%W_ind_in=trapz(time_vec(charge_process),W_dot_ind_in);
%W_ind_out=trapz(time_vec(discharge_process),W_dot_ind_out);
W_ind_in=trapz(V_air(charge_process),P_air(charge_process));
W_ind_out=trapz(V_air(discharge_process),P_air(discharge_process));

%account for pump & turbine efficiency
W_dot_act_in=W_dot_ind_in./eta_pump_vec;
W_dot_act_in2=W_dot_act_in./eta_motor_vec;
W_dot_act_out=W_dot_ind_out.*eta_turb;
W_act_in=trapz(time_vec(charge_process),W_dot_act_in);
W_act_in2=trapz(time_vec(charge_process),W_dot_act_in2);
W_act_out=trapz(time_vec(discharge_process),W_dot_act_out);

%good generator start
%regression tree
fn='efficiency_data.xlsx';
sn='regression data';
range='D8:F104';
data=xlsread(fn,sn,range);
x_reg=data(:,2:3);
y=data(:,1);
tree=fitrtree(x_reg,y);

eta_gen_guess=0.85*ones(length(W_dot_act_out),1);
power=zeros(length(W_dot_act_out),1);
eta_gen=zeros(length(W_dot_act_out),1);
stop_crit=0.0001;
for i=1:length(W_dot_act_out)
    power(i)=(W_dot_ind_out(i)*eta_turb(i)*eta_gen_guess(i));
    eta_gen(i)=predict(tree,[real(power(i)),real(N(i))]);
    while abs(eta_gen_guess(i)-eta_gen(i))>stop_crit
        power(i)=(W_dot_ind_out(i)*eta_turb(i)*eta_gen_guess(i));
        eta_gen(i)=predict(tree,[real(power(i)),real(N(i))]);
        eta_gen_guess(i)=eta_gen(i);
    end
end

power=real((W_dot_ind_out.*eta_turb.*eta_gen_guess));
I=power./120;
W_dot_act_out2=W_dot_act_out.*eta_gen;
W_act_out2=trapz(time_vec(discharge_process),W_dot_act_out2);
%good generator end

% %bad generator start
% gen_volt=120;
% eta_gen_guess=0.85*ones(length(W_dot_act_out),1);
% I=zeros(length(W_dot_act_out),1);
% eta_gen=zeros(length(W_dot_act_out),1);
% stop_crit=0.0001;
% for i=1:length(W_dot_act_out)
%     I(i)=(W_dot_ind_out(i)*eta_turb(i)*eta_gen_guess(i))/gen_volt;
%     eta_gen(i)=(71.3931819915863+2.43125564707891*I(i)+-0.0577927509063142*I(i)^2+-
0.00799868154509985*N(i)+-3.16589896506066E-07*N(i)^2+0.000216227680853878*I(i)*N(i))/100;
```

```
%     while abs(eta_gen_guess(i)-eta_gen(i))>stop_crit
%         I(i)=(W_dot_ind_out(i)*eta_turb(i)*eta_gen_guess(i))/gen_volt;
%         eta_gen(i)=(71.3931819915863+2.43125564707891*I(i)+-0.0577927509063142*I(i)^2+-
0.00799868154509985*N(i)+-3.16589896506066E-07*N(i)^2+0.000216227680853878*I(i)*N(i))/100;
%         eta_gen_guess(i)=eta_gen(i);
%     end
% end
%
% I=(W_dot_ind_out.*eta_turb.*eta_gen)./120;
% W_dot_act_out2=W_dot_act_out.*eta_gen;
% power=W_dot_act_out2;
% W_act_out2=trapz(time_vec(begin_exp_time:end_exp_time),W_dot_act_out2);
% %bad generator end

%plot(time_vec(begin_exp_time:end_exp_time),W_dot_act_out.*eta_gen,time_vec(begin_exp_time:end_ex
p_time),120.*I)
%plot(time_vec(begin_exp_time:end_exp_time),W_dot_act_out2,time_vec(begin_exp_time:end_exp_time),
W_dot_ind_out.*eta_turb.*eta_gen)

%recirculation pump
W_dot_recirc_charge=W_dot_recirc.*ones(length(charge_process),1);
W_dot_recirc_discharge=W_dot_recirc.*ones(length(discharge_process),1);
W_recirc_charge=trapz(time_vec(charge_process),W_dot_recirc_charge);
W_recirc_discharge=trapz(time_vec(discharge_process),W_dot_recirc_discharge);
W_recirc_total=W_recirc_charge+W_recirc_discharge;

%make everything real
W_ind_out=real(W_ind_out);
W_ind_in=real(W_ind_in);
W_act_out2=real(W_act_out2);
W_act_in2=real(W_act_in2);
W_recirc_total=real(W_recirc_total);
heat_input=heat_input_2_kJ*1000;
heat_input=real(heat_input);

%RTE
%RTE_ind=abs(W_ind_out/W_ind_in);
%RTE_act=W_act_out2/(-W_act_in2-W_recirc_total);
%RTE_ex=W_act_out2/((-W_act_in2-W_recirc_total)+eta_carnot*heat_input);

RTE_ind=abs(W_ind_out/W_ind_in);
RTE_act=abs(W_act_out2/(W_act_in2-W_recirc_total));
%RTE_ex=abs(W_act_out2/((W_act_in2-W_recirc_total)-eta_carnot*heat_input));
RTE_ex_ind=abs(W_ind_out/(W_ind_in-eta_carnot*heat_input));
RTE_ex_elec=abs(W_act_out2/(W_act_in2-eta_carnot*heat_input));
Q_ex_in=eta_carnot*heat_input;

%specific energy
SE_ind=real((W_ind_out/1000)/max(V_air));
SE_act=real((W_act_out2/1000)/max(V_air));

%efficiencies
eta_iso=abs(W_out_iso/W_in_iso);
eta_ind=abs(W_ind_out/W_ind_in);
eta_4=abs(W_ind_out/W_act_in);
eta_3=abs(W_ind_out/W_act_in2);
eta_2=abs(W_act_out/W_act_in2);
eta_1=abs(W_act_out2/W_act_in2);

%losses
total_eff_loss=eta_iso-eta_1;
exp_comp_loss=eta_iso-eta_ind;
pump_losses=eta_ind-eta_4;
motor_losses=eta_4-eta_3;
turb_losses=eta_3-eta_2;
gen_losses=eta_2-eta_1;
```

Supporting Function 2:

This function is a flow model which calculates the discharge flow rate of the GLIDES system using the fluid flow equations for a piping network. It calculates the flow rate in liters per min and the pressure drop through the piping system. Inputs are the pressure at the inlet, the number of jets, number of tanks, the fluid density and viscosity.

```
function [total_lit_min_SI,total_lit_min,ploss,loss_check] =
glides_flow(initial_pressure,num_jets,num_tanks,kinematic_viscosity,rho)


%friction factor correlation from (Evangleids, Papaevangelou, Tzimopoulos
%2010)
pipe_diameter = 0.78 * 0.0254; % meter
area = pi * pipe_diameter ^ 2 / 4;
pipe_1_length = 27 * 0.0254;
pipe_2_length = 22 * 0.0254;
pipe_3_length = 83.5 * 0.0254;
%initial_pressure = 130e5; % N/m2
flow = 0.00006; % initial guess (flow from each vessel), m3/s
%kinematic_viscosity = 1e-6; %m2/s
%rho = 1000; % kg/m3
roughness = 0.061e-3;
%knozzle = 0.04;
nozzle_diameter = 0.00143; % mm
condition = 0;
while (condition > 1.02 || condition < 0.98)
    % Calculate friction coefficient based on flow
    Re = flow * pipe_diameter / (kinematic_viscosity * area);
    if Re < 3200
        f = Re / 64;
    else
        f=(0.2479-0.0000947*(7-
log10(Re))^4)/(log10(roughness/(3.615*pipe_diameter)+7.366/Re^0.9142))^2;
    end
    p2 = initial_pressure - flow^2 * rho / pi^2 * (24 / pipe_diameter ^ 4 + 8 * f * pipe_1_length
/ pipe_diameter^5);
    %p2 = initial_pressure - flow^2 * rho / pi^2 * ((6*num_tanks) / pipe_diameter ^ 4 +
2*num_tanks * f * pipe_1_length / pipe_diameter^5);
    Re = (num_tanks/2) * flow * pipe_diameter / (kinematic_viscosity * area);
    if Re < 3200
        f = Re / 64;
    else
        f=(0.2479-0.0000947*(7-
log10(Re))^4)/(log10(roughness/(3.615*pipe_diameter)+7.366/Re^0.9142))^2;
    end
    p3 = p2 - 4 * flow^2 * rho / pi^2 * (12 / pipe_diameter ^ 4 + 8 * f * pipe_2_length /
pipe_diameter^5);
    %p3 = p2 - num_tanks * flow^2 * rho / pi^2 * ((3*num_tanks) / pipe_diameter ^ 4 + 2*num_tanks
* f * pipe_2_length / pipe_diameter^5);
    %Re = 4 * flow * pipe_diameter / (kinematic_viscosity * area);
    Re = num_tanks * flow * pipe_diameter / (kinematic_viscosity * area);
    c_d=0.9900-0.2262*(nozzle_diameter/pipe_diameter)^4.1-
(0.00175*(nozzle_diameter/pipe_diameter)^2-
0.0033*(nozzle_diameter/pipe_diameter)^4.15)*(10^6/Re)^1.15;
    knozzle=1/c_d^2-1;
    if Re < 3200
        f = Re / 64;
    else
        f=(0.2479-0.0000947*(7-
log10(Re))^4)/(log10(roughness/(3.615*pipe_diameter)+7.366/Re^0.9142))^2;
    end
    flow_check = sqrt(p3 * pi^2 / rho / 16 / ((8 + 8 * knozzle) / nozzle_diameter^4 + 32 /
pipe_diameter^4 + 8 * f * pipe_3_length / pipe_diameter^5));
    %flow_check = sqrt(p3 * pi^2 / rho / (4*num_tanks) / (((2*num_tanks) + (2*num_tanks) *
knozzle) / nozzle_diameter^4 + (8*num_tanks) / pipe_diameter^4 + (2*num_tanks) * f *
pipe_3_length / pipe_diameter^5));
    condition = flow_check / flow;
    flow = flow_check;
end
% Individual vessel discharge
```

```
flow_lit_min = flow * 1000 * 60;
% Total flow to the turbine
total_lit_min = num_tanks * num_jets * flow_lit_min;
V_dot_noloss=num_jets*pi*nozzle_diameter^2/4*sqrt(2*initial_pressure/rho);
total_lit_min_SI=total_lit_min/60*10^-3;
ploss=(initial_pressure-
(rho/2*((total_lit_min_SI/num_jets)/(c_d*pi/4*nozzle_diameter^2))^2))/10^5;
loss_check=100*(total_lit_min_SI/V_dot_noloss);
```

Published with MATLAB® R2016b

APPENDIX B: CONDENSABLE GAS SIMULATION CODES

written in: MATLAB R2016b

This code simulates the compression and expansion of condensable gases such as R134a and carbon dioxide. It requires the CoolProp thermodynamic properties package to run. Outputs are the transient pressure, temperature, volume, quality profiles of the working fluid, (liquid and vapor). Inputs are the working fluid, the system parameters (storage volume, oil charging flow rate, overall heat transfer coefficient, pause lengths), and the initial conditions (temperature).

```
clear
clc

%add CoolProp to path
addpath('C:\Program Files\MATLAB\R2016b\CoolPropMatlab')

%knowns
V_tube=2;
deltat=8;
V_dot_val=20;
V_dot_oil=V_dot_val*1.6667e-5; %liters/min converted to m^3/s
fluid='CarbonDioxide'; %working fluid
R=(CoolProp.PropsSI('gas_constant','T',0,'Q',0,fluid))/(CoolProp.PropsSI('M','T',0,'Q',0,fluid));
UA=100000;
%UA=0;
%UA=200;
T_amb=25+273.15;
pause_length=1*60*60;
pause_length2=1*60*60;

%initialize vectors
c_liq=zeros(5,1);
c_vap=zeros(5,1);
V_dot_oil_vec=zeros(5,1);
dV_dt_liq=zeros(5,1);
dV_dt_vap=zeros(5,1);
h_fg=zeros(5,1);
m_dot_cond=zeros(5,1);
m_liq=zeros(5,1);
m_vap=zeros(5,1);
rho_ave=zeros(5,1);
P=zeros(5,1);
```

```
Q=zeros(5,1);
rho_liq=zeros(5,1);
rho_rat=zeros(5,1);
rho_vap=zeros(5,1);
T=zeros(5,1);
V_liq=zeros(5,1);
V_oil=zeros(5,1);
V_tot=zeros(5,1);
V_vap=zeros(5,1);
vol_check=zeros(5,1);
UA_vec=zeros(5,1);

%initial conditions - saturated vapor
T(1)=25+273.15;
P(1)=CoolProp.PropsSI('P','T',T(1),'Q',Q(1),fluid);
V_oil(1)=0;
V_vap(1)=V_tube-V_oil(1); %m^3
V_liq(1)=V_tube-V_vap(1)-V_oil(1); %m^3
V_tot(1)=V_vap(1)+V_liq(1);
rho_vap(1)=CoolProp.PropsSI('D','T',T(1),'Q',1,fluid);
rho_liq(1)=CoolProp.PropsSI('D','T',T(1),'Q',0,fluid);
m_vap(1)=rho_vap(1)*V_vap(1);
m_liq(1)=rho_liq(1)*V_liq(1);
m_tot=m_vap(1)+m_liq(1);
%Q(1)=m_vap(1)/m_tot;
rho_ave(1)=m_tot/V_tot(1);
Q(1)=((1/rho_ave(1))-(1/rho_liq(1)))/(1/(rho_vap(1))-(1/rho_liq(1)));
rho_rat(1)=rho_vap(1)/rho_liq(1);
V_dot_oil_vec(1)=V_dot_oil;
dV_dt_vap(1)=0;
dV_dt_liq(1)=0;
vol_check(1)=V_oil(1)+V_vap(1)+V_liq(1);
m_dot_cond(1)=abs(rho_vap(1)*dV_dt_vap(1));
c_liq(1)=CoolProp.PropsSI('C','T',T(1),'Q',1-Q(1),fluid);
c_vap(1)=CoolProp.PropsSI('C','T',T(1),'Q',Q(1),fluid);
h_fg(1)=(CoolProp.PropsSI('H','T',T(1),'Q',1,fluid))-
(CoolProp.PropsSI('H','T',T(1),'Q',0,fluid));
UA_vec(1)=UA;

%loop to step through time
time=1;
i=2;
while Q(i-1)>0 %time<2*60*60
    %update rate of oil flow rate vec
    V_dot_oil_vec(i)=V_dot_oil;

    %update oil volume and co2 volume
    V_oil(i)=V_oil(i-1)+V_dot_oil_vec(i)*deltat;
    V_tot(i)=V_tot(i-1)-(V_oil(i)-V_oil(i-1));
    %V_tot(i)=V_tot(1)-V_oil(i)

    %evaluate properties
    rho_vap(i)=CoolProp.PropsSI('D','T',T(i-1),'Q',1,fluid);
    rho_liq(i)=CoolProp.PropsSI('D','T',T(i-1),'Q',0,fluid);
```

```
    rho_rat(i)=rho_vap(i)/rho_liq(i);
    h_fg(i)=(CoolProp.PropsSI('H','T',T(i-1),'Q',1,fluid))-(CoolProp.PropsSI('H','T',T(i-
1),'Q',0,fluid));
    c_vap(i)=CoolProp.PropsSI('C','T',T(i-1),'Q',1,fluid);
    c_liq(i)=CoolProp.PropsSI('C','T',T(i-1),'Q',0,fluid);

    %calculate quality
    rho_ave(i)=m_tot/V_tot(i);
    Q(i)=((1/rho_ave(i))-(1/rho_liq(i)))/((1/rho_vap(i))-(1/rho_liq(i)));

    %update masses
    m_vap(i)=Q(i)*m_tot;
    m_liq(i)=(1-Q(i))*m_tot;

    %calculate mass rate of condensation
    m_dot_cond(i)=abs(m_vap(i)-m_vap(i-1))/deltat;

    %update vapor and liquid volumes
    V_vap(i)=m_vap(i)/rho_vap(i);
    V_liq(i)=V_tot(i)-V_vap(i);
    vol_check(i)=(V_oil(i)+V_vap(i)+V_liq(i))-V_tot(1);

    %update rate of change of volumes
    dV_dt_vap(i)=(V_vap(i)-V_vap(i-1))/deltat;
    dV_dt_liq(i)=(V_liq(i)-V_liq(i-1))/deltat;

    %update temperature
    UA_vec(i)=UA;
    %UA_vec(i)=UA*(V_tot(i)./V_tot(1));
    T(i)=T(i-1)+(((-rho_vap(i)*dV_dt_vap(i)*h_fg(i))-UA_vec(i)*(T(i-1)-T_amb)-P(i-
1)*V_dot_oil_vec(i))/(m_tot*(Q(i)*c_vap(i)+(1-Q(i))*c_liq(i))))*deltat;

    %update pressure
    P(i)=CoolProp.PropsSI('P','T',T(i),'Q',Q(i),fluid);

    time=time+deltat;
    i=i+1;
end
comp_time=time;

%calculate charging pi number
%T_sat=CoolProp.PropsSI('T','P',P(1),'Q',Q(1),fluid);
pi_c=(UA*1*time)/(rho_vap(1)*h_fg(1)*V_tot(1));

%calculate stored energy
W_dot_in=P.*V_dot_oil;
W_in=trapz(1:deltat:comp_time,W_dot_in);

%calculate isothermal compression work
W_iso=m_tot*(CoolProp.PropsSI('H','T',T(1),'Q',Q(1),fluid)-
CoolProp.PropsSI('H','T',T(1),'Q',Q(end),fluid));

%i=i+1;
%time=time+deltat;
```

```
V_dot_oil=0;
%pause loop
while time<(comp_time+pause_length)
    %update rate of oil flow rate vec
    V_dot_oil_vec(i)=V_dot_oil;

    %update oil volume and co2 volume
    V_oil(i)=V_oil(i-1)+V_dot_oil_vec(i)*deltat;
    V_tot(i)=V_tot(i-1)-(V_oil(i)-V_oil(i-1));
    %V_tot(i)=V_tot(1)-V_oil(i);

    %evaluate properties
    rho_vap(i)=CoolProp.PropsSI('D','T',T(i-1),'Q',1,fluid);
    rho_liq(i)=CoolProp.PropsSI('D','T',T(i-1),'Q',0,fluid);
    rho_rat(i)=rho_vap(i)/rho_liq(i);
    h_fg(i)=(CoolProp.PropsSI('H','T',T(i-1),'Q',1,fluid))-(CoolProp.PropsSI('H','T',T(i-
1),'Q',0,fluid));
    c_vap(i)=CoolProp.PropsSI('C','T',T(i-1),'Q',1,fluid);
    c_liq(i)=CoolProp.PropsSI('C','T',T(i-1),'Q',0,fluid);

    %calculate quality
    rho_ave(i)=m_tot/V_tot(i);
    Q(i)=((1/rho_ave(i))-(1/rho_liq(i)))/((1/rho_vap(i))-(1/rho_liq(i)));

    %update masses
    m_vap(i)=Q(i)*m_tot;
    m_liq(i)=(1-Q(i))*m_tot;

    %calculate mass rate of condensation
    m_dot_cond(i)=abs(m_vap(i)-m_vap(i-1))/deltat;

    %update vapor and liquid volumes
    V_vap(i)=m_vap(i)/rho_vap(i);
    %V_liq(i)=V_tot(i)-V_vap(i);
    V_liq(i)=m_liq(i)/rho_liq(i);
    vol_check(i)=(V_oil(i)+V_vap(i)+V_liq(i))-V_tot(1);

    %update rate of change of volumes
    dV_dt_vap(i)=(V_vap(i)-V_vap(i-1))/deltat;
    dV_dt_liq(i)=(V_liq(i)-V_liq(i-1))/deltat;

    %update temperature
    UA_vec(i)=UA;
    %UA_vec(i)=UA*(V_tot(i)./V_tot(1));
    T(i)=T(i-1)+(((-rho_vap(i)*dV_dt_vap(i)*h_fg(i))-UA_vec(i)*(T(i-1)-T_amb)-P(i-
1)*V_dot_oil_vec(i))/(m_tot*(Q(i)*c_vap(i)+(1-Q(i))*c_liq(i))))*deltat;

    %update pressure
    P(i)=CoolProp.PropsSI('P','T',T(i),'Q',Q(i),fluid);

    time=time+deltat;
    i=i+1;
end
pause_time=time;
```

```
%expansion loop
V_dot_oil=-V_dot_val*1.6667e-5;
while V_tot(i-1)<V_tube %V_oil(i-1)>0.05
    %update rate of oil flow rate vec
    V_dot_oil_vec(i)=V_dot_oil;

    %update oil volume and co2 volume
    V_oil(i)=V_oil(i-1)+V_dot_oil_vec(i)*deltat;
    V_tot(i)=V_tot(i-1)-(V_oil(i)-V_oil(i-1));
    %V_tot(i)=V_tot(1)-V_oil(i);

    %evaluate properties
    rho_vap(i)=CoolProp.PropsSI('D','T',T(i-1),'Q',1,fluid);
    rho_liq(i)=CoolProp.PropsSI('D','T',T(i-1),'Q',0,fluid);
    rho_rat(i)=rho_vap(i)/rho_liq(i);
    h_fg(i)=(CoolProp.PropsSI('H','T',T(i-1),'Q',1,fluid))-(CoolProp.PropsSI('H','T',T(i-
1),'Q',0,fluid));
    c_vap(i)=CoolProp.PropsSI('C','T',T(i-1),'Q',1,fluid);
    c_liq(i)=CoolProp.PropsSI('C','T',T(i-1),'Q',0,fluid);

    %calculate quality
    rho_ave(i)=m_tot/V_tot(i);
    Q(i)=((1/rho_ave(i))-(1/rho_liq(i)))/((1/rho_vap(i))-(1/rho_liq(i)));

    %update masses
    m_vap(i)=Q(i)*m_tot;
    m_liq(i)=(1-Q(i))*m_tot;

    %calculate mass rate of condensation
    m_dot_cond(i)=abs(m_vap(i)-m_vap(i-1))/deltat;

    %update vapor and liquid volumes
    V_vap(i)=m_vap(i)/rho_vap(i);
    V_liq(i)=V_tot(i)-V_vap(i);
    vol_check(i)=(V_oil(i)+V_vap(i)+V_liq(i))-V_tot(1);

    %update rate of change of volumes
    dV_dt_vap(i)=(V_vap(i)-V_vap(i-1))/deltat;
    dV_dt_liq(i)=(V_liq(i)-V_liq(i-1))/deltat;

    %update temperature
    UA_vec(i)=UA;
    %UA_vec(i)=UA*(V_tot(i)./V_tot(1));
    T(i)=T(i-1)+(((-rho_vap(i)*dV_dt_vap(i)*h_fg(i))-UA_vec(i)*(T(i-1)-T_amb)-P(i-
1)*V_dot_oil_vec(i))/(m_tot*(Q(i)*c_vap(i)+(1-Q(i))*c_liq(i))))*deltat;

    %update pressure
    P(i)=CoolProp.PropsSI('P','T',T(i),'Q',Q(i),fluid);

    time=time+deltat;
    i=i+1;
end
exp_time=time;
```

```
%calculate recovered energy
start=(pause_time-1)/deltat;
through=start+((exp_time-pause_time)/deltat);
W_dot_out=P(start:through).*-V_dot_oil;
W_out=trapz(pause_time:deltat:exp_time,W_dot_out);

V_dot_oil=0;
%second pause loop
while time<(exp_time+pause_length2)
    %update rate of oil flow rate vec
    V_dot_oil_vec(i)=V_dot_oil;

    %update oil volume and co2 volume
    V_oil(i)=V_oil(i-1)+V_dot_oil_vec(i)*deltat;
    V_tot(i)=V_tot(i-1)-(V_oil(i)-V_oil(i-1));
    %V_tot(i)=V_tot(1)-V_oil(i);

    %evaluate properties
    rho_vap(i)=CoolProp.PropsSI('D','T',T(i-1),'Q',1,fluid);
    rho_liq(i)=CoolProp.PropsSI('D','T',T(i-1),'Q',0,fluid);
    rho_rat(i)=rho_vap(i)/rho_liq(i);
    h_fg(i)=(CoolProp.PropsSI('H','T',T(i-1),'Q',1,fluid))-(CoolProp.PropsSI('H','T',T(i-
1),'Q',0,fluid));
    c_vap(i)=CoolProp.PropsSI('C','T',T(i-1),'Q',1,fluid);
    c_liq(i)=CoolProp.PropsSI('C','T',T(i-1),'Q',0,fluid);

    %calculate quality
    rho_ave(i)=m_tot/V_tot(i);
    Q(i)=((1/rho_ave(i))-(1/rho_liq(i)))/((1/rho_vap(i))-(1/rho_liq(i)));

    %update masses
    m_vap(i)=Q(i)*m_tot;
    m_liq(i)=(1-Q(i))*m_tot;

    %calculate mass rate of condensation
    m_dot_cond(i)=abs(m_vap(i)-m_vap(i-1))/deltat;

    %update vapor and liquid volumes
    V_vap(i)=m_vap(i)/rho_vap(i);
    %V_liq(i)=V_tot(i)-V_vap(i);
    V_liq(i)=m_liq(i)/rho_liq(i);
    vol_check(i)=(V_oil(i)+V_vap(i)+V_liq(i))-V_tot(1);

    %update rate of change of volumes
    dV_dt_vap(i)=(V_vap(i)-V_vap(i-1))/deltat;
    dV_dt_liq(i)=(V_liq(i)-V_liq(i-1))/deltat;

    %update temperature
    UA_vec(i)=UA;
    %UA_vec(i)=UA*(V_tot(i)./V_tot(1));
    T(i)=T(i-1)+(((-rho_vap(i)*dV_dt_vap(i)*h_fg(i))-UA_vec(i)*(T(i-1)-T_amb)-P(i-
1)*V_dot_oil_vec(i))/(m_tot*(Q(i)*c_vap(i)+(1-Q(i))*c_liq(i))))*deltat;
```

```
    %update pressure
    P(i)=CoolProp.PropsSI('P','T',T(i),'Q',Q(i),fluid);

    time=time+deltat;
    i=i+1;
end

%calculate efficiency & energy density
eta_ind=W_out/W_in
ED_ind=(W_out*2.77778e-7)/V_vap(1)

%time vector in mins
time_mins=(1:deltat:time)./60;

%plot volumes

%plot masses
plot(time_mins,V_vap,time_mins,V_liq,time_mins,V_liq+V_vap,time_mins,V_oil,time_mins,V_liq+V_vap+
V_oil);
set(gca,'FontSize',14)
legend('Volume of Vapor','Volume of Liquid','Total CO_2 Volume','Volume of Oil','Total Volume')
xlabel('Time [minutes]','FontSize',16,'FontWeight','bold')
ylabel('Volume [m^3]','FontSize',16,'FontWeight','bold')
ylim([0,1.2])

figure
plot(time_mins,m_vap,time_mins,m_liq,time_mins,m_vap+m_liq)
set(gca,'FontSize',14)
xlabel('Time [minutes]','FontSize',16,'FontWeight','bold')
ylabel('Mass [kg]','FontSize',16,'FontWeight','bold')
legend('Mass of Vapor','Mass of Liquid','Total Mass of CO_2')
ylim([0,250])

%plot temperature & pressure
figure
plot(time_mins,T-273.15)
set(gca,'FontSize',14)
xlabel('Time [minutes]','FontSize',16,'FontWeight','bold')
hold on
yyaxis right
plot(time_mins,P./10^5)
yyaxis left
ylabel('Temperature [°C]','FontSize',16,'FontWeight','bold')
yyaxis right
ylabel('Pressure [bar]','FontSize',16,'FontWeight','bold')
legend('Temperature','Pressure')

%plot quality
figure
plot(time_mins,Q)
set(gca,'FontSize',14)
xlabel('Time [minutes]','FontSize',16,'FontWeight','bold')
ylabel('Quality [-]','FontSize',16,'FontWeight','bold')
ylim([0,1.2])
```

```
%plot p-V
figure
plot(V_tot./m_tot,P./100000)
set(gca,'FontSize',14)
xlabel('Specific Volume [m^3/kg]','FontSize',16,'FontWeight','bold')
ylabel('Pressure [bar]','FontSize',16,'FontWeight','bold')
ylim([55,75])
%axis([1.5E-3,4.5E-3,55,75])
```

Published with MATLAB® R2016b

APPENDIX C: FORWARD COST ANALYSIS ASSUMPTIONS

Equipment assumptions for steel pressure vessels and carbon fiber cylinders as storage

- Storage medium
  - Steel pressure vessels
    - Pressure vessel design optimized
    - GLIDES max/min pressure optimized for PV cost
  - Carbon fiber cylinders
    - Cost data for various cylinder volumes from manufacturer
    - Cylinder volume resulting in lowest total cylinder cost chosen
- Additional piping
  - 10 ft./tank, $15/ft.
- Fittings (tees, crosses, bends, etc.)
  - 2 fittings/tank, $40/fitting
- Valves
  - 5 valves plus 2 valves/tank, $250/valve
- Electromechanical equipment (pump/turbine)
  - The electromechanical equipment, including the pump/motor and turbine/generator/governor costs ($/kW), are assumed to scale with installed capacity. Five small hydropower Pelton turbine/generator/governor concept cost estimate curves available in the literature [79-83] were average to give a concept cost per installed kW. Pump/motor concept cost estimates were developed from a cost catalog [84], and concept costs also scaled with installed capacity.

Equipment assumptions for steel pipe segments as storage

- Storage medium
  - 30 in. diameter pipe, sched. 80 (Pmax=153 bar)
  - GLIDES operates b/w 70 bar and 140 bar
- Additional piping
  - 10 ft./kWh, $15/ft.
- Fittings (tees, crosses, bends, etc.)
  - 4 fittings/kWh, $40/fitting
- Valves
  - 5 valves plus 1 valve/500 m of piping, $250/valve
- Electromechanical equipment (pump/turbine)

- The electromechanical equipment, including the pump/motor and turbine/generator/governor costs ($/kW), are assumed to scale with installed capacity. Five small hydropower Pelton turbine/generator/governor concept cost estimate curves available in the literature [79-83] were average to give a concept cost per installed kW. Pump/motor concept cost estimates were developed from a cost catalog [84], and concept costs also scaled with installed capacity.

REFERENCES

[1] G. Crabtree, "Perspective: The energy-storage revolution," *Nature,* vol. 526, pp. S92-S92, 10/29/print 2015.

[2] R. C. Armstrong, C. Wolfram, K. P. de Jong, R. Gross, N. S. Lewis, B. Boardman, *et al.*, "The frontiers of energy," *Nature Energy,* vol. 1, p. 15020, 01/11/online 2016.

[3] United States Energy Information Administration. (2012, Electricity storage can smooth out moment-to-moment variations in electricity demand. *Today in Energy*.

[4] S. Chu and A. Majumdar, "Opportunities and challenges for a sustainable energy future," *Nature,* vol. 488, pp. 294-303, 08/16/print 2012.

[5] A. M. Momen, O. Abdelaziz, K. Gluesenkamp, and E. A. Vineyard, "High Efficiency Ground-Level Pumped Hydro Electricity Storage," United States Patent, 2013.

[6] H. H. J. Tackett, J. A. Cripe, and G. Dyson, "Positive Displacement Reciprocating Pump Fundamentals—Power And Direct Active Types," presented at the Proceedings of the Twenty-Fourth International Pump Users Symposium, College Station, TX, USA, 2008.

[7] Oak Ridge National Laboratory and Mesa Associates, "Pelton Turbine Best Practice," ORNL, Ed., ed. Oak Ridge, TN, USA, 2012.

[8] A. Odukomaiya, A. M. Momen, A. Abu-Heiba, K. Gluesenkamp, O. Abdelaziz, and S. Graham, "Transient Thermofluids Analysis of a Ground-Level Integrated Diverse Energy Storage (GLIDES) System," presented at the 2015 International Mechanical Engineering Congress & Exposition, Houston, TX, United States, 2015.

[9] A. Odukomaiya, A. Abu-Heiba, K. Gluesenkamp, O. Abdelaziz, R. Jackson, C. Daniel, *et al.*, "Thermal Analysis of Direct Contact Waste Heat Utilization In a Ground-Level Integrated Diverse Energy Storage (GLIDES) System," O. R. N. Laboratory and G. I. o. Technology, Eds., ed. Oak Ridge, TN, 2016.

[10] R. Guerrero-Lemus, *Renewable Energies and CO2 Cost Analysis, Environmental Impacts and Technological Trends- 2012 Edition*. Dordrecht: Dordrecht : Springer, 2012.

[11] Electrical Power Research Institute, "Bulk Energy Storage Impact and Value Analysis," EPRI 2012.

[12] H. Zhao, Q. Wu, S. Hu, H. Xu, and C. N. Rasmussen, "Review of energy storage system for wind power integration support," *Applied Energy,* vol. 137, pp. 545-553, 2015.

[13] X. Luo, J. Wang, M. Dooner, and J. Clarke, "Overview of current development in electrical energy storage technologies and the application potential in power system operation," *Applied Energy,* vol. 137, pp. 511-536, 2015.

[14] F. Díaz-González, A. Sumper, O. Gomis-Bellmunt, and R. Villafáfila-Robles, "A review of energy storage technologies for wind power applications," *Renewable and Sustainable Energy Reviews,* vol. 16, pp. 2154-2171, 2012.

[15] T. M. I. Mahlia, T. J. Saktisahdan, A. Jannifar, M. H. Hasan, and H. S. C. Matseelar, "A review of available methods and development on energy storage; technology update," *Renewable and Sustainable Energy Reviews,* vol. 33, pp. 532-545, 5// 2014.

[16] J. J. Proczka, K. Muralidharan, D. Villela, J. H. Simmons, and G. Frantziskonis, "Guidelines for the pressure and efficient sizing of pressure vessels for compressed air energy storage," *Energy Conversion and Management,* vol. 65, pp. 597-605, 1// 2013.

[17] A. Chatzivasileiadi, E. Ampatzi, and I. Knight, "Characteristics of electrical energy storage technologies and their applications in buildings," *Renewable and Sustainable Energy Reviews,* vol. 25, pp. 814-830, 9// 2013.

[18] R. Madlener and J. Latz, "Economics of centralized and decentralized compressed air energy storage for enhanced grid integration of wind power," *Applied Energy,* vol. 101, pp. 299-309, 2011.

[19] B. Zakeri and S. Syri, "Electrical energy storage systems: A comparative life cycle cost analysis," *Renewable and Sustainable Energy Reviews,* vol. 42, pp. 569-596, 2// 2015.

[20] Y. Zhang, K. Yang, X. Li, and J. Xu, "The thermodynamic effect of thermal energy storage on compressed air energy storage system," *Renewable Energy,* vol. 50, pp. 227-235, 2// 2013.

[21] C. Bullough, C. Gatzen, C. Jakiel, M. Koller, A. Nowi, and S. Zunft, "Advanced adiabatic compressed air energy storage for the integration of wind energy," in *Proceedings of the European Wind Energy Conference, EWEC,* 2004, p. 25.

[22] N. Hartmann, O. Vöhringer, C. Kruck, and L. Eltrop, "Simulation and analysis of different adiabatic Compressed Air Energy Storage plant configurations," *Applied Energy,* vol. 93, pp. 541-548, 5// 2012.

[23] RWE. *Energy Storage*. Available: http://www.rwe.com/web/cms/en/183748/rwe/innovation/projects-technologies/energy-storage/

[24] Y. M. Kim and D. Favrat, "Energy and exergy analysis of a micro-compressed air energy storage and air cycle heating and cooling system," *Energy,* vol. 35, pp. 213-220, 1// 2010.

[25] A. L. Facci, D. Sanchez, E. Jannelli, and S. Ubertini, "Trigenerative micro compressed air energy storage: Concept and thermodynamic assessment," *Applied Energy,* vol. 158, pp. 243-254, 2015.

[26] Y. Li, X. Wang, D. Li, and Y. Ding, "A trigeneration system based on compressed air and thermal energy storage," *Applied Energy,* vol. 99, pp. 316-323, 11// 2012.

[27] D. Wolf and M. Budt, "LTA-CAES – A low-temperature approach to Adiabatic Compressed Air Energy Storage," *Applied Energy*, vol. 125, pp. 158-164, 7/15/ 2014.

[28] R. Morgan, S. Nelmes, E. Gibson, and G. Brett, "Liquid air energy storage – Analysis and first results from a pilot scale demonstration plant," *Applied Energy*, vol. 137, pp. 845-853, 1/1/ 2015.

[29] B. Kantharaj, S. Garvey, and A. Pimm, "Compressed air energy storage with liquid air capacity extension," *Applied Energy*, vol. 157, pp. 152-164, 2015.

[30] B. Kantharaj, S. Garvey, and A. Pimm, "Thermodynamic analysis of a hybrid energy storage system based on compressed air and liquid air," *Sustainable Energy Technologies and Assessments*, 2014.

[31] J. Howes, "Concept and Development of a Pumped Heat Electricity Storage Device," *Proceedings of the IEEE*, vol. 100, pp. 493-503, 2012.

[32] D. O. Akinyele and R. K. Rayudu, "Review of energy storage technologies for sustainable power networks," *Sustainable Energy Technologies and Assessments*, vol. 8, pp. 74-91, 12// 2014.

[33] J. D. McTigue, A. J. White, and C. N. Markides, "Parametric studies and optimisation of pumped thermal electricity storage," *Applied Energy*, vol. 137, pp. 800-811, 1/1/ 2015.

[34] Energy Technologies Institute. (2016). *Energy Storage and Distribution*. Available: http://www.eti.co.uk/project/distribution-scale-energy-storage/

[35] C. Qin and E. Loth, "Liquid piston compression efficiency with droplet heat transfer," *Applied Energy*, vol. 114, pp. 539-550, 2// 2014.

[36] C. Qin, E. Loth, P. Li, T. Simon, and J. Van de Ven, "Spray-cooling concept for wind-based compressed air energy storage," *Journal of Renewable and Sustainable Energy*, vol. 6, p. 043125, 2014.

[37] LightSail Energy. *Technology*. Available: http://www.lightsail.com/

[38] M. Minutillo, A. L. Lavadera, and E. Jannelli, "Assessment of design and operating parameters for a small compressed air energy storage system integrated with a stand-alone renewable power plant," *Journal of Energy Storage*, vol. 4, pp. 135-144, 2015.

[39] Z. Wang, D. S.-K. Ting, R. Carriveau, W. Xiong, and Z. Wang, "Design and thermodynamic analysis of a multi-level underwater compressed air energy storage system," *Journal of Energy Storage*, vol. 5, pp. 203-211, 2016.

[40] T. McBride, A. Bell, and D. Kepshire, "ICAES innovation: foam-based heat exchange," 2013.

[41] V. C. Patil, "Efficiency Improvement Techniques for Liquid Piston based Ocean Compressed Air Energy Storage," in *TechConnect World Innovation Conference & Expo*, Washington D.C., 2017, pp. 136-139.

[42] Tesla Motors. (2016). *PowerWall Tesla Home Battery*. Available: https://www.teslamotors.com/powerwall

[43] D. Lisbona and T. Snee, "A review of hazards associated with primary lithium and lithium-ion batteries," *Process Safety and Environmental Protection*, vol. 89, pp. 434-442, 11// 2011.

[44] S. M. Schoenung and W. V. Hassenzahl, "Long- vs. Short-Term Energy Storage Technologies Analysis: A Life-Cycle Cost Study," Sandia National Laboratories, Albuquerque, NM, United States 2003.

[45] V. Shah and J. Booream-Phelps, "Solar Grid Parity in a Low Oil Price Era," Deutsche Bank - Markets Research, United States2015.

[46] H. Wang, L. Wang, X. Wang, and E. Yao, "A Novel Pumped Hydro Combined with Compressed Air Energy Storage System," *Energies*, vol. 6, pp. 1554-1567, 2013.

[47] E. Yao, H. Wang, L. Liu, and G. Xi, "A Novel Constant-Pressure Pumped Hydro Combined with Compressed Air Energy Storage System," *Energies*, vol. 8, pp. 154-171, 2015.

[48] Y. M. Kim, D. G. Shin, and D. Favrat, "Operating characteristics of constant-pressure compressed air energy storage (CAES) system combined with pumped hydro storage based on energy and exergy analysis," *Energy*, vol. 36, pp. 6220-6233, 2011.

[49] S. D. Lim, A. P. Mazzoleni, J.-k. Park, P. I. Ro, and B. Quinlan, "Conceptual design of ocean compressed air energy storage system," *Marine Technology Society Journal*, vol. 47, pp. 70-81, 2013.

[50] S. Lemofouet-Gatsi, "Investigation and optimisation of hybrid electricity storage systems based on compressed air and supercapacitors," 2006.

[51] A. Odukomaiya, A. Abu-Heiba, K. R. Gluesenkamp, O. Abdelaziz, R. K. Jackson, C. Daniel, *et al.*, "Thermal analysis of near-isothermal compressed gas energy storage system," *Applied Energy*, vol. 179, pp. 948-960, 10/1/ 2016.

[52] J. Thake, *The Micro-hydro Pelton Turbine Manual: Design, Manufacture and Installation for Small-scale Hydro-power*: ITDG Pub., 2000.

[53] O. Redlich and J. N. S. Kwong, "On the Thermodynamics of Solutions. V. An Equation of State. Fugacities of Gaseous Solutions," *Chemical Reviews*, vol. 44, pp. 233-244, 1949/02/01 1949.

[54] J. R. Lloyd and W. R. Moran, "Natural Convection Adjacent to Horizontal Surface of Various Planforms," *Journal of Heat Transfer*, vol. 96, p. 443, 1974.

[55] E. J. Lefevre, "Laminar Free Convection from a Vertical Plane Surface," in *Ninth International Congress on Applied Mechanics*, Brussels, 1956.

[56] S. W. Churchill and M. Bernstein, "A Correlating Equation for Forced Convection From Gases and Liquids to a Circular Cylinder in Crossflow," *Journal of Heat Transfer*, vol. 99, p. 300, 1977.

[57] F. Cascella and A. Teyssedou, "Modeling a Direct Contact Heat Exchanger used in a supercritical water loop," *Applied Thermal Engineering*, vol. 79, pp. 132-139, 2015.

[58] W. E. Ranz and W. R. Marshall Jr., "Evaporation From Drops (Part I)," *Chemical Engineering Progress*, vol. 48, pp. 141-146, 1952.

[59] R. K. Shah, "Advances in Science and Technology of Compact Heat Exchangers," *Heat Transfer Engineering*, vol. 27, pp. 3-22, 2006/06/01 2006.

[60] A. Odukomaiya, A. Abu-Heiba, S. Graham, and A. M. Momen, "Preliminary Performance Evaluation of a Ground-Level Integrated Diverse Energy Storage (GLIDES) Prototype System," in *TechConnect World Innovation Conference & Expo*, Washington D.C., United States, 2017, pp. 140-143.

[61] A. Odukomaiya, "Experimental and Analytical Evaluation of a Hydro-Pneumatic Compressed-Air Ground-Level Integrated Diverse Energy Storage (GLIDES) System," ed. Applied Energy, 2017.

[62] R. Foster, M. Ghassemi, and A. Cota, "Premium Efficiency Motor Selection and Application Guide: A Handbook for Industry," U.S. Department of Energy, Washington, D.C.2014.

[63] A. Odukomaiya, E. Kokou, Z. Hussein, A. Abu-Heiba, S. Graham, and A. M. Momen, "Near-isothermal-isobaric compressed gas energy storage," *Journal of Energy Storage*, vol. 12, pp. 276-287, 2017.

[64] L. Nielsen and R. Leithner, "Dynamic simulation of an innovative compressed air energy storage plant-detailed modelling of the storage cavern," *WSEAS Transactions on Power Systems*, vol. 4, pp. 253-263, 2009.

[65] Y. Mazloum, H. Sayah, and M. Nemer, "Dynamic modeling and simulation of an Isobaric Adiabatic Compressed Air Energy Storage (IA-CAES) system," *Journal of Energy Storage*, vol. 11, pp. 178-190, 2017.

[66] B. C. Cheung, R. Carriveau, and D. S.-K. Ting, "Parameters affecting scalable underwater compressed air energy storage," *Applied Energy*, vol. 134, pp. 239-247, 2014.

[67] Z. Wang, W. Xiong, D. S.-K. Ting, R. Carriveau, and Z. Wang, "Conventional and advanced exergy analyses of an underwater compressed air energy storage system," *Applied energy,* vol. 180, pp. 810-822, 2016.

[68] A. J. Pimm, S. D. Garvey, and M. de Jong, "Design and testing of energy bags for underwater compressed air energy storage," *Energy,* vol. 66, pp. 496-508, 2014.

[69] L. X. Chen, M. N. Xie, P. P. Zhao, F. X. Wang, P. Hu, and D. X. Wang, "A novel isobaric adiabatic compressed air energy storage (IA-CAES) system on the base of volatile fluid," *Applied Energy,* vol. 210, pp. 198-210, 2018.

[70] I. H. Bell, J. Wronski, S. Quoilin, and V. Lemort, "Pure and Pseudo-pure Fluid Thermophysical Property Evaluation and the Open-Source Thermophysical Property Library CoolProp," *Industrial & Engineering Chemistry Research,* vol. 53, pp. 2498-2508, 2014.

[71] Z. Zhang, *Pelton Turbines*: Springer, 2016.

[72] United States Department of Energy. (2012). *New Construction - Commercial Reference Buildings*. Available: https://energy.gov/eere/buildings/new-construction-commercial-reference-buildings

[73] D. B. Crawley, L. K. Lawrie, F. C. Winkelmann, W. F. Buhl, Y. J. Huang, C. O. Pedersen, *et al.*, "EnergyPlus: creating a new-generation building energy simulation program," *Energy and Buildings,* vol. 33, pp. 319-331, 4// 2001.

[74] Southern California Edison (SCE). (2015). *Time-of-Use Electricity Schedule*. Available: https://www.sce.com/NR/sc3/tm2/pdf/ce54-12.pdf

[75] Nevada Power Company. *STATEMENT OF RATES EFFECTIVE RATES APPLICABLE TO NEVADA POWER COMPANY ELECTRIC SCHEDULES*. Available: https://www.nvenergy.com/publish/content/dam/nvenergy/brochures_arch/about-nvenergy/rates-regulatory/electric-schedules-south/StatementofRates.pdf

[76] Hawaii Electricity Company. (2012). *SCHEDULE TOU-P - LARGE POWER TIME-OF-USE SERVICE*. Available: https://www.hawaiielectriclight.com/Documents/my_account/rates/hawaii_electric_light_rates/helco_rates_sch_tou_p.pdf

[77] Alaska Electric Light and Power Company (AEL&P). *Current Rates*. Available: https://www.aelp.com/Customer-Service/Rates-Billing/Current-Rates

[78] S. T. McCoy and E. S. Rubin, "An engineering-economic model of pipeline transport of CO2 with application to carbon capture and storage," *International Journal of Greenhouse Gas Control,* vol. 2, pp. 219-229, 4// 2008.

[79] J. L. Gordon and A. C. Penman, "Quick estimating techniques for small hydro potential," *Journal of Water Power and Dam Construction,* vol. 31, pp. 46-51, 1979.

[80] F. Masoudinia, "Retscreen -- Small Hydro Project Software," ed, 2013, pp. 858-861.

[81] B. Ogayar and P. G. Vidal, "Cost determination of the electro-mechanical equipment of a small hydro-power plant," *Renewable Energy,* vol. 34, pp. 6-13, 2009.

[82] NVEnergy, "Cost base for hydropower plants," Norwegian Water Resources and Energy Directorate (NVE) 2012.

[83] *Hydro Resource Evaluation Tool*. Available: http://www.engineering.lancs.ac.uk/lureg/nwhrm/engineering/turbine_costs.php?#tab

[84] McMasterCarr. *Hydraulic Pumps*. Available: http://www.mcmaster.com/#positive-displacement-hydraulic-pumps/=10ojtm3